STUDY OF LINEAR STABILITY AND HEAT TRANSFER CHARACTERISTICS OF WATER FLOWS WITH DENSITY INVERSION

A thesis submitted in partial fulfillment of the requirement
for the degree of

DOCTOR OF PHILOSOPHY

by

RAJENDRA PRASAD SONI
(Roll No. - 146103014)

DEPARTMENT OF MECHANICAL ENGINEERING
INDIAN INSTITUTE OF TECHNOLOGY GUWAHATI, ASSAM
GUWAHATI-781039, INDIA

AUGUST 2021

"*Dedicated to my Parents & Family.*"

DECLARATION

I hereby declare that the work comprises in the Ph.D. thesis, is the outcome of the research work carried out by me in the institute. All the ethics and integrity of the research are taken into consideration while preparing the thesis. The contents used in the present thesis from the literature or any other sources, are properly cited and referred. I also confirm that the contents embodied in the thesis have not been submitted for the award of any other degree or diploma to the current institute or elsewhere.

Signature of the student

Rajendra Prasad Soni
Roll Number : 146103014
Department of Mechanical Engineering
Indian Institute of Technology Guwahati
Guwahati-781039, Assam, India

Date :
Place : Guwahati

ABSTRACT

The present work is concerned about the study of convective flows of water near its density inversion. Linear stability and heat transfer characteristics of the water flows are studied. The present study focuses on the temperature range in which water shows density inversion. First, the solutions of convection boundary layer flows are obtained using perturbation and similarity transformation methods. The linear stability analysis of natural and mixed convection boundary layer flows is carried out for temporal and spatial stability. The global stability of mixed convection flows in lid driven cavity is studied.

Solutions of mixed convection boundary layer flows of water, with density inversion, about a vertical plate are presented using perturbation method. Solutions are presented for both varying wall temperature and heat flux. Aiding as well as opposing mixed convection flow configurations are considered in the study. The perturbation solutions are presented in terms of universal functions which are valid for arbitrary continuous variation of wall temperature or wall heat flux thermal conditions, and hence, the solutions of boundary layer flows with arbitrarily varying wall temperature or wall heat flux can be obtained. Similarity solutions for natural and mixed convection boundary layer flows over a vertical plate with power law varying wall heat flux, are presented which are not available in the literature. The similarity solutions for mixed convection are presented for both assisting and opposing mixed convection configurations. The above perturbation solutions and similarity solutions are presented for velocity, temperature, velocity and thermal boundary layer thicknesses, skin friction coefficients, Nusselt numbers for various flow parameters such as Richardson number and Reynolds number.

Further, linear stability analysis of natural convection boundary layer flows of water near its density inversion is carried out. Both the temporal and spatial stability analysis are carried out. The stability of natural convection is studied for isothermal and isoflux wall conditions. Inclination effect on the natural convection is presented. The critical value of buoyancy parameter for natural convection over isothermal plate is found to be 22.84 and the corresponding wave number and circular frequencies are 0.604, and 0.0944. The critical value of buoyancy parameter for natural convection over isoflux plate is found to be 75.481 and the corresponding wave number, circular frequency and phase speed are found to be 0.633, 0.056 and 0.036, respectively. For both isothermal and isoflux plates, when the plate is tilted in anti-clockwise and clockwise directions, the convection becomes more unstable and more stable, respectively, compared to vertical orientation. For both thermal conditions, critical wave number and critical frequency of the most unstable disturbance increases with inclination. However, the phase speed is not affected by the inclination. The inclination has stronger effect at higher wave numbers. The instability at lower wave numbers are not affected by the inclination.

Linear stability analysis is also carried out for mixed convection boundary layer flows over an isothermal vertical flat plate. The stability is studied for both temporal and spatial stability characteristics. The results are presented for neutral stability curves, Eigenvalue spectrum, critical Eigenfunctions and critical convection parameters. Mixed convection flow is formulated such a way that when Richardson number varies from 0 to ∞, the convection varies smoothly from pure forced convection to pure natural convection through mixed convection. For $Ri = 0$ and $Ri \to \infty$, from the

mixed convection formulation, the results of forced and natural convection asymptotes are recovered accurately. Such formulation is carried out by choosing an appropriate scaling parameters for non-dimensionalisation. The inclination effect is also studied.

The work is extended to study global linear stability of mixed convection flows of water with density inversion in a lid driven differentially side heated square cavity. The stability characteristics show dramatic changes with variation of Richardson number. In the range of Richardson number 0 to 0.4, the critical Reynolds number is almost constant with a value of about 4550. In the range of 0.4 to 0.6, the critical Reynolds number decreases drastically to a values of 1325. For Richardson number 0.6 to 1, critical Reynolds number increases to 2354.23. Beyond which the Reynolds number decreases with Richardson numbers. The drastic instability near Richardson number 0.4 to 0.5 is found to be due to the formation of thin recirculation under primary recirculation, which is highly unstable. In the range of Richardson number 0 to 0.4, the most unstable Eigenvalue has zero real part indicating a stationary mode which does not change with time. For Richardson number greater than 0.4, the most unstable Eigenvalue is a pair of complex conjugate Eigenvalues indicating a Hopf mode which is a time dependent disturbance. For pure forced convection asymptote, the most unstable mode is found to be thermal mode.

Contents

Nomenclature

A	constant in power law variation of wall temperature or wall heat flux
A_{11}, A_{12}, A_{21}, A_{22}	matrices in temporal Eigenvalue formulation
B_{11}, B_{12}, B_{21}, B_{22}	matrices in temporal Eigenvalue formulation
c_p	specific heat (J/kg-K)
c	dimensional phase speed (m/s)
C	dimensionless phase speed
C_i	imaginary part of dimensionless phase speed
C_r	real part of dimensionless phase speed
C_f	skin friction coefficient
C_0, C_1, C_2, C_3, C_4,	matrices of spatial stability Eigenvalue formulation
C_5, C_6, C_7, C_8, C_9	
E_0, E_1, E_2, E_3, E_4, E_5	matrices of spatial stability Eigenvalue formulation
D	differential operator
f	non-dimensional stream function
$F, f_0, f_1, \ldots,$	universal functions for velocity in
$f_{00}, f_{11}(\eta) \ldots$	perturbation technique
g	gravitational acceleration (m/s^2)
G	dimensionless buoyancy parameter
Gr	Grashof number
h	heat transfer coefficient (W/m^2 K)
$H, \theta_0, \theta_1, \ldots,$	universal functions for temperature
$\theta_{00}, \theta_{11}(\eta) \ldots$	in perturbation technique
i	imaginary unit in complex number
k	thermal conductivity of fluid (W/m K)
L	length of the cavity (m)
m	power index of power law variation of wall temperature or wall heat flux
N	number of grid points
Nu	Nusselt number
$\bar{p}$	base flow pressure (kg-m/s^2)
$\hat{p}$	disturbance pressure (kg-m/s^2)
Pr	Prandtl number
q_w	wall heat flux (W/m^2)
Ra	Rayleigh number
Ri	Richardson number
Re	Reynolds number
Re_x	Reynolds number based on stream wise distance from the leading edge

Re_δ	Reynolds number based on boundary layer thickness
S	dimensionless disturbance temperature
t	time (s)
T	temperature (°C)
$T_k(x)$	Chebyshev polynomials
T_1, T_2, T_3, T_4	the most unstable Eigen modes
$\bar{T}$	base flow temperature (K)
$\hat{T}$	disturbance temperature (K)
$\bar{T}_0$	base flow temperature corresponds to maximum density of water near density inversion (K)
T_0	dimensional temperature at maximum density of water in the temperature range of density inversion (3.98°C)
u, v	velocity components in x and y-directions, respectively (m/s)
u_0	velocity of lid in lid driven cavity (m/s)
u_{ref}	reference velocity (m/s)
$\bar{u}, \bar{v}$	base flow velocity components in x and y-directions, respectively (m/s)
$\hat{u}, \hat{v}$	disturbance velocity components in x and y- directions, respectively (m/s)
U, V	dimensionless velocities in x and y-directions, respectively
$\hat{U}, \hat{V}$	dimensionless disturbance velocities in x and y-directions, respectively
x, y	Cartesian coordinates (m)
X, Y	dimensionless coordinates

Greek Symbols

α	thermal diffusivity in boundary layer equations (m^2/s), dimensionless wave number in stability analysis
α_i	imaginary part of dimensionless wave number
α_r	real part of dimensionless wave number
$\bar{\alpha}$	wave number (1/m)
δ	boundary layer thickness (m)
δ_v	velocity boundary layer thickness (m)
δ_T	thermal boundary layer thickness (m)
Δ_T	temperature difference (K)
η	dimensionless independent variable, similarity variable in similarity solutions
γ	constant in function (Eq. (2.1)) of density variation of water with temperature
λ	Eigenvalue in Eigenvalue problem
$\lambda_0, \lambda_1, \ldots, \lambda_n$	a set of variables which are functions of y

μ dynamic viscosity (kg/m-s)

ν kinematic viscosity (m^2/s)

ω dimensionless circular frequency of the disturbance

ω_i real part of dimensionless circular frequency of the disturbance

ω_r imaginary part of dimensionless circular frequency of the disturbance

$\bar{\omega}$ dimensional circular frequency of the disturbance (1/s)

$\bar{\phi}$ amplitude of disturbance stream function

$\hat{\phi}$ disturbance stream function (m^2/s)

ϕ dimensionless disturbance stream function

Φ plate inclination with vertical direction measured in anti-clockwise direction ($^\circ$)

ψ dimensional stream function (m^2/s)

ρ density (1/specific volume) (kg/m^3)

ρ_0 maximum density of water in the density inversion temperature range (1/specific volume) (kg/m^3)

τ shear stress (N/m^2)

θ dimensionless temperature

ξ amplitude of temperature disturbance

Subscripts

i imaginary part

r real part

cheb Chebyshev grid points

cr critical value

max maximum value

ref reference value

w wall

x local quantity at location x

y local quantity at location y

δ boundary layer thickness

∞ free stream quantity

Superscripts

$\bar{(\cdot)}$ base flow quantity

$\hat{(\cdot)}$ disturbance quantity

List of Figures

List of Tables

Chapter 1

Introduction and literature review

In the present chapter, introduction and literature review is presented. Objectives of the present work, the organisation of the thesis are also presented.

1.1 Introduction

It is well known that for most of the fluids, the density decreases with increasing temperature due to thermal expansion of fluids. However, some fluids such as water, molten bismuth, antimony and gallium, liquid helium and pseudobinary electronic alloy ($Hg_{1-x}Cd_xTe$) show increase in density with increasing temperature in certain range of temperatures and then decreases. The peculiar phenomena of increasing density with respect to temperature is referred as density inversion. It is observed from the experiments that the density of the fluid shows local maximum near the density inversion. For example, water, liquid helium and pseudobinary electronic alloy ($Hg_{1-x}Cd_xTe$) show local density maximum at 3.98°C, -271.15 °C and 750 °C at atmospheric pressure, respectively. The high density of liquid water is mainly due to the cohesive nature of the hydrogen-bonded network, with each water molecule capable of forming four hydrogen bonds. This reduces the free volume and ensures a relatively high-density, partially compensating for the open nature of the hydrogen-bonded network.

Near the density maximum point, density shows nonlinear variation with temperature. A typical variation of water density near density inversion is shown in Fig. 1.1. This nonlinear behaviour is unlike the usual density variation which varies linearly with temperature. The buoyancy forces are induced in fluids due to the density differences created. The above peculiar density variation leads to peculiar behaviour of convection process near the density inversion point. Such peculiarities bring complications in flow and heat transfer characteristics. Many models are used in the literature for the density variation with temperature near the density maximum. Some of them are as following.

A relation for density with respect to temperature near the density inversion is given by Mcdonugh and Faghri [7] is as

$$\frac{\rho}{\rho_0} = [1 + \beta_1 T + \beta_2 T^2 + \beta_3 T^3 + \beta_4 T^4]^{-1}, \tag{1.1}$$

where ρ_0 is the maximum density of water. Values of density maximum and the coefficients are as follows: $\rho_0 = 999.8396(\text{kg m}^{-3})$, $\beta_1 = -0.678964520 \times 10^{-4}(^{\circ}\text{C}^{-1})$, $\beta_2 = 0.907294338 \times$

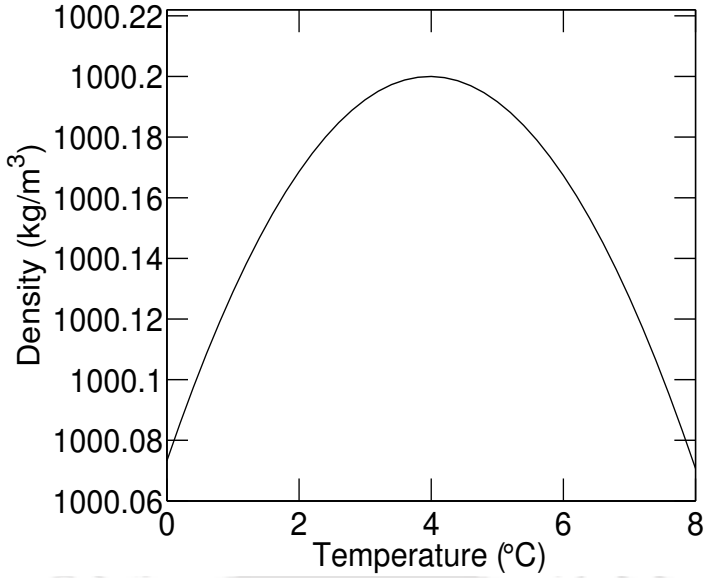

Figure 1.1: Density variation of water with temperature near density inversion according to Eq. (1.3) given by Tong and Koster [1]

$10^{-5}(^{\circ}\mathrm{C}^{-2})$, $\beta_3 = -0.964568125 \times 10^{-7}(^{\circ}\mathrm{C}^{-3})$ and $\beta_4 = 0.873702983 \times 10^{-9}(^{\circ}\mathrm{C}^{-4})$.

Few authors such as Lin and Nansteel [8], Gebhart and Mollendorf [9] have used the following density temperature relation which is given by,

$$\frac{\rho}{\rho_0} = 1 - \gamma|T - T_0|^q, \tag{1.2}$$

where, $\rho_0 = 999.9720(\mathrm{kg\ m}^{-3})$, $\gamma = 9.297173 \times 10^{-6}(^{\circ}\mathrm{C}^{-q})$, $T_0 = 4.029325(^{\circ}\mathrm{C})$ and $q = 1.894816$. Lin and Nansteel [8] reported that the correlation shows good agreement with Kell [10] which gives them confidence to use this density-temperature relation in their studies.

Tong and Koster [1] used density variation with temperature through polynomial of second degree which is defined as

$$\frac{\rho}{\rho_0} = 1 - \beta_T(T - T_0)^2, \tag{1.3}$$

where, ρ_0 is the density maximum of water and T_0 is the respective maximum temperature. The values of constants are $\rho_0 = 1000.2(\mathrm{kg\ m}^{-3})$, $T_0 = 3.98^{\circ}\mathrm{C}$ and $\beta_T = 8.00026 \times 10^{-6}\ (^{\circ}\mathrm{C})^{-2}$. The above density relation with temperature is shown in Fig. 1.1. In the present work, the density-temperature relation (1.3) is used. This correlation given by Eq. (1.3) is valid for the temperature range $0 - 12^{\circ}\mathrm{C}$ with admissible error limit which was reported by Tong and Koster [1].

Applications of density inversion of water

The density inversion of water plays an important role in many applications. Some of such applications are

1. Density inversion in water has many practical implications in the nature. The density maximum ensures that the bottoms of freezing fresh water lakes generally remain at about 4°C and unfrozen.

2. Formation and melting of ice, freezing of water, atmospheric flows and oceanic movements.

3. The industrial applications of density inversion can be seen in cryogenic industry, refrigeration and air-conditioning applications, heat exchangers etc.

4. Thermal energy storage system using ice by melting and freezing process.

Boundary layer flows play an important role in many applications in engineering and science. Boundary layers along with heat transfer are crucial in many industrial applications and in nature. The study of convective boundary layers has been an active research area for many decades due to its importance. Finding the solutions of boundary layers play the key step for understanding the physical phenomena. Stability of the boundary layers are important to find the process of laminar state undergoes instability and eventually becoming completely turbulent through a transition process. Hence, finding out the solutions of boundary layer flows of water with density inversion and study of their stability is carried out in the present work. Along with boundary layer flows, the stability of convection flows of water in a cavity with density inversion effect is carried out. The issues of boundary layer solutions, the solution methodologies of stability of boundary layers and cavity flows are discussed below.

As the boundary layer flows are governed by partial differential equations, the solutions of such flows pose mathematical challenges. In general, finding the analytical solution of the boundary layer flows is not possible. However, with the advent of computational power and development of numerical methods paved a way to find the solution numerically for a given set of conditions of the flow. The following methodologies are followed for the boundary layer solutions depending on the type of problem.

1. Similarity solutions

2. Approximate integral solutions

3. Asymptotic analysis

4. Perturbation methods

5. Numerical methods

When a boundary layer flow admits similarity in the profiles of the flow variables such as velocity, the similarity variable method is used. In the similarity variable method, the governing equations along with the boundary conditions which are in partial differential equations are transformed into ordinary differential equations using similarity coordinate transformations. In the integral method, the equations are expressed in the integral form. An approximate profiles are assumed for the flow variables. The constants of the assumed profiles are found by applying the boundary conditions. The asymptotic analysis is carried out by applying the asymptotic limit to the governing equations. In the perturbation methods, the flow variables are expanded in terms of powers of perturbation elements. Equating the terms of same powers of perturbation elements, a series of system of ordinary differential equations are derived. By solving the system of ordinary differential equations, we get the perturbation solutions. In the numerical methods, we directly solve the governing equations of the boundary

layer flow by discretising the equations using methods such as Finite Difference Method (FDM), Finite Volume Method (FVM), Finite Element Method (FEM). Methods such as space marching from the leading edge towards the downstream direction, Keller-Box method, etc. are well known methods for solving boundary layer flows, numerically.

When we consider heat transfer along with the fluid flow, we need to solve the energy equation along with the fluid flow equations. When buoyancy forces are present in the convection, additional complexities arise. Large number of studies have been conducted to find the solutions of boundary layer convective flows due to their enormous important applications.

In boundary layers, the flow remains laminar up to certain distance from the leading edge. The laminar boundary layers undergo instability when the governing parameters such as Reynolds number, Grashof number, Richardson number become more than critical values. The instabilities in the flow can further undergo transition to make the flow completely turbulent. The knowledge of the critical parameter values below which all the disturbances decay with time is extremely important. The critical parameter values can be predicted using linear stability analysis. Theory of linear stability is the subject matter of numerous books such as Lamb [11], Lin [12], Chandrasekhar [13], Drazin and Reid [14], Drazin [15], Charru [16], Schmid and Henningson [4] and Sengupta [17].

One of the methods of studying instability is the application of parallel flow stability analysis in which the base state is assumed to be homogeneous in two coordinate direction and inhomogeneous in the other direction. Then, the problem is mathematically formulated to be an Eigenvalue problem. The Eigenvalue problem is given by the system of Orr-Sommerfeld Equation (OSE) and Square equations. Many studies attempted to extend the parallel linear stability theory to incorporate non-parallel and non-linear phenomenon. In non-parallel flow analysis, the base flow is assumed to be inhomogeneous in more than one coordinate directions. One of such analyses is carried out by using Parabolised Stability Equations (PSE) which are derived by assuming the base flow to be varying in the cross-stream direction and also weakly varying in the streamwise direction. For example, Bertolotti et al. [18] used PSE in the study of boundary layer flows to include the effect of development of boundary layers. Similar weakly variation of base flow in the streamwise direction is adopted in the references by Sahu and Govindrajan [19, 20], and Sahu et al. [21].

In the non-linear analysis, we consider the terms which are weakly non-linear. The linear stability can predict behaviour of the disturbances when the disturbances are small and as long as the disturbance size is in the range at which linearisation is valid. Another method of studying stability is through Direct Numerical Simulation (DNS). In DNS, we solve the governing equations such as Navier-Stokes equations and energy equation in time and observe the linear and non-linear dynamics of the disturbances.

The stability of boundary layer flows are usually carried out using parallel flow assumption. For example, Wazzan et al. [22], Kaplan [23] used parallel flow stability analysis. The accuracy of those predictions are improved by adopting the Parabolised Stability Equations which were carried out by studies Bertolotti [24], Bertolotti [25], Bertolotti et al. [18], and Herbert [26]. Some of the studies considered the view point of whether the stability is of convectively unstable or absolutely unstable. The convective and absolute instabilities are reviewed by Huerre and Monkewitz [27].

Many studies considered receptivity of boundary layer flows. A review of receptivity of boundary layers can be found in Saric et al. [28]. When the infinitesimal disturbances in the boundary layer grow to a finite amplitude and saturates, the disturbance along with the base flow forms a new base flow state. The new base flow state can undergo further instability. Such instabilities are known as secondary instability. The secondary instability of boundary layers has been studied using Floquet theory in the works such as by Herbert [26].

In a pure hydrodynamic situation, instabilities are caused due to the interaction of viscous, inertial and pressure forces. However, when heat transfer is also involved additionally, the instability mechanism becomes more complex in which the energy and momentum will be coupled to each other. The added buoyancy effects will make the analysis further complex. Prandtl number will be an additional parameter which comes into play its own role in the instability mechanism.

The stability analysis of convective flows using Orr-Sommerfeld equation (OSE) or PSE are usually applicable when the basic flow is parallel or nearly parallel such as channel flows and boundary layer flows. However, when the base flow is highly inhomogeneous in more than one directions, the linear stability predictions by these methods would be inaccurate. For the flows which are inhomogeneous in multiple dimensions, the linear stability is studied using global stability analysis.

In the following sections, the literature on convection boundary layer flows, the boundary layer solutions, the stability of boundary layer convective flows are presented. Literature on the stability of flows in enclosures are also reviewed.

1.2 Literature on convection boundary layer flows and their solutions

1.2.1 Mixed convection over temperature specified wall

Many authors studied the mixed convection flow over vertical plate with different wall thermal conditions. Study of mixed convection flow over isothermally heated vertical surface for various Prandtl number was carried out by [29, 30]. Lloyd and Sparrow [29] used local similarity method for mixed convection flows, for various values of Richardson number and found that method was not accurate for large values of Richardson number for studied Prandtl number range. However, Acrivos [30] theoretically investigated the combined effect of free and forced convection using asymptotic solution for various Prandtl number. The author reported that mixed convection depended on both Richardson and Prandtl numbers when Prandtl number was greater than 1, while the convection depends on Richardson number only, for lower Prandtl number. Szewczyk [31] presented series solution for aiding and opposing mixed convection flow for few Prandtl number. The results were demonstrated using velocity and temperature distributions, shear stress, and heat transfer for various values of Richardson number. Hussain and Afzal [32] numerically investigated aiding and opposing mixed convection flow over vertical plate for uniform wall temperature/heat flux conditions. The authors implemented computer extension perturbation series method and predicted the results up to three-digit accuracy for skin friction coefficient and heat transfer rates. The obtained results were compared with available numer-

ical results and found good agreement. Lin and Chen [33] numerically studied aiding and opposing mixed convection over isothermal vertical plate for wide range of Prandtl number using Keller's box method. They proposed a new mixed convection parameter, which was valid for any Prandtl number value, to replace usual mixed convection parameter (Richardson number).

Both free and forced convection from an isothermal vertical moving plate was numerically examined for wide range of Prandtl number by Lin and Hoh [34]. The plate was moving either in streamwise or in opposite to streamwise direction. They presented correlations for heat transfer in terms of Prandtl number. Raju et al. [35] investigated mixed convection boundary layer flow over vertical and horizontal isothermal surfaces for aiding and opposing flow situations. The authors found out flow separation points in case of opposing flow and obtained the relationship for local Nusselt number with Prandtl number. Chen et al. [36] studied the effect of Prandtl number on mixed convection flow for various plate orientation. Correlations were obtained for local and average Nusselt number for both aiding and opposing flow situations. The results were compared with those of experimental and numerical results.

The effect of variable wall temperature on mixed convection boundary layer flow was studied by few researchers. Merkin and Pop [37] numerically studied the effect of small and large Prandtl numbers on mixed convection flow over vertical surface for various values of mixed convection parameter. The surface temperature of plate was inversely proportional to the distance from leading edge. It was found that unique solutions exist for all considered mixed convection parameter in case of aiding flow, while dual solutions were observed for opposing flow. Saeid [38] numerically studied the effect of surface temperature variation on mixed convection flow for air and water. The author analyzed the convection for wall temperature varying with periodic oscillations with time and constant wall temperature. It was reported that Nusselt number and skin friction coefficient showed periodical variations for different amplitudes and frequencies of temperature for both aiding and opposing flows. Numerical investigation of mixed convection boundary layer flow in a stable stratified medium adjacent to a vertical surface for various Prandtl number was carried out by Ishak et al. [39], using Keller's box method. The wall temperature is a linear function of vertical distance. They found the existence of dual solutions and boundary layer separation due to thermal stratification for assisting flow.

Several experimental results were reported for mixed convection flows over vertical plate. An experimental investigation of combined forced and free convection boundary layer flow over vertical isothermal surface was carried out by Gryzagoridis [40]. The velocity and temperature profiles, obtained using hot wire anemometry, were presented for various governing parameters. The calculated heat transfer rates were compared with those of theoretical results available in literature. Kobus and Wedekind [41] analysed development of thermal boundary layer along a vertical isothermal surface by introducing a special model. Special closed-form solutions for local and average Nusselt numbers were presented for various Prandtl numbers for both aiding and opposing mixed convection. The experimental study was also performed and experimental results matched well with those of theoretical results available in literature. An experiment was conducted for mixed convection flows over isothermally heated vertical plate by Venugopal et al. [42]. The correlation for Nusselt number was

presented and experimental results found good agreement with available numerical results.

The effect of porous medium on mixed convection is area of interest by few authors. In another analysis, Kumaran and Pop [43] theoretically studied the free convection boundary layer flow over a vertical plate in a porous medium with water near its density inversion. They studied the effect of wall temperature, heat flux on natural convection which were a power law function of vertical distance from leading edge of the plate. They derived the similarity form of boundary layer equations and presented their numerical and analytical results for velocity and temperature distributions and heat transfer rates. The effect of variable viscosity of fluid with temperature on mixed convection flow in a porous medium over an isothermal vertical surface, was studied by Chin et al. [44]. They studied the effect of mixed convection and variable viscosity parameters on fluid flow and heat transfer characteristics. They observed dual solutions and boundary layer separations in case of opposing flows.

1.2.2 Mixed convection over flux specified wall

Mixed convection boundary layer flow over vertical wall with uniform heat flux surface condition was numerically studied by [45–47]. Wilks [45] presented series solutions for leading and trailing edges which are valid for Prandtl number of order 1. For the same mixed convection problem Carey and Gebhart [46] considered higher order series solutions. They compared their results with those of Wilks [45] at trailing edge and found that Wilks results were of lower accuracy due to first order approximation. Accurate finite-difference marching technique was used to investigate the effect of buoyancy in forced convection flow over vertical wall by Moulic and Yao [47]. It was found that forced convection was the dominant mode of heat transfer at the leading edge, whereas, free convection prevails at the trailing edge of the plate. Merkin and Mahmood [48] used similarity solutions to analyse the effect of buoyancy parameter on mixed convection flows. It was reported that solutions approach free convection asymptote for large value of buoyancy parameter in aiding flows, while dual solutions exist for opposing flows. Consequently, the same problem was extended in Merkin et al. [49] to study the Prandtl number effect on mixed convection. The results imply that, for fixed values of other parameters, solutions approach pure forced convection with increasing Prandtl number.

The orientation of the surface shows strong influence on mixed convection. Such effect was the subject of several studies. The effect of plate orientation on mixed convection flows was numerically studied by Wickern [50] for both aiding and opposing flows. It was found that the flow separations were reported for opposing flow situation which could be singular or regular. The same author extended the study, in [51], to investigate the effect of Prandtl number on mixed convection. The convection characteristics ware studied using asymptotic expansion for wide range of Prandtl number and compared with results obtained using numerical method. The asymptotic analysis results were consistent with the numerical results. Yeh et al. [52] analysed the effect of Prandtl number, buoyancy induced pressure gradient and ratio of wall to free-stream velocity on mixed convection over a horizontal plate using local non-similarity method. The results showed profound influence of buoyancy on overall heat transfer for certain range of parameters. Armaly et al. [53] analytically studied the combined effect of free and forced convection over heated vertical surface for a wide range of Prandtl

number. They presented the correlations for local and average Nusselt number for both aiding and opposing flow situations. Mixed convection flow over vertical plate with specified heat flux in water with nanofluid was studied by Trimbitas et al. [54] using similarity solution. Higher values of skin friction coefficient and heat transfer rates were found with inclusion of nanofluids in water, compared to those without nanofluids.

Mixed convection in porous medium was the focus of many studies. Finite-difference scheme was used by Ranganathan and Viskanta [55] to study the mixed convection boundary layer over a vertical surface in a porous medium. Various parameters such as Prandtl number, Gr/Re and low blowing velocity showed significant impact on velocity and temperature distributions, while porosity variation showed insignificant effect. Mixed convection boundary layer flow in a porous medium over vertical plate was numerically investigated by Ahmad and Pop [56] for various nanofluids. For the same parameter values, significant amount of heat transfer enhancement was registered when nanofluids were used compared to that without nanofluids.

In many works, the radiation effect is included in the mixed convection study. The effect of variable viscosity and thermal conductivity of air along with the effect of radiation over a non-isothermal horizontal permeable surface on fluid flow and heat transfer were studied by Mahmoud [57]. The local skin friction coefficient and Nusselt number were found to be increasing with increasing values of radiation and suction parameters, while decreasing with increasing value of blowing parameter. Combined effect of conduction, mixed convection and surface radiation from a vertical plate with internal heat generation was numerically studied by Sawant and Rao [58]. The effect of surface emissivity and modified Richardson number on fluid flow behaviours were investigated. Correlations were presented for average temperature, average Nusselt number and skin friction coefficients for a wide range of parameters. The effect of thermal radiation and variable heat source or sink on unsteady mixed convection on stretching permeable sheet was studied by Pal [59]. The effect of Prandtl number, buoyancy, radiation and unsteadiness parameters on aiding and opposing mixed convection was studied. The local Nusselt number increased with increasing values of unsteadiness parameter, buoyancy parameter and Prandtl number.

1.2.3 Literature on convection boundary layers of water including density inversion

Boundary layer flows of water near its density inversion are investigated in many studies such as [5, 9, 60]. The effect of buoyancy force on boundary layer flow of water over a vertical plate was numerical investigated by Goren [60]. The author studied the free convection boundary layer flow of water near its density inversion about a vertical plate. The author presented the results for temperature and velocity distributions. It was found that for a small temperature difference, at maximum density, convective currents becomes weak compared to that of water without density inversion. Gebhart et al. [9] numerically examined buoyancy induced flows adjacent to a horizontal surface of water density inversion for constant wall temperature and heat flux conditions. They presented the solutions for various values of wall temperature variation parameter. They found sudden decreases in heat transfer rate near density inversion point. Vighnesam and Soundalgekar [5] studied mixed convection flow of

water near its density inversion about a vertical plate with power-law varying wall temperature using similarity solution. The effect of various values of Gr_y/Re_y^2 and power-law index were studied for both aiding and opposing flows. They reported that Nusselt number increased with increasing value of power-law index for both aiding and opposing flows. But, skin friction coefficient decreased with power-law index values in aiding flow, while it increased in opposing flow situation. The authors presented similarity solutions for velocity, temperature, and Nusselt number variations for various values of modified Richardson number. Numerical study of free convection flows over isothermal horizontal plate in a porous medium filled with water was carried out by Lin and Gebhart [61]. The authors studied the effect of density inversion parameter on free convection and reported the existence of reversal of normal component of velocity in the inner region of flow. Kumaran and Pop [43] investigated free convection boundary layer flows of water near its density inversion over vertical plate in a porous medium for various wall thermal conditions such as variable wall temperature, variable heat flux conditions etc., and presented similarity solutions for the flow and thermal field.

1.3 Literature on linear stability of convection flows

1.3.1 Stability of natural convection boundary layers

A comprehensive review of buoyancy driven flows can be found in Gebhart et al. [62]. In this reference, the linear stability of natural convection was also reviewed. Szewczyk [63] studied instability and transition of natural convection along a vertical plate through experiments and linear stability analysis. The double-row vortex system formed in the convection layer was reported. The wave motion provoke outside the velocity maximum was found to be of stronger instability than that provoked inside the velocity maximum. The mechanics and overall effects of the instability and transition of the natural convection were presented. The marginal stability curves for vortex mode instability were reported by Haaland and Sparrow [64] by including non-parallel effect of the boundary layer flow. Iyer and Kelly [65] studied Tollmien-Schlichting mode and vortex mode of spatial linear stability under the parallel flow assumptions. The flow showed subharmonic instability. Wakitani [66] reported non-parallel effects of buoyant plumes by applying multiple scale analysis. Day et al. [67] carried out parallel and non-parallel Gortler instability analysis. They found the neutral point which depends on the initial conditions at some locations from the leading edge of the plate. However, non-parallel analysis results became independent at locations farther from the leading edge. Lee et al. [68] performed non-parallel stability analysis. Hall and Morris [69] carried out linear stability analysis using space marching for forced convection boundary layer and found results similar to Gortler instability. Luchni and Bottaro [70] reported results of marching solutions and obtained a universal disturbance shape.

Daniels and Patterson [71] studied long-wave instability of natural convection boundary layer formed due to sudden heating of a vertical infinite wall. With a quasi-steady approximation, the authors analysed asymptotic form of lower range of neutral curves. This branch of disturbances were of wavelengths much greater than the boundary layer width. The critical wave number for neutral stability and maximum speed of travelling waves were obtained for a range of Prandtl numbers. In a

subsequent study, the same authors, Daniels and Patterson [72] conducted investigation on short wave instability of natural convection boundary layers over a vertical wall. Natural convection boundary layer was formed due to sudden heating of a vertical wall. Asymptotic form of growth rate and phase speed of disturbances, whose wavelength was comparable to the width, was obtained using quasi-steady state approximation. Both inviscid and viscous instability were considered. The phase speed of the disturbances were found to approach the maximum speed of the boundary layer when the wavelength was increased. A five star structure was found to extend outside and across the boundary layer. Dachun and Hanxun [73] presented instability analysis of natural convection boundary layer about a vertical heated plate. Parallel flow stability analysis and experimental results were presented.

Williamson and Armfield [74, 75] studied conjugate natural convection boundary layers to investigate stability characteristics. The boundary layers were formed by joining adjacent two dimensional rectangular vertical cavities, joined along the vertical wall with infinite thermal conductivity. The conjugate nature of boundary layers preponed the absolute instability. The aspect ratio of the cavities showed weak influence on the instability. Aberra et al. [76] studied instability of natural convection boundary layer flow on a vertical plate subjected to uniform heat flux. They performed direct numerical simulations and linear stability analysis for air and water. The critical Rayleigh numbers were obtained separately for velocity and temperature signals. The dependence of instability on Prandtl number, Rayleigh number and excitation frequency was presented.

The inclination of the plate can show a dramatic influence on the stability characteristics of the natural convection boundary layers as the orientation of the plate is changed the direction of interaction of buoyancy forces with the viscous and inertial forces change. Many studies have reported the inclination effect on the instability. Sparrow and Husar [77] reported an array of longitudinal vortices in natural convection of water flows on an inclined plate. At the downstream locations, vortex pairing was observed. The vortex pairing resulted in turbulent flow. Lloyd and Sparrow [78] performed experiment on instability of flow over inclined plate. Two types of instability modes were found depending on the inclination angle of the plate with respect to vertical direction. Tollmien-Schlichting waves were found for inclinations less then 14°. For inclination angle greater than 17°, a system of longitudinal vortices were generated as a result of instability. For inclinations between 13° and 17°, both Tollmien-Schlichting type and longitudinal vortices were present. Pera and Gebhart [79] conducted analytical and experimental study on natural convection boundary layer flow about a horizontal and slightly inclined surfaces. The study also included diffusion of chemical species. Their linear stability results predicted the correct trends of stability limits for both horizontal and slightly inclined surfaces. However, the actual values were not in good agreement with experimental observations. The difference between theory and experiment may be due to three dimensional effects in the attached boundary layer region and from separation like phenomenon in the downstream. Natural convection over inclined plate was studied by Shaukatullah and Gebhart [80].

Temporal linear stability of inclined natural convection boundary layer was studied by Chen et al. [81]. Zeurcher et al. [82] presented experimental results of pairing of vortices. Natural convection flow over an inclined plate subjected to constant heat flux was studied by Jeshke and Ber [83]. The authors performed analysis of linear and non-linear vortex instabilities by adopting marching proce-

dure. Spatial stability of natural convection flows over inclined plates was studied by Tumin [84]. Modes of travelling waves and stationary longitudinal vortices were analysed in the study. Method of multiple scales was adopted for non-parallel stability analysis. The results showed that non-parallel effects show stabilising influence. For the vortex instability mode, neutral point at some location from the leading edge depended on the initial conditions. However, at farther locations downstream, the neutral points became independent of the initial conditions.

Stratification of the medium outside of the boundary layer is another important parameter which influenced the stability of natural convection boundary layers. Several studies investigated the effect of stratification of the medium. Jaluria and Gebhart [85] experimentally and theoretically studied the effect of stratified medium on the stability of buoyancy induced flow about a vertical plate subjected to uniform heat flux. The stratification was found to stabilise the flow initially, but destabilise the flow in the downstream. Results were presented for air and water, for several degree of ambiance stratification. Their theoretical results agreed well with their experiment results conducted with water. Tao and Zhuang [86] presented theoretical investigation of spatio-temporal instability of natural convection in a vertical heated slot. Two unstable modes which were travelling waves and secondary cell, were found. The travelling wave mode showed convective instability and secondary cell showed absolute instability. Lei and Patterson [87] studied natural convection instability of water filled in a shallow wedge. The wedge bottom was subjected to absorption of radiative heat transfer. The boundary layer formed on the wedge was shown to be potentially unstable to the Rayleigh-Benard instability. The study presented critical Grashof number value.

Tao et al. [88] investigated spatio-temporal instability of vertical natural convection boundary layer which was immersed in a thermally stratified medium. The study was carried out for plate temperature varying linearly. Absolute-convective instability transition of this flow was observed in the context of parallel stability analysis. Increasing of the temperature gradient along the plate decreased the domain of absolute instability and at sufficiently large temperature gradient, absolute instability disappeared. When the plate was isothermal, the absolute instability decreased with Prandtl number and absolute instability disappears for Prandtl number greater than 70. For uniform flux surface condition, the instability was found to be convective for wide range of Prandtl numbers. The base flow showing the absolute-convective instability transition were found to have inviscid origins of convective instability. In a similar study, Tao et al. [89] reported spatio-temporal instability of natural convection over a heated plate immersed in a thermally stratified medium. The temperature gradient ratio between the wall and ambient fluid caused many absolute-convective instability transitions. The authors presented numerical simulations which were consistent with their theoretical results. McBain et al. [90] studied linear stability of buoyancy layer about a uniformally heated vertical wall embedded in a stratified fluid. The authors carried out the study using linear stability and direct numerical simulation. The base flow considered was varying in time and height. For Reynolds number greater than critical value, two dimensional unstable travelling waves were found for certain Prandtl number values. Their linear stability results were in good agreement with those results of direct numerical simulations. Dodgson et al. [91] studied vortex instability of natural convection boundary layers embedded in a porous medium. The results showed that vortex instability was not an absolute instability

as a result of growing disturbances travel in the downstream direction faster than upstream direction. Their computations were in good agreement with the parabolic simulation which was valid for near vertical limit.

1.3.2 Stability of mixed convection boundary layers

Mucoglu and Chen [92] performed linear stability analysis of mixed convection flow over a vertical plate of uniform surface temperature. The study included assisting and opposing mixed convection flows. The buoyancy makes the flow more stable in assisting flow situation, and makes the opposing flow to be more unstable. Wave instability characteristic of mixed convection flow about an isothermal vertical flat plate was carried out by Lee et al. [93] for the Prandtl number of 0.7 and 7. Dual solutions for critical parameter values were reported in certain parameter range. This showed the limiting case of Blasius flow and pure free convection flow correspond to two different modes. Brewster and Gebhart [94] studied linear stability of mixed convection boundary layer over an isothermal surface. The study was carried out for aiding and opposing mixed convection where the forced convection effects were small compared to natural convection effects. For aiding mixed convection of air, a small separated region of instability in the upstream of usual neutral curve. In this region, selective amplification of narrow band of disturbance frequencies with small growth rate was found. In the further downstream locations, disturbance growth for aiding free stream were found to be slower than those of natural convection. However, for opposing mixed convection, the growth rates were faster than those of natural convection. For the case of water, aiding flow was destabilising factor compared to the natural convection. The opposing flows stabilise the flow compared to pure natural convection.

Moresco and Healey [3] performed study on spatio-temporal instability in mixed convection boundary layer over vertical isothermal plate. The study adapted mixed convection formulation such a way that as Richardson number varied from 0 to ∞, the formulation represented smooth variation from pure forced convection to pure natural convection through the mixed convection regime. The base flow equations were solved using Keller-Box method. Disturbance equations were discretised using spectral method. The study showed that for aiding mixed convection, the instability mode was of convective instability. Absolute instability was observed for certain parameter value for opposing mixed convection configuration. Their analysis of Rayleigh equation showed that the absolute instability had inviscid origin. Venkatasubbaiah and Sengupta [95] reported spatial stability analysis of mixed convection boundary layer flows using linear stability analysis and direct numerical simulation. A double loop in the neutral curve was reported in the opposing mixed convection for small Richardson numbers. They also performed direct numerical simulation to verify the linear stability analysis results. Mureithi and Denier [96] investigated mixed convection boundary layer flows which were subjected to external pressure gradient. Their study showed that the flow was convectively unstable below a critical buoyancy parameter and was absolutely unstable greater than the critical buoyancy parameter. The convective type spatial mode was found in the study showed mode crossing behaviour at lower frequencies. Thermal buoyancy acted as destabilising factor to the absolutely unstable spatial mode.

The mixed convection boundary layers adjacent to vertical plate differ much from the boundary

layers formed over a horizontal plate due to the difference in the direction of heating and gravity force. Stability of mixed convection over horizontal plates were examined in many studies. For instance, thermal instability of mixed convection along an isothermal horizontal plate was reported by Wu and Cheng [97]. The study was based on non-parallel base flow assumption. The critical Grashof number values were presented for wide range of Prandtl numbers. The vortex instability mode was examined in this study. For the same flow configuration, linear stability results for wave instability were reported by Chen and Mucoglu [98]. Sengupta et al. [99] studied spatial stability of mixed convection boundary layer flow over a horizontal plate. The study was carried out for wall temperature varying inversely proportional to square root of the distance from the leading edge. Compound Matrix Method (CMM) was used for the solution of the disturbance equations. For certain Richardson number values, the study reported two-lobed neutral curve. The above study reported some corrections of the results presented in Sengupta and Venkatasubbaiah [100]. In a similar study, stability analysis of mixed convection flow over an isothermal horizontal plate was performed by Venkatasubbaiah [101]. The mixed convection flow was considered for small Richardson numbers. The non-similar mixed convection boundary layer equations were solved numerically. Neutral and critical parameters were reported for assisting and opposing mixed convection flows. The results showed that as the buoyancy force was increased, the flow became less stable in assisting mixed convection, and more stable in the opposing mixed convection flow.

Sengupta et al. [102] performed study on direct numerical simulation of mixed convection instability over a horizontal and wedged flow. The receptivity study of mixed convection flow was carried out for an adiabatic horizontal plate, significantly cooled and strongly heated isothermal wedge flow. The receptivity study was carried out for disturbance due to wall excitation. The authors initially tried to find equilibrium solutions using direct numerical simulation of Navier-Stokes equations. However, the equilibrium solutions could not be achieved, which prompted to re-investigate various instability mechanism of mixed convection flows. The authors presented the necessary conditions for inviscid instability, for a mixed convection parallel flow. The study explained relative rules of inviscid and viscous mechanism for strong heat transfer effects. Lee et al. [103] carried out non-parallel flow analysis of linear wave instability of mixed convection flow along an inclined isothermal plate. The results showed that net effect of buoyancy force on critical Reynolds number became zero for inclination angle of 1.05°. For inclination greater than 1.05°, increase in Richardson number stabilised the flow. For the inclination less than 1.05°, increasing value of Richardson number destabilised the flow.

1.3.3 Stability of lid driven cavity flows

The linear stability of boundary layer flows can be carried out by assuming the base flow to be parallel or varying weakly in the streamwise direction. However, for the flows in enclosures such as lid driven cavity, such parallel flow assumptions can not be made as the base flow is highly non-parallel. Hence, for the flows in the enclosures, base flow should be considered as two dimensional or three dimensional. To study linear stability of such flows, global linear stability analysis is used. The global stability analysis is computationally much more expensive than the parallel linear stability analysis. The studies on linear stability of lid driven cavity flows are reviewed below.

The detailed review of flows in lid driven cavities are provided by Shankar and Deshpande [104]. Ramanan and Homsy [105] studied linear stablity of lid driven cavity flow. They presented the critical Reynolds number and damping rate. The variation of damping rate with respect to spanwise wave number was presented. The results were analysed through energy calculations. The stability curves were found to be relatively flat implying any shorter wavelength modes at a slightly higher values of Reynolds number. For Reynolds number 730, second competing mode with a wave length close to the cavity width was found. In a series of papers, Ding and Kawahara [106–108] studied instability of two dimensional cavity flow with applied three dimensional disturbances over a range of Reynolds numbers. The presented the critical wave lengths, stability curves. They obtained Taylor-Gortler like vortices in the cavity by means of reconstruction of three dimensional flows. Linear stability results of three dimensional lid driven magneto hydrodynamic cavity flows were presented by Shatrov et al. [109]. In their study, the flow was subjected to external magnetic field in the direction parallel to the lid. Two dimensional flow structure was strongly influenced by the Lorentz forces resulting change in shape, strength and number of the eddies. In some parametric range, magnetic field was found to stabilise the 3D flow. However, the flow around $Re = 3100$, several branches of neutral stability curves existed. In this range, for a given Reynolds number, the increased magnetic field could lead to transition from steady state to oscillatory unstable flow. Theofilis et al. [110] presented linear viscous global stability results for rectangular duct flow, Coutte flow, cavity flows and 2D-Coutte lid driven cavity flows. For lid driven cavities, they presented critical Reynolds number and the first few Eigen modes for various values of spanwise wave numbers. Comparison was made with the results of Ramanan and Homsy [105], Ding and Kuwahara [106]. For lid driven cavity flows, the authors also presented results for various cavity aspect ratios and they found that most unstable mode was stationary mode which followed three traveling wave modes. The variation of growth rate with wave number for various Reynolds number were presented.

Non et al. [111] extended the linear global stability analysis for three dimensional lid driven cavity flows. The computation was extended for larger range of spanwise wave numbers (in the range of 0 to 25). The authors discussed rich dynamics of flow beyond the bifurcation. They used adaptive piecewise linear continuation method for finding the neutral stability curves in the wide range of spanwise wave numbers. Global stabiliy analysis of lid driven cavity was studied by Chicheportiche et al. [112]. The first bifurcation characterised by three-dimensional Taylor-Gortler like stabilities were studied for cubical cavity applying periodic boundary condition in spanwise direction for $Re = 1000$. The modes predicted by linear global stability analysis were compared to their direct numerical simulation. The bifurcation found in the study differed much with the bifurcation found in the cavity with no slip walls in the spanwise direction. Their study predicted a stationary mode as most unstable mode. Bopanna and Gajjar [113] presented global linear stability analysis results for lid driven cavity using a hybrid scheme with spectral collocation and high order finite difference schemes. They reported global stability of lid driven cavities for various aspect ratios. Kuhlmann and Stefan Albensoeder [114] studied stability of three dimensional flow in a lid driven cube using collocation method. They found the bifurcation was of Hopf type and slight sub-critical. The flow above critical point was oscillatory and symmetric with respect to symmetric mid-plane. The oscillation amplitude grew

slowly and appeared to saturate for a longer duration. The constant amplitude oscillations were unstable. The periodic oscillations were interrupted by sharp bursts. During the bursts, amplitude of oscillations substantially grew and the spatial structure of stream wise vortices changed. The instability of lid driven flow in a cube was studied by Gelfgat [115], for the case of lid moving parallel to the cube side wall and lid moving parallel to diagonal plane. Their results showed the bifurcation to be sub-critical for zero spanwise wave number. For the case of lid velocity parallel to wall, the flow was found to be symmetric with respect to mid plane. The corresponding limit cycle was unstable. Hence, the flow was oscillatory and non-symmetric. For the case of lid driven in direction parallel to the diagonal, the most unstable disturbance was non-symmetric.

1.3.4 Stability of convection flows of water including density inversion

Hwang et al. [116] reported that the density inversion effect stabilised the fluid layer. Malkus and Veronis [117] carried out non-linear analysis through perturbation technique. They expanded non-linear equations as a sequence of linear equations for small deviations from neutral stability. Veronis [118] studied linear stability of water layer near density inversion. The bottom wall was kept at 0°C and the top wall was kept at 4°C or 8°C. The author presented critical Rayleigh number based on the height of the unstable layer. Yen [119] investigated linear stability of water layer by melting ice from below. The study suggested that the critical value of Rayleigh number was not a unique value. The critical Rayleigh number varied with temperature of lower rigid surface. In a subsequent work, the same problem was also studied by including heating from the top in the study by Yen and Galea [120]. Sun et. al [121] examined linear stability of water layer near its density inversion which was subjected to heating from above and below. The authors reported the critical Rayleigh number of instability which depended on two defined thermal parameters. Moore and Weiss [122] studied water layer subjected to stress free boundary conditions. Their transient simulations showed that the convection could show oscillations in the stable upper layer. The authors reported sub-critical bifurcation. The non-linear oscillations were found to be pronounced near the density interface separating the unstable and stable fluid layers. Wu and Cheng [123] performed study on the thermal instability of horizontal fluid layer. The effect of surface tension and buoyancy force on the instability in the layer is studied. The stability results reported for Rayleigh, Morangoni and Biot numbers. Merker et al. [124] conducted an analytical and experimental study on stability of horizontal water layer. The study also investigated the effect of non-linear density variation with respect to temperature versus linear density variation with temperature.

Seki et al. [125] studied horizontal water layer including density inversion with a rigid-rigid boundary condition on top and bottom walls. In the study, the horizontal ice was melted due to the applied heat on the top surface. The study was carried out using both analytical and experimental methods. Their analytical results agreed well with the experimental results. The same authors [126] conducted study on stability of horizontal water layer near its density inversion with free and rigid boundary condition. Solutions were obtained using linear perturbation analysis. The neutral curves were presented for various Rayleigh and Biot numbers. Merker et al. [127] performed linear stability analysis of horizontal water layer near with density inversion point. They used Galarkin method to

solve perturbation equations. The stability analysis was carried out for top boundary subjected to either constant temperature or constant heat flux, while the temperature of bottom boundary kept as variable. Experiments were conducted to study the above problem by Merker and Straub [128]. Blake et al. [129] carried out numerical study to find the effect of Rayleigh number, bottom wall temperature and aspect ratio on the conduction characteristics. They reported critical Rayleigh number were an agreement with the critical Rayleigh number obtained from linear stability. Natural convection of water near its density inversion was discussed in detail in the monograph by Yen [130]. The convection in confined horozontal layers, confined vertical layers and rectangular enclosures and annulus, were addressed. The stability of horizontal water layers and vertical water layers were presented in detail. Tong and Koster [131] presented numerical solutions for the onset of stability of an infinite horizontal layer of water near its density inversion using finite element method. The study was carried out for both heating from top and heating from bottom. The influence of aspect ratio on critical Rayleigh number was presented. The study also presented correlation for critical Rayleigh number when the water layer was heated from below and above. Mamou et al. [132] conducted linear stability analysis of a horizontal porous cavity filled with water near its density inversion. The study used Brinkman-extended Darcy model. The disturbance equations were solved using Galarkin and finite element method. The results are presented for onset of convection for various cavity aspect ratios and Darcy number.

1.4 Summary of the literature review

Several mathematical techniques were used in the literature to solve the boundary layer convective flows. For the solutions of boundary layer flows, similarity methods by [29, 37], approximate solutions such as local non-similarity method by [133, 134] and series expansion method by [135] were used. Perturbation method were used to solve boundary layer flows by few authors such as Yang and Jerger [136] and Seetharamu and Dutta [137], due to its inherent advantages. In a recent study, Gavara et al. [138] used perturbation method to solve the boundary layer mixed convection over a vertical plate in air with temperature boundary condition. The main advantage of perturbation method is that the calculated universal functions are valid for an arbitrary wall temperature variation. Hence, the results can be easily used to get solutions for any arbitrary wall temperature variation condition without need for solving any differential equation again for different temperature variation. From the literature, it can be found that perturbation solutions of boundary layer mixed convection of water flows with the effect of density inversion for arbitrary varying wall temperature and wall heat flux are not available in the literature.

The similarity solutions for boundary layer flows of water with density inversion are presented in few studies. Goren [60] presented similarity solution of free convection boundary layer flow over isothermal plate for density inversion of water. Similarity solutions of natural convection boundary later flows of water near its density inversion over a surface of power-law varying temperature, are presented by Soundalgekar [139]. Similarity solutions for natural convection boundary layer flow over a plate subjected to constant heat flux in a porous media filled with water near density inversion

is reported by Kumaran and Pop [43]. Vighnesam and Soundalgekar [5] presented similarity solutions for mixed convection boundary layer flows over a surface with power-law varying temperature. However, it is found from the literature that similarity solutions for natural convection and mixed convection boundary layer flows over a vertical plate of power-law varying surface flux were not reported in the literature.

Stability of natural and mixed convection boundary layer flows were addressed in numerous studies. Most of the studies on boundary layer flows treated the base flow with the assumption of parallel or weakly non-parallel. Wave type and Taylor-Gortler type of instabilities are reported for natural as well as mixed convection boundary layer flows. Some flows considered the non-linear stability through weakly non-linear assumption or through Direct Numerical Simulations (DNS). Many studies in the past, performed non-linear direct numerical simulation to validate the predictions of linear stability analysis. Many experimental studies are also reported for natural as well as mixed convection boundary layers. Several linear instability studies are reported for lid driven cavity flows. The critical Reynolds number, the type of most unstable disturbance whether it is a stationary or time varying mode, was the focus of the studies. The studies were carried out by assuming wave type disturbance in the third direction.

From the literature survey on linear stability, it can be concluded that even though the boundary layer convection flows without density inversion were addressed in large number of studies, the convection flows of water with density inversion, has not been addressed sufficiently. Even though, the linear stability of lid driven cavity flows without heat transfer were reported in many studies, the stability characteristics of lid driven flow including heat transfer with density inversion was not addressed. The present study aims to address the above gaps in the literature.

Novelty

The following novelties are drawn from the literature;

- Perturbation solutions of mixed convection boundary layer with effect of density inversion for arbitrary wall temperature/heat flux.
- Similarity solution for mixed/natural convection boundary layer with power-law varying surface flux.
- Linear stability of natural/mixed convection boundary layers with density inversion.
- Stability characteristics of lid driven cavity with density inversion.

1.5 Objectives of the thesis

The objective of the present work is to study the effect of density inversion of water on stability and convection characteristics of water flows. The objectives are set as following regarding the convection flows of water with density inversion:

- Perturbation and similarity solutions for arbitrarily varying wall temperature and heat flux with density inversion.

- Temporal and spatial stability analysis with density inversion.
- Global stability of lid driven cavity.

1.6 Organisation of the thesis

In chapter 1, introduction to convection of density inversion in water is described along with the applications. It also includes the literature survey and conclusions from the literature, followed by the objectives of the present work. In chapter 2, study of mixed convection boundary layer flows about a vertical plate with varying temperature near density inversion of water, is presented. In chapter 3, the effect of density inversion of water in convective flows of varying heat flux over vertical plate is described. Chapter 4 reports the similarity solutions of natural and mixed convection flow of water about a vertical plate specified with variable wall heat flux. In chapter 5, numerical formulations of linear stability analysis of boundary layer flows is presented. Linear stability analysis of natural convection boundary layer flow over a flat plate of uniform surface temperature and uniform heat flux is described. The plate inclination study on stability is also described in chapter 6. Chapter 7 consists of linear stability analysis of mixed convection boundary layer flows over vertical isothermal plate. Chapter 8 reports linear global stability analysis of mixed convection flows in a lid driven square cavity. The conclusions and future scope of the present work are discussed in chapter 9.

Chapter 2

Aiding and opposing mixed convection about a wall of varying temperature

In this chapter, mixed convection boundary layer flows over a wall of arbitrarily varying surface temperature, including density inversion effect is solved using perturbation method. The physical system, solution methodology and the obtained results are presented.

2.1 Physical system

The physical system of the present study is shown in figure 2.1. Water flows over the vertical surface and forms the mixed convection boundary layer. The free stream velocity is v_∞ and free stream temperature of the water is T_0, which is the temperature corresponding to density maximum (ρ_0). The temperature of the wall and water are considered in the range, for which the density inversion of water is valid. The plate is subject to an arbitrarily varying wall temperature which is a function of vertical distance. Both the aiding as well as opposing mixed convection are solved in this study. The physical and coordinate systems are shown in figures 2.1(a) and 2.1(b) for aiding and opposing mixed convection, respectively.

2.2 Mathematical model

The steady, laminar and incompressible flow is assumed. The effect of viscous dissipation and radiation on mixed convection, are assumed to be negligible. The study is carried out for which the boundary layer approximations are valid. The temperature in the boundary layer is assumed in the range for which water show density inversion. The properties of water are assumed to be constant, except the density variation with respect to temperature in buoyancy term. The variation of density with respect to temperature is approximated using different function by various authors such as [1,5,9] in the literature. In the present study, the following density-temperature approximation is taken which is used in [5],

$$\frac{\rho}{\rho_0} = 1 - \gamma(T - T_0)^2 \tag{2.1}$$

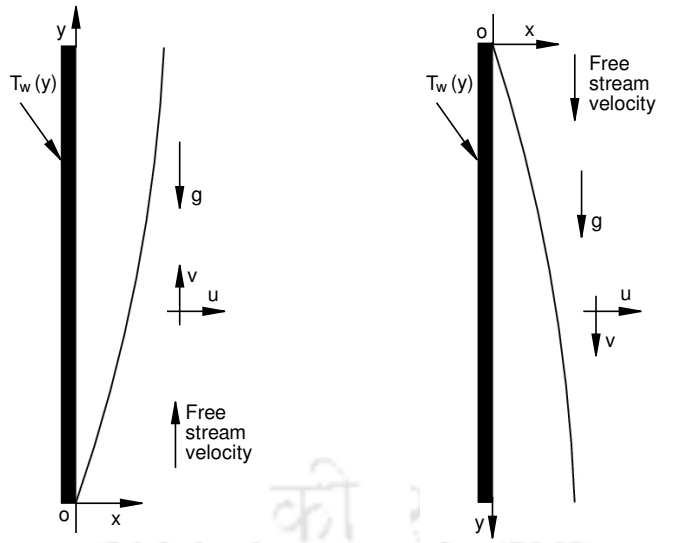

(a) Aiding mixed convection

(b) Opposing mixed convection

Figure 2.1: Schematic of physical and coordinate systems

where, ρ_0 is the maximum density at temperature of $T_0 = 3.98°$C and $\gamma = 8.0\times10^{-6}$ C^{-2} is a constant. This correlation is valid for the temperature range $0 - 12°$C with admissible error limit which was reported in [1]. Under the above assumptions, the governing equations for mixed convection flows can be written as follows,

Continuity equation

$$\frac{\partial u}{\partial x} + \frac{\partial v}{\partial y} = 0 \tag{2.2}$$

y-momentum equation

$$u\frac{\partial v}{\partial x} + v\frac{\partial v}{\partial y} = \nu\frac{\partial^2 v}{\partial x^2} \pm g\gamma(T - T_0)^2 \tag{2.3}$$

Energy equation

$$u\frac{\partial T}{\partial x} + v\frac{\partial T}{\partial y} = \alpha\frac{\partial^2 T}{\partial x^2} \tag{2.4}$$

The '$+$' and '$-$' signs in Eq. (2.3) refer to aiding and opposing mixed convection flows, respectively.

No slip and no penetration conditions are specified at the wall. The free stream velocity and temperature are uniform and v_∞ and T_0, respectively. Mathematically, the boundary conditions are

$$\text{At} \quad x = 0: \quad u = v = 0, \quad T = T_w(y) \tag{2.5}$$

$$\text{At} \quad x \to \infty: \quad v \to v_\infty, \quad T \to T_0 \tag{2.6}$$

To eliminate the coupling between continuity and momentum equations, u and v velocities are expressed in terms of stream function as

$$u = -\frac{\partial \psi}{\partial y}, \quad v = \frac{\partial \psi}{\partial x}. \tag{2.7}$$

With these u and v velocities definitions, the momentum and energy equations given by Eqs. (2.3) and (2.4), respectively, are converted into

$$\frac{\partial\psi}{\partial x}\frac{\partial^2\psi}{\partial x\partial y} - \frac{\partial\psi}{\partial y}\frac{\partial^2\psi}{\partial x^2} = \nu\frac{\partial^3\psi}{\partial x^3} \pm g\gamma(T - T_0)^2 \tag{2.8}$$

$$\frac{\partial\psi}{\partial x}\frac{\partial T}{\partial y} - \frac{\partial\psi}{\partial y}\frac{\partial T}{\partial x} = \alpha\frac{\partial^2 T}{\partial x^2} \tag{2.9}$$

The boundary conditions (2.5) and (2.6) in stream function forms are as following,

$$\text{At} \quad x = 0: \quad \frac{\partial\psi}{\partial x} = \frac{\partial\psi}{\partial y} = 0, \quad T = T_w(y) \tag{2.10}$$

$$\text{At} \quad x \to \infty: \quad \frac{\partial\psi}{\partial x} \to v_\infty, \quad T \to T_0. \tag{2.11}$$

2.3 Solution of the governing equations

For the solutions of the governing equations, the following transformations are applied in terms of dimensionless stream function f, dimensionless temperature θ and independent variable η

$$f(\eta, \lambda_0, \lambda_1, \cdots, \lambda_n, \cdots) = \frac{\psi(x,y)}{\sqrt{\nu v_\infty y}} \tag{2.12}$$

$$\theta(\eta, \lambda_0, \lambda_1, \cdots, \lambda_n, \cdots) = \frac{T(x,y) - T_0}{T_w(y) - T_0} \tag{2.13}$$

$$\eta(x,y) = x\sqrt{\frac{v_\infty}{\nu y}} \tag{2.14}$$

In the above transformations, $\lambda_0, \lambda_1, \cdots, \lambda_n$ are a set of perturbation variables which are functions of vertical distance y. It can be observed that the above transformations are similar to the transformations by similarity variable method except that in the above transformations, perturbation variables present additionally.

Using the transformations, given by Eqs. (2.12), (2.13) and (2.14), the momentum and energy equations (2.8) and (2.9), respectively, transformed into the following forms

$$\frac{\partial^3 f}{\partial\eta^3} = -\frac{f}{2}\frac{\partial^2 f}{\partial\eta^2} \pm \frac{Gr_y}{Re_y^2}\theta^2 - \frac{\partial^2 f}{\partial\eta^2}y\sum_{n=0}^{\infty}\frac{\partial f}{\partial\lambda_n}\frac{\partial\lambda_n}{\partial y} + \frac{\partial f}{\partial\eta}y\sum_{n=0}^{\infty}\frac{\partial^2 f}{\partial\lambda_n\partial\eta}\frac{\partial\lambda_n}{\partial y} \tag{2.15}$$

$$\frac{1}{Pr}\frac{\partial^2\theta}{\partial\eta^2} = -\frac{f}{2}\frac{\partial\theta}{\partial\eta} - \frac{\partial f}{\partial\eta}y\sum_{n=0}^{\infty}\frac{\partial\theta}{\partial\lambda_n}\frac{\partial\lambda_n}{\partial y} + \frac{\partial\theta}{\partial\eta}y\sum_{n=0}^{\infty}\frac{\partial f}{\partial\lambda_n}\frac{\partial\lambda_n}{\partial y} + y\frac{\partial f}{\partial\eta}\left(\frac{\theta}{T_w - T_0}\right)\frac{\partial T_w}{\partial y} \tag{2.16}$$

In the above equations, Gr_y/Re_y^2 is the governing parameter which is local modified Richardson number. Gr_y and Re_y are modified Grashof number and Reynolds number, respectively, which are

$$Gr_y = \frac{g\gamma(T_w - T_0)^2 y^3}{\nu^2} \tag{2.17}$$

and

$$Re_y = \frac{v_\infty y}{\nu}\,. \tag{2.18}$$

The boundary conditions (2.10) and (2.11) in terms of dimensionless parameters f, θ and η are as

$$\text{At} \quad \eta = 0: \quad f = 0, \quad \frac{\partial f}{\partial \eta} = 0, \quad \theta = 1 \tag{2.19}$$

$$\text{At} \quad \eta \to \infty: \quad \frac{\partial f}{\partial \eta} \to 1, \quad \theta \to 0 \tag{2.20}$$

It is examined that Eqs. (2.15) and (2.16) involve two independent variables y and η and the equations are in the form of partial differential equations. It can also be observed from the analysis that Eqs. (2.15) and (2.16) become functions of η and λ_n if $\lambda_n(y)$ is taken in the following form ([137])

$$\lambda_n(y) = \frac{y^{n+1}}{T_w - T_0}\frac{d^{n+1}}{dy^{n+1}}(T_w - T_0) \tag{2.21}$$

where, $T_w - T_0$ is infinitely differentiable with respect to y. It is found that even with above definition of $\lambda_n(y)$, the resulting equations contain independent variables as η and $\lambda_n(y)$ and the equations are still partial differential equations. To convert these equations into sets of ordinary differential equations, the dimensionless stream function and dimensionless temperature are expanded in the following forms

$$f(\eta, \lambda_0, \lambda_1, \cdots, \lambda_n, \cdots) = F(\eta) + \lambda_0 f_0(\eta) + \lambda_1 f_1(\eta) + \lambda_2 f_2(\eta) + \cdots + \lambda_0^2 f_{00}(\eta) + \cdots \tag{2.22}$$

$$\theta(\eta, \lambda_0, \lambda_1, \cdots, \lambda_n, \cdots) = H(\eta) + \lambda_0 \theta_0(\eta) + \lambda_1 \theta_1(\eta) + \lambda_2 \theta_2(\eta) + \cdots + \lambda_0^2 \theta_{00}(\eta) + \cdots \tag{2.23}$$

where, $\lambda_0, \lambda_1, \cdots, \lambda_n(y), \cdots$ are the perturbation variables while $F(\eta)$, $f_0(\eta)$, $f_1(\eta)$, $\cdots$, $f_{00}(\eta)$, $\cdots$ and $H(\eta)$, $\theta_0(\eta)$, $\theta_1(\eta)$, $\cdots$, $\theta_{00}(\eta)$, $\cdots$ are coefficient functions for stream function and temperature, respectively. Substituting Eqs. (2.21), (2.22) and (2.23) into the Eqs. (2.15) and (2.16), the equations take the following forms

$$\begin{aligned}
&F''' + \lambda_0 f_0''' + \lambda_1 f_1''' + \lambda_2 f_2''' + \ldots + \lambda_0^2 f_{00}''' + \lambda_1^2 f_{11}''' + \cdots = -\frac{1}{2}FF'' \pm \frac{Gr_y}{Re_y^2}H^2 + \lambda_0\left(-\frac{1}{2}Ff_0{}'' \right.\\
&\left. -\frac{3}{2}f_0F'' + F'f_0' \pm \frac{Gr_y}{Re_y^2}2H\theta_0\right) + \lambda_1\left(-\frac{1}{2}Ff_1{}'' - \frac{5}{2}f_1F'' \pm \frac{Gr_y}{Re_y^2}2H\theta_1 - F''f_0 + F'f_0 + 2F'f_1'\right)\\
&+ \lambda_2\left(-\frac{1}{2}Ff_2'' - \frac{7}{2}f_2F'' \pm \frac{Gr_y}{Re_y^2}2H\theta_2 - F''f_1 + F'f_1' + 3F'f_2'\right)\\
&+ \lambda_0^2\left(-\frac{1}{2}Ff_{00}'' - \frac{5}{2}f_{00}F'' - \frac{3}{2}f_0f_0'' \pm \frac{Gr_y}{Re_y^2}(H\theta_{00} + 2H\theta_0) + F''f_0 + 2F'F_{00}' + f_0'f_0' - F'f_0'\right)\\
&+ \lambda_1^2\left(-\frac{1}{2}Ff_{11}'' - \frac{5}{2}F''f_{11} - \frac{3}{2}f_1f_1'' - f_0f_1'' + 2F'F_{11}' \pm \frac{Gr_y}{Re_y^2}(\theta_1^2 + 2H\theta_{11}) + f_0'f_1' + 2f_1'f_1'\right) + \cdots
\end{aligned} \tag{2.24}$$

$$\frac{1}{Pr}(H'' + \lambda_0\theta_0'' + \lambda_1\theta_1'' + \lambda_2\theta_2'' + \ldots + \lambda_0^2\theta_{00}'' + \lambda_1^2\theta_{11}'' + \ldots) = -\frac{1}{2}FH' + \lambda_0\left(-\frac{1}{2}F\theta_0' - \frac{3}{2}f_0H' + F'\theta_0 + HF'\right) + \lambda_1\left(-\frac{1}{2}F\theta_1' - \frac{5}{2}f_1H' + F'\theta_0 + 2F'\theta_1 - H'f_0\right) + \lambda_2\left(-\frac{1}{2}F\theta_2' - \frac{7}{2}f_2H' + F'\theta_1 + 3F'\theta_2 - H'f_1\right) + \lambda_0^2\left(-\frac{1}{2}F\theta_{00}' - \frac{5}{2}f_{00}H' + 2F'\theta_{00} - \frac{3}{2}f_0\theta_0' + f_0'\theta_0 + H'f_0 + Hf_0\right) + \lambda_1^2\left(-\frac{1}{2}F\theta_{11}' - \frac{9}{2}f_{11}H' + 4F'\theta_{11} - \frac{5}{2}f_1\theta_1' + f_0'\theta_0 + 2f_1'\theta_1 - f_0\theta_1'\right) + \cdots \tag{2.25}$$

Note that in the above equations, primes ($'$) denotes the differential with respect to η.

Equating on either sides of coefficients such as λ_0, λ_1, λ_2, $\cdots$, $\cdots$, $\lambda_n(y)$, $\cdots$ of above ordinary differential equations, we get infinite number of sets of ordinary differential equations of various universal functions. More number of sets of equations considered in the calculation, more will be the accuracy of the solutions ([140, 141]). The change in the solutions was found to be negligible, if the sets of equations are considered beyond λ_0, λ_1, λ_2, λ_0^2 and λ_1^2. The sets of equations considered in the present study are as following.

Constant term:

$$\begin{aligned} F''' &= -\frac{1}{2}FF'' \pm \frac{Gr_y}{Re_y^2}H^2 \\ \frac{1}{Pr}H'' &= -\frac{1}{2}FH' \end{aligned} \tag{2.26}$$

The set of coefficient of λ_0:

$$\begin{aligned} f_0''' &= -\frac{1}{2}Ff_0'' - \frac{3}{2}f_0F'' \pm \frac{Gr_y}{Re_y^2}2H\theta_0 + F'f_0' \\ \frac{1}{Pr}\theta_0'' &= -\frac{1}{2}F\theta_0' - \frac{3}{2}f_0H' + F'\theta_0 + HF' \end{aligned} \tag{2.27}$$

The set of coefficient of λ_1:

$$\begin{aligned} f_1''' &= -\frac{1}{2}Ff_1'' - \frac{5}{2}f_1F'' \pm \frac{Gr_y}{Re_y^2}2H\theta_1 - F''f_0 + F'f_0 + 2F'f_1' \\ \frac{1}{Pr}\theta_1'' &= -\frac{1}{2}F\theta_1' - \frac{5}{2}f_1H' + F'\theta_0 + 2F'\theta_1 - H'f_0 \end{aligned} \tag{2.28}$$

The set of coefficient of λ_2:

$$\begin{aligned} f_2''' &= -\frac{1}{2}Ff_2'' - \frac{7}{2}f_2F'' \pm \frac{Gr_y}{Re_y^2}2H\theta_2 - F''f_1 + F'f_1' + 3F'f_2' \\ \frac{1}{Pr}\theta_2'' &= -\frac{1}{2}F\theta_2' - \frac{7}{2}f_2H' + F'\theta_1 + 3F'\theta_2 - H'f_1 \end{aligned} \tag{2.29}$$

The set of coefficient of λ_0^2:

$$
\begin{aligned}
f_{00}''' &= -\frac{1}{2}Ff_{00}'' - \frac{5}{2}f_{00}F'' - \frac{3}{2}f_0f_0'' \pm \frac{Gr_y}{Re_y^2}(\theta_0^2 + 2H\theta_{00}) + F''f_0 + 2F'F_{00}' + f_0'f_0' - F'f_0' \\
\frac{1}{Pr}\theta_{00}'' &= -\frac{1}{2}F\theta_{00}' - \frac{5}{2}f_{00}H' + 2F'\theta_{00} - \frac{3}{2}f_0\theta_0' + f_0'\theta_0 + H'f_0 + Hf_0'
\end{aligned}
\tag{2.30}
$$

The set of coefficient of λ_1^2:

$$
\begin{aligned}
f_{11}''' &= -\frac{1}{2}Ff_{11}'' - \frac{5}{2}F''f_{11} - \frac{3}{2}f_1f_1'' \pm \frac{Gr_y}{Re_y^2}(\theta_1^2 + 2H\theta_{11}) - f_0f_1'' + 2F'F_{11}' + f_0'f_1' + 2f_1'f_1' \\
\frac{1}{Pr}\theta_{11}'' &= -\frac{1}{2}F\theta_{11}' - \frac{9}{2}f_{11}H' + 4F'\theta_{11} - \frac{5}{2}f_1\theta_1' + f_0'\theta_0 + 2f_1'\theta_1 - f_0\theta_1'
\end{aligned}
\tag{2.31}
$$

Expanding Eqs. (2.19) and (2.20) using Eqs. (2.22) and (2.23) and comparing the same powers of $\lambda_n(y)$, we get the following forms of boundary conditions for the above sets of differential equations of coefficient functions.

$$
\begin{aligned}
\text{At } \eta = 0: \quad & F = 0, \quad f_0 = f_1 = f_2 = f_{00} = f_{11} = 0 \\
& H = 1, \theta_0 = \theta_1 = \theta_2 = \theta_{00} = \theta_{11} = 0 \\
& F' = 0, f_0' = f_1' = f_2' = f_{00}' = f_{11}' = 0
\end{aligned}
\tag{2.32}
$$

$$
\begin{aligned}
\text{At } \eta \to \infty: \quad & F' = 1, \quad f_0' = f_1' = f_2' = f_{00}' = f_{11}' = 0 \\
& H = 0, \theta_0 = \theta_1 = \theta_2 = \theta_{00} = \theta_{11} = 0
\end{aligned}
\tag{2.33}
$$

The above sets of ordinary differential equations are coupled equations. For a given wall temperature variation, these equations are solved using shooting method. The ordinary differential equations are integrated using fourth-order Runge-Kutta method. In the solutions, Prandtl number of water near density inversion is taken to be 11.4. The solutions of the differential equations yield values of coefficient functions with respect to independent variable η. The solutions of these functions are valid for any arbitrary wall temperature variation. These functions are of general nature and hence, called as "universal functions".

For the fluid flow and heat transfer calculations of both aiding and opposing flows, universal functions of stream function and temperature are required along with perturbation variables (see Eqs. (2.22) and (2.23)). The universal functions for various Gr_y/Re_y^2 values are shown in figures 2.2–2.3 for aiding and opposing flows. Figure 2.2 shows the universal functions of stream function and temperature for $Gr_y/Re_y^2 = 0$, which corresponds to forced convection extreme. It can be seen from figure 2.2(a) that the universal functions such as f_0, f_1 and f_{00} come out to be zero, for forced convection. This is due to the fact that forced convection flow field remains independent of wall temperature variation. Since, perturbation variables λ_0, λ_1, ..., λ_{00}, ... depend on wall temperature variation, to get velocity independent of these functions, we need to have f_0, f_1 and f_{00} as zeros from Eq. (2.22). Hence, the universal functions associated with perturbation variables do not contribute in the calculation of skin friction coefficient for forced convection. Figures 2.3(a) and 2.3(b) show the variation of universal functions of stream function and temperature for aiding and opposing flows, respectively.

2.4 Velocity, skin friction coefficient and Nusselt number calculations in terms of universal functions

The study predicts the velocity and temperature distributions in the boundary layer, drag and heat transfer rates along the wall in mixed convection flows. The temperature distribution in terms of universal functions can be directly calculated by Eq. (2.23). The velocity distribution and skin friction coefficient and heat transfer rates along the wall, in terms of universal functions are derived as following.

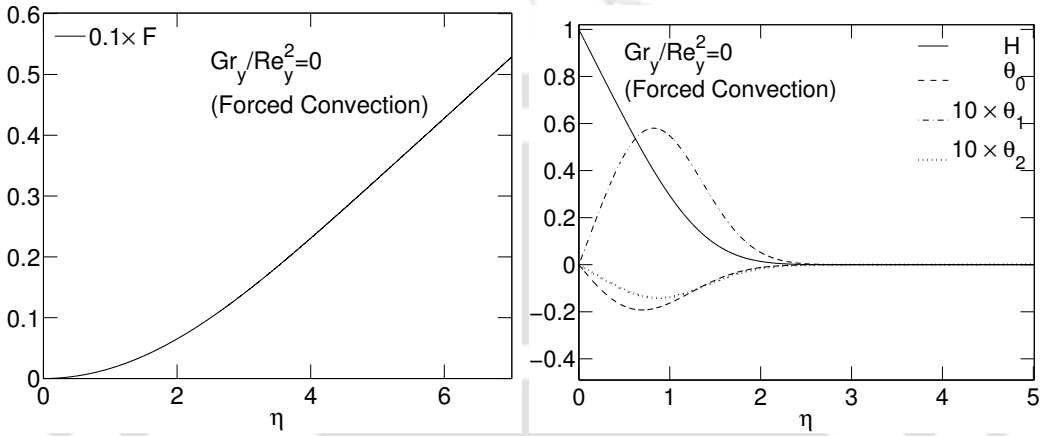

(a) $Gr_y/Re_y^2 = 0$ (b) $Gr_y/Re_y^2 = 0$

Figure 2.2: Universal functions of stream function and temperature for $Gr_y/Re_y^2 = 0$ (forced convection asymptote)

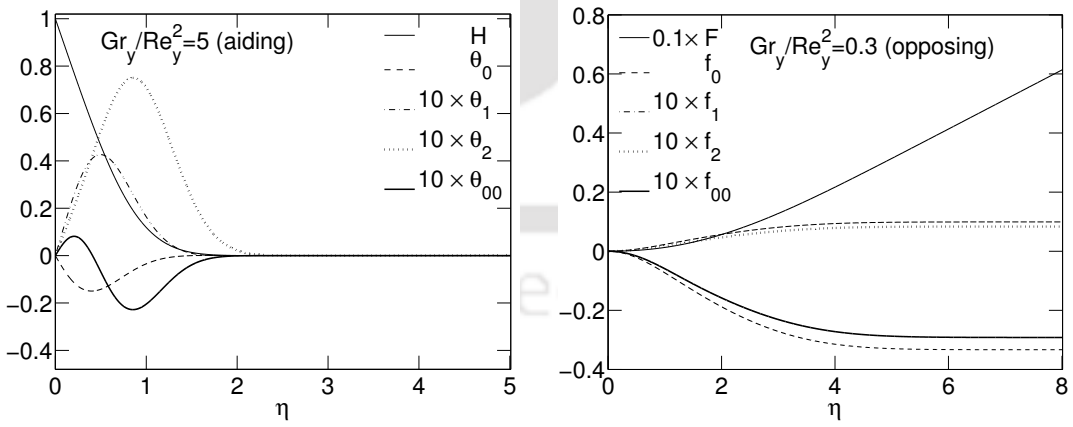

(a) $Gr_y/Re_y^2 = 5$ (b) $Gr_y/Re_y^2 = 0.3$

Figure 2.3: Universal functions of temperature and stream function for aiding and opposing flow

In stream function form, the vertical component of velocity can be written as $v = \dfrac{\partial \psi}{\partial x}$. From this expression, v is obtained, using Eqs. (2.12) and (2.14), as follows

$$v = \frac{\partial \psi}{\partial x} = \sqrt{v_\infty \nu y}\frac{\partial f}{\partial \eta}\frac{\partial \eta}{\partial x} = v_\infty f'(\eta) \tag{2.34}$$

Substituting Eq. (2.22) in above equation, the dimensionless form of vertical component of velocity in terms of universal functions is derived as,

$$\frac{v}{v_\infty} = f'(\eta) = F'(\eta) + \lambda_0 f_0'(\eta) + \lambda_1 f_1'(\eta) + \lambda_2 f_2'(\eta) + \ldots + \lambda_0^2 f_{00}'(\eta) + \lambda_1^2 f_{11}'(\eta) + \ldots \quad (2.35)$$

Skin friction drag in terms of universal functions is derived below. The local skin friction coefficient can be written as,

$$C_{fy} = \frac{\tau_w}{\rho v_\infty^2} \quad (2.36)$$

where, v_∞ is free-stream velocity and τ_w is shear stress at wall ($x = 0$). Now, the wall shear stress in the form of universal functions becomes,

$$\tau_w = \mu \left.\frac{\partial v}{\partial x}\right|_{x=0} = \mu \left.\frac{\partial}{\partial x}\left(\frac{\partial \psi}{\partial x}\right)\right|_{x=0} = \mu v_\infty \sqrt{\frac{v_\infty}{\nu y}} \left.\frac{\partial^2 f}{\partial \eta^2}\right|_{\eta=0} \quad (2.37)$$

Using Eq. (2.36) and Eq. (2.37) we get

$$\frac{C_{fy}}{Re_y^{-1/2}} = f''(\eta)|_{\eta=0} = F''(0) + \lambda_0 f_0''(0) + \lambda_1 f_1''(0) + \lambda_2 f_2''(0) + \cdots + \lambda_0^2 f_{00}''(0) + \lambda_1^2 f_{11}''(0) + \cdots \quad (2.38)$$

To calculate the heat transfer rates along the wall, the local heat transfer coefficient $h(y)$ can be written as following,

$$h(y) = \frac{q_w(y)}{T_w - T_0} \quad (2.39)$$

Now, the local Nusselt number is given as,

$$Nu_y = \frac{h(y)\, y}{k} \quad (2.40)$$

Using Eq.(2.39) in above equation, the local Nusselt number is derived,

$$Nu_y = \frac{q_w(y)}{T_w - T_0} \frac{y}{k} \quad (2.41)$$

From Eq. (2.13), the temperature difference $(T_w - T_0)$ can be given as,

$$T_w - T_0 = \theta_{\eta=0} \frac{q_w(y)}{k} y\, Re_y^{-1/2} \quad (2.42)$$

where, $\theta_{\eta=0}$ is the dimensionless temperature corresponds to wall ($\eta = 0$). Substituting Eq. (2.42) in Eq. (2.41) we get the heat transfer rates as

$$\frac{Nu_y}{Re_y^{1/2}} = \frac{1}{\theta_{\eta=0}} \quad (2.43)$$

Using Eq. (2.23), the heat transfer rates in Eq. (2.43) in the form of $Nu_y/Re_y^{1/2}$ becomes

$$\frac{Nu_y}{Re_y^{1/2}} = \left[H(0) + \lambda_0\theta_0(0) + \lambda_1\theta_1(0) + \lambda_2\theta_2(0) + \cdots + \lambda_0^2\theta_{00}(0) + \lambda_1^2\theta_{11}(0) + \cdots\right]^{-1} \tag{2.44}$$

Table 2.1: Values of universal constants of stream function for aiding mixed convection flow for various Gr_y/Re_y^2 values

$\frac{Gr_y}{Re_y^2}$	$F''(0)$	$f_0''(0)$	$f_1''(0)$	$f_2''(0)$	$f_{00}''(0)$	$f_{11}''(0)$
0	0.3321	0.0000	0.0000	0.0000	0.0000	0.0000
0.5	0.5366	-0.0655	0.0206	-0.0051	0.0030	0.0007
1	0.7170	-0.1162	0.0366	-0.0091	0.0032	0.0012
5	1.8496	-0.3998	0.1253	-0.0311	0.0014	0.0038
10	2.9790	-0.6695	0.2088	-0.0518	0.0003	0.0061
15	3.9730	-0.9045	0.2813	-0.0698	0.0001	0.0080

Table 2.2: Values of universal constants of stream function for opposing mixed convection flows for various Gr_y/Re_y^2 values

$\frac{Gr_y}{Re_y^2}$	$F''(0)$	$f_0''(0)$	$f_1''(0)$	$f_2''(0)$	$f_{00}''(0)$	$f_{11}''(0)$
0	0.3321	0.0000	0.0000	0.0000	0.0000	0.0000
0.05	0.3096	0.0082	-0.0026	-0.0006	-0.0009	-0.0001
0.1	0.2865	0.0170	-0.0053	-0.0013	-0.0021	-0.0002
0.2	0.2385	0.0367	-0.0112	-0.0027	-0.0058	-0.0004
0.3	0.1875	0.0607	-0.0183	-0.0044	-0.0132	-0.0006

Table 2.3: Values of universal constants of temperature for aiding mixed convection flow

$\frac{Gr_y}{Re_y^2}$	$H'(0)$	$\theta_0'(0)$	$\theta_1'(0)$	$\theta_2'(0)$	$\theta_{00}'(0)$	$\theta_{11}'(0)$
0	-0.7609	-0.4675	0.1028	-0.0228	0.0000	0.0000
0.5	-0.8297	-0.4958	0.1055	-0.0233	0.0162	0.0004
1	-0.8816	-0.5227	0.1088	-0.0239	0.0272	0.0007
5	-1.1160	-0.6628	0.1302	-0.0279	0.0635	0.0014
10	-1.2773	-0.7640	0.1473	-0.0312	0.0817	0.0019
20	-1.4810	-0.8923	0.1698	-0.0357	0.1016	0.0024

It can be seen from the Eqs. (2.38) and (2.44) that $C_{fy}/Re_y^{-1/2}$ and $Nu_y/Re_y^{1/2}$ depend on the universal functions of stream function ($F''(0)$, $f_0''(0)$, $f_1''(0)$, $f_2''(0)$, $f_{00}''(0)$, $f_{11}''(0)$, $\cdots$) and temperature ($\theta(0)$, $\theta_0(0)$, $\theta_1(0)$, $\theta_2(0)$, $\theta_{00}(0)$, $\theta_{11}(0)$, $\cdots$), respectively, and also on the perturbation variables (λ_0,

Table 2.4: Values of universal constants of temperature for opposing mixed convection flow

$\frac{Gr_y}{Re_y^2}$	$H'(0)$	$\theta_0'(0)$	$\theta_1'(0)$	$\theta_2'(0)$	$\theta_{00}'(0)$	$\theta_{11}'(0)$
0	-0.7609	-0.4675	0.1028	-0.0228	0.0000	-0.0000
0.05	-0.7524	-0.4650	0.1026	-0.0228	-0.0019	-0.0001
0.1	-0.7436	-0.4627	0.1025	-0.0227	-0.0037	-0.0002
0.2	-0.7244	-0.4592	0.1025	-0.0227	-0.0068	-0.0004
0.3	-0.7026	-0.4584	0.1030	-0.0227	-0.0076	-0.0008

λ_1, λ_2, λ_0^2, λ_1^2, $\cdots$). Since, the universal functions need to be calculated only once for any particular flow, the calculation of skin friction coefficient and heat transfer rates require perturbation variables. As the perturbation variables depend on boundary conditions then for a given wall temperature, the perturbation variables can be calculated. For a particular wall temperature, velocity, temperature, skin friction coefficient and heat transfer rates can be calculated using universal functions and perturbation variables using simple algebraic calculations, without solving any differential equations. To calculate the skin friction coefficient, the universal functions of stream function at $\eta = 0$ for aiding and opposing convection are shown in tables 2.1 and 2.2, respectively for various values of Gr_y/Re_y^2. For calculation of heat transfer rates, the required universal functions for temperature are given in tables 2.3 and 2.4 for aiding and opposing flows, respectively.

2.5 Mixed convection flow for power law wall temperature variation

The universal functions found above are valid for any arbitrary wall temperature variation. In this section, the results are applied for power law wall temperature. Power law variation of wall temperature is chosen because many functions can be expressed in terms of power series. Hence, these results are applicable for functions expressible in power series. The wall temperature is taken in the following form

$$T_w - T_0 = Ay^m \tag{2.45}$$

where, A and m are constants. For the above power law wall temperature, the variables λ_0, λ_1, λ_0^2, $\cdots$ can be calculated using Eq. (2.21). They can be expressed in terms of m as

$$\begin{aligned} \lambda_0 = m,\ \lambda_1 = m(m-1),\ \lambda_2 = m(m-1)(m-2), \\ \lambda_0^2 = m^2,\ \lambda_1^2 = m^2(m-1)^2, \cdots \end{aligned} \tag{2.46}$$

From the above expressions, for a given m value, perturbation variables (λ_0, λ_1, λ_2, λ_0^2, λ_1^2, $\cdots$) can be calculated. Since, the perturbation variables and universal functions are known, velocity, skin friction coefficient and heat transfer rates can be calculated from Eqs. (2.35), (2.38) and (2.44), respectively. It is noticed that calculation of velocity and skin friction coefficient require derivatives of universal functions for stream function which come as a solution of system of ordinary differential

equations. The temperature variation with respect to η is found out using Eq. (2.23).

2.5.1 Validation

To validate the present methodology, mixed convection boundary layer flow of water over a vertical plate, with density inversion effect, is simulated. The plate is specified with power law varying temperature. The boundary layer flow is solved for various Gr_y/Re_y^2 and power law index values. The skin friction coefficient for various values of Gr_y/Re_y^2 and power law index m is shown in table 2.5. From the table, it can be seen that the present results show good agreement with the results obtained by Vighnesam and Soundalgekar [5].

Table 2.5: Comparison of $C_{fy}/Re_y^{-1/2}$ for power law wall temperature variation obtained in the present study to those presented by Vighnesam and Soundalgekar [5]

m	$\frac{Gr_y}{Re_y^2}$	Present study	Vighnesam and Soundalgekar [5]	% Deviation
0	0	0.3321	0.3320	0.03
0	-0.5	0.0705	0.0705	0
1	0.5	0.4741	0.4743	0.04
1	0.7	0.5272	0.5273	0.02

2.5.2 Fluid flow solutions

The dimensionless velocity ($v/v_\infty = f'$) for different η can be calculated using Eq. (2.35). The variation of dimensionless velocity with respect to η is shown in figures 2.4 and 2.5 for aiding and opposing flows, respectively for various values of Gr_y/Re_y^2 and wall temperature power index $m = 0$ and $m = 1$. It can be seen from the figures that for a given η value, the dimensionless velocity increases with Gr_y/Re_y^2 values in aiding flow, whereas, it decreases in opposing flows, for both m values. This is due to the fact that external and buoyancy forces act in the same direction in aiding flow situation. For a given values of Re_y, increase in Gr_y/Re_y^2 represents increase in Gr_y. Increase in Gr_y value physically represents increase in buoyancy force. Hence, in aiding mixed convection, as the values of Gr_y/Re_y^2 increases, the strength of fluid flow increases resulting increase in dimensionless velocity. However, in opposing flow, the buoyancy forces oppose the external forces. Hence, increased buoyancy forces results in decreased effective driving force. This leads to reduction in dimensionless velocity as the value of Gr_y/Re_y^2 increases.

From the variation of dimensionless velocity with respect to η, we can find out velocity boundary layer thickness. The velocity boundary layer thickness corresponds to η at which v/v_∞ equal to 0.99. The variation of dimensionless velocity boundary layer thickness ($\delta_y[v_\infty/\nu y]^{1/2}$) with Gr_y/Re_y^2 for various values of m are shown in figures 2.6(a) and 2.6(b), respectively, for aiding and opposing

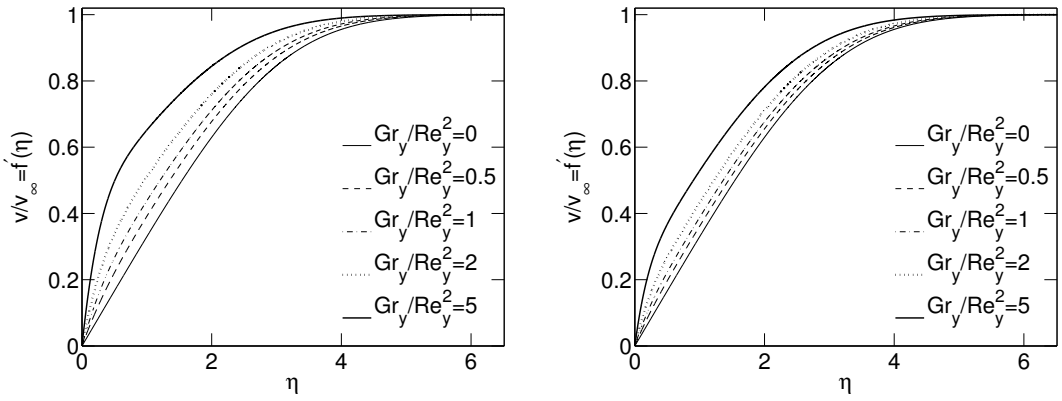

(a) $m = 0$ (b) $m = 1$

Figure 2.4: Variation of dimensionless velocity with η for various values of Gr_y/Re_y^2 for aiding flow

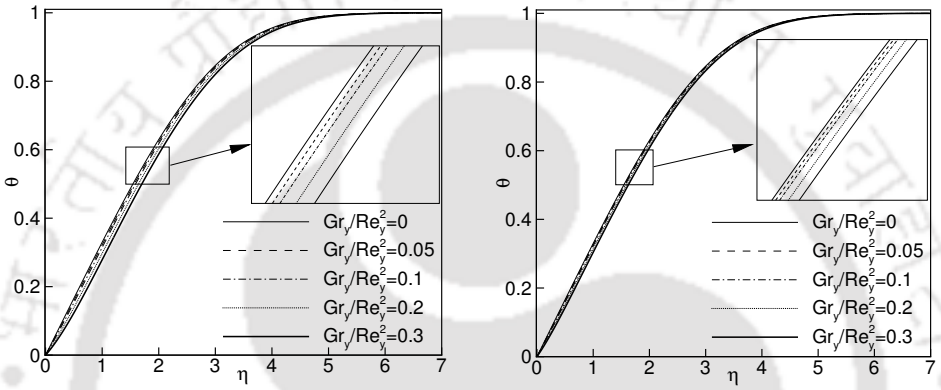

(a) $m = 0$ (b) $m = 1$

Figure 2.5: Variation of dimensionless velocity with η for various values of Gr_y/Re_y^2 for opposing flow

flows. For a given m value, the boundary layer thickness decreases with increasing values of Gr_y/Re_y^2 in case of aiding mixed convection. This is because convection becomes stronger with increasing Gr_y/Re_y^2 values resulting thinner boundary layer. The opposite trend is observed for opposing flow due to weaker convection as a result of opposing interaction of buoyancy and external forces. It may be noted that dimensionless velocity curves for different m values coincide for $Gr_y/Re_y^2 = 0$ for both aiding and opposing mixed convection. This is due to the fact that $Gr_y/Re_y^2 = 0$ represents forced convection. In forced convection, velocity boundary layer is not affected by the wall temperature boundary condition. Hence, it should be independent of m values. Hence, for $Gr_y/Re_y^2 = 0$, boundary layer thickness becomes same for all m values.

The variation of skin friction coefficient ($C_{fy}/Re_y^{-1/2}$) with Gr_y/Re_y^2 values is shown in figures 2.7(a) and 2.7(b) for aiding and opposing flows, respectively, for various m values. In both the above flows, $C_{fy}/Re_y^{-1/2}$ values start with forced convection values and vary towards natural convection asymptote with increasing values of Gr_y/Re_y^2 for all power-index values. For a given m value, value of skin friction coefficient is greater than corresponding forced convection values in aiding mixed convection and $C_{fy}/Re_y^{-1/2}$ increases with increasing Gr_y/Re_y^2 values because buoyancy and external forces act in same direction in aiding flow. Here, higher the value of Gr_y/Re_y^2, stronger the

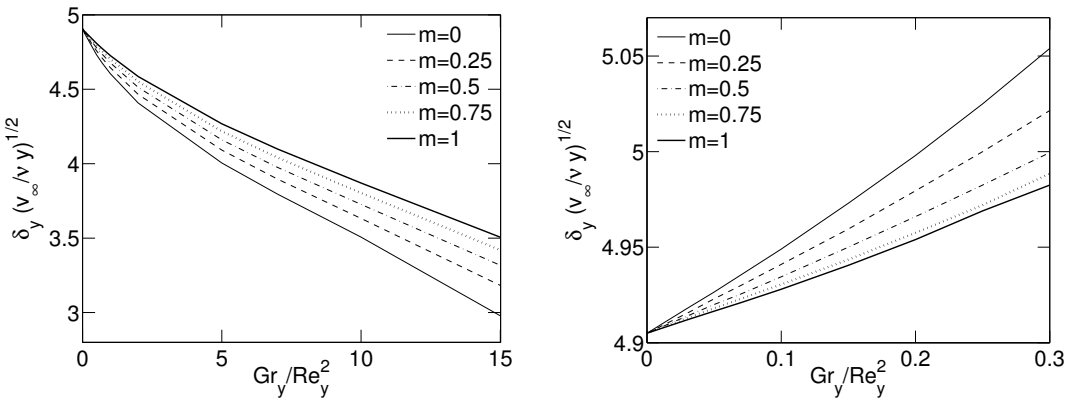

(a) Aiding flow (b) Opposing flow

Figure 2.6: Variation of velocity boundary layer thickness ($\delta_y[v_\infty/\nu y]^{1/2}$) with Gr_y/Re_y^2 for various m values

flow. Due to increased flow strength, the shear stress on the wall increases due to increased velocity gradient on plate. Hence, skin friction coefficient increases with increasing Gr_y/Re_y^2 values.

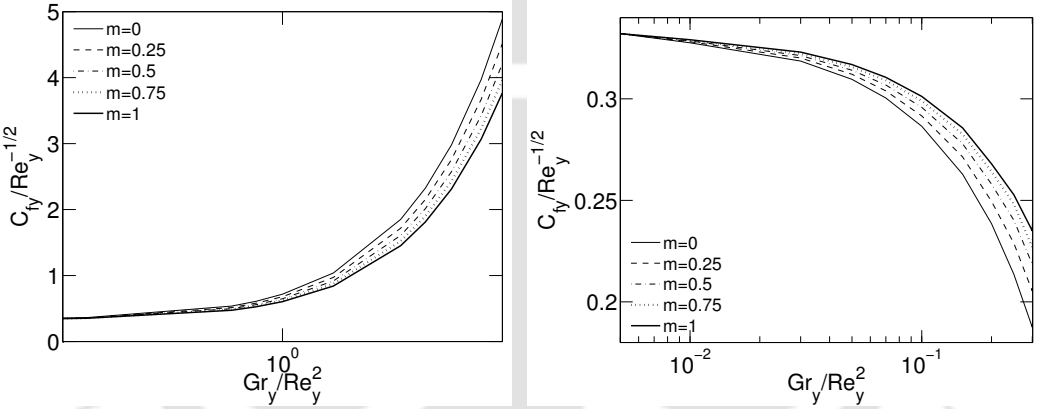

(a) Aiding flow (b) Opposing flow

Figure 2.7: Variation of skin friction coefficient with Gr_y/Re_y^2 for various power index values m

In opposing flow, the value of skin friction coefficient is lower than corresponding forced convection values and it decreases with increasing Gr_y/Re_y^2 values. This trend is opposite to the trend in aiding mixed convection. This is due to the opposite nature of interaction of buoyancy and external forces in opposing flows.

The variation of skin friction coefficient with m values for various Gr/Re^2 values is shown in Figs. 2.8(a) and 2.8(b), for aiding and opposing flows, respectively. For aiding flow, it can be seen from the figure 2.8(a) that the skin friction coefficient decreases with increasing value of m for higher Gr/Re^2 values while it remains almost constant for small Gr/Re^2 values. It can be seen from Eq. (2.38) that skin friction coefficient depends on universal constants ($F''(0)$, $f_0''(0)$, $f_1''(0)$, etc.) and associated constants such as λ_0, λ_1, λ_0^2, $\cdots$, etc. in Eq. (2.38), where λ_0, λ_1, λ_0^2, $\cdots$, etc. are proportional to m values. In Eq. (2.38), first few terms dominate the skin friction coefficient and remaining terms have comparatively less effect on skin friction coefficient. Table 2.1 shows that the first most dominant term $F''(0)$ is having big and positive values whereas the second most dominant term $f_0''(0)$

is having negative and relatively small values for different Gr/Re^2 values. Hence, the overall effect of all dominating terms in the calculation decrease skin friction coefficient with increasing values of m for aiding flow. While, in case of opposing flow, both $F''(0)$ and $f_0''(0)$ are found to be positive, resulting increase in the value of skin friction coefficient with increasing values of m. In the figures, plot for $Gr_y/Re_y^2 = 0$ corresponds to forced convection in both aiding and opposing flows. It also can be observed that for $Gr_y/Re_y^2 = 0$, the value of skin friction coefficient remains constant with increasing m values because forced convection flow is independent of the wall temperature boundary condition.

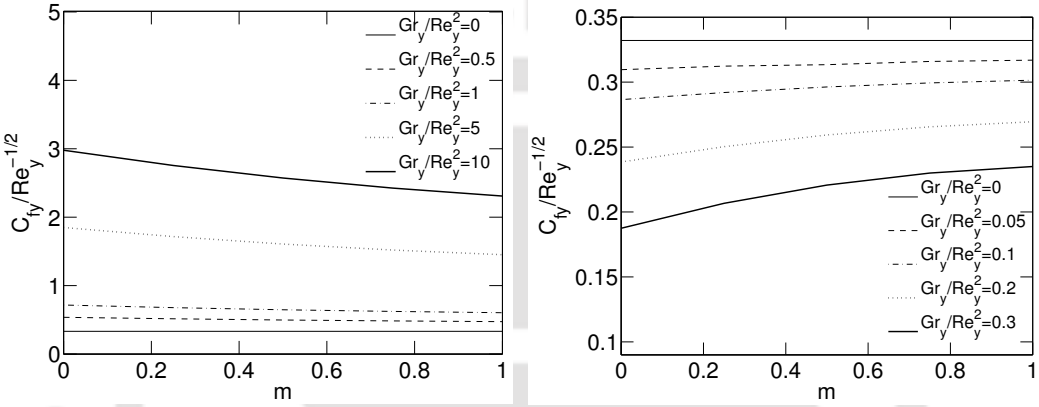

(a) Aiding flow (b) Opposing flow

Figure 2.8: Variation of skin friction coefficient with m for various Gr_y/Re_y^2 values

2.5.3 Heat transfer solutions

The variation of dimensionless temperature with η is presented for $m = 0$ and $m = 1$ which is shown in figures 2.9 and 2.10 for aiding and opposing mixed convection, respectively for various Gr_y/Re_y^2 values. It is observed from the figures that at particular η value, the dimensionless temperature decreases with increasing values of Gr_y/Re_y^2 for aiding flow, while the reverse trend is observed for opposing flow. As the increased Gr_y/Re_y^2 represents strengthened resulting convection in aiding flow, it leads to lowered temperatures. But in opposing flow increasing Gr_y/Re_y^2 represents weakened convection leading to higher temperatures.

From the computations of θ variations with η, the thermal boundary layer thickness can be found out. Thermal boundary layer thickness corresponds to horizontal distance from wall to a point in boundary layer at which θ value becomes 0.01. This means that the boundary layer thickness corresponds to η value at which θ value becomes 0.01. The variation of dimensionless boundary layer thickness $\delta_T(v_\infty/\nu y)^{1/2}$ with Gr_y/Re_y^2 for various values of power-index m is shown in figure 2.11 for both cases of aiding and opposing mixed convection. It can be observed from figures that boundary layer thickness, at a given y value, decreases monotonically with increasing Gr_y/Re_y^2 values for aiding mixed convection. In aiding flow, as buoyancy complement external forces, increasing Gr_y/Re_y^2

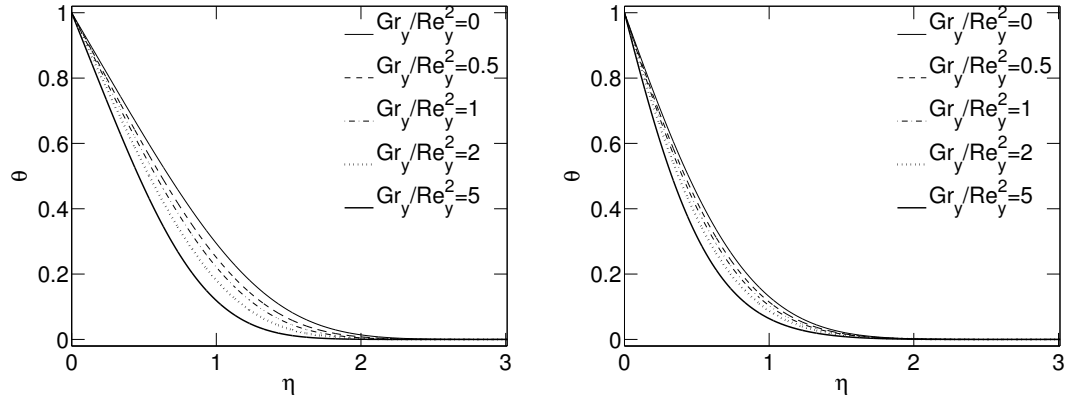

(a) $m = 0$ (b) $m = 1$

Figure 2.9: Variation of dimensionless temperature with η for various values of Gr_y/Re_y^2 for aiding flow

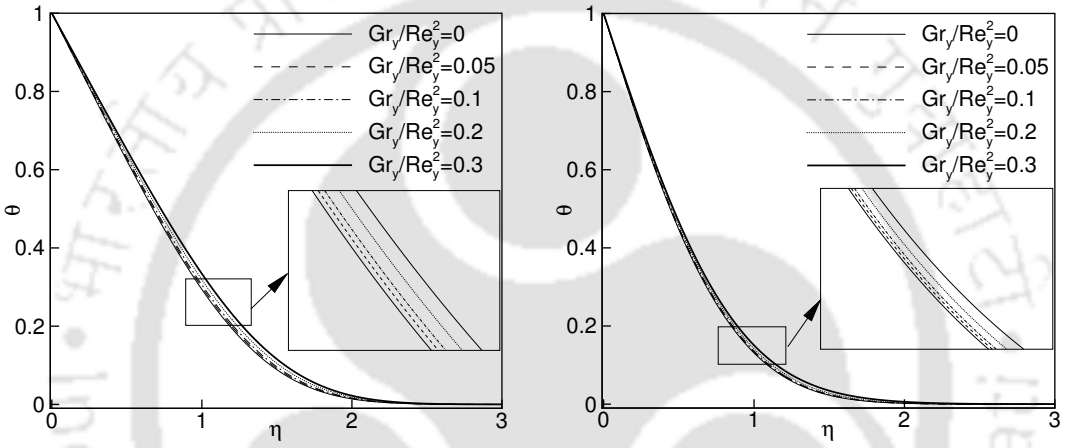

(a) $m = 0$ (b) $m = 1$

Figure 2.10: Variation of dimensionless temperature with η for various values of Gr_y/Re_y^2 for opposing flow

value results in stronger convection and thinner boundary layer. The opposite trend is observed for the case of opposing flow because, in this case, buoyancy opposes external forces.

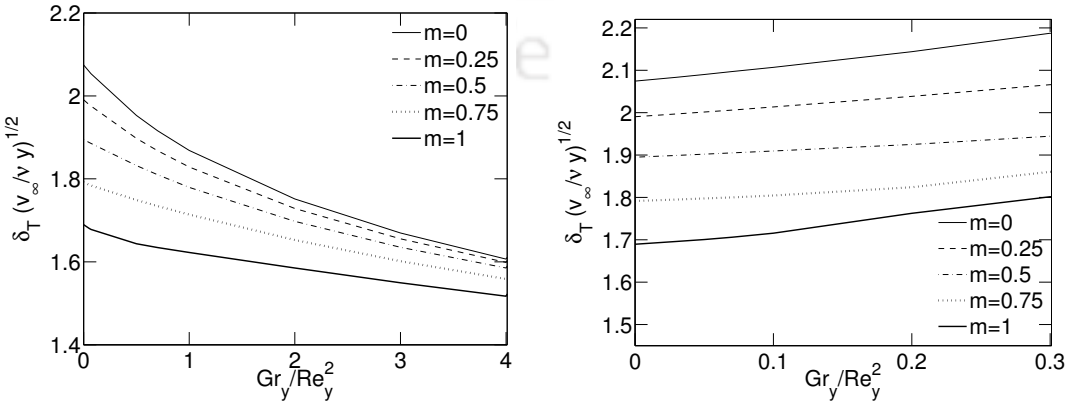

(a) Aiding flow (b) Opposing flow

Figure 2.11: Variation of thermal boundary layer thickness ($\delta_T[v_\infty/\nu y]^{1/2}$) with Gr_y/Re_y^2 for various m values

To see the effect of Gr_y/Re_y^2 values on heat rates, the variation of $Nu_y/Re_y^{1/2}$ with Gr_y/Re_y^2 values for aiding case is shown in figure 2.12(a), for various m values. The corresponding plots for opposing mixed convection are shown in figure 2.12(b). In aiding flow case, for a given m value, heat rates increase with increasing Gr_y/Re_y^2 values. However, the heat rates decrease with values of Gr_y/Re_y^2 in opposing flow case. In the above results, $Nu_y/Re_y^{1/2}$ values for $Gr_y/Re_y^2 = 0$, corresponds to forced convection asymptote. The Nusselt number starts with forced convection values and varies towards natural convection asymptote with increasing Gr_y/Re_y^2. When mixed convection approaches forced convection extreme, the variation of Nusselt number becomes constant. This is typical in mixed convection flows. It can be seen from the figures that for a given value of Re_y, Nusselt number increases with Grashof number. This is due to the fact that increased Grashof number represents higher buoyancy forces, hence higher the heat transfer rates. For a given set of Gr_y and Re_y values, the Nusselt numbers in case of aiding mixed convection are higher than those of opposing flow. This is because the external flow complement buoyancy forces in aiding flow. However, in opposing flow, the external forces oppose buoyancy forces, resulting lower heat transfer rates. For opposing mixed convection, solutions are obtained for lower values of Gr_y/Re_y^2, because at higher values, flow separation takes place for which boundary layer approximations are not applicable as the boundary layer tends to separate.

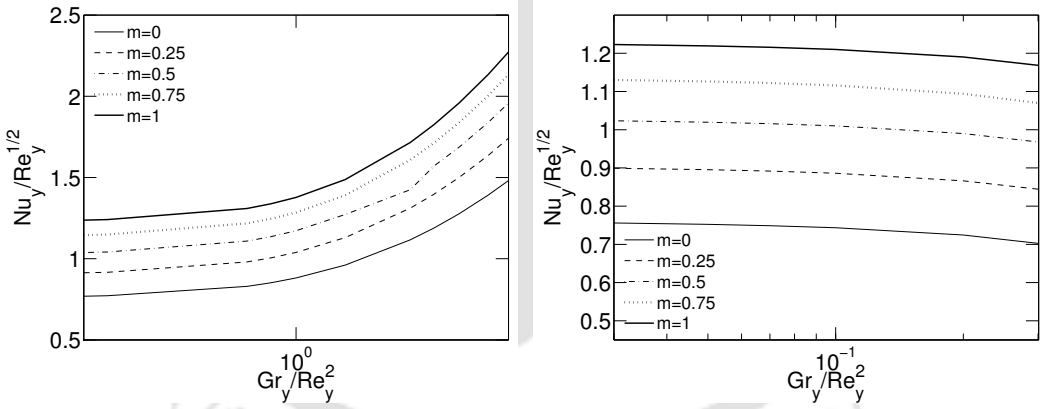

(a) Aiding flow (b) Opposing flow

Figure 2.12: Variation of $Nu_y/Re_y^{1/2}$ with Gr_y/Re_y^2 for various values of m

The variation of heat transfer rates in terms of $Nu_y/Re_y^{1/2}$ with variation of power index value m is shown in figures 2.13(a) and 2.13(b), respectively, for aiding and opposing cases for various Gr_y/Re_y^2 values. From these figures, it is observed that the heat transfer rates increases with power index m for a given Gr_y/Re_y^2 value for both aiding and opposing flow situations. This is because with increasing m value, temperatures increase at all points on the plate. Hence, at any given location of the plate, the temperature difference between the plate and fluid increases with increasing m for any given Gr_y/Re_y^2 value, resulting higher heat transfer rates. This is the reason why heat transfer rates increase with increasing m values for all Gr_y/Re_y^2 values in both the cases of aiding and opposing flows.

The essence of the perturbation method used in the present study is that the above results can

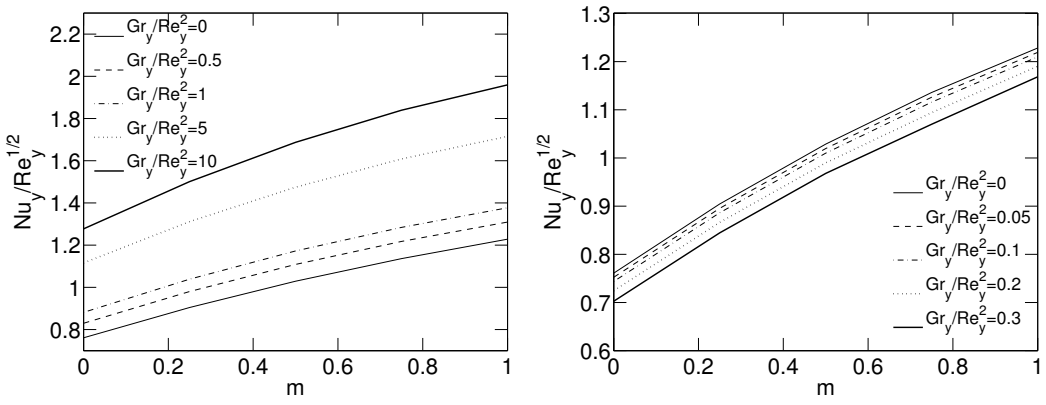

(a) Aiding flow (b) Opposing flow

Figure 2.13: Variation of $Nu_y/Re_y^{1/2}$ with m for various values of Gr_y/Re_y^2

be readily used for any arbitrary wall temperature variation without need for solving any differential equation. For different temperature variations, λ_0, λ_1, λ_2, λ_0^2, λ_1^2, ... need to be calculated from Eq. (2.46) which involves simple algebraic calculations.

2.6 Conclusion

Mixed convection flow over a vertical surface varying wall temperature is studied using perturbation method. The wall temperature differentials are taken as perturbation functions. The sets of coupled differential equations are solved to find out universal functions for stream function and temperature which are independent of any arbitrarily wall temperature. Power law variation for wall temperature is taken to demonstrate the universal applicability of universal functions. The results are presented for velocity and temperature distributions in boundary layer, velocity and thermal boundary layer thicknesses, skin friction coefficient and heat transfer rates along the plate for various values of Gr_y/Re_y^2 and wall temperature power law index. It is found that heat transfer rates increase linearly with increasing value of power law index for both aiding and opposing flows, for all Gr_y/Re_y^2 values, for the range of Gr_y/Re_y^2 values considered in the study. The main advantage of the perturbation method is that the obtained universal functions are valid for any arbitrarily temperature variation. Hence, for different boundary condition, solutions can be obtained by calculating only perturbation variables along with simple algebraic calculations. We do not need to solve any differential equation additionally to get the solutions.

Chapter 3

Mixed convection heat transfer about a vertical surface of variable heat flux

In this chapter, mixed convection boundary layer flows over a wall of arbitrarily varying surface heat flux, including density inversion effect is solved using perturbation method. The physical system, solution methodology and the obtained results are presented.

3.1 Physical system

The physical system consist of a vertical flat plate. Water flows over the plate such that mixed convection boundary layer is formed. The surface of the plate is subjected to wall heat flux varying with arbitrary function of vertical distance. The free stream velocity and temperature are v_∞ and T_0, respectively, where T_0 is the temperature corresponds to the density maximum point near density inversion. The temperature of the plate and water are in the range of temperatures in which water shows density inversion. The schematic of the physical and coordinate systems are shown in figures 3.1(a) and 3.1(b) for aiding and opposing mixed convection conditions, respectively.

3.2 Mathematical model

In the present study, mixed convection is assumed to be steady, laminar and incompressible. The flow is assumed to be such that boundary layer approximations are valid. The viscous dissipation and radiation effects are assumed to be negligible. The properties of the water are considered to be constant except for the density variation with temperature in buoyancy term. The temperatures within the boundary layer are assumed to be in the range of temperatures in which water shows density inversion. The density variation of water with temperature in the buoyancy term is modelled with different functions in different studies such as [1, 5, 43]. In the present study, the density variation considered in the work of [1] is adopted, which is given by

$$\frac{\rho}{\rho_0} = 1 - \gamma(T - T_0)^2 \tag{3.1}$$

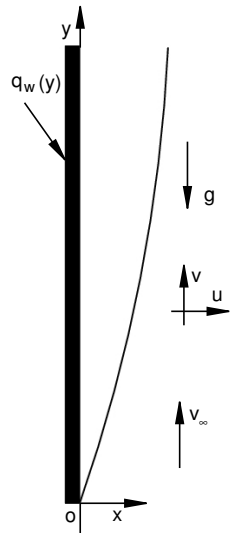

(a) Aiding mixed convection

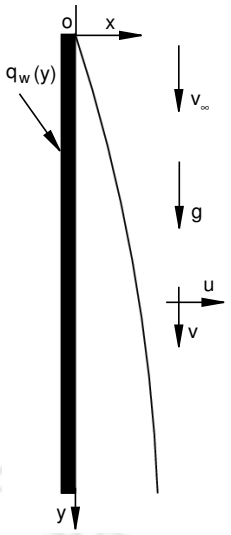

(b) Opposing mixed convection

Figure 3.1: Schematic of physical and coordinate systems

where, ρ_0 is the maximum density at the temperature of $T_0 = 3.98°C$ and γ = 8.0×10^{-6} $°C^{-2}$ is a constant. This correlation is within acceptable error limit in temperature range $0 - 12°C$ [1]. With the above considerations, governing equations for boundary layer flows take the following form

Continuity equation

$$\frac{\partial u}{\partial x} + \frac{\partial v}{\partial y} = 0 \tag{3.2}$$

y-momentum equation

$$u\frac{\partial v}{\partial x} + v\frac{\partial v}{\partial y} = \nu\frac{\partial^2 v}{\partial x^2} \pm g\gamma(T - T_0)^2 \tag{3.3}$$

Energy equation

$$u\frac{\partial T}{\partial x} + v\frac{\partial T}{\partial y} = \alpha\frac{\partial^2 T}{\partial x^2} \tag{3.4}$$

where, α is thermal diffusivity of water. The '+' and '-' signs associated with body force term in Eq. (3.3) represent the aiding and opposing mixed convection flows, respectively. The above governing equations are subjected to following boundary conditions. No slip, no penetration conditions prevail at the plate surface. The velocity and temperature outside of the boundary layer are uniform with v_∞ and T_0, respectively. These boundary conditions can be mathematically expressed as

$$\text{At} \quad x = 0: \quad u = v = 0, \quad q = q_w(y) \tag{3.5}$$

$$\text{At} \quad x \to \infty: \quad v \to v_\infty, \quad T \to T_0 \tag{3.6}$$

To convert the above governing equations in the form of stream function, the velocity components are expressed in stream function as

$$u = -\frac{\partial \psi}{\partial y}, \quad v = \frac{\partial \psi}{\partial x} \tag{3.7}$$

Substituting Eq. (3.7) in Eqs. (3.3) and (3.4), resulting stream function forms of momentum and

energy equations are

$$\frac{\partial\psi}{\partial x}\frac{\partial^2\psi}{\partial x\partial y}-\frac{\partial\psi}{\partial y}\frac{\partial^2\psi}{\partial x^2}=\nu\frac{\partial^3\psi}{\partial x^3}\pm g\gamma(T-T_0)^2 \tag{3.8}$$

$$\frac{\partial\psi}{\partial x}\frac{\partial T}{\partial y}-\frac{\partial\psi}{\partial y}\frac{\partial T}{\partial x}=\alpha\frac{\partial^2 T}{\partial x^2} \tag{3.9}$$

The boundary conditions in stream function form take the following form

$$\text{At}\quad x=0:\quad \frac{\partial\psi}{\partial x}=\frac{\partial\psi}{\partial y}=0,\quad q=q_w(y) \tag{3.10}$$

$$\text{At}\quad x\to\infty:\quad \frac{\partial\psi}{\partial x}\to v_\infty,\quad T\to T_0 \tag{3.11}$$

3.3 Solutions of the equations

To seek perturbation type of solutions, the governing Eqs. (3.8) and (3.9) need to be suitably transformed. The momentum and energy equations are transformed using the following dimensionless variables

$$f(\eta,\lambda_0,\lambda_1,\cdots,\lambda_n,\cdots)=\frac{\psi(x,y)}{\sqrt{\nu v_\infty y}} \tag{3.12}$$

$$\theta(\eta,\lambda_0,\lambda_1,\cdots,\lambda_n,\cdots)=\frac{T(x,y)-T_0}{\frac{q_w y}{k}\sqrt{\frac{\nu}{v_\infty y}}} \tag{3.13}$$

$$\eta(x,y)=x\sqrt{\frac{v_\infty}{\nu y}} \tag{3.14}$$

Here, $\lambda_0, \lambda_1, \ldots, \lambda_n$ are set of infinite number of variables which are functions of y. These variables are the perturbation elements which are yet unknown functions of y. The above transformations closely resemble with the similarity transformations, except that in the present form additional set of functions $\lambda_n(y)$ are present. Applying the above transformations, the governing equations become

$$\frac{\partial^3 f}{\partial\eta^3}=-\frac{f}{2}\frac{\partial^2 f}{\partial\eta^2}\pm\left(\frac{Gr_y}{Re_y^3}\right)\theta^2-\frac{\partial^2 f}{\partial\eta^2}y\sum_{n=0}^{\infty}\frac{\partial f}{\partial\lambda_n}\frac{\partial\lambda_n}{\partial y}+\frac{\partial f}{\partial\eta}y\sum_{n=0}^{\infty}\frac{\partial^2 f}{\partial\lambda_n\partial\eta}\frac{\partial\lambda_n}{\partial y} \tag{3.15}$$

$$\frac{1}{Pr}\frac{\partial^2\theta}{\partial\eta^2}=-\frac{f}{2}\frac{\partial\theta}{\partial\eta}-\frac{\partial f}{\partial\eta}y\sum_{n=0}^{\infty}\frac{\partial\theta}{\partial\lambda_n}\frac{\partial\lambda_n}{\partial y}+\frac{\partial\theta}{\partial\eta}y\sum_{n=0}^{\infty}\frac{\partial f}{\partial\lambda_n}\frac{\partial\lambda_n}{\partial y}+y\frac{\partial f}{\partial\eta}\frac{\theta}{q_w(y)}\frac{d}{dy}q_w(y) \tag{3.16}$$

where, modified Grashof number is given by

$$Gr_y=\frac{g\gamma(q_w y/k)^2 y^3}{\nu^2} \tag{3.17}$$

and Reynolds number is given by

$$Re_y=\frac{v_\infty y}{\nu}\,. \tag{3.18}$$

The difference in the above form of expression for modified Grashof number compared to the

usual form of Grashof number is due to the presence of density inversion effect, being represented by γ and given by Eq. (3.1), which brings peculiarities.

From the above equations, we can see that Gr_y/Re_y^3 is an important governing parameter of the mixed convection with density inversion. The boundary conditions in terms of dimensionless variables f and θ are

$$\text{At} \quad \eta = 0: \quad f = 0, \quad \frac{\partial f}{\partial \eta} = 0, \quad \frac{\partial \theta}{\partial \eta} = -1 \tag{3.19}$$

$$\text{At} \quad \eta \to \infty: \quad \frac{\partial f}{\partial \eta} \to 1, \quad \theta \to 0 \tag{3.20}$$

Study of Eqs. (3.15) and (3.16) reveals that the equations become function of η and λ_n, if we define $\lambda_n(y)$ as ([137])

$$\lambda_n = \frac{y^{n+1}}{q_w(y)} \frac{d^{n+1}}{dy^{n+1}}(q_w(y)) \tag{3.21}$$

Here, $q_w(y)$ is infinitely differentiable with respect to y. After substitution of λ_n from Eq. (3.21), the governing equations (3.15) and (3.16) are still be in the form of partial differential equations. To convert the partial differential equations into ordinary differential equations, the functions f and θ are expressed in following power series of $\lambda_n(y)$ with coefficients which are functions of η

$$f(\eta, \lambda_0, \lambda_1, \cdots, \lambda_n, \cdots) = F(\eta) + \lambda_0 f_0(\eta) + \lambda_1 f_1(\eta) + \cdots + \lambda_0^2 f_{00}(\eta) + \lambda_1^2 f_{11}(\eta) + \cdots \tag{3.22}$$

$$\theta(\eta, \lambda_0, \lambda_1, \cdots, \lambda_n, \cdots) = H(\eta) + \lambda_0 \theta_0(\eta) + \lambda_1 \theta_1(\eta) + \cdots + \lambda_0^2 \theta_{00}(\eta) + \lambda_1^2 \theta_{11}(\eta) + \cdots \tag{3.23}$$

Substituting Eqs. (3.21), (3.22) and (3.23) in Eqs. (3.15) and (3.16), we get the governing equations in the following form.

$$\begin{aligned}
F''' + \lambda_0 f_0''' + \lambda_1 f_1''' + \cdots + \lambda_0^2 f_{00}''' + \cdots = & -\frac{1}{2} F F'' \pm \frac{Gr_y}{Re_y^3} H^2 \\
& + \lambda_0 \left(-\frac{1}{2} F f_0'' - \frac{3}{2} f_0 F'' \pm \frac{Gr_y}{Re_y^3} 2H\theta_0 + F' f_0' \right) \\
& + \lambda_1 \left(-\frac{1}{2} F f_1'' - \frac{5}{2} f_1 F'' \pm \frac{Gr_y}{Re_y^3} 2H\theta_1 - F'' f_0 + F' f_0 + 2F' f_1' \right) \\
& + \lambda_0^2 \left(-\frac{1}{2} F f_{00}'' - \frac{5}{2} f_{00} F'' - \frac{3}{2} f_0 f_0'' \pm \frac{Gr_y}{Re_y^3} (H\theta_{00} + 2H\theta_0) \right. \\
& \left. + F'' f_0 + 2F' F_{00}' + f_0' f_0' - F' f_0' \right)
\end{aligned} \tag{3.24}$$

$$\frac{1}{Pr}(H'' + \lambda_0\theta_0'' + \lambda_1\theta_1'' + \cdots + \lambda_0^2\theta_{00}'' + \cdots) = -\frac{1}{2}FH' + \frac{1}{2}F'H$$
$$+ \lambda_0\left(-\frac{1}{2}F\theta_0' - \frac{3}{2}f_0H' + F'\theta_0 + HF' + \frac{1}{2}f_0H' + \frac{1}{2}F'\theta_0\right)$$
$$+ \lambda_1\left(-\frac{1}{2}F\theta_1' - \frac{5}{2}f_1H' + F'\theta_0 + 2F'\theta_1 - H'f_0 + \frac{1}{2}F'\theta_1 + \frac{1}{2}f_1'H\right) \quad (3.25)$$
$$+ \lambda_0^2\left(-\frac{1}{2}F\theta_{00}' - \frac{5}{2}f_{00}H' + 2F'\theta_{00} - \frac{3}{2}f_0\theta_0' + f_0'\theta_0 + H'f_0 + Hf_0\right.$$
$$\left.+\frac{1}{2}f_{00}'H + \frac{1}{2}\theta_0f_0' + \frac{1}{2}F'\theta_{00}\right)$$

From the Eqs. (3.24) and (3.25), if we equate the coefficient of λ_0 on either sides of the governing equations, we obtain a set of ordinary differential equations of coefficient functions. Similarly, equating the coefficients of λ_1, λ_0^2, ..., other sets of ordinary differential equations will be obtained. Similarly, infinite number of sets of ordinary differential equations can be obtained equating the coefficients of same power of $\lambda_n(y)$ variables. The above sets of equations are coupled equations. In the calculations, larger the number of equation sets considered, higher is the accuracy of results we obtain ([140, 141]). It is found in the calculation that when we include beyond sets of equations corresponding to constants, λ_0, λ_1 and λ_0^2, the change in the solution is found to be negligible. Hence, the sets correspond to constant, λ_0, λ_1, λ_0^2 only are considered in the present study, which are as following.
Constant terms:

$$F''' = -\frac{1}{2}FF'' \pm \left(\frac{Gr}{Re^3}\right)H^2$$
$$\frac{1}{Pr}H'' = -\frac{1}{2}FH' + \frac{1}{2}F'H \quad (3.26)$$

The set of coefficient of λ_0:

$$f_0''' = -\frac{1}{2}Ff_0'' - \frac{3}{2}f_0F'' \pm \left(\frac{Gr}{Re^3}\right)2H\theta_0 + F'f_0'$$
$$\frac{1}{Pr}\theta_0'' = -\frac{1}{2}F\theta_0' - \frac{3}{2}f_0H' + F'\theta_0 + HF' + \frac{1}{2}f_0H' + \frac{1}{2}F'\theta_0 \quad (3.27)$$

The set of coefficient of λ_1:

$$f_1''' = -\frac{1}{2}Ff_1'' - \frac{5}{2}f_1F'' \pm \left(\frac{Gr}{Re^3}\right)2H\theta_1 - F''f_0 + F'f_0' + 2F'f_1'$$
$$\frac{1}{Pr}\theta_1'' = -\frac{1}{2}F\theta_1' - \frac{5}{2}f_1H' + F'\theta_0 + 2F'\theta_1 - H'f_0 + \frac{1}{2}F'\theta_1 + \frac{1}{2}f_1'H \quad (3.28)$$

The set of coefficient of λ_0^2:

$$f_{00}''' = -\frac{1}{2}Ff_{00}'' - \frac{5}{2}f_{00}F'' - \frac{3}{2}f_0f_0'' \pm \left(\frac{Gr}{Re^3}\right)(\theta_0^2 + 2H\theta_{00}) + F''f_0 + 2F'F_{00}' + f_0'f_0' - F'f_0'$$
$$\frac{1}{Pr}\theta_{00}'' = -\frac{1}{2}F\theta_{00}' - \frac{5}{2}f_{00}H' + 2F'\theta_{00} - \frac{3}{2}f_0\theta_0' + f_0'\theta_0 + H'f_0 + Hf_0' + \frac{1}{2}f_{00}'H + \frac{1}{2}\theta_0f_0' + \frac{1}{2}F'\theta_{00} \quad (3.29)$$

The sets of differential equations correspond to other λ_n and higher powers of λ_n contribute negligibly small to the solutions, and hence they are neglected. The '+' and '-' signs associated with

Gr_y/Re_y^3 in above equations correspond to aiding and opposing mixed convection flows, respectively. The boundary conditions for the above differential equations are as follows:

$$\begin{aligned} \text{At } \eta = 0: \quad F &= 0, \quad & f_0 = f_1 = f_{00} = f_2 &= 0 \\ H' &= -1, \quad & \theta_0' = \theta_1' = \theta_{00}' = \theta_2' &= 0 \\ F' &= 0, \quad & f_0^{'} = f_1^{'} = f_{00}^{'} = f_2^{'} &= 0 \end{aligned} \tag{3.30}$$

$$\begin{aligned} \text{At } \eta \to \infty: \quad F' &= 1, \quad & f_0^{'} = f_1^{'} = f_{00}^{'} = f_2^{'} &= 0 \\ H &= 0, \quad & \theta_0 = \theta_1 = \theta_{00} = \theta_2 &= 0 \end{aligned} \tag{3.31}$$

The above sets of coupled equations for the subjected boundary conditions are solved using shooting method to find the coefficient functions. Fourth order Runge-Kutta method is used for the integration of ordinary differential equations. The value of Prandtl number of water near density inversion is taken as 11.4 in the calculations. The solutions of the above equations yield the values of coefficient functions for various η values. The above coefficient functions are obtained for any arbitrary wall heat flux variation and hence, they are valid for any continuous wall heat flux variation. They are independent of type of wall heat flux variation and hence, they are called "universal functions" for a given fluid. The obtained universal functions for stream function and temperature are shown in figures 3.2–3.4 for various values of Gr_y/Re_y^3. Figure 3.2 for $Gr_y/Re_y^3 = 0$ corresponds to forced convection asymptote. Figures 3.3– 3.4 shows the universal function of stream function and temperature, respectively for aiding and opposing mixed convection flows.

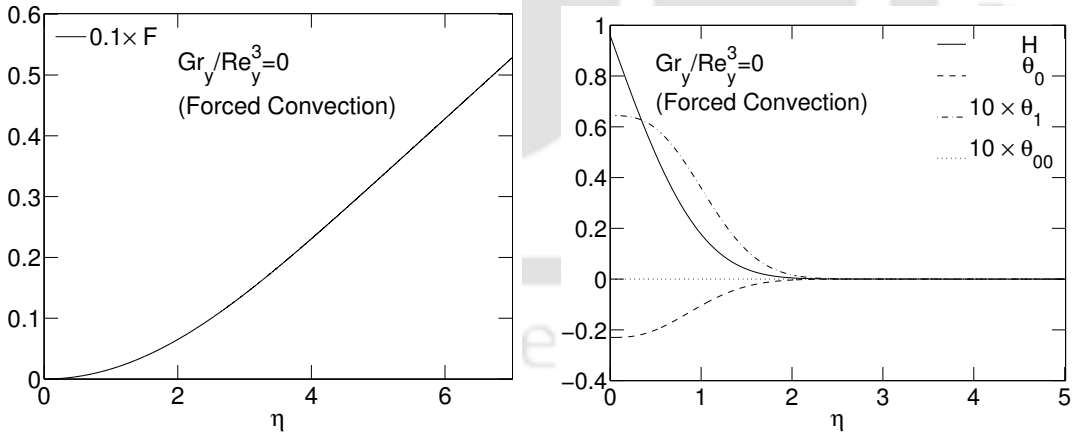

(a) $Gr_y/Re_y^3 = 0$ (b) $Gr_y/Re_y^3 = 0$

Figure 3.2: Variation of universal functions of stream function and temperature for forced convection asymptote

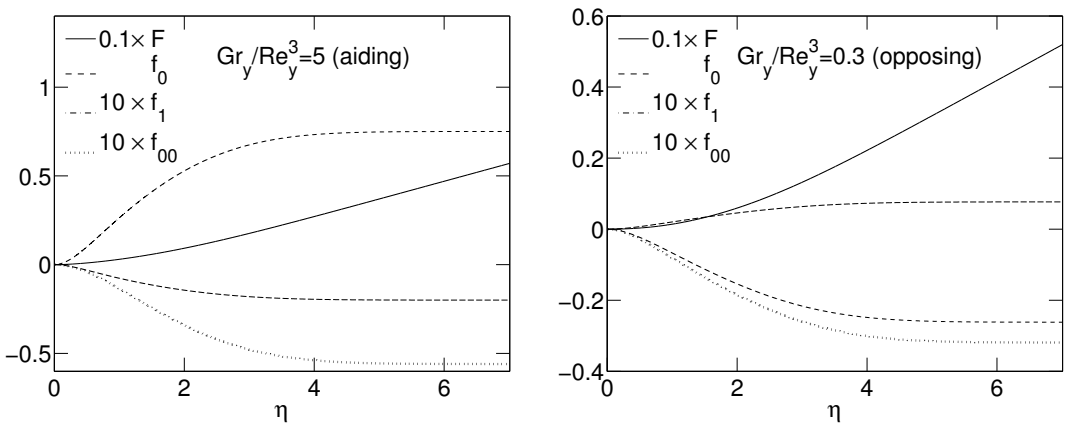

(a) $Gr_y/Re_y^3 = 5$ (b) $Gr_y/Re_y^3 = 0.3$

Figure 3.3: Universal functions of stream function for Gr_y/Re_y^3 values in aiding and opposing flows

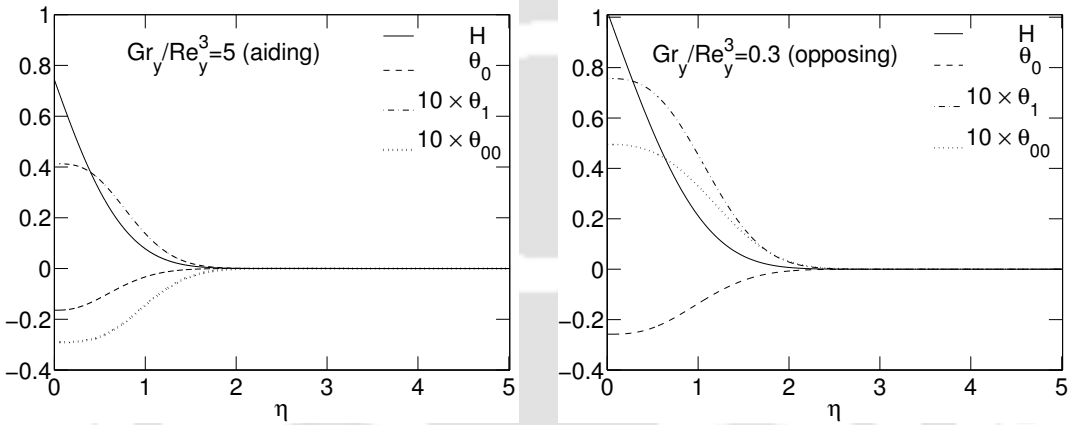

(a) $Gr_y/Re_y^3 = 5$ (b) $Gr_y/Re_y^3 = 0.3$

Figure 3.4: Universal functions of temperature for Gr_y/Re_y^3 values in aiding and opposing flows

3.4 Velocity, skin friction coefficient and Nusselt number in terms of universal functions

In mixed convection flows, the objective is to find important quantities which are velocity and temperature distribution in the boundary layer, and drag and heat transfer rates along the wall. The temperature distribution is given by Eq. (3.23). The velocity, drag in the form of skin friction coefficient and heat transfer rates in the form of Nusselt number can be expressed in terms of universal functions. The relations can be obtained as following.

The vertical component of the velocity can be expressed as $v = \dfrac{\partial \psi}{\partial x}$. Using Eqs. (3.12) and (3.14) in this expression, v becomes

$$v = \frac{\partial \psi}{\partial x} = \sqrt{v_\infty \nu y}\frac{\partial f}{\partial \eta}\frac{\partial \eta}{\partial x} = v_\infty f'(\eta) \tag{3.32}$$

Using Eq. (3.22) in the above equation, vertical velocity in terms of universal functions can be expressed as

$$\frac{v}{v_\infty} = f'(\eta) = F'(\eta) + \lambda_0 f_0'(\eta) + \lambda_1 f_1'(\eta) + \ldots + \lambda_0^2 f_{00}'(\eta) + \ldots \tag{3.33}$$

To calculate skin friction drag, the local skin friction coefficient can be expressed as,

$$C_{fy} = \frac{\tau_{\mathrm{w}}}{\rho v_\infty^2} \tag{3.34}$$

where, v_∞ is free-stream velocity and τ_{w} is shear stress at wall ($x = 0$). The wall shear stress can be expressed as

$$\tau_{\mathrm{w}} = \mu \left.\frac{\partial v}{\partial x}\right|_{x=0} = \mu \left.\frac{\partial}{\partial x}\left(\frac{\partial \psi}{\partial x}\right)\right|_{x=0} = \mu v_\infty \sqrt{\frac{v_\infty}{\nu y}} \left.\frac{\partial^2 f}{\partial \eta^2}\right|_{\eta=0} \tag{3.35}$$

Using Eq. (3.34) and Eq. (3.35) we get

$$\frac{C_{fy}}{Re_y^{-1/2}} = f''(\eta)|_{\eta=0} = F''(0) + \lambda_0 f_0''(0) + \lambda_1 f_1''(0) + \cdots + \lambda_0^2 f_{00}''(0) + \cdots \tag{3.36}$$

Similarly, the relation between local heat transfer coefficient $h(y)$ and local wall heat flux is given as

$$h(y) = \frac{q_w(y)}{T_w - T_0} \tag{3.37}$$

Heat transfer rates are expressed in terms of local Nusselt number which is expressed as

$$Nu_y = \frac{h(y)\ y}{k} \tag{3.38}$$

Combining Eqs. (3.37) and (3.38), we get

$$Nu_y = \frac{q_w(y)}{T_w - T_0}\frac{y}{k} \tag{3.39}$$

From the definition of dimensionless temperature given by Eq. (3.13) we can express $(T_w - T_0)$ as

$$T_w - T_0 = \theta_{\eta=0}\frac{q_w(y)}{k} y\ Re_y^{-1/2} \tag{3.40}$$

where, $\theta_{\eta=0}$ is the dimensionless temperature corresponds to wall for which $x = 0$ and hence $\eta = 0$. Substituting Eq. (3.40) in Eq. (3.39) we get the heat transfer rates as

$$\frac{Nu_y}{Re_y^{1/2}} = \frac{1}{\theta_{\eta=0}} \tag{3.41}$$

The heat transfer rates in Eq. (3.41) can be expressed in form of universal constants, using Eq. (3.23), as

$$\frac{Nu_y}{Re_y^{1/2}} = \left[H(0) + \lambda_0\theta_0(0) + \lambda_1\theta_1(0) + \cdots + \lambda_0^2\theta_{00}(0) + \cdots\right]^{-1} \tag{3.42}$$

Table 3.1: Values of universal constants of stream function for various Gr_y/Re_y^3 values (aiding flow)

Gr_y/Re_y^3	$F''(0)$	$f_0''(0)$	$f_1''(0)$	$f_{00}''(0)$
0	0.3321	0.0000	0.0000	0.0000
0.05	0.3477	-0.0100	0.0031	0.0013
0.5	0.4658	-0.0815	0.0247	0.0030
1	0.5694	-0.1406	0.0423	-0.0014
5	0.9865	-0.3632	0.1073	-0.0334
10	1.5105	-0.6302	0.1842	-0.0804
20	2.1153	-0.9327	0.2708	-0.1366

Table 3.2: Values of universal constants of stream function for various Gr_y/Re_y^3 values (opposing flow)

Gr_y/Re_y^3	$F''(0)$	$f_0''(0)$	$f_1''(0)$	$f_{00}''(0)$
0	0.3321	0.0000	0.0000	0.0000
0.05	0.3157	0.0106	-0.0033	-0.0018
0.1	0.2984	0.0220	-0.0068	-0.0042
0.2	0.2605	0.0480	-0.0149	-0.0125
0.3	0.2162	0.0802	-0.0251	-0.0300

Table 3.3: Values of universal constants of temperature for aiding mixed convection flow for various Gr_y/Re_y^3 values

Gr_y/Re_y^3	$H(0)$	$\theta_0(0)$	$\theta_1(0)$	$\theta_{00}(0)$
0	0.9591	-0.2301	0.0644	0.0000
0.05	0.9516	-0.2272	0.0633	-0.0032
0.5	0.9017	-0.2095	0.0566	-0.0178
1	0.8656	-0.1980	0.0525	-0.0234
5	0.7436	-0.1644	0.0412	-0.0290
10	0.6826	-0.1494	0.0368	-0.0286
20	0.6214	-0.1352	0.0327	-0.0273

Table 3.4: Values of universal constants of temperature for opposing mixed convection flow for various Gr_y/Re_y^3 values

Gr_y/Re_y^3	$H(0)$	$\theta_0(0)$	$\theta_1(0)$	$\theta_{00}(0)$
0	0.9591	-0.2301	0.0644	0.0000
0.05	0.9673	-0.2332	0.0656	0.0039
0.1	0.9761	-0.2368	0.0671	0.0088
0.2	0.9968	-0.2456	0.0706	0.0230
0.3	1.0235	-0.2579	0.0757	0.0495

Eq. (3.36) and Eq. (3.42) show that $C_{fy}/Re_y^{-1/2}$ and $Nu_y/Re_y^{1/2}$ depend on universal functions of stream function ($F''(0)$, $f_0''(0)$, $f_1''(0)$, $f_{00}''(0)$, ...) and temperature ($H(0)$, $\theta_0(0)$, $\theta_1(0)$, $\theta_{00}(0)$, ...), respectively as well as the perturbation variables λ_0, λ_1, λ_0^2, ... Since, universal constants are same for all boundary conditions, the skin friction drag and heat transfer rates depend on the

perturbation variables. For a given wall flux variation, one can find out the values of perturbation variables of velocity and temperature to find out the skin friction drag and heat transfer rates along the wall. It may be noted that the calculations of skin friction drag and heat transfer rates for different boundary conditions involve only finding the perturbation variables, which require simple algebraic calculations, and we do not need to solve any differential equation. The universal functions of stream function (correspond to $\eta = 0$) for aiding and opposing flows are shown in tables 3.1 and 3.2 which are required to calculate the skin friction drag. For calculation of heat transfer rates, the required universal functions of temperature (correspond to $\eta = 0$) are given in tables 3.3 and 3.4 for aiding and opposing cases, respectively, for various Gr_y/Re_y^3 values.

3.5 Mixed convection for power-law wall heat flux variation

As the above results are valid for any arbitrary wall heat flux variation, the results are applied for power-law wall flux variation. The results of power-law wall heat flux can be extended to any wall heat flux variation function which can be expanded in power-law series. The wall heat flux is assumed to vary in the form

$$q_w(y) = Ay^m \tag{3.43}$$

where, A and m are constants. Wall heat flux variation corresponds to constant heat flux when $m = 0$.

For the above form of wall heat flux variation, perturbation functions can be calculated using Eq. (3.21). The perturbation functions λ_0, λ_1, λ_0^2, $\cdots$ are as follows

$$\lambda_0 = m, \quad \lambda_1 = m(m-1), \quad \lambda_0^2 = m^2, \quad \cdots \tag{3.44}$$

For any given m value, perturbation function values are calculated using Eq. (3.44). Once the perturbation function values are known, velocity, skin friction coefficient and Nusselt number calculations require the derivatives of universal functions with respect to η in the expressions given by Eq. (3.33), Eq. (3.36) and Eq. (3.42), respectively. These derivatives are available as part of the solutions of sets of ordinary differential equations, hence they are known. Temperature is given by Eq. (3.23).

3.5.1 Validation

Before presenting the results for present problem, the code is validated by computing heat transfer rates for special case of forced convection for which results are available in Sparrow and Lin [6]. In the present study $Gr_y/Re_y^3 = 0$ corresponds to forced convection case. The heat transfer rates for forced convection obtained using Eq. (3.44) and Eq. (3.42), by setting $Gr_y/Re_y^3 = 0$ in the present study, are compared with those of Sparrow and Lin [6] in table 3.5. From the table 3.5 we can see that the present results closely match with the reference results.

Table 3.5: Comparison of $Nu_y/Re_y^{1/2}$ values obtained in the present study with those obtained by Sparrow and Lin [6] for $Gr_y/Re_y^3 = 0$ in power-law varying wall heat flux

	m	Present study	Sparrow and Lin [6]	% error
$Pr = 0.7$	0	0.45710	0.46320	0.013
	1	0.60550	0.60940	0.010
	2	0.70470	0.70770	0.004
$Pr = 10$	0	0.45716	0.46318	0.004
	1	0.60544	0.60938	0.003
	2	0.70467	0.70766	0.005

3.5.2 Flow field calculations

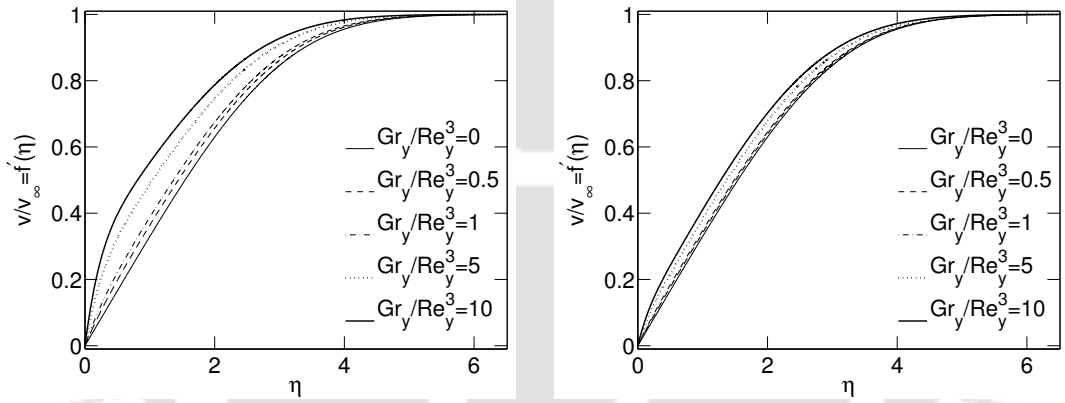

(a) $m = 0$ (b) $m = 1$

Figure 3.5: Variation of dimensionless vertical velocity with η for various values of Gr_y/Re_y^3 in aiding flow

The dimensionless velocity variation is obtained using Eq. (3.33) and Eq. (3.44) for various Gr_y/Re_y^3 values and power-index values of $m = 0$ and $m = 1$, which are presented in figures 3.5 and 3.6. Figure 3.5 corresponds to aiding mixed convection, and figure 3.6 corresponds to opposing mixed convection. In figures, the curves for $Gr_y/Re_y^3 = 0$ corresponds to forced convection extreme. It can be seen from the figures that velocities are greater than corresponding forced convection velocities in aiding mixed convection. However, in opposing mixed convection, the velocities are lower than corresponding forced convection.

From the obtained velocity variations with η, we can find out the velocity boundary layer thickness $\delta_v(v_\infty/\nu y)^{1/2}$. The boundary layer thickness corresponds to η at which v/v_∞ becomes 0.99. The variation of dimensionless boundary layer thickness with various Gr_y/Re_y^3 for various m values are shown in figure 3.7, for both aiding and opposing situations. We can see from the figures that for a given m value, $\delta_v(v_\infty/\nu y)^{1/2}$ decreases with increasing Gr_y/Re_y^3 for aiding mixed convection. In this case, for a given Gr_y/Re_y^3, $\delta_v(v_\infty/\nu y)^{1/2}$ increases with given m values. The opposite trends can be observed for opposing mixed convection in which $\delta_v(v_\infty/\nu y)^{1/2}$ increases with increasing values of

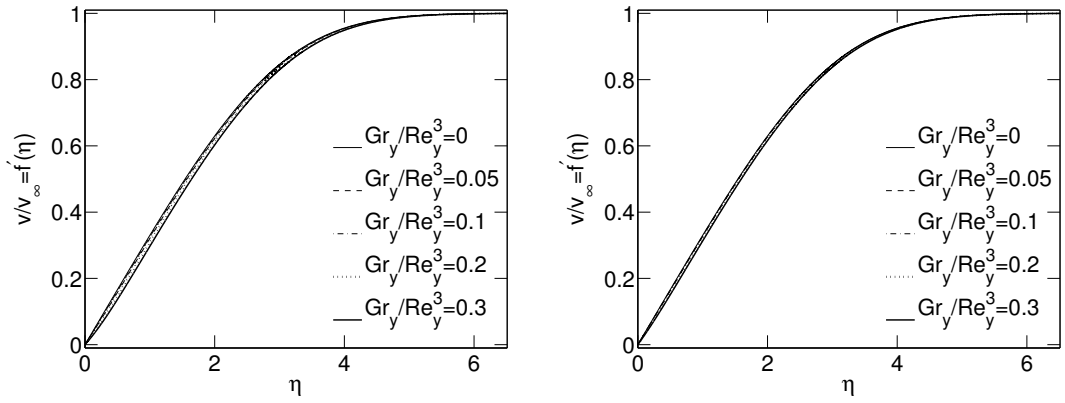

(a) $m = 0$ (b) $m = 1$

Figure 3.6: Variation of dimensionless vertical velocity with η for various values of Gr_y/Re_y^3 in opposing flow

Gr_y/Re_y^3 and decreases with power index values m.

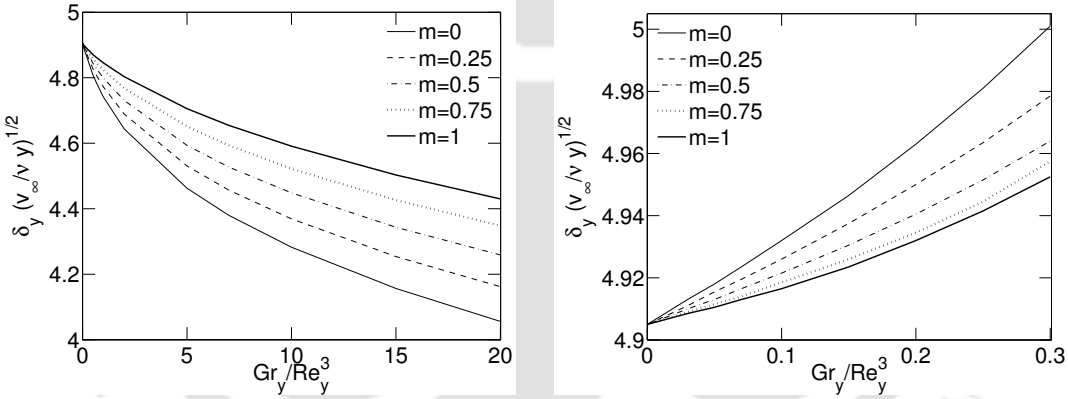

(a) Aiding (b) Opposing

Figure 3.7: Variation of velocity boundary layer thickness with Gr_y/Re_y^3 for various m values

The variation of skin friction coefficient in the form of $C_{fy}/Re_y^{-1/2}$ with respect to m, for various Gr_y/Re_y^3 values, is shown in figure 3.8(a) for aiding mixed convection. The figure corresponds to $Gr_y/Re_y^3 = 0$ is for forced convection and the skin friction coefficient increases with increasing m values and also with values of Gr_y/Re_y^3. The values of skin friction coefficient in mixed convection are higher than the forced convection and its value increases with Gr_y/Re_y^3.

The variation of $C_{fy}/Re_y^{-1/2}$ with m for various values of Gr_y/Re_y^3 for opposing mixed convection is shown in figure 3.8(b). The skin friction coefficient increases with increasing m values. Skin friction coefficient values, in opposing mixed convection are less than those of forced convection values. With increasing Gr_y/Re_y^3 values, the value of $C_{fy}/Re_y^{-1/2}$ decreases which is opposite to the trend of aiding mixed convection in which skin friction coefficient increases with increasing Gr_y/Re_y^3. This is due to the fact that buoyancy and external forces cooperate each other to increase the velocity in aiding flow resulting increasing skin friction coefficient. However, in opposing case, these forces resist each other resulting decreased velocity shows decreased wall skin friction coefficient. In this

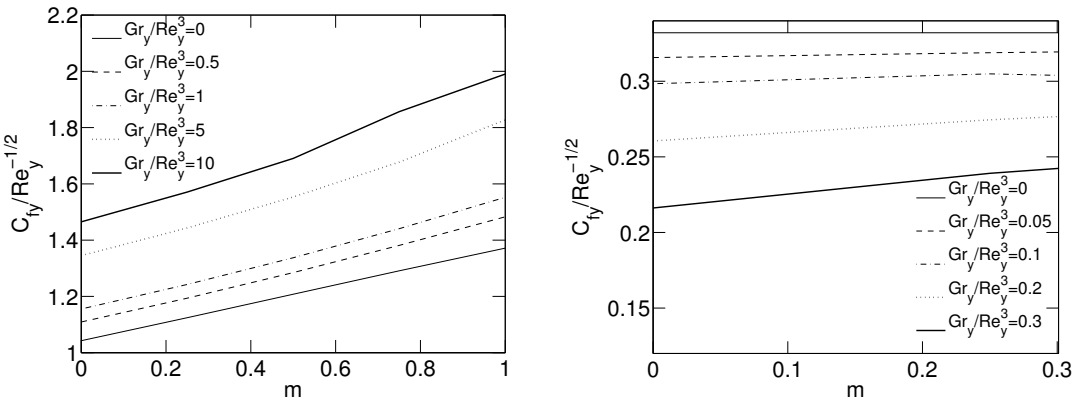

(a) aiding flow (b) opposing flow

Figure 3.8: Variation of skin friction coefficient with power index m for various Gr_y/Re_y^3

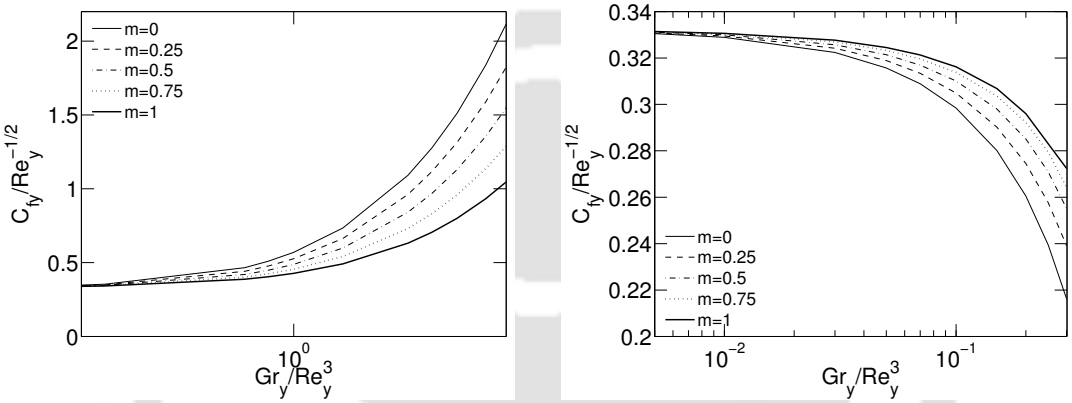

(a) aiding flow (b) opposing flow

Figure 3.9: Variation of skin friction coefficient with Gr_y/Re_y^3 for various power index values m

opposing mixed convection, flow reaches to flow separation conditions for higher Gr_y/Re_y^3 values. Hence, the solutions are obtained for lower values of Gr_y/Re_y^3 in opposing mixed convection.

The variation of $C_{fy}/Re_y^{-1/2}$ with respect to Gr_y/Re_y^3 for various power index values is shown in figures 3.9(a) and 3.9(b), respectively, for aiding and opposing mixed convection. At $Gr_y/Re_y^3 = 0$, the plot shows the skin friction coefficient for forced convection flow. In aiding mixed convection, skin friction coefficient values start from forced convection values and increases towards natural convection asymptote, with increasing Gr_y/Re_y^3 values. In case of opposing mixed convection flow, skin friction coefficient begins with forced convection values and decreases as Gr_y/Re_y^3 increases. When Gr_y/Re_y^3 is increased till the skin friction coefficient becomes zero, the flow separation occurs, beyond which the boundary layer approximations are not applicable.

3.5.3 Heat transfer calculations

The variation of θ is presented for various Gr_y/Re_y^3 values for $m = 0$ and $m = 1$, and shown in figures 3.10 and 3.11 for aiding and opposing mixed convection, respectively. From the figures, we can see that for a given η value, values of θ decrease with increasing values of Gr_y/Re_y^3 in case of

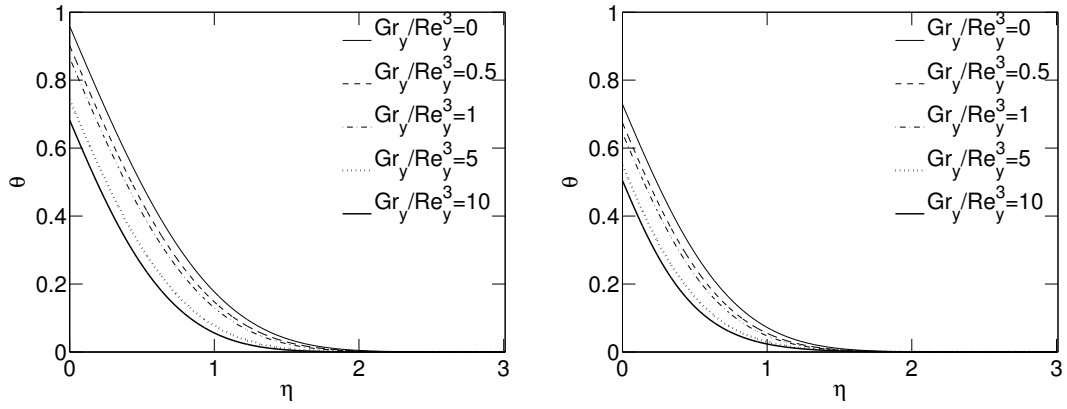

(a) $m = 0$ (b) $m = 1$

Figure 3.10: Variation of dimensionless temperature with η for aiding mixed convection

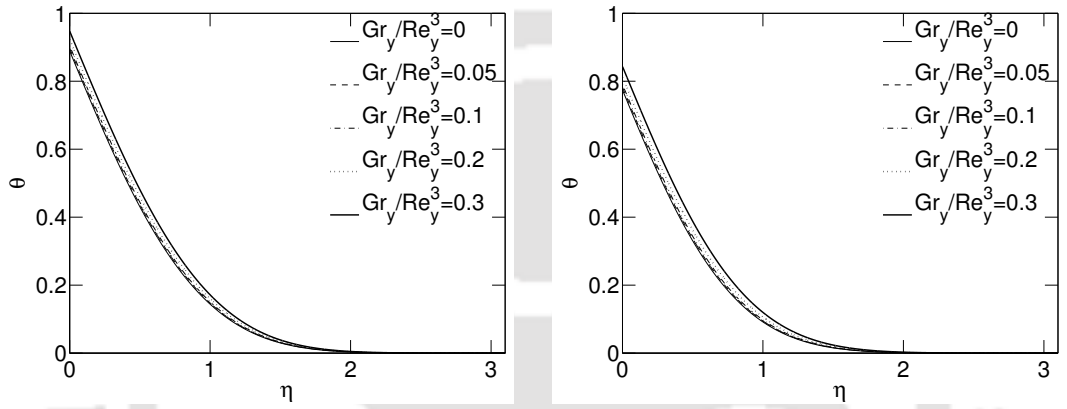

(a) $m = 0$ (b) $m = 1$

Figure 3.11: Variation of dimensionless temperature with η for opposing mixed convection

aiding mixed convection. However, the opposite trend is found for opposing mixed convection.

From the θ variation with η, the thermal boundary layer thickness $\delta_T \left(v_\infty/\nu y\right)^{1/2}$ can be found. From this η value, boundary layer thickness can be calculated using Eq. (3.14). The thermal boundary layer thickness corresponds to η value at which dimensionless temperature θ equals to 0.01. The thermal boundary layer thickness is found for various Gr_y/Re_y^3 and m values, which are derived in dimensionless form as $\delta_T \left(v_\infty/\nu y\right)^{1/2}$. The variation of boundary layer thickness with Gr_y/Re_y^3 for various m values are presented in figure 3.12 for both aiding and opposing mixed convection. The figures show that the boundary layer thickness at given y location decreases with increasing Gr_y/Re_y^3 values in aiding mixed convection. However, for opposing mixed convection, boundary layer thickness increases with Gr_y/Re_y^3 values.

The heat transfer rates calculated using Eqs. (3.42) and (3.44) are presented in tables 3.3–3.4. The heat transfer rates are calculated in dimensionless form of $Nu_y/Re_y^{1/2}$ for various values of m and Gr_y/Re_y^3. The values for $m = 0$ correspond to the case of uniform wall heat flux.

The variation of $Nu_y/Re_y^{1/2}$ with power index value m for various values of Gr_y/Re_y^3 is shown in figures 3.13(a) and 3.13(b), respectively, for aiding and opposing mixed convection. The Nusselt number increases with power index for all Gr_y/Re_y^3 values. The plot for $Gr_y/Re_y^3 = 0$ in the figures

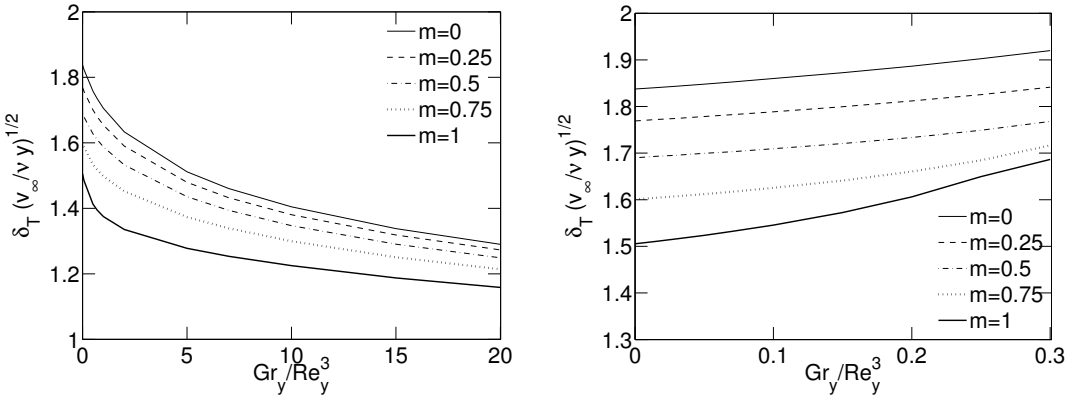

(a) Aiding (b) Opposing

Figure 3.12: Variation of thermal boundary layer thickness with Gr_y/Re_y^3 for various m values in mixed convection

corresponds to forced convection asymptote. The heat transfer rates increase with increasing Gr_y/Re_y^3 and wall heat flux power-index value. The value of $Nu_y/Re_y^{1/2}$ varies almost linearly with power index m in the range of 0 to 1. In aiding mixed convection, heat transfer rates are higher than those of forced convection values. Heat transfer rates increase with increasing values of Gr_y/Re_y^3.

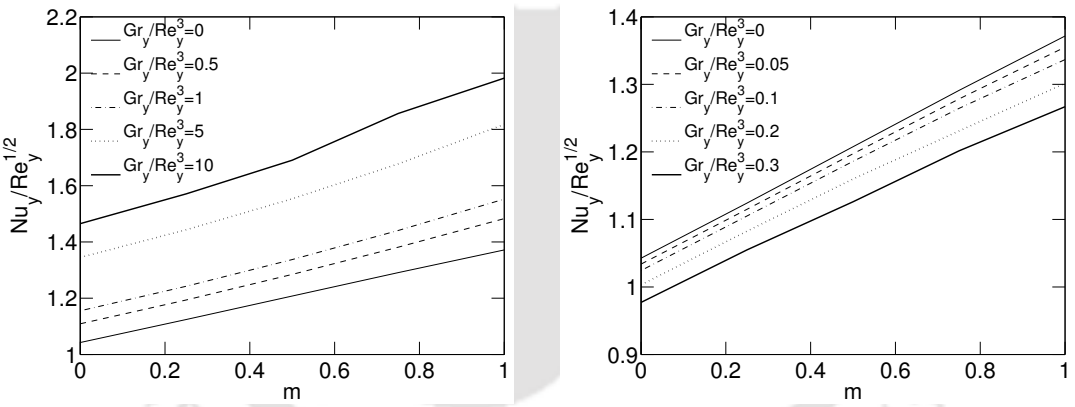

(a) aiding flow (b) opposing flow

Figure 3.13: Variation of heat transfer rate with m for various Gr_y/Re_y^3 values for aiding and opposing flows

In opposing mixed convection, heat transfer rates are less than those correspond to forced convection. The heat transfer rates decrease with increasing Gr_y/Re_y^3. This is opposite to the trend of aiding mixed convection. This is due to the fact that in aiding mixed convection buoyancy forces act in the same direction of external forces and results in increasing flow velocities. The increased flow velocities result in high heat transfer rates. In opposing mixed convection, buoyancy forces opposes external forces resulting separation of convection. In this case, heat transfer rates are lower than that of forced convection values. It may be noted that the opposing mixed convection is solved for Gr_y/Re_y^3 values lower than those values for which aiding mixed convection is solved. This is because for higher Gr_y/Re_y^3 values in the opposing mixed convection boundary layer tends towards flow separation where boundary layer approximations are no longer applicable. Hence, opposing

mixed convection is solved for lower values of Gr_y/Re_y^3.

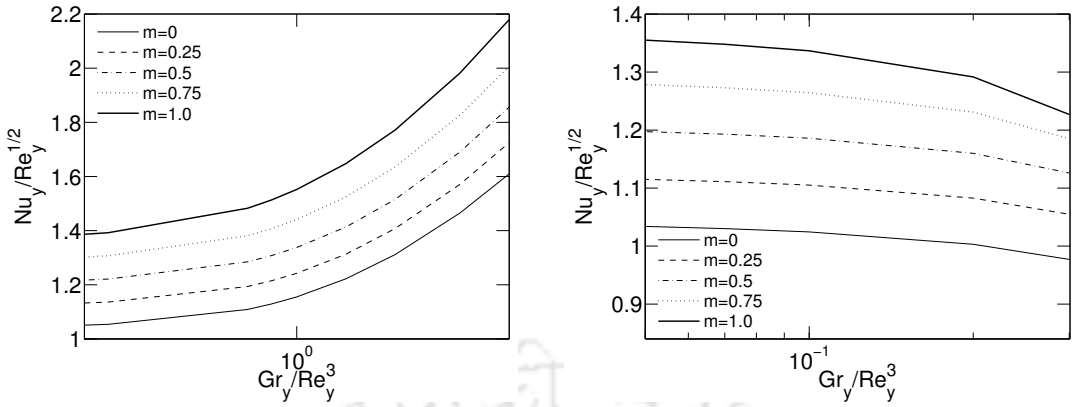

(a) aiding flow (b) opposing flow

Figure 3.14: Variation of heat transfer rate with Gr_y/Re_y^3 for various m values for aiding and opposing flows

To study the effect of Gr_y/Re_y^3 on heat transfer rates, the variation of $Nu_y/Re_y^{1/2}$ with Gr_y/Re_y^3 is plotted for various values of m in figures 3.14(a) and 3.14(b) for aiding and opposing mixed convection, respectively. In the figures, the plot for $Gr_y/Re_y^3 = 0$ corresponds to forced convection asymptote. From the figures, we can see that heat transfer rates start with forced convection values and vary towards natural convection with increasing values of Gr_y/Re_y^3. This is typical in mixed convection heat transfer.

3.6 Conclusions

The steady laminar boundary layer mixed convection of water over vertical flat surface of varying heat flux with density inversion is solved using perturbation technique. Heat flux differentials are used as perturbation elements. The solutions are obtained in terms of universal functions which are valid for any arbitrary wall heat flux variation. The solutions are applied to power law varying wall heat flux condition. The velocity and temperature distributions in the boundary layer, boundary layer thickness, local skin friction coefficient and heat transfer rates along the wall are presented for various Gr_y/Re_y^3 values and power law index values. It is observed that, in the parameter range of the present study, heat transfer rates and skin friction coefficient are found to increase almost linearly with wall flux power index, for a given combination of Grashof and Reynolds numbers, for both the cases of aiding and opposing mixed convection. The solutions from perturbation method have advantage that the solutions are valid for any arbitrary wall heat flux variation. Solutions for different wall heat flux varying conditions can be obtained using simple algebraic calculations without need for solving any differential equations.

Chapter 4

Similarity solutions of natural and mixed convection boundary layer flows over flux specified vertical plate

As discussed in the literature review section, the similarity solutions for boundary layer flows of water with density inversion are presented in few studies. Goren [60] presented similarity solution of free convection boundary layer flow over isothermal plate for density inversion of water. Similarity solutions of natural convection boundary layer flows of water near its density inversion over a surface of power-law varying temperature, were presented by Soundalgekar [139]. Similarity solutions for natural convection boundary layer flow over a plate subjected to constant heat flux in a porous media filled with water near density inversion was reported by Kumaran and Pop [43]. Vighnesam and Soundalgekar [5] presented similarity solutions for mixed convection boundary layer flows over a surface with power-law varying temperature. However, it is found from the literature that similarity solutions for natural convection and mixed convection boundary layer flows over a vertical plate of power-law varying surface flux are not reported in the literature. Similarity solutions for such flows are obtained in the present study which are presented in this chapter.

4.1 Similarity solutions of natural convection boundary layer

4.1.1 Physical system

The physical system of free convection boundary layer flows over a vertical plate is shown in Fig. 4.1. The plate is specified with power-law varying surface heat flux. The temperature of water in the boundary layer are within the temperature range in which water shows density inversion. The temperature outside the boundary layer is T_0 which is the temperature corresponds to density maximum point in the density inversion temperature range. The variation of wall heat flux (q_w) is given by

$$q_w(y) = A\, y^m, \tag{4.1}$$

where, A is a constant and m is power index. The above wall heat flux represents uniform heat flux plate for $m = 0$.

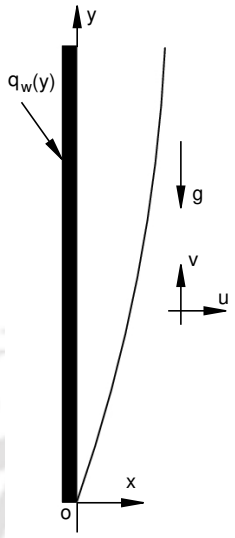

Figure 4.1: Schematic of natural convection boundary layer flow over a plate of power-law varying surface heat flux

4.1.2 Mathematical model

The flow is assumed to be steady state, laminar, incompressible. Thermo-physical properties of water are considered to be constant with temperature except for density in buoyancy term. The density variation of water with temperature, in the density inversion range, is taken [1,5] in the form

$$\frac{\rho}{\rho_0} = 1 - \gamma(T - T_0)^2 \,, \tag{4.2}$$

where, ρ_0 and T_0 are density and temperature corresponding to density maximum point (at 3.98°C) and γ is a constant. Under the above assumptions, the governing equations for natural convection boundary layer flow are as following

Continuity equation

$$\frac{\partial u}{\partial x} + \frac{\partial v}{\partial y} = 0, \tag{4.3}$$

y-momentum equation

$$u\frac{\partial v}{\partial x} + v\frac{\partial v}{\partial y} = \nu\frac{\partial^2 v}{\partial x^2} + g\gamma(T - T_0)^2, \tag{4.4}$$

Energy equation

$$u\frac{\partial T}{\partial x} + v\frac{\partial T}{\partial y} = \alpha\frac{\partial^2 T}{\partial x^2}. \tag{4.5}$$

The above equations are subjected to following boundary conditions,

$$\text{At} \quad x = 0: \quad u = v = 0, \quad q = q_w(y), \tag{4.6}$$

$$\text{At} \quad x \to \infty: \quad v = 0, \quad T = T_0. \tag{4.7}$$

Introducing stream function in the form,

$$u = \frac{\partial \psi}{\partial y}, \quad v = -\frac{\partial \psi}{\partial x}. \tag{4.8}$$

The equations (4.4)–(4.5) in the stream function form can be written as,

$$\frac{\partial \psi}{\partial x}\frac{\partial^2 \psi}{\partial x \partial y} - \frac{\partial \psi}{\partial y}\frac{\partial^2 \psi}{\partial x^2} = \nu \frac{\partial^3 \psi}{\partial x^3} + g\gamma (T - T_0)^2, \tag{4.9}$$

$$\frac{\partial \psi}{\partial x}\frac{\partial T}{\partial y} - \frac{\partial \psi}{\partial y}\frac{\partial T}{\partial x} = \alpha \frac{\partial^2 T}{\partial x^2}. \tag{4.10}$$

The boundary conditions (4.6)–(4.7) in stream function form are

$$\text{At} \quad x = 0: \quad \frac{\partial \psi}{\partial x} = \frac{\partial \psi}{\partial y} = 0, \quad q = q_w(y), \tag{4.11}$$

$$\text{At} \quad x \to \infty: \quad \frac{\partial \psi}{\partial x} = 0, \qquad T = T_0. \tag{4.12}$$

4.1.3 Solution of the equations

To find the similarity transformation which can converts the governing equations and boundary conditions into ordinary differential equations, we define the variables as

$$\theta = c_3 \frac{T - T_0}{x^{m-r}}, \ \psi = c_1 x^{s-r} f(\eta), \ \eta = c_2 y x^r. \tag{4.13}$$

In the above, the values of r and s needs to be found so that the converted governing equations and boundary conditions will not contain x and y variables. Substituting expressions in the Eqs. (4.13) in Eqs. (4.9)–(4.10), after some algebra, we get

$$s x^{2(s+r-m-1)} f'^2 - (s-r) x^{2(s+r-m)-1} f f'' = \nu \frac{c_2}{c_1} x^{s+4r-2m} + g\gamma \frac{1}{(c_1 c_2 c_3)^2} \theta^2, \tag{4.14}$$

$$\alpha \frac{c_2}{c_1} \theta'' + (s-r) x^{s-2r+2m-1} f \theta' + r x^{s-2r-2m-1} f' \theta = 0. \tag{4.15}$$

If the above transformation needs to be similarity transformation, the above equations should contain only η as independent variable and no other independent variables should present. To make x variable go out of the equation, the power of x should be made zero. Equating powers of x to be zero in the left and right sides of the equation (4.14), we get

$$s + r - m - 1 = 0, \tag{4.16}$$

$$2(s + r - m) - 1 = 0, \tag{4.17}$$

which gives r and s values as

$$r = \frac{1}{3}(m - \frac{1}{2}), \tag{4.18}$$

$$s = \frac{2}{3}(m + 1). \tag{4.19}$$

Note that if we substitute the above values of r and s in Eq. (4.14), all the powers of x in the equations become zero and the equations contain only η as independent variable. This means that the above values of r and s represent similarity transformation.

Now, we can choose the constants c_1, c_2, c_3 such a way that the resulting coefficients in the equations will be constants. Choosing c_2 as

$$c_2 = \left(\frac{A^2 g\gamma}{6k^2\nu^2}\right)^{1/6}, \tag{4.20}$$

and making the choice of c_1 and c_3 in terms of constants and fluid properties, we can express the similarity variable in the following form.

$$f = \frac{\psi}{6\nu\,(Gr_y/6)^{1/6}}, \tag{4.21}$$

$$\theta = 6\,\frac{T(x,y) - T_0}{q_w x/k}\left(\frac{Gr_y}{6}\right)^{1/6}, \tag{4.22}$$

$$\eta = \frac{x}{y}\left(\frac{Gr_y}{6}\right)^{1/6}, \tag{4.23}$$

where, $Gr_y = g\gamma(q_w y/k)^2 y^3/\nu^2$.

Using the definitions given by Eqs. (4.21)–(4.23) in Eqs. (4.9) and (4.10), the momentum and energy equations are converted into ordinary differential equations,

$$f''' + (2m+5)\,ff'' - 4\,(m+1)\,f'^2 + \theta^2 = 0, \tag{4.24}$$

$$\theta'' + Pr\,(2m+5)\,f\theta' - Pr\,(4m+1)\,f'\theta = 0. \tag{4.25}$$

The respective boundary conditions in the form of similarity variables are

$$\text{At} \quad \eta = 0: \quad f = 0, \quad f' = 0, \quad \theta' = -1, \tag{4.26}$$

$$\text{At} \quad \eta \to \infty: \quad f' = 0, \quad \theta = 0. \tag{4.27}$$

4.1.4 Results and discussion

From the definitions given by Eqs. (4.21)–(4.23), the dimensionless streamwise velocity can be expressed as

$$V = \frac{v}{(6\nu/x)\left(\frac{Gr_y}{6}\right)^{1/6}} = f'(\eta). \tag{4.28}$$

From Eq. (2.7), we know that

$$v = \frac{\partial \psi}{\partial x}.$$

Using Eqs. (4.47) and (4.49) in the above expression, the velocity is expressed as

$$v = \frac{\partial \psi}{\partial x} = \frac{\partial \psi}{\partial \eta}\frac{\partial \eta}{\partial x} = \frac{\partial}{\partial x}\left[f 6\nu \left(\frac{Gr_y}{6}\right)^{1/6}\right] = \frac{6\nu}{x}\left(\frac{Gr_y}{6}\right)^{1/6} f'. \tag{4.29}$$

Now, we define dimensionless streamwise velocity as

$$V = \frac{v}{(6\nu/x)\left(\frac{Gr_y}{6}\right)^{1/6}} = f'(\eta). \tag{4.30}$$

The local heat transfer coefficient is expressed as

$$h(y) = \frac{q_w(y)}{T_w(y) - T_0}. \tag{4.31}$$

Heat transfer rates are expressed in terms of local Nusselt number which is expressed as

$$Nu_y = \frac{h(y)\ y}{k}. \tag{4.32}$$

Combining Eqs. (4.31) and (4.32), we get

$$Nu_y = \frac{q_w(y)}{T_w - T_0}\frac{y}{k}. \tag{4.33}$$

From the definition of dimensionless temperature given by Eq. (4.22), wall temperature can be expressed as

$$T_w - T_0 = \frac{\theta_{\eta=0}}{6}\frac{q_w(y)}{k} y\ Gr_y^{-1/6}, \tag{4.34}$$

where, $\theta_{\eta=0}$ is the dimensionless temperature corresponds to wall for which $x = 0$ and hence $\eta = 0$. Substituting Eq. (4.34) in Eq. (4.33) we get the heat transfer rates as

$$\frac{Nu_y}{(Gr_y/6)^{1/6}} = \frac{6}{\theta_{\eta=0}}. \tag{4.35}$$

The governing ordinary differential equations (4.24)–(4.25) along with the boundary conditions (4.26)–(4.27) are solved using shooting method utilising fourth order Runge-Kutta method for the integration. Prandtl number value of 11.57 is used for water in the calculations. Dimensionless velocity and temperature profiles are shown in Fig. 4.2 for various values of power index m. With increasing power index, the dimensionless velocity and temperature decreases for a given dimensionless η value. However, the dimensional velocities and temperatures may increase with increasing power-law index value. The decrease of dimensionless velocity and temperature with increasing m is due to the definition of dimensionless values given by the Eqs. (4.13). With increasing m value, the dimensional velocity and temperature increase, but denominator which contains the reference quantities

which also increase with increasing m. With increasing m, the numerical values of denominator grows faster than the numerator, resulting increase of dimensional velocities and temperatures with m, despite their dimensional values increase.

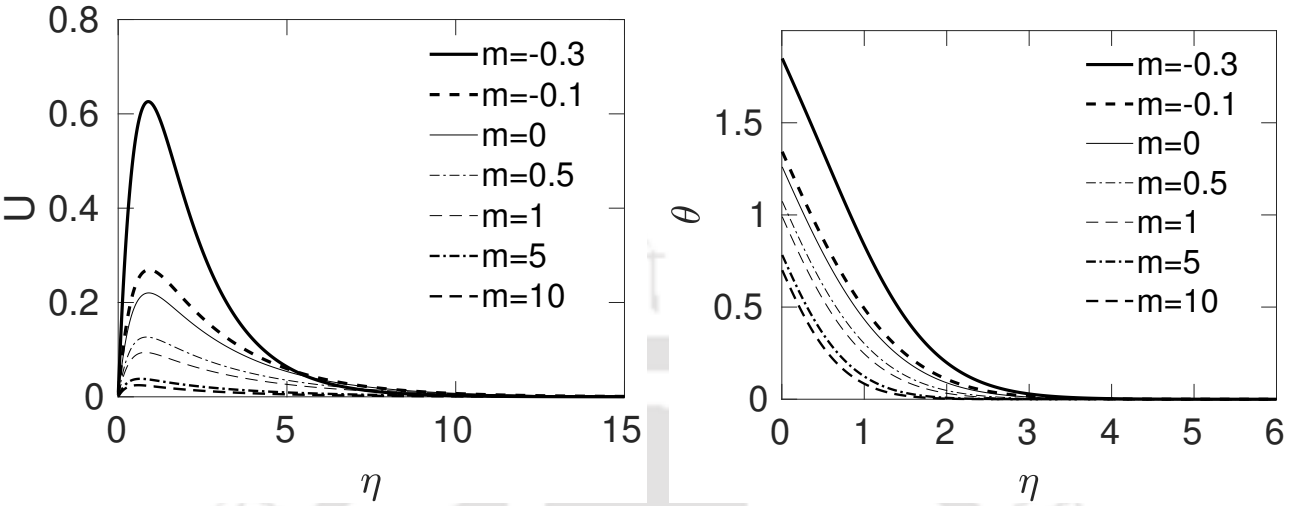

(a) Velocity profile (b) Temperature profile

Figure 4.2: Variation of dimensionless velocity and temperature with η for various of power index value m

Fig. 4.3 shows the variation of velocity and thermal boundary layer thickness. The velocity boundary layer thickness (δ_v) is the normal distance from the wall to the location at which dimensionless velocity becomes 0.01. Similarly, thermal boundary layer thickness (δ_T) is the normal distance from the wall to the location at which the dimensionless temperature reaches to a value of 0.01. The velocity boundary layer thickness decreases with increasing m value, as increasing m represents higher heat flux, higher velocities and hence, thinner boundary layer. Similarly, thermal boundary thickness also decreases with m.

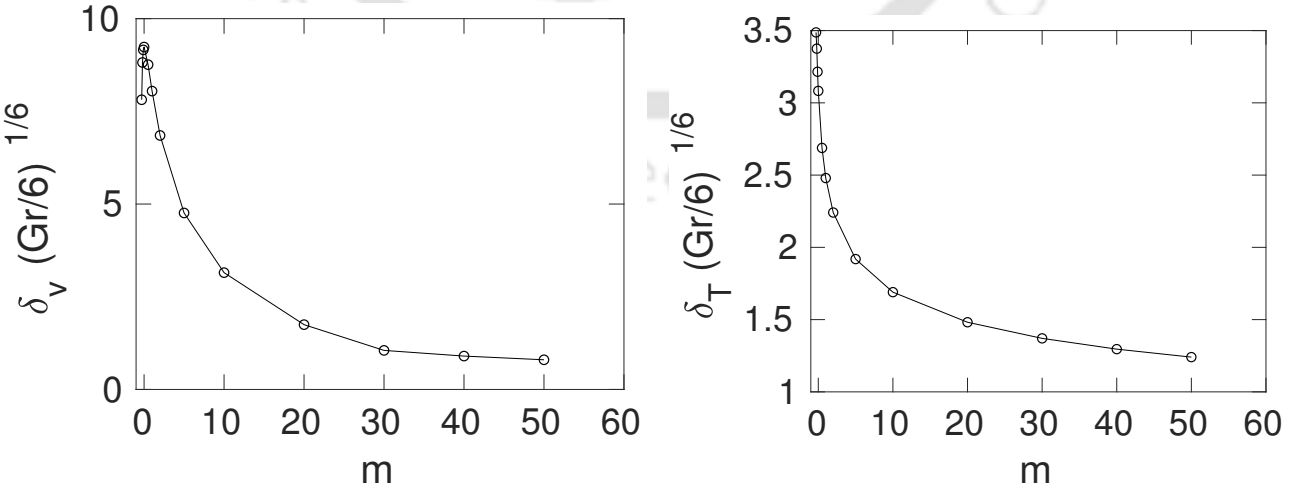

(a) Velocity boundary layer thickness (b) Thermal boundary layer thickness

Figure 4.3: Variation of velocity and thermal boundary layer thickness with power index m

The variation of dimensionless heat transfer rates with m value is shown in Fig. 4.4. The Nusselt

number increases with increasing power-law index value m. When we increase m value from 0 to 50, Nusselt number increases from 5 to 11. The Nusselt number increases almost linearly with m in the m values range of 0 to 1. The rate of increase in Nusselt number is much higher for this range of m values 0 to 1, compared to m greater than 1. The Nusselt number for uniform heat flux ($m = 0$) is found to be about 4.35.

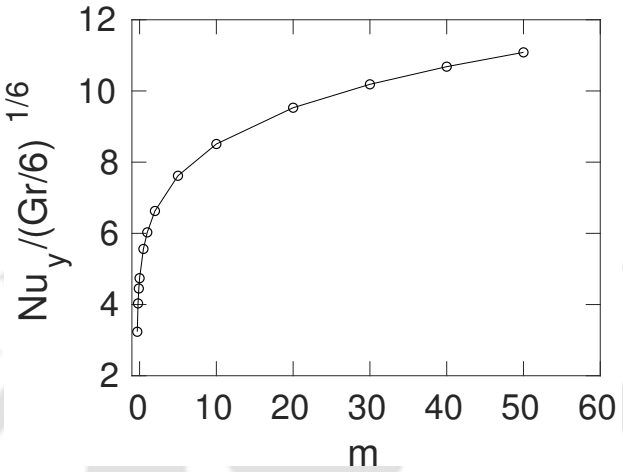

Figure 4.4: Effect of power index value m on heat transfer rates

4.2 Similarity solutions of mixed convection boundary layer

4.2.1 Physical system

The physical system consists of a vertical surface of power-law varying surface heat flux. Water near its density inversion flows over the vertical surface and the mixed convection boundary layer is formed. The free-stream velocity and temperature are v_∞ and T_0, respectively. The temperature in the boundary layer are in the range in which water shows density inversion near its density inversion point (about 3.98°C). The mixed convection is studied for cases of aiding and opposing mixed flows. The physical and co-ordinate systems are shown in Figs. 4.5(a) and 4.5(b) respectively, for aiding and opposing flows.

4.2.2 Mathematical model

The flow is assumed to be steady state, laminar, incompressible with negligible radiation and viscous dissipation effects. Thermo-physical properties of water are considered to be constant with temperature except for density in buoyancy term. The density variation of water with temperature, in the density inversion range, is taken [1, 5] in the form

$$\frac{\rho}{\rho_0} = 1 - \gamma(T - T_0)^2 \,, \tag{4.36}$$

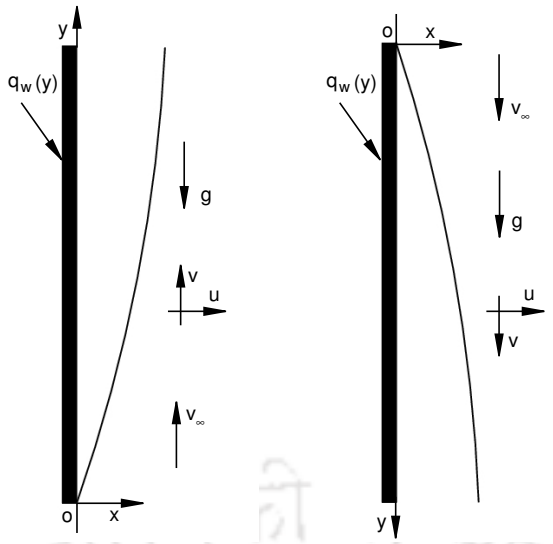

(a) Aiding flow (b) Opposing flow

Figure 4.5: Physical and coordinate systems

where, ρ_0 and T_0 are density and temperature corresponding to density maximum point (at 3.98°C) and γ is a constant. Under the above assumptions, the governing equations for mixed convection boundary layer flow are as following

Continuity equation

$$\frac{\partial u}{\partial x} + \frac{\partial v}{\partial y} = 0, \tag{4.37}$$

y-momentum equation

$$u\frac{\partial v}{\partial x} + v\frac{\partial v}{\partial y} = \nu\frac{\partial^2 v}{\partial x^2} \pm g\gamma(T - T_0)^2, \tag{4.38}$$

Energy equation

$$u\frac{\partial T}{\partial x} + v\frac{\partial T}{\partial y} = \alpha\frac{\partial^2 T}{\partial x^2}. \tag{4.39}$$

The '+' and '-' signs associated with buoyancy term show the aiding and opposing flows of mixed convection. The above equations are subjected to following boundary conditions

$$\text{At} \quad x = 0: \quad u = v = 0, \quad q = q_w, \tag{4.40}$$

$$\text{At} \quad x \to \infty: \quad v \to v_\infty, \quad T \to T_0. \tag{4.41}$$

Introducing stream function in the form,

$$u = -\frac{\partial \psi}{\partial y}, \quad v = \frac{\partial \psi}{\partial x}. \tag{4.42}$$

The above governing equations in stream function form can be written as,

$$\frac{\partial \psi}{\partial x}\frac{\partial^2 \psi}{\partial x \partial y} - \frac{\partial \psi}{\partial y}\frac{\partial^2 \psi}{\partial x^2} = \nu\frac{\partial^3 \psi}{\partial x^3} \pm g\gamma(T - T_0)^2, \tag{4.43}$$

$$\frac{\partial \psi}{\partial x}\frac{\partial T}{\partial y} - \frac{\partial \psi}{\partial y}\frac{\partial T}{\partial x} = \alpha \frac{\partial^2 T}{\partial x^2}, \tag{4.44}$$

and the boundary conditions become

$$\text{At} \quad x = 0: \quad \frac{\partial \psi}{\partial x} = \frac{\partial \psi}{\partial y} = 0, \quad q = q_w(y), \tag{4.45}$$

$$\text{At} \quad x \to \infty: \quad \frac{\partial \psi}{\partial x} \to v_\infty, \quad T \to T_0. \tag{4.46}$$

4.2.3 Solution of the equations

Now the following dimensionless stream function f, temperature θ and similarity variable η are introduced

$$f = \frac{\psi(x,y)}{\sqrt{\nu v_\infty y}}, \tag{4.47}$$

$$\theta = \frac{T(x,y) - T_0}{\frac{q_w y}{k}\sqrt{\frac{\nu}{v_\infty y}}}, \tag{4.48}$$

$$\eta(x,y) = x\sqrt{\frac{v_\infty}{\nu y}}. \tag{4.49}$$

In the definition of θ in Eq. (4.48), the wall heat flux (q_w) is given by

$$q_w(y) = A\, y^m, \tag{4.50}$$

where, A and m are constants. The above wall heat flux represents uniform heat flux plate for $m = 0$. Using Eqs. (4.47)–(4.49) in Eqs. (4.43) and (4.44), the momentum and energy equations are converted into ordinary differential equations,

$$f''' + \frac{1}{2} f f'' \pm \frac{Gr_y}{Re_y^3}\theta^2 = 0, \tag{4.51}$$

$$\theta'' + \frac{1}{2} Pr\, f\theta' - Pr\left(m + \frac{1}{2}\right) f'\theta = 0, \tag{4.52}$$

where, Re_y and Gr_y are local Reynolds and modified Grashof numbers, respectively, which are given by

$$Gr_y = \frac{g\gamma(q_w y/k)^2 y^3}{\nu^2}, \tag{4.53}$$

and

$$Re_y = \frac{v_\infty y}{\nu}. \tag{4.54}$$

Boundary conditions in terms of similarity variables are

$$\text{At} \quad \eta = 0: \quad f = 0, \quad f' = 0, \quad \theta' = -1, \tag{4.55}$$

$$\text{At} \quad \eta \to \infty: \quad f' \to 1, \quad \theta \to 0. \tag{4.56}$$

4.2.4 Results and discussion

The above obtained ordinary differential equations (4.51)–(4.52) along with the boundary conditions (4.55) and (4.56) are solved using fourth-order Runge-Kutta method. Prandtl number value of 11.57 is used for water in the calculations. The dimensionless velocity in terms of similarity variables can be expressed according to the following.

From Eq. (4.42), we know that

$$v = \frac{\partial \psi}{\partial x}.$$

Using Eqs. (4.47) and (4.49) in the above expression, the velocity is expressed as

$$v = \frac{\partial \psi}{\partial x} = \sqrt{v_\infty \nu y}\frac{\partial f}{\partial \eta}\frac{\partial \eta}{\partial x} = v_\infty f'(\eta). \tag{4.57}$$

Now, from above equation, the dimensionless velocity is given by

$$\frac{v}{v_\infty} = f'(\eta). \tag{4.58}$$

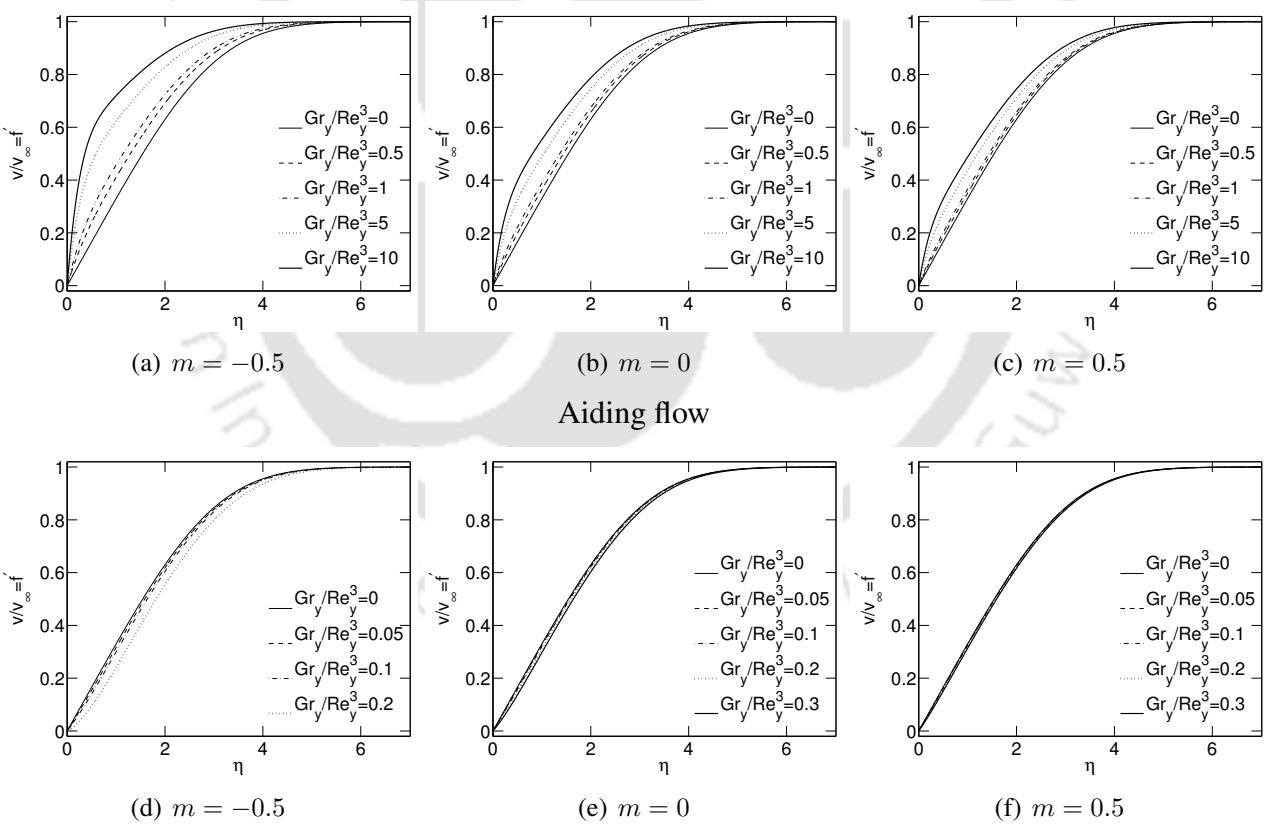

(a) $m = -0.5$ (b) $m = 0$ (c) $m = 0.5$

Aiding flow

(d) $m = -0.5$ (e) $m = 0$ (f) $m = 0.5$

Opposing flow

Figure 4.6: Variation of dimensionless velocity ($v/v_\infty = f'$) with η for various Gr_y/Re_y^3 values for aiding flow (a-c) and opposing flow (d-f)

The variation of dimensionless velocity ($v/v_\infty = f'$) with η for various values of Gr_y/Re_y^3 is shown in Fig. 4.6 for aiding and opposing flows. From the figure, it can be seen that for a given η value, the dimensionless velocity increases with increasing Gr_y/Re_y^3 values in case of aiding flow.

The opposite trend is observed for opposing flow. This is due to the fact that in aiding flow, buoyancy forces complement external forces with increasing Gr_y/Re_y^3 value. However, buoyancy forces oppose external forces in case of opposing mixed convection. It may be noted that the plots corresponding to $Gr_y/Re_y^3 = 0$ in the figure are for forced convection extreme, and the plots for $m = 0$ correspond to uniform heat flux case.

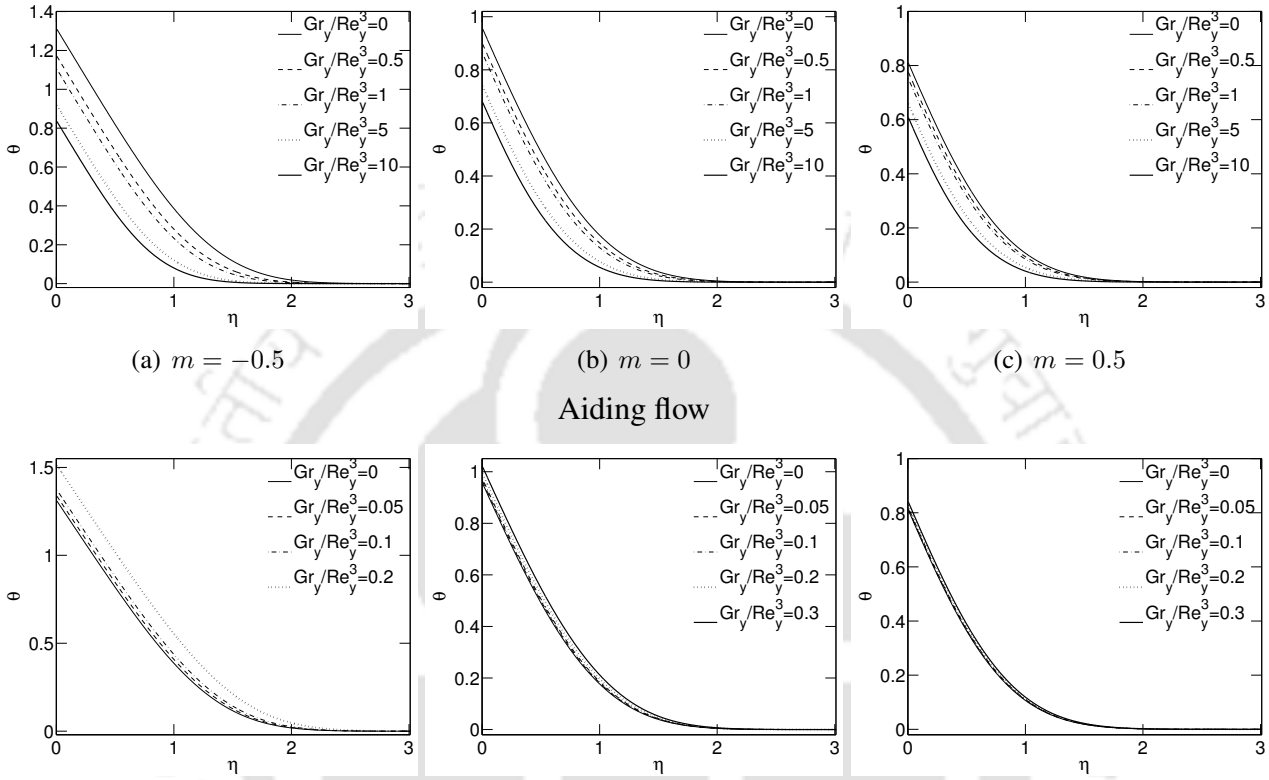

(a) $m = -0.5$ (b) $m = 0$ (c) $m = 0.5$

Aiding flow

(d) $m = -0.5$ (e) $m = 0$ (f) $m = 0.5$

Opposing flow

Figure 4.7: Variation of dimensionless temperature with η for various Gr_y/Re_y^3 values for aiding flow (a-c) and opposing flow (d-f)

Fig. 4.7 shows the variation of dimensionless temperature (θ) with η for various Gr_y/Re_y^3 values for aiding and opposing flows. Figure shows that the dimensionless temperature decreases with increasing Gr_y/Re_y^3 values, for a given value of η in aiding mixed convection, while increases with increasing Gr_y/Re_y^3 for opposing flow. In aiding mixed convection, increased fluid velocity due to complementing nature of both buoyancy and external forces leads to increased heat transfer rates, and hence, the dimensionless temperature decreases. The opposite trend can be observed for opposing flows because buoyancy and external forces oppose each other in this case.

The effect of power index m on the variation of dimensionless velocity and temperature with η are shown in Fig. 4.8 for both aiding and opposing flows. It may be noted from the figure that for a given Gr_y/Re_y^3 value, the value of dimensionless velocity v/v_∞ decreases with increasing m values for individual η value for aiding flow. The trend is reversed in opposing flow, meaning v/v_∞ increases with increasing m values. The dimensionless temperature decreases with increasing m values for both aiding and opposing flows. This shows that the velocity field responds in opposing trend to that

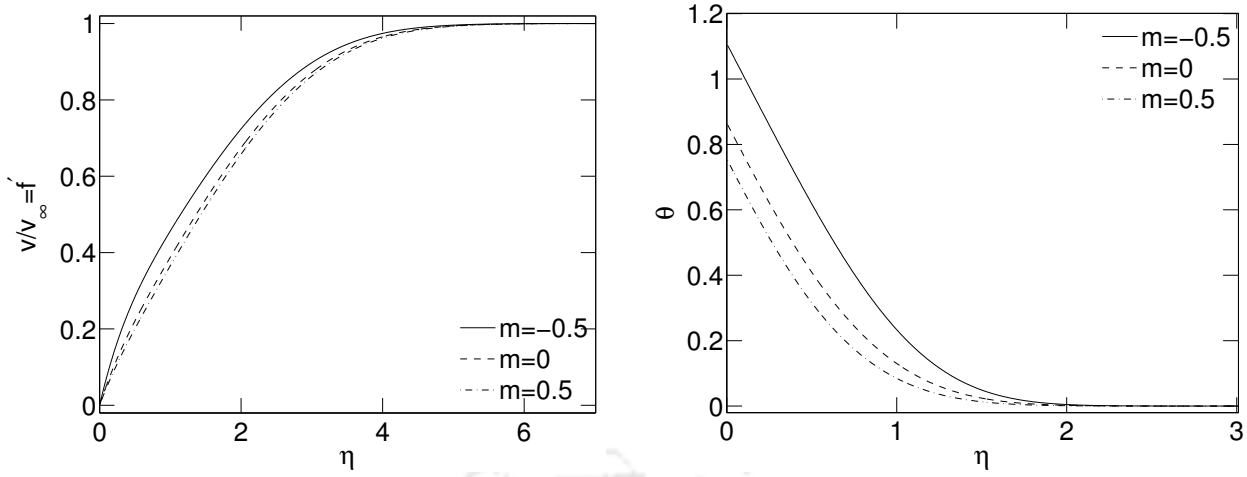

(a) Velocity (b) Temperature

Aiding flow ($Gr_y/Re_y^3 = 1$)

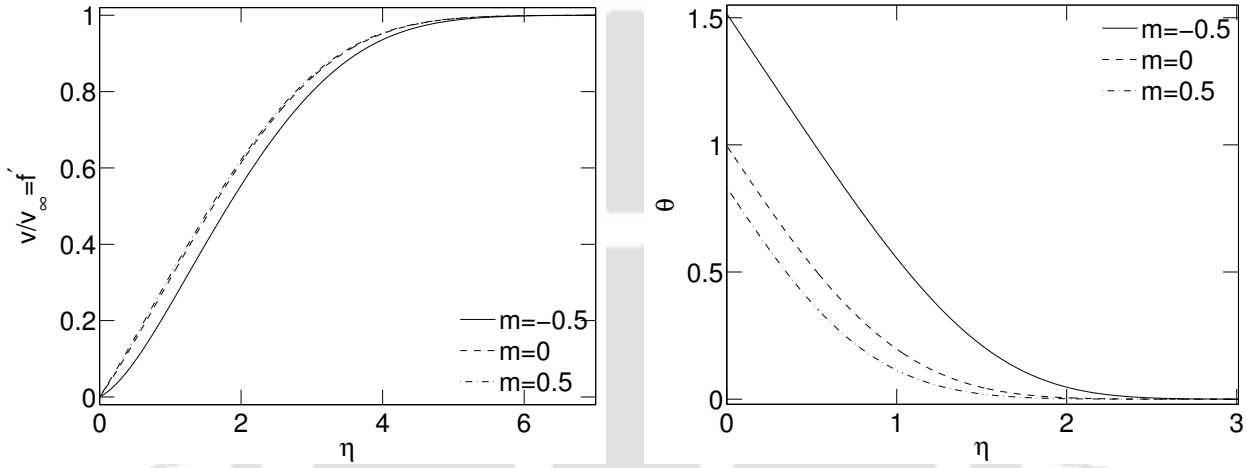

(c) Velocity (d) Temperature

Opposing flow ($Gr_y/Re_y^3 = 0.2$)

Figure 4.8: Effect of m on velocity and temperature: variation of dimensionless velocity ($v/v_\infty = f'$) and dimensionless temperature (θ) with η for various m values for aiding (a-b) and opposing (c-d) flow

of temperature field with variation of m values for aiding and opposing flows. But the temperature responds in the similar way on the variation of m value for both aiding and opposing flows. This is due to the fact that momentum equation contains $\pm \left(Gr_y/Re_y^3\right) \theta^2$ which changes corresponding to aiding and opposing flow condition, hence velocity variation trend is changed, when the flow is changed from aiding to opposing flow. However, the energy equation does not contain $\pm \left(Gr_y/Re_y^3\right) \theta^2$ term and hence, the temperature variation shows similar trends for aiding and opposing flows, with variation of m values.

The variation of dimensionless temperature with η for various m values in case of both aiding and opposing flows is shown in figures 4.8(b) and 4.8(d), respectively. It can be seen from the figures that for a given η value, the dimensionless temperature decreases with increasing m values. This is due to the fact that increasing m value implies increase in wall heat flux resulting decrease in dimensionless

temperature. This can be verified from the fact that heat flux is present in denominator in the definition of dimensionless temperature θ in Eq. (4.48). Since, heat flux increases with increasing m value according to Eq. (4.50), dimensionless temperature decreases with increasing m values.

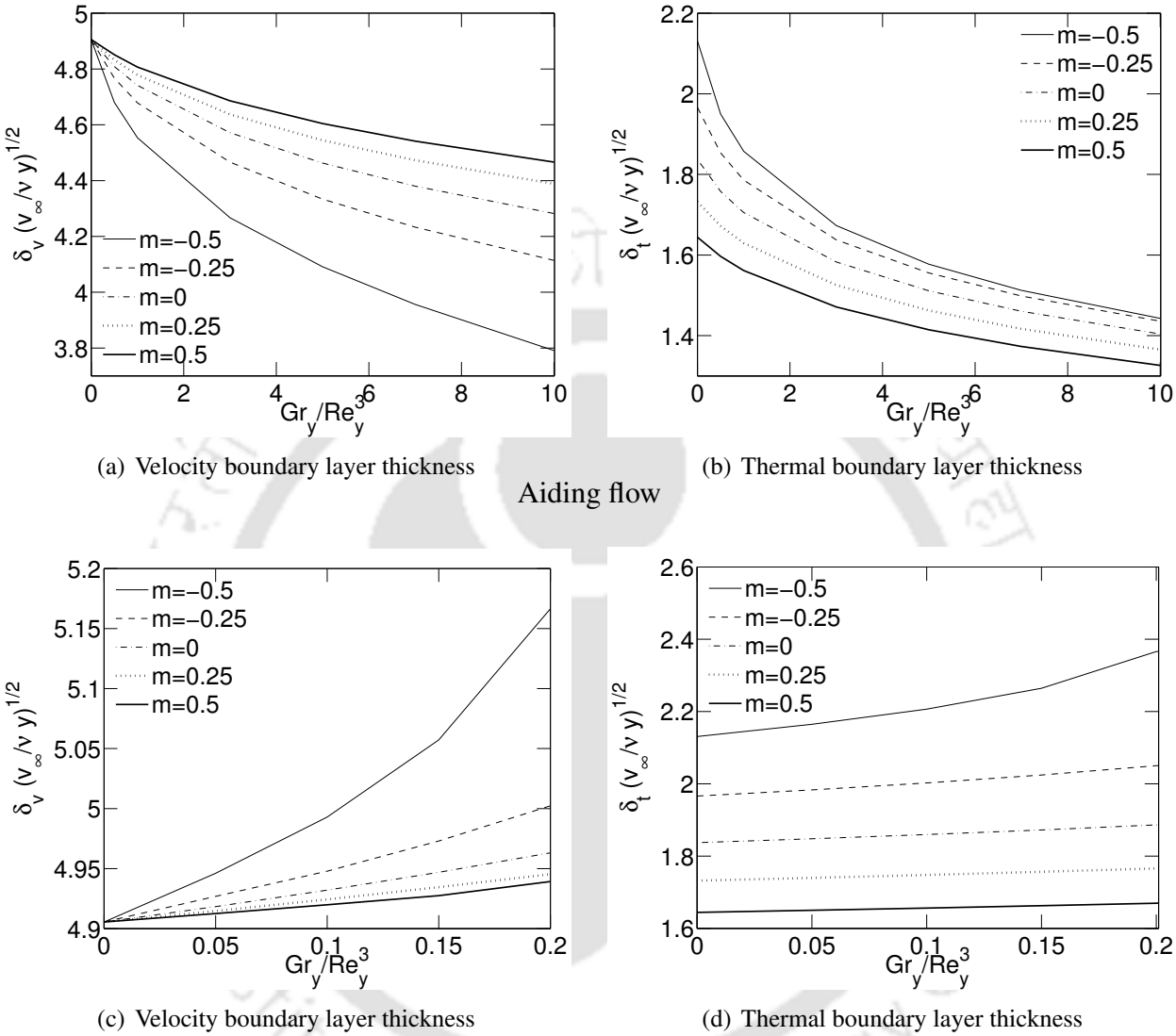

(a) Velocity boundary layer thickness (b) Thermal boundary layer thickness

(c) Velocity boundary layer thickness (d) Thermal boundary layer thickness

Figure 4.9: Variation of velocity and thermal boundary layer thickness with Gr_y/Re_y^3 for various m values for aiding (a-b) and opposing (c-d) flow

From the calculated dimensionless variation of velocity with η, we can calculate velocity boundary layer thickness. The velocity boundary layer thickness corresponds to η value, which is expressed in dimensionless form as $\delta_v(v_\infty/\nu y)^{1/2}$, at which v/v_∞ becomes 0.99. The dimensionless velocity boundary layer thickness for various Gr_y/Re_y^3 values and power-law index m values, are computed. Similarly, thermal boundary layer thickness can be found from the dimensionless temperature variation with η. The thermal boundary layer thickness corresponds to η values at which θ becomes 0.01. Thermal and velocity boundary layer thickness are computed for various Gr_y/Re_y^3 and power-law index values. The variation of velocity and thermal boundary layer thickness with Gr_y/Re_y^3 values are shown in Fig. 4.9 for both aiding and opposing flows. In aiding flow, the velocity and thermal

Table 4.1: Values of velocity boundary layer thickness ($\delta_v(v_\infty/\nu y)^{1/2}$) and thermal boundary layer thickness ($\delta_t(v_\infty/\nu y)^{1/2}$)

	aiding			opposing		
	$\frac{Gr_y}{Re_y^3}$	$\delta_v\left(\frac{v_\infty}{\nu y}\right)^{\frac{1}{2}}$	$\delta_t\left(\frac{v_\infty}{\nu y}\right)^{\frac{1}{2}}$	$\frac{Gr_y}{Re_y^3}$	$\delta_v\left(\frac{v_\infty}{\nu y}\right)^{\frac{1}{2}}$	$\delta_t\left(\frac{v_\infty}{\nu y}\right)^{\frac{1}{2}}$
	0	4.9055	2.1309	0	4.9055	2.1309
	0.5	4.6804	1.9500	0.05	4.9461	2.1646
$m = -0.5$	1	4.5536	1.8574	0.1	4.9929	2.2067
	5	4.0912	1.5773	0.15	5.0572	2.2644
	10	3.7911	1.4429	0.2	5.1665	2.3659
	0	4.9055	1.9662	0	4.9055	1.9662
	0.5	4.7674	1.8537	0.05	4.9268	1.9832
$m = -0.25$	1	4.6769	1.7858	0.1	4.9478	2.0023
	5	4.3337	1.5555	0.15	4.9730	2.0242
	10	4.1141	1.4359	0.2	5.0023	2.0501
	0	4.9055	1.8371	0	4.9055	1.8371
	0.5	4.8088	1.7580	0.05	4.9183	1.8479
$m = 0$	1	4.7414	1.7055	0.1	4.9320	1.8596
	5	4.4629	1.5113	0.15	4.9469	1.8723
	10	4.2822	1.4041	0.2	4.9631	1.8864
	0	4.9055	1.7320	0	4.9055	1.7320
	0.5	4.8324	1.6722	0.05	4.9147	1.7397
$m = 0.25$	1	4.7786	1.6298	0.1	4.9243	1.7479
	5	4.5443	1.4623	0.15	4.9345	1.7565
	10	4.3884	1.3654	0.2	4.9454	1.7658
	0	4.9055	1.6443	0	4.9055	1.6443
	0.5	4.8513	1.5968	0.05	4.9125	1.6501
$m = 0.5$	1	4.8069	1.5616	0.1	4.9198	1.6563
	5	4.6045	1.4146	0.15	4.9275	1.6627
	10	4.4664	1.3261	0.2	4.9392	1.6696

boundary layer thickness decreases with increasing Gr_y/Re_y^3 values. It may be noted that curves for velocity boundary layer thickness for various m values coincide for $Gr_y/Re_y^3 = 0$ for both aiding and opposing flows. This is due to the fact that velocity boundary layer is unaffected by thermal conditions of the wall and hence, it is independent of m value which involves in representation of thermal condition. It can be seen from the figure that for a given Gr_y/Re_y^3 value, both velocity boundary layer thickness and thermal boundary layer thickness decreases for both aiding and opposing flows. The values of velocity and thermal boundary layer thickness in dimensionless form for various Gr_y/Re_y^3 and m values are tabulated in table 4.1, for both aiding and opposing mixed convection.

The local Nusselt number and skin friction coefficient are calculated along the vertical wall to study the heat transfer characteristics and drag on the vertical wall. These dimensionless quantities can be expressed as following.

Local skin friction coefficient can be expressed as

$$C_{fy} = \frac{\tau_{\rm w}}{\rho v_\infty^2}, \tag{4.59}$$

where, v_∞ is free-stream velocity and $\tau_{\rm w}$ is shear stress at wall ($x = 0$). The wall shear stress is given by

$$\tau_{\rm w} = \mu \left.\frac{\partial v}{\partial x}\right|_{x=0} = \mu v_\infty \sqrt{\frac{v_\infty}{\nu y}} \left.\frac{d^2 f}{d\eta^2}\right|_{\eta=0}. \tag{4.60}$$

Using Eq. (4.59) and Eq. (4.60) we get

$$\frac{C_{fy}}{Re_y^{-1/2}} = f''(0) \tag{4.61}$$

Now, skin friction coefficient can be calculated from Eq. (4.61) which is a function of dimensionless stream function.

The local heat transfer coefficient is expressed as

$$h(y) = \frac{q_w(y)}{T_w - T_0}, \tag{4.62}$$

and local Nusselt number is expressed as

$$Nu_y = \frac{h(y)\ y}{k}. \tag{4.63}$$

Using Eqs. (4.62), (4.63) and (4.48), we can express Nusselt number in the form

$$\frac{Nu_y}{Re_y^{1/2}} = \frac{1}{\theta_{\eta=0}}. \tag{4.64}$$

The values of $C_{fy}/Re_y^{-1/2}$ and $Nu_y/Re_y^{1/2}$ are calculated using Eqs. (4.61) and (4.64), respectively. The values of Nusselt number and skin friction coefficient for various values of m and Gr_y/Re_y^3 are presented in table 4.2 for both aiding and opposing flows. It can be seen from the table that for a given m value, both Nusselt number and skin friction coefficient increase with increasing values of Gr_y/Re_y^3 in case of aiding mixed convection. However, Nusselt number and skin friction coefficient decreases with increasing Gr_y/Re_y^3 values in opposing mixed convection. This is due to the fact that both buoyancy and external forces assist each other in aiding flow, resulting increased fluid velocity leads to increase in Nusselt number and skin friction coefficient. However, buoyancy and external forces oppose each other in opposing mixed convection, resulting lower the fluid velocity, reduces the values of Nusselt number and skin friction coefficient.

The variation of heat transfer rates $Nu_y/Re_y^{1/2}$ with Gr_y/Re_y^3 values, for various power-law index m values, is shown Figs. 4.10(a) and 4.10(b), for aiding and opposing mixed convection, respectively. It can be observed from the figures that heat transfer rates increase with increasing Gr_y/Re_y^3 values

Table 4.2: Values of $Nu_y/Re_y^{1/2}$ and $C_{fy}/Re_y^{-1/2}$ for variable heat flux ($q_w = Ay^m$)

	aiding			opposing		
	Gr_y/Re_y^3	$Nu_y/Re_y^{1/2}$	$C_{fy}/Re_y^{-1/2}$	Gr_y/Re_y^3	$Nu_y/Re_y^{1/2}$	$C_{fy}/Re_y^{-1/2}$
	0	0.7609	0.3321	0	0.7609	0.3321
	0.5	0.8509	0.6075	0.05	0.7454	0.2912
$m = -0.5$	1	0.9020	0.7944	0.1	0.7265	0.2437
	5	1.0841	1.6619	0.15	0.7015	0.1849
	10	1.1910	2.3355	0.2	0.6596	0.0964
	0	0.9206	0.3321	0	0.9206	0.3321
	0.5	0.9968	0.5121	0.05	0.9096	0.3085
$m = -0.25$	1	1.0459	0.6446	0.1	0.8975	0.2831
	5	1.2348	1.2869	0.15	0.8837	0.2552
	10	1.3504	1.7947	0.2	0.8676	0.2239
	0	1.0426	0.3321	0	1.0426	0.3321
	0.5	1.1090	0.4658	0.05	1.0339	0.3157
$m = 0$	1	1.1552	0.5694	0.1	1.0244	0.2984
	5	1.3449	1.0911	0.2	1.0032	0.2605
	10	1.4651	1.5105	0.3	0.9771	0.2162
	0	1.1427	0.3321	0	1.1427	0.3321
	0.5	1.2018	0.4385	0.05	1.1353	0.3196
$m = 0.25$	1	1.2453	0.5240	0.1	1.1275	0.3065
	5	1.4332	0.9685	0.2	1.1104	0.2786
	10	1.5560	1.3314	0.3	1.0908	0.2476
	0	1.2284	0.3321	0	1.2284	0.3321
	0.5	1.2819	0.4205	0.05	1.2219	0.3219
$m = 0.5$	1	1.3229	0.4934	0.1	1.2152	0.3115
	5	1.5079	0.8834	0.2	1.2006	0.2894
	10	1.6321	1.2063	0.3	1.1846	0.2655

for all m values in aiding mixed convection, whereas opposite trends is observed for opposing flow. It can also be seen that for a given Gr_y/Re_y^3 values, heat transfer rate increases with m for aiding flow. In opposing flow, for a given Gr_y/Re_y^3 value, decreasing behaviour of heat transfer rates are observed with increasing m values.

Figs. 4.11(a) and 4.11(b) show the variation of skin friction coefficient with Gr_y/Re_y^3 values for various power-law index values m for aiding and opposing mixed convection, respectively. In aiding mixed convection, the skin friction coefficient increases with Gr_y/Re_y^3 values for all power-law index values. However, skin friction coefficient follows decreasing trend with values of Gr_y/Re_y^3 in case of opposing mixed convection, for all power-law index values. It can also be seen from the figures that for a given Gr_y/Re_y^3 value, skin friction coefficient decreases with increasing m values for aiding mixed convection, while it increases with m values for opposing mixed convection. The curves for different m values converge towards decreasing values of Gr_y/Re_y^3. They coincide for $Gr_y/Re_y^3 = 0$ indicating the friction coefficients are independent of m values. This is due to the fact that small

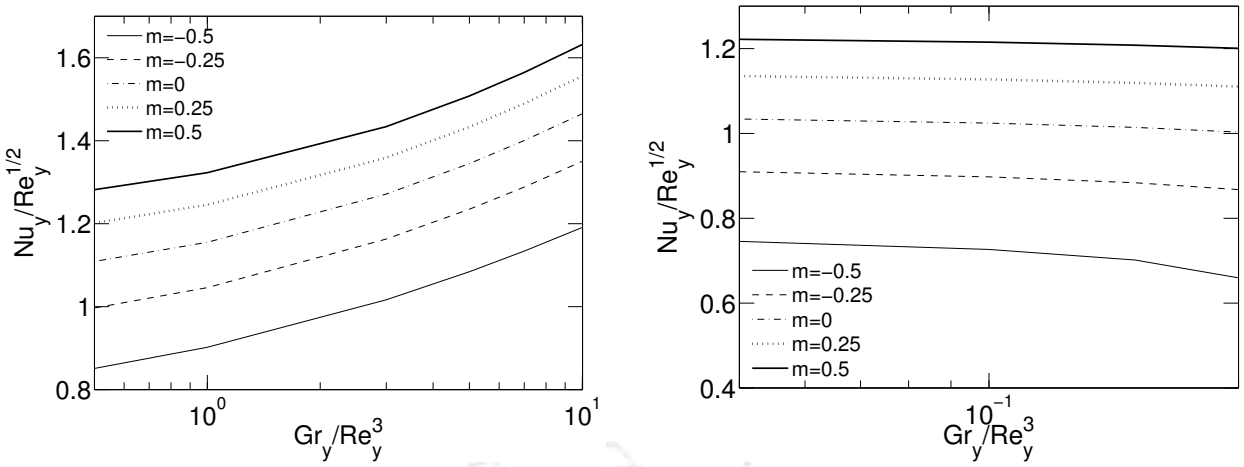

(a) Aiding (b) Opposing

Figure 4.10: Variation of $Nu_y/Re_y^{1/2}$ with Gr_y/Re_y^3 for various m values

values of $Gr_y/Re_y^3 = 0$ indicate the values near the forced convection asymptote and the velocity is not effected by temperature. Hence, the friction factor is independent of m values, as the variable m is associated with thermal boundary condition.

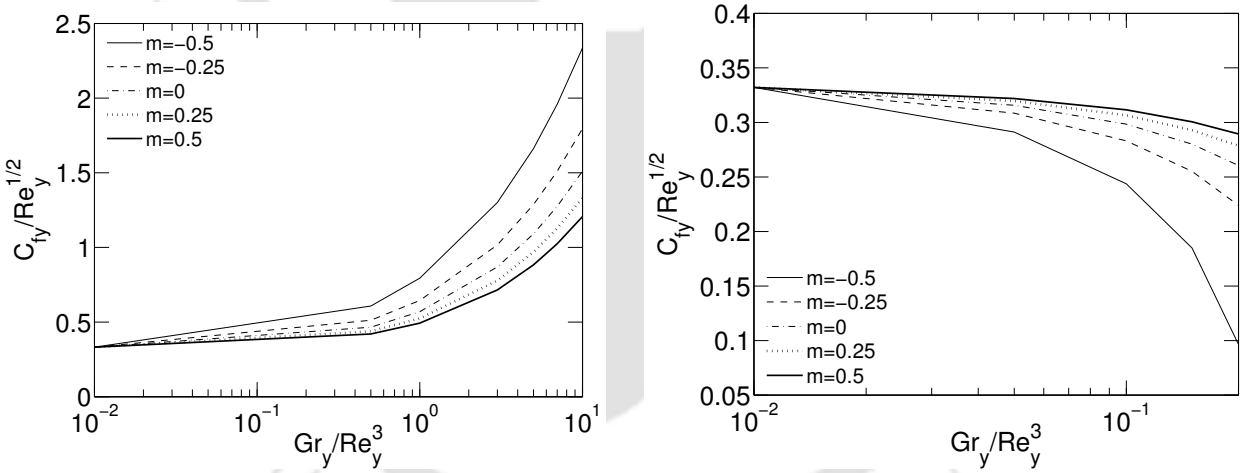

(a) Aiding (b) Opposing

Figure 4.11: Variation of skin friction coefficient with Gr_y/Re_y^3 for various m values

4.3 Summary

In the present chapter, the similarity solutions are presented for the natural and mixed convection boundary layer flows over a flat plate of power-law varying surface heat flux condition. The mixed convection is solved for both assisting and opposing flow configurations. The following conclusions are drawn from the natural convection study.

1. In the natural convection, at a given location, the dimensionless streamwise velocity and dimensionless temperature decreases with increasing power-law index despite the fact that the corresponding dimensional velocity and temperature increases with power-law index.

2. Velocity and thermal boundary layer thickness decreases with increasing power index.

3. Local Nusselt number increases with increasing power-law index.

The conclusions from mixed convection boundary layer flows are as following.

1. For a given value of power-law index, dimensionless velocity and temperature increases and decrease with respect to Gr_y/Re_y^3 for aiding flow. The reverse trend is observed for opposing flow.

2. For a given Gr_y/Re_y^3, dimensionless velocity decreases with power-law index value for aiding flow, and increases for opposing flow. However, dimensionless temperature decreases for both aiding and opposing flows.

3. The velocity and thermal boundary layer thicknesses increases and decreases, respectively, with increasing power-law index value for a given values Gr/Re^3 for aiding flow. The opposite trends are observed for opposing flow.

4. For a given Gr_y/Re_y^3, Nusselt number increases with power-law index for aiding flow. However, the opposite trend is observed for opposing flow.

Chapter 5

Formulation for linear stability analysis of boundary layer flows

In the present study, the stability of natural and mixed convection boundary layer flows of water including density inversion are studied. The stability analysis is carried out for temporal and spatial stability. First, the details of temporal and spatial stability analysis are presented. Then, the discretisation of governing equations, using spectral Chebyshev collocation method, and formation of Eigenvalue problem, which are followed in the present study, are described.

5.1 Parallel stability analysis

In the literature, the stability of boundary layer flows are studied using parallel stability analysis with large extent of success. For example, studies of Wazzan et al. [22] and Kaplan [23]. In the present work, parallel flow stability analysis is adapted for natural and mixed convection boundary layer flows. First to begin with, the basic steps of parallel flow stability which leads to Orr-Sommerfeld equation is briefed here.

In parallel stability analysis, the base flow is assumed to be parallel and the flow variables are assumed to vary only in cross-stream direction. Mathematically, parallel flow assumptions for base flow quantities are written as,

$$\bar{u} = \bar{u}(y), \quad \bar{v} = 0, \quad \bar{p} = \bar{p}(y). \tag{5.1}$$

In parallel flow stability, first we write a governing equation for base flow. Then, the variables such as velocity and pressure are added with perturbations. The governing equations for the combination of base flows and disturbance fields are written. Then, the equations of combined flow are subtracted with the equations of base flow which give the disturbance governing equations. After applying the parallel flow conditions on base flow, we obtain the following disturbance governing equations.

$$\frac{\partial \hat{u}}{\partial x} + \frac{\partial \hat{v}}{\partial y} = 0, \tag{5.2}$$

$$\frac{\partial \hat{u}}{\partial t} + \bar{u}\frac{\partial \hat{u}}{\partial x} + \hat{u}\frac{\partial \bar{u}}{\partial x} + \bar{v}\frac{\partial \hat{u}}{\partial y} + \hat{v}\frac{\partial \bar{u}}{\partial y} + \frac{1}{\rho}\frac{\partial \hat{p}}{\partial x} = \nu\left(\frac{\partial^2 \hat{u}}{\partial x^2} + \frac{\partial^2 \hat{u}}{\partial y^2}\right), \tag{5.3}$$

$$\frac{\partial \hat{v}}{\partial t} + \bar{u}\frac{\partial \hat{v}}{\partial x} + \hat{u}\frac{\partial \bar{v}}{\partial x} + \bar{v}\frac{\partial \hat{v}}{\partial y} + \hat{v}\frac{\partial \bar{v}}{\partial y} + \frac{1}{\rho}\frac{\partial \hat{p}}{\partial y} = \nu\left(\frac{\partial^2 \hat{v}}{\partial x^2} + \frac{\partial^2 \hat{v}}{\partial y^2}\right). \tag{5.4}$$

Neglecting the non-linear terms of disturbance, the linearized form of the disturbance equations are,

$$\frac{\partial \hat{u}}{\partial x} + \frac{\partial \hat{v}}{\partial y} = 0, \tag{5.5}$$

$$\frac{\partial \hat{u}}{\partial t} + \bar{u}\frac{\partial \hat{u}}{\partial x} + \hat{v}\frac{\partial \bar{u}}{\partial y} + \frac{1}{\rho}\frac{\partial \hat{p}}{\partial x} = \nu\left(\frac{\partial^2 \hat{u}}{\partial x^2} + \frac{\partial^2 \hat{u}}{\partial y^2}\right), \tag{5.6}$$

$$\frac{\partial \hat{v}}{\partial t} + \bar{u}\frac{\partial \hat{v}}{\partial x} + \frac{1}{\rho}\frac{\partial \hat{p}}{\partial y} = \nu\left(\frac{\partial^2 \hat{v}}{\partial x^2} + \frac{\partial^2 \hat{v}}{\partial y^2}\right). \tag{5.7}$$

To eliminate the variable $\hat{p}$, differentiate Eq. (5.6) and (5.7) with respect to y and x, respectively and subtract them from each other, we get

$$\frac{\partial^2 \hat{u}}{\partial t \partial y} - \frac{\partial^2 \hat{v}}{\partial t \partial x} + \bar{u}\left(\frac{\partial^2 \hat{u}}{\partial x \partial y} - \frac{\partial^2 \hat{v}}{\partial x^2}\right) + \frac{\partial \bar{u}}{\partial y}\frac{\partial \hat{u}}{\partial x} + \hat{v}\frac{\partial^2 \bar{u}}{\partial y^2} + \frac{\partial \bar{u}}{\partial y}\frac{\partial \hat{v}}{\partial y} = \nu\left(\frac{\partial^3 \hat{u}}{\partial y^3} + \frac{\partial^3 \hat{u}}{\partial x^2 \partial y} - \frac{\partial^3 \hat{v}}{\partial x \partial y^2} - \frac{\partial^3 \hat{v}}{\partial x^3}\right). \tag{5.8}$$

Now, disturbance stream function ($\hat{\psi}$) is introduced and $\hat{u}$ and $\hat{v}$ are expressed in terms of disturbance stream functions as,

$$\hat{u} = \frac{\partial \hat{\psi}}{\partial y}, \quad \hat{v} = -\frac{\partial \hat{\psi}}{\partial x}. \tag{5.9}$$

The stream function is expanded in normal modes in the form

$$\hat{\psi}(x, y, t) = \psi(y) e^{i\bar{\alpha}(x - \bar{c}t)}. \tag{5.10}$$

Substituting Eqs. (5.9) and (5.10) in the Eq. (5.8), we get the following form of disturbance equation

$$-\psi'' c + \bar{\alpha}^2 c\psi + \psi''\bar{u} - \psi\bar{\alpha}^2\bar{u} + \psi'\bar{u}' - \psi\bar{u}'' - \psi'\bar{u}' = \frac{\nu}{i\bar{\alpha}}\left(\psi'''' - 2\bar{\alpha}^2\psi'' + \bar{\alpha}^4\psi\right).$$

Arranging the above disturbance equation, the following equation is obtained

$$(\bar{u} - c)(\psi'' - \bar{\alpha}^2\psi) - \bar{u}''\psi = \frac{\nu}{i\bar{\alpha}}\left(\psi'''' - 2\bar{\alpha}^2\psi'' + \bar{\alpha}^4\psi\right). \tag{5.11}$$

The above equation is generalized disturbance equation for fluid flow in dimensional form. To convert the equation into dimensionless form, the following dimensionless parameters are used,

$$\eta = \frac{y}{\delta}, \quad \phi = \frac{\psi}{U_e \delta}, \quad U = \frac{\bar{u}}{U_e}, \quad C = \frac{c}{U_e}, \quad \alpha = \bar{\alpha}\delta. \tag{5.12}$$

Substituting the above dimensionless parameters in Eq. (5.11), the dimensionless form of governing

equation becomes,

$$(U-C)\left(\phi''-\alpha^2\phi\right)-U''\phi=\frac{1}{i\alpha Re_\delta}\left(\phi''''-2\alpha^2\phi''+\alpha^4\phi\right), \tag{5.13}$$

where, $Re_\delta=\dfrac{U_e\delta}{\nu}$ and $C=\omega/\alpha$. The above equation (5.13) is well known Orr-Sommerfeld equation. The Orr-Sommerfeld equation governs the disturbance equations for velocities. Similarly, we can also derive the disturbance equation for temperature. With appropriate non-dimensional parameters, we can obtain the temperature disturbance equation as

$$(U-C)S-\theta'\phi=\frac{1}{i\alpha Re_\delta Pr}(D^2-\alpha^2)S, \tag{5.14}$$

where, S is the dimensionless temperature disturbance, θ is dimensionless base flow temperature. Re_δ is Reynolds number based on boundary layer thickness and Pr is Prandtl number. The stability of convection flows governed by the combination of both the above Orr-Sommerfeld equation (5.13) and disturbance temperature equation (5.14).

5.2 Temporal stability analysis

In temporal stability analysis, we study evolution of the disturbance in time for a specified periodic variation in space. This means, in the disturbance variation of the form given by Eq. (5.15), we seek values of C which satisfies the disturbance equation along with boundary conditions for a specified real value of α for a given combination of parameter values such as Reynolds number, Prandtl number. This means that in temporal stability analysis, α is specified as given real value and C is, in general, a complex value which acts as an Eigenvalue.

$$\begin{aligned}\hat{\phi}(x,y,t)&=\phi(y)e^{i\alpha(x-ct)}\\&=\phi(y)e^{i\alpha x}e^{-i\alpha(c_r+ic_i)t}.\end{aligned} \tag{5.15}$$

In the above, α is a real value. From the above equations, we can see if c_i

flow is stable:	$c_i<0$	for all Eigenvalues
flow is unstable:	$c_i>0$	atleast for one Eigenvalue
flow is neutrally stable:	$c_i\leq 0$	for all and $c_i=0$ for atleast for one Eigenvalue

5.3 Spatial stability analysis

In spatial stability analysis, we study evolution of the disturbance in space for a specified periodic variation in time at a given location. This means, in the disturbance variation of the form given by Eq. (5.16), we seek value of α which satisfies the disturbance equation along with boundary conditions for a specified real value of ω for a given combination of parameter values such as Reynolds number,

Prandtl number. This means in spatial stability analysis, ω is specified as given real value and α is in general a complex value which acts as an Eigenvalue.

$$\begin{aligned}\hat{\phi}(x,y,t) &= \phi(y)e^{i\alpha(x-ct)} \\ &= \phi(y)e^{i(\alpha_r+i\alpha_i)x}e^{-i\alpha ct} \\ &= \phi(y)e^{i(\alpha_r+i\alpha_i)x}e^{-i\omega t}\end{aligned} \tag{5.16}$$

where, $\omega = \alpha c$.

In the above, ω is the real value. From the above equations, we can see that if α_i

flow is stable:	$\alpha_i > 0$	for all Eigenvalues
flow is unstable:	$\alpha_i < 0$	atleast for one Eigenvalue
flow is neutrally stable:	$\alpha_i \leq 0$	for all and $\alpha_i = 0$ for atleast for one Eigenvalue

5.4 Numerical methodology

5.4.1 Discritization of disturbance equation

The stability of the system is governed by the Eigenvalues of Eigenvalue problem given by velocity disturbance and temperature disturbance equations. From the Eigenvalue problem, we need to extract the information:

1. To find the most unstable Eigenvalue which represents fastest growing mode consequently finding the neutral curve (marginal stability curve).
2. Structure of Eigenvalue spectrum.
3. Eigen vectors.

A review of numerical methods used for the solutions of the disturbance equations is given in Drazin and Reid [14]. In the linear stability analysis, the prediction of instability can be influenced by the accuracy of the discretisation method. Hence, higher accurate methods are needed for the discretisation. The following methods are usually used for the discretisation of disturbance equations.

Finite difference method (FDM): When we want to solve only the most unstable Eigenvalue, finite difference method is an efficient method which needs less computation than that of spectral methods. However, the computation of complete spectrum, FDM may not be the better method.

Spectral method: Spectral methods provide accurate solutions of the governing equations. Chebyshev spectral methods are usually used for the non-periodic configurations.

Initial value methods (Shooting method): In the initial value method, the solution of the governing equations are written into a form of initial value problem and the equations are integrated from $y = 0$ to $y = y_{\text{max}}$. When we use initial value methods for solving Orr-Sommerfeld equation, the parasitic growth problem inherently present in the solutions as different independent solutions have

growth rates of large difference. The use of Riccati method and compound matrix methods are used as remedy for overcoming the parasitic error growth.

Due to the high accuracy and possibility of obtaining the complete Eigenvalue spectrum and Eigen functions, Chebyshev spectral method is used in the present study for the discretisation of disturbance equations. There are many references on the topic of spectral methods such as books by Trefethen [142], Canuto et al. [143] and Boyd [144]. Next, the details of Chebyshev polynomials and discretisation of differentials using Chebyshev polynomials are given below. The details of Chebyshev polynomial can be found in references such as Schmid and Hennigson book [4].

5.4.2 Chebyshev polynomials

The Chebyshev polynomials are the solutions of Sturm-Liouville problem which is given by

$$\frac{d}{dx}\left(\sqrt{1-x^2}\frac{d}{dx}T_k(x)\right)+\frac{k^2}{\sqrt{1-x^2}}T_k(x)=0. \tag{5.17}$$

The Chebyshev polyomial of its first order in the interval [-1,1] can be defined by

$$T_k(x)=\cos(k\cos^{-1}x), \qquad k=0,1,2,\cdots. \tag{5.18}$$

The above Eq. (5.18) is the solution of an Eigenvalue problem given by Eq. (5.17). From the Eq. (5.18), it is clear that $-1 \leq T_k \leq 1$. If we put $x=\cos z$ in Eq. (5.18), we get

$$T_k=\cos kz. \tag{5.19}$$

From the above equation, the Chebyshev polynomial functions can be expressed as

$$\begin{aligned} T_0&=1,\\ T_1&=\cos z=x\\ T_2&=\cos 2z=2\cos^2 z-1=2x^2-1,\\ &\cdots. \end{aligned} \tag{5.20}$$

From the Moivre formula, we can write as

$$\cos kz=Re\left\{(\cos z+i\sin z)^k\right\} \tag{5.21}$$

and then using the Binomial formula, the expression for Chebyshev polynomial (T_k) given by Eq. (5.19) converts into following form,

$$T_k=\frac{k}{2}\sum_{m=0}^{[k/2]}(-1)^m\frac{(k-m-1)!}{m!(k-2m)!}(2x)^{k-2m}, \tag{5.22}$$

where, the quantity $[k/2]$ represents the integer part of $[k/2]$. From the property of trigonometrical

identity

$$\cos(k+1)z + \cos(k-1)z = 2\cos z \cos kz \tag{5.23}$$

and using the relations Eqs. (5.18), (5.19), the recurrence relation for Chebyshev polynomial between $k-1$, k and $k+1$ can be written as

$$T_{k+1} - 2xT_k + T_{k-1} = 0, \qquad k \geq 1. \tag{5.24}$$

From the above equations, for $k \geq 2$, we can find out the series of polynomials expressions for T_k using the expressions for T_{k-1} and T_{k-2}, starting from known expressions for T_0 and T_1 as initial expressions for the recurrence formula.

The expression for polynomial T_k and its first order derivatives T'_k at point $x = \pm 1$ is given by,

$$T_k(\pm 1) = (\pm 1)^k, \quad T'_k(\pm 1) = (\pm 1)^{k+1} k^2. \tag{5.25}$$

The values at above points are useful for the boundary conditions.

$$T_k(-x) = (-1)^k T_k(x). \tag{5.26}$$

The polynomial values of T_k become zero at points x_i which are called Gauss point and given by,

$$x_i = \cos\left(i + \frac{1}{2}\right)\frac{\pi}{k}, \quad i = 0, \cdots, k-1. \tag{5.27}$$

The above expression reaches its extremum values (+1 or -1) at points x_i which are called Gauss-Lobatto points. The expression for Gauss-Lobatto points are defined by,

$$x_i = \cos\frac{\pi i}{k}, \quad i = 0, \cdots, k. \tag{5.28}$$

The Gauss and Gauss-Lobatto points are zeros of the polynomial $(1-x^2)T'_k(x)$.

The differentiation of $T_k = \cos kz$ becomes,

$$T'_k = \frac{d}{dz}(\cos kz)\frac{dz}{dx} = k\frac{\sin kz}{\sin z}. \tag{5.29}$$

Using trigonometric relations, we can write the recurrence formula for derivatives

$$\frac{T'_{k+1}}{k+1} - \frac{T'_{k-1}}{k-1} = 2T_k, \qquad \text{valid for } k > 1. \tag{5.30}$$

One of the important properties of Chebyshev polynomial is the orthogonal property. Chebyshev polynomials are orthogonal on [-1,1] with the weight

$$w = (1-x^2)^{-1/2}. \tag{5.31}$$

The spectrum of functions are orthogonal which means, for any two functions u and v in the spectrum, the scaler product becomes

$$(u, v)_w = \int_{-1}^{1} u\ v\ w dx, \tag{5.32}$$

$$= 0 \quad \text{if } u \text{ and } v \text{ are not the same functions,} \tag{5.33}$$

$$\neq 0 \quad \text{if } u \text{ and } v \text{ are same functions.} \tag{5.34}$$

For Chebyshev polynomials, the orthogonal property is according to

$$(T_k, T_l)_w = \int_{-1}^{1} T_k\ T_l\ w dx = \frac{\pi}{2} c_k\ \delta_{k,l}, \tag{5.35}$$

where, $\delta_{k,l}$ is Kronecker delta and c_k is given by

$$c_k = 2 \quad \text{if } k = 0, \tag{5.36}$$

$$c_k = 1 \quad \text{if } k \geq 1. \tag{5.37}$$

In the Chebyshev approximations to any function governed by differential equation, Gauss quadrature formula is used. The quadrature formula applied to any function $p(x)$ using Gauss-Lobatto points $x_i = \cos \pi i/N, i = 0, \ldots, N$ (which are generally used in any collocation methods) is given by

$$\int_{-1}^{1} p\ w dx \approx \frac{\pi}{N} \sum_{i=0}^{N} \frac{p(x_i)}{\bar{c}_i}, \tag{5.38}$$

where,

$$c_k = 2 \quad \text{if } k = 0, \tag{5.39}$$

$$c_k = 1 \quad \text{if } 1 \leq N - 1, \tag{5.40}$$

$$c_k = 2 \quad \text{if } k = N. \tag{5.41}$$

The relation given by Eq. (5.38) is exact if $p(x)$ is a polynomial of degree $2N - 1$ at most.

$$\frac{\pi}{2} c_k\ \delta_{k,l} = \int_{-1}^{1} T_k\ T_l\ w dx = \frac{\pi}{N} \sum_{i=0}^{N} \frac{1}{\bar{c}_i} T_k(x_i) T_l(x_i). \tag{5.42}$$

$$\sum_{i=0}^{N} \frac{1}{\bar{c}_i} T_k(x_i) T_l(x_i) = \frac{\bar{c}_k}{2} N \delta_{k,l}, \tag{5.43}$$

which is valid for $0 < k, l \leq N$.

5.4.3 Calculation of Chebyshev coefficients

Residue $R_N = u - u_N$ at the collocation points $x_i = \cos(\pi i/N)$, $i = 0, 1, 2, \cdots, N$

$$u(x_i) = u_N(x_i) \qquad i = 0, \cdots, N, \tag{5.44}$$

writing $u_i = u(x_i) = u_N(x_i)$, the above equation becomes,

$$u_i = \sum_{k=0}^{N} \hat{u}_k \cos\left(\frac{k\pi i}{N}\right), \qquad i = 0, \cdots, N. \tag{5.45}$$

Eqs. (5.44) and (5.45) give us algebraic system of equations for $\hat{u}$ with $2(N+1)$ coefficients. The associated matrix $T = \cos\left(\frac{k\pi i}{N}\right)$, $k, i = 0, \cdots, N$ is invertible. $T^{-1} = [2(\cos \pi i/N)/(\bar{c}_k \bar{c}_i N)]$, $k, i = 0, \cdots, N$

$$\hat{u}_k = \frac{2}{\bar{c}_k N} \sum_{i=0}^{N} \frac{1}{\bar{c}_i} u_i T_k(x_i), \qquad k = 0, \cdots, N, \tag{5.46}$$

or

$$\hat{u}_k = \frac{2}{\bar{c}_k N} \sum_{i=0}^{N} \frac{1}{\bar{c}_i} u_i \cos\left(\frac{k\pi i}{N}\right), \qquad k = 0, \cdots, N. \tag{5.47}$$

In the form of matrix-vector products, the above can be written as,

$$U = T\hat{U}, \quad \hat{U} = T^{-1}U, \tag{5.48}$$

where, U and $\hat{U}$ are vectors contain grid points and expansion coefficients, respectively.

5.4.4 Lagrange interpolation polynomial

Let us approximate a function $u(x)$ in terms of the values of $T_k(x)$ at $N+1$ Gauss-Lobatto points given by $x_i = \cos \pi i/N, i = 0, \ldots, N$

$$u_N(x) = \sum_{k=0}^{N} \hat{u}_k T_k(x). \tag{5.49}$$

Eq. (5.49) is a polynomial of degree N and $\hat{u}_k$ are the coefficients of the polynomial. The approximation given by Eq. (5.49) is nothing but the Lagrange interpolation polynomial based on the set of points $\{x_i\}$. Hence, it can be written as

$$u_N(x) = \sum_{j=0}^{N} h_j(x) u(x_j), \tag{5.50}$$

where $u_N(x_j) = u(x_j)$ and $h_j(x)$ is the N^{th} degree polynomial which is given as

$$h_j(x) = \frac{(-1)^{j+1}(1-x^2)T'_N(x)}{\bar{c}_j N^2 (x - x_j)}. \tag{5.51}$$

The expression for $h_j(x)$ can be constructed from the fact that the collocation points given by Gauss-Lobatto points are zeros of polynomial $(1-x^2)T'_N(x)$ (as given in section 5.4.3). The derivative of $(1-x^2)T'_N(x)$ at the limit of Gauss-Lobatto points is given by

$$\lim_{x \to x_j} \frac{(1-x^2)T'_N(x)}{x - x_j} \to (-1)^{j+1}\bar{c}_j N^2 \quad \text{for } j = 0, \ldots, N. \tag{5.52}$$

5.4.5 Differentiation in the physical space

To approximate p^{th} derivative values of polynomial $u(x_i)$ at collocation points given by Gauss-Lobatto points, first we approximate the polynomial using the expression given by Eq. (5.49) as

$$u_N(x) = \sum_{k=0}^{N} \hat{u}_k T_k(x). \tag{5.53}$$

To find the derivative values at the collocation points, we apply derivatives on both sides of the above expression which gives

$$u_N^{(p)}(x) = \sum_{j=0}^{N} h_j^p(x_i) U_N(x_j). \tag{5.54}$$

The values of $h_j^p(x_i)$ can be calculated using expression given by Eq. (5.51). Hence, the derivative $h_j^p(x)$ can be obtained by finding the p^{th} derivative of $h_j(x)$ given by Eq. (5.51) at the collocation points using the limit of $x - x_j \to 0$. The expression for $d_{i,j}^{(p)}$ for first order derivatives ($p = 1$) are given by

$$\begin{aligned} d_{i,j}^{(1)} &= \frac{\bar{c}_i}{\bar{c}_j} \frac{(-1)^{i+j}}{(x_i - x_j)}, \qquad 0 \le i, j \le N, \quad i \ne j \\ d_{i,i}^{(1)} &= -\frac{x_i}{2(1-x_i^2)}, \qquad 1 \le i \le N-1 \\ d_{0,0}^{(1)} &= d_{N,N}^{(1)} = \frac{2N^2+1}{6}, \end{aligned} \tag{5.55}$$

where, $x_i = \cos(\pi i/N)$, $\bar{c}_0 = \bar{c}_N = 2$, $\bar{c}_j = 1$ for $1 \le j \le N-1$.

The vector of first derivative of any variable U can be written as

$$U^{(1)} = DU. \tag{5.56}$$

Here, D is the derivative matrix whose components are given by Eq. (5.55). Once, we find derivative matrix D, the derivative matrix for second order derivatives is given by

$$U^{(2)} = D^2 U, \tag{5.57}$$

where, D^2 is the matrix multiplication of matrix D and D (matmul(D, D))

Similarly, for any p^{th} order derivative vector can be expressed as

$$U^{(p)} = D^p U, \tag{5.58}$$

where, D^p is derivative matrix for p^{th} order derivative which is found by multiplying matrix D, p times to itself.

5.4.6 Gauss-Lobatto grid points

In Chebyshev spectral methods, we need to use Gauss-Lobatto points as grid nodal points for the discretisation. In Chebyshev spectral method with Gauss-Lobatto points, once we choose number of grid points N, then the distribution of the grid points will be fixed by the Gauss-Lobatto grid distribution. The grid distribution according to the Gauss-Lobatto points deploy finer mesh near the boundaries of computation domain at $x = -1$ and $x = 1$. This type of grid inherently shows advantage if the variables show sharp variation at the boundaries. For example, if the physical problems have solid wall at $x = -1$ and $x = 1$, as in channel flows, physically the velocity and temperature show sharp gradients near the walls. For such problems, the Gauss-Lobatto point distribution captures the sharp variation naturally. On the other hand, if in any problem, due to physical reasoning, we need uniform mesh then we have to use grid transformation to map from the Gauss-Lobatto grid to uniform grid. Such transformation is used by Jotkar et. al [145] to distribute grid in streamwise direction uniformly for solving flows in a converging-diverging channel.

The Chebyshev polynomial varies between -1 to 1 and hence, the computational domain has to be in range of -1 to 1. If the physical system has a different coordinate ranges, then we have to transform the physical domain to the computational domain of [-1, 1] in which the Chebyshev spectral method can be applied. When we perform such transformation, the derivatives in the physical domain need to be converted from physical to computational domain using the relation,

$$\frac{d\phi}{dy} = \frac{d\phi}{d\eta}\frac{d\eta}{dy}, \tag{5.59}$$

where, y and η are coordinate systems in physical and computational domain, respectively. ϕ is the general dependent variable.

5.4.7 Mapping from infinite to finite domain

In certain flows, the physical system consists of infinite or semi-infinite domains. For example, boundary layer flows, which are analysed in the present study, the physical system extends to infinity on one side (semi-infinite domain). However, if we use Chebyshev spectral methods for discretisation of disturbance governing differential equations, we need to use coordinate transformation from semi-infinite domain ([0 ∞)) to a domain of [-1,1]. This is because Chebyshev polynomials are defined only in the domain of [-1,1]. In the literature, various mapping functions have been used. Some

mapping functions are (Schmid and Henningson [4])

$$\eta = \frac{1+x}{1-x}, \quad x = \frac{\eta-1}{\eta+1}, \tag{5.60}$$

and,

$$\eta = -\ln\left(\frac{1-x}{2}\right), \quad x = 1 - 2e^{-\eta}, \tag{5.61}$$

$$x = a\frac{1+\eta}{b-\eta}, \tag{5.62}$$

where, $a = \dfrac{x_i x_{\max}}{x_{\max} - 2x_i}$ and $b = 1 + \dfrac{a}{x_{\max}}$. a is the stretching parameter which cluster the grids near the wall that gives accurate solutions. $x_{\max}$ is the length of infinite domain (in computation, $x_{\max}$ is finite but sufficiently large depending on the problems). To get the accurate solutions, the half of the total grid points should be located in region $0 \leq x \leq x_i$. In the present study, the following mapping function is used which is given by Malik [146],

$$x = a\frac{1+\eta}{b-\eta}, \tag{5.63}$$

where, a is constant and $b = 1 + \dfrac{a}{x_{\max}}$. a is stretching parameter and $x_{\max}$ is length of infinite domain.

The mapping functions given by Eqs. (5.62) and (5.63) are almost same. The only difference is that in Eq. (5.62), a is a function of variable η, whereas a is a constant in Eq. (5.63).

5.4.8 Numerical solution of temporal stability Eigenvalue problem

As mentioned in the section 5.2, for a particular combination of parameters such as Reynolds number, Grashof number, we specify real value for α then find the C value as an Eigenvalue. In the disturbance equations for flow α appears with power 1 (linearly). Hence, we can convert the governing equations and boundary conditions of the disturbance equations into the form of $A\bar{\phi} = \lambda B\bar{\phi}$, where A and B matrices are obtained from the disturbance governing equations. For a given set of values of parameters such as Re, Gr and α values, we first construct the matrices A and B then the Eigenvalue problem is solved using open source code LAPACK.

In a general form, the velocity disturbance equation can be written in the form of Eigenvalue problem as follows,

$$\left(a_4\phi'''' + a_3\phi''' + a_2\phi'' + a_1\phi' + a_0\phi\right) + \left(b_2S'' + b_1S' + b_0S\right) = \lambda\left[\left(a_5\phi'' + a_6\phi' + a_7\phi\right) + \left(b_3S'' + b_4S' + b_5S\right)\right]. \tag{5.64}$$

Similarly, the disturbance energy equation in the form of Eigenvalue problem, can be given as,

$$\left(a_8\phi'''' + a_9\phi''' + a_{10}\phi'' + a_{11}\phi' + a_{12}\phi\right) + \left(b_6S'' + b_7S' + b_8S\right) = \lambda\left[\left(a_{13}\phi'' + a_{14}\phi' + a_{15}\phi\right) + \left(b_9S'' + b_{10}S' + b_{11}S\right)\right]. \tag{5.65}$$

Using the differentials defined in the section 5.4.5, the above disturbance equations can be written into the following forms,

$$A_{11}\phi + A_{12}S = C\left(B_{11}\phi + B_{12}S\right), \tag{5.66}$$

$$A_{21}\phi + A_{22}S = C\left(B_{21}\phi + B_{22}S\right), \tag{5.67}$$

where, $C = \omega/\alpha$ is the Eigenvalue in temporal stability and A_{11}, A_{21}, B_{11}, B_{21} are coefficient matrices of ϕ of size $N \times N$, and A_{12}, A_{22}, B_{12}, B_{22} are coefficient matrices of S of size $N \times N$. ϕ and S are vectors of disturbance stream function and temperature, respectively, of the size N. The coefficient matrices are,

$$\begin{aligned}
A_{11} &= a_4D^4 + a_3D^3 + a_2D^2 + a_1D + a_0,\\
A_{12} &= b_2D^2 + b_1D + b_0,\\
A_{21} &= a_8D^4 + a_9D^3 + a_{10}D^2 + a_{11}D + a_{12},\\
A_{22} &= b_6D^2 + b_7D + b_8,\\
B_{11} &= a_5D^2 + a_6D + a_7,\\
B_{12} &= b_3D^2 + b_4D + b_5,\\
B_{21} &= a_{13}D^2 + a_{14}D + a_{15},\\
B_{22} &= b_9D^2 + b_{10}D + b_{11}.
\end{aligned}$$

Eqs. (5.66) and (5.67) together, can be written in the Eigenvalue form as,

$$\begin{bmatrix} A_{11} & A_{12} \\ A_{21} & A_{22} \end{bmatrix} \begin{bmatrix} \phi \\ S \end{bmatrix} = C \begin{bmatrix} B_{11} & B_{12} \\ B_{21} & B_{22} \end{bmatrix} \begin{bmatrix} \phi \\ S \end{bmatrix}. \tag{5.68}$$

The above equation is in the form of generalized Eigenvalue problem, so it can be solved by any Eigenvalue problem solver.

For example, using above procedure, pure Orr-Sommerfeld equation (5.13) can be written as,

$$a_4\phi'''' + a_3\phi''' + a_2\phi'' + a_1\phi' + a_0\phi = \lambda\left(a_5\phi'' + a_6\phi' + a_7\phi\right). \tag{5.69}$$

Using the differentials, the above equations can be written as

$$\left(a_4D^4 + a_3D^3 + a_2D^2 + a_1D + a_0\right)\phi = \lambda\left(a_5D^2 + a_6D + a_7\right)\phi, \tag{5.70}$$

where,

$$
\begin{aligned}
a_0 &= -U\alpha^2 - U'' - \alpha^4 \frac{1}{i\alpha Re_\delta}, \\
a_1 &= 0, \\
a_2 &= U + 2\alpha^2 \frac{1}{i\alpha Re_\delta}, \\
a_3 &= 0, \\
a_4 &= -\frac{1}{i\alpha Re_\delta}, \\
a_5 &= 1, \\
a_6 &= 0, \\
a_7 &= -\alpha^2.
\end{aligned}
$$

5.4.9 Numerical solution of Eigenvalue problem of spatial stability analysis

Solutions of polynomial Eigenvalue problem

As mention in the section 5.3, in spatial stability analysis, we specify a real value for ω (which is proportional to C) and find the value of α as an Eigenvalue which is in general a complex number. However, in the disturbance equations, α appears with non-linear powers. For example, in Orr-Sommerfeld equation α appears with highest power 4. Hence, in spatial stability of heat transfer and fluid flow problems, we get an eigenvalue problem in the form of

$$\left[C_4\alpha^4 + C_3\alpha^3 + C_2\alpha^2 + C_1\alpha + C_0\right]\phi + \left[E_2\alpha^2 + E_1\alpha + E_0\right]S = 0, \tag{5.71}$$

$$\left[C_9\alpha^4 + C_8\alpha^3 + C_7\alpha^2 + C_6\alpha + C_5\right]\phi + \left[E_5\alpha^2 + E_4\alpha + E_3\right]S = 0. \tag{5.72}$$

The Eigenvalue problem in which the Eigenvalue appears in power more than 1, is called polynomial Eigenvalue problem. To solve a Polynomial Eigenvalue problem, first we have to convert this into generalized Eigenvalue problem of the form $AX = \lambda BX$. The conversion of polynomial Eigenvalue problem is done using the following linearisation

$$\phi_1 = \phi, \tag{5.73}$$

$$\phi_2 = \alpha\phi = \alpha\phi_1, \tag{5.74}$$

$$\phi_3 = \alpha^2\phi = \alpha\phi_2, \tag{5.75}$$

$$\phi_4 = \alpha^3\phi = \alpha\phi_3, \tag{5.76}$$

$$S_1 = S, \tag{5.77}$$

$$S_2 = \alpha S = \alpha S_1. \tag{5.78}$$

Eq. (5.71) can be written as following in terms of ϕ_1, ϕ_2, ϕ_3, ϕ_4, S_1 and S_2 as,

$$-C_0\phi_1 - C_1\phi_2 - C_2\phi_3 - C_3\phi_4 - E_0S_1 - E_1S_2 = \alpha\left(C_4\phi_4 + E_2S_2\right) \tag{5.79}$$

$$-C_5\phi_1 - C_6\phi_2 - C_7\phi_3 - C_8\phi_4 - E_3S_1 - E_4S_2 = \alpha\left(C_9\phi_4 + E_5S_2\right) \tag{5.80}$$

From Eqs. (5.74)–(5.79), the polynomial Eigenvalue problem can be written in the form of system of Eigenvalue problem which is given by,

$$\begin{bmatrix} 0 & I & 0 & 0 & 0 & 0 \\ 0 & 0 & I & 0 & 0 & 0 \\ 0 & 0 & 0 & I & 0 & 0 \\ -C_0 & -C_1 & -C_2 & -C_3 & -E_0 & -E_1 \\ 0 & 0 & 0 & 0 & 0 & I \\ -C_5 & -C_6 & -C_7 & -C_8 & -E_3 & -E_4 \end{bmatrix} \begin{bmatrix} \phi_1 \\ \phi_2 \\ \phi_3 \\ \phi_4 \\ S_1 \\ S_2 \end{bmatrix} = \alpha \begin{bmatrix} I & 0 & 0 & 0 & 0 & 0 \\ 0 & I & 0 & 0 & 0 & 0 \\ 0 & 0 & I & 0 & 0 & 0 \\ 0 & 0 & 0 & C_4 & 0 & E_2 \\ 0 & 0 & 0 & 0 & I & 0 \\ 0 & 0 & 0 & C_9 & 0 & E5 \end{bmatrix} \begin{bmatrix} \phi_1 \\ \phi_2 \\ \phi_3 \\ \phi_4 \\ S_1 \\ S_2 \end{bmatrix}, \tag{5.81}$$

where, ϕ_1, ϕ_2, ϕ_3 and ϕ_4 are Eigen functions of disturbance stream function and S_1 and S_2 are the Eigenfunctions of disturbance temperature. The coefficient C_0, C_1, C_2, C_3, C_4, C_5, C_6, C_7, C_8, C_9 are coefficient square matrices for ϕ and I is identity matrix.E_0, E_1, E_2, E_3, E_4 and E_5 are coefficient matrices for S.

Chapter 6

Stability analysis of natural convection boundary layer flows

In this chapter, the study of stability of natural convection boundary layer flows of water near its density inversion is presented. The stability of natural convection is studied for uniform temperature and uniform heat flux wall conditions. For both the wall conditions, temporal and spatial stability analysis is carried out. The effect of inclination on the stability is also studied.

6.1 Stability of natural convection boundary layer over an isothermal plate

6.1.1 Physical system

The physical system of the problem consists of a vertical plate of constant wall temperature T_w. The schematic of the problem is shown in Fig. 6.1. The ambient fluid is stationary and at temperature T_0, where T_0 is the temperature corresponding to density maximum point. Due to the induced buoyancy caused by temperature differences, water near its density inversion forms the free convection boundary layer flow over the vertical plate.

6.1.2 Governing equations for base flow

The base flows is assumed to be steady and incompressible. The viscous dissipation and effect of radiation are considered to be negligible. The thermo-physical properties of the water are taken constant except for the density in buoyancy term in y-momentum equation. The variation of density with temperature is taken according to the parabolic profile given by Eq. (1.3)

$$\rho = \rho_0[1 - (T/T_0)^2],$$

where, ρ is the density of water and ρ_0 and T_0 are the density and temperature of the maximum density point near the density inversion. Under the above assumptions, continuity, momentum and

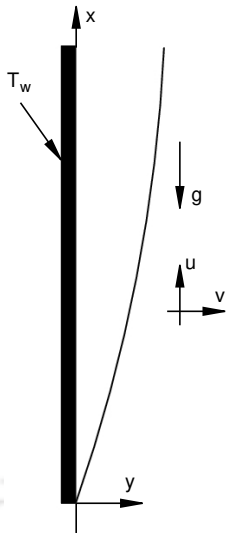

Figure 6.1: Natural convection boundary layer flow over a plate of constant wall temperature

energy equations, respectively, can be written as

$$\frac{\partial u}{\partial x} + \frac{\partial v}{\partial y} = 0, \tag{6.1}$$

$$\frac{\partial u}{\partial t} + u\frac{\partial u}{\partial x} + v\frac{\partial u}{\partial y} = -\frac{1}{\rho}\frac{\partial p}{\partial x} + \nu\left(\frac{\partial^2 u}{\partial x^2} + \frac{\partial^2 u}{\partial y^2}\right), \tag{6.2}$$

$$\frac{\partial v}{\partial t} + u\frac{\partial v}{\partial x} + v\frac{\partial v}{\partial y} = -\frac{1}{\rho}\frac{\partial p}{\partial y} + \nu\left(\frac{\partial^2 v}{\partial x^2} + \frac{\partial^2 v}{\partial y^2}\right) + g\gamma(T - T_0)^2, \tag{6.3}$$

$$\frac{\partial T}{\partial t} + u\frac{\partial T}{\partial x} + v\frac{\partial T}{\partial y} = \frac{k}{\rho c_p}\left(\frac{\partial^2 T}{\partial x^2} + \frac{\partial^2 T}{\partial y^2}\right). \tag{6.4}$$

After applying the boundary layer approximations to the above equations, the following equations are obtained.

$$\frac{\partial u}{\partial x} + \frac{\partial v}{\partial y} = 0, \tag{6.5}$$

$$u\frac{\partial u}{\partial x} + v\frac{\partial u}{\partial y} = \nu\frac{\partial^2 u}{\partial y^2} + g\gamma(T - T_0)^2, \tag{6.6}$$

$$u\frac{\partial T}{\partial x} + v\frac{\partial T}{\partial y} = \frac{k}{\rho c_p}\frac{\partial^2 T}{\partial y^2}. \tag{6.7}$$

No-slip and no penetration conditions are applied at the plate wall. The plate wall is at constant temperature T_w, whereas the ambient temperature of fluid is T_0. For the base flow, the boundary conditions are given by

$$\text{At } y = 0, \qquad u = v = 0, \quad T = T_w, \tag{6.8}$$

$$\text{At } y \to \infty, \qquad u = 0, \quad T = T_0. \tag{6.9}$$

The above governing equations along with the boundary conditions admit similarity solutions. To convert the above partial differential equations into ordinary differential equations, the following sim-

ilarity transformation is used.

$$\eta = \frac{y}{x}\left(\frac{Gr_x}{4}\right)^{1/4}, \quad U = f' = \frac{\bar{v}}{\nu}\left(\frac{x}{Gr_x^{1/2}}\right), \quad \theta = \frac{\bar{T}-\bar{T}_0}{\Delta\bar{T}},$$
$$Gr_x = \frac{g\gamma(\Delta\bar{T})^2x^3}{\nu^2}, \quad \Delta\bar{T} = \bar{T}_w - \bar{T}_0. \tag{6.10}$$

With the above transformation, the governing equations (6.5)–(6.7) and boundary conditions (6.8)–(6.9) convert into the following form.

$$f''' + \frac{3}{2}ff'' - \frac{1}{2}f'^2 + 2\theta^2 = 0 \tag{6.11}$$
$$\theta'' + \frac{3}{2}Prf\theta' = 0 \tag{6.12}$$

where, derivative of above variables are derivative with respect to dimensionless variable η, f is dimensionless stream function and θ is dimensionless temperature.

$$\text{At } \eta = 0, \qquad f = f' = 0, \quad \theta = 1 \tag{6.13}$$
$$\text{At } \eta \to \infty, \qquad f' = 0, \quad \theta = 0. \tag{6.14}$$

The above ordinary differential equations are solved using shooting method. Fourth order Runge-Kutta method is used for the numerical integration of the ODEs.

6.1.3 Disturbance equations

Now, parallel flow stability analysis is considered to study the natural convection boundary layer flow. In parallel flow stability, the base flow is assumed to be parallel. Hence, streamwise velocity, pressure, temperature are functions of x only. The cross stream velocity components are zero.

$$\bar{u} = \bar{u}(y), \quad \bar{v} = 0, \quad \bar{p} = \bar{p}(y), \quad \bar{T} = \bar{T}(y). \tag{6.15}$$

Imposing perturbations u', v', p' and T' on base flow defined by variables $\bar{u}$, $\bar{v}$, $\bar{p}$ and $\bar{T}$, the governing equations for combined flow become

$$\frac{\partial\bar{u}}{\partial x} + \frac{\partial\bar{v}}{\partial y} + \frac{\partial u'}{\partial x} + \frac{\partial v'}{\partial y} = 0, \tag{6.16}$$

$$\begin{aligned}&\left(\cancel{\frac{\partial\bar{u}}{\partial t}} + \bar{u}\frac{\partial\bar{u}}{\partial x} + \bar{v}\frac{\partial\bar{u}}{\partial y}\right) + \left(\frac{\partial u'}{\partial t} + u'\frac{\partial u'}{\partial x} + v'\frac{\partial u'}{\partial y}\right) + \bar{u}\frac{\partial u'}{\partial x} + u'\frac{\partial\bar{u}}{\partial x} + \bar{v}\frac{\partial u'}{\partial y} + v'\frac{\partial\bar{u}}{\partial y}\\ &= -\frac{1}{\rho}\frac{\partial\bar{p}}{\partial x} + \nu\left(\frac{\partial^2\bar{u}}{\partial x^2} + \frac{\partial^2\bar{u}}{\partial y^2}\right) - \frac{1}{\rho}\frac{\partial p'}{\partial x} + \nu\left(\frac{\partial^2u'}{\partial x^2} + \frac{\partial^2u'}{\partial y^2}\right),\end{aligned} \tag{6.17}$$

$$\begin{aligned}&\left(\cancel{\frac{\partial\bar{v}}{\partial t}} + \bar{u}\frac{\partial\bar{v}}{\partial x} + \bar{v}\frac{\partial\bar{v}}{\partial y}\right) + \left(\frac{\partial v'}{\partial t} + u'\frac{\partial v'}{\partial x} + v'\frac{\partial v'}{\partial y}\right) + \bar{u}\frac{\partial v'}{\partial x} + u'\frac{\partial\bar{v}}{\partial x} + \bar{v}\frac{\partial v'}{\partial y} + v'\frac{\partial\bar{v}}{\partial y}\\ &= -\frac{1}{\rho}\frac{\partial\bar{p}}{\partial y} + \nu\left(\frac{\partial^2\bar{v}}{\partial x^2} + \frac{\partial^2\bar{v}}{\partial y^2}\right) - \frac{1}{\rho}\frac{\partial p'}{\partial y} + \nu\left(\frac{\partial^2v'}{\partial x^2} + \frac{\partial^2v'}{\partial y^2}\right),\end{aligned} \tag{6.18}$$

$$\left(\frac{\partial \bar{T}}{\partial t}+\bar{u}\frac{\partial \bar{T}}{\partial x}+\bar{v}\frac{\partial \bar{T}}{\partial y}\right)+\frac{\partial \hat{T}}{\partial t}+u'\frac{\partial T'}{\partial x}+v'\frac{\partial T'}{\partial y}+\bar{u}\frac{\partial T'}{\partial x}+u'\frac{\partial \bar{T}}{\partial x}+\bar{v}\frac{\partial T'}{\partial y}+v'\frac{\partial \bar{T}}{\partial y}$$
$$=\frac{k}{\rho c_p}\left(\frac{\partial^2 \bar{T}}{\partial x^2}+\frac{\partial^2 \bar{T}}{\partial y^2}\right)+\frac{k}{\rho c_p}\left(\frac{\partial^2 \hat{T}}{\partial x^2}+\frac{\partial^2 \hat{T}}{\partial y^2}\right). \tag{6.19}$$

After subtracting the base flow equations from the above combined flow equations and linearising the resulting equations, the following linearised disturbance equations are obtained.

$$\frac{\partial \hat{u}}{\partial x}+\frac{\partial \hat{v}}{\partial y}=0, \tag{6.20}$$

$$\frac{\partial \hat{u}}{\partial t}+\bar{u}\frac{\partial \hat{u}}{\partial x}+\hat{v}\frac{\partial \bar{u}}{\partial y}=-\frac{1}{\rho}\frac{\partial \hat{p}}{\partial x}+\nu\left(\frac{\partial^2 \hat{u}}{\partial x^2}+\frac{\partial^2 \hat{u}}{\partial y^2}\right)+2g\gamma(\bar{T}-\bar{T}_0)\hat{T}, \tag{6.21}$$

$$\frac{\partial \hat{v}}{\partial t}+\bar{u}\frac{\partial \hat{v}}{\partial x}=-\frac{1}{\rho}\frac{\partial \hat{p}}{\partial y}+\nu\left(\frac{\partial^2 \hat{v}}{\partial x^2}+\frac{\partial^2 \hat{v}}{\partial y^2}\right), \tag{6.22}$$

$$\frac{\partial \hat{T}}{\partial t}+\bar{u}\frac{\partial \hat{T}}{\partial x}+\hat{v}\frac{\partial \bar{T}}{\partial y}=\frac{k}{\rho c_p}\left(\frac{\partial^2 \hat{T}}{\partial x^2}+\frac{\partial^2 \hat{T}}{\partial y^2}\right). \tag{6.23}$$

The disturbance pressure $\hat{p}$ is eliminated by differentiating Eq. (6.21) and (6.22) with respect to x and y, respectively, and subtracting them from each other, we get

$$\frac{\partial}{\partial t}\left(\frac{\partial \hat{u}}{\partial y}-\frac{\partial \hat{v}}{\partial x}\right)+\bar{u}\left(\frac{\partial^2 \hat{u}}{\partial x\partial y}-\frac{\partial^2 \hat{v}}{\partial x^2}\right)+\frac{\partial \bar{u}}{\partial y}\frac{\partial \hat{u}}{\partial x}+\hat{v}\frac{\partial^2 \bar{u}}{\partial y^2}+\frac{\partial \bar{u}}{\partial y}\frac{\partial \hat{v}}{\partial y}$$
$$=\nu\left(\frac{\partial^3 \hat{u}}{\partial y^3}+\frac{\partial^3 \hat{u}}{\partial x^2\partial y}-\frac{\partial^3 \hat{v}}{\partial x\partial y^2}-\frac{\partial^3 \hat{v}}{\partial x^3}\right)+2g\gamma\left[(\bar{T}-\bar{T}_0)\frac{\partial \hat{T}}{\partial y}+\hat{T}\frac{\partial}{\partial y}(\bar{T}-\bar{T}_0)\right], \tag{6.24}$$

$$\frac{\partial \hat{T}}{\partial t}+\bar{u}\frac{\partial \hat{T}}{\partial x}+\hat{v}\frac{\partial \bar{T}}{\partial y}=\frac{k}{\rho c_p}\left(\frac{\partial^2 \hat{T}}{\partial x^2}+\frac{\partial^2 \hat{T}}{\partial y^2}\right). \tag{6.25}$$

Expressing the disturbance variables in terms of normal mode form as

$$\hat{\phi}(x,y,t)=\bar{\phi}(y)e^{i\bar{\alpha}(x-ct)}, \qquad \hat{T}(x,y,t)=s(y)e^{i\bar{\alpha}(x-ct)}, \tag{6.26}$$

where, $\bar{\phi}$ and s are amplitude of disturbance stream function and temperature, respectively. $\bar{\alpha}$ is wave number and c is phase speed. Now, disturbance velocity $\hat{u}$ and $\hat{v}$ can be expressed as,

$$\hat{u}=\frac{\partial \hat{\phi}}{\partial y}, \quad \hat{v}=-\frac{\partial \hat{\phi}}{\partial x}. \tag{6.27}$$

Using the definitions of $\hat{\phi}$, $\hat{T}$, $\hat{u}$ and $\hat{v}$ in the Eqs. (6.24) and (6.25), the final disturbance equations for momentum and energy equations in the dimensional forms are as following,

$$(\bar{u}-c)(\bar{\phi}''-\bar{\alpha}^2\bar{\phi})-\bar{u}''\bar{\phi}=\frac{\nu}{i\bar{\alpha}}\left(\bar{\phi}''''-2\bar{\alpha}^2\bar{\phi}''+\bar{\alpha}^4\bar{\phi}\right),$$
$$+\frac{2g\gamma}{i\bar{\alpha}}\left[(\bar{T}-\bar{T}_0)s'+s(\bar{T}-\bar{T}_0)'\right], \tag{6.28}$$

$$i\bar{\alpha}(\bar{u}-c)s - i\bar{\alpha}(\bar{T}-\bar{T}_0)'\bar{\phi} = \frac{k}{\rho c_p}\left(s'' - \bar{\alpha}^2 s\right). \tag{6.29}$$

Here, $c = \omega/\alpha$ is phase speed of disturbance.

At the plate surface, x and y components of disturbance velocity are zero as there is no disturbance at the solid plate. Similarly, the temperature disturbance at the plate is zero. Mathematically, the boundary conditions for the above disturbance equations in dimensional form are,

$$\text{At} \quad y = 0: \qquad \bar{\phi} = \bar{\phi}' = 0, \quad s = 0, \tag{6.30}$$

$$\text{At} \quad y \to \infty: \qquad \bar{\phi}' = 0, \quad s = 0. \tag{6.31}$$

The equations are non-dimensionised using the following form of dimensionless variables,

$$\delta = \frac{x\sqrt{2}}{Gr_x^{1/4}},\ \eta = \frac{y}{\delta},\ u_{\text{ref}} = \frac{\nu}{x}Gr_x^{1/2},\ \phi = \frac{\bar{\phi}}{u_{\text{ref}}\,\delta},\ S = \frac{s}{T_w - T_0},\ C = \frac{c}{u_{\text{ref}}},\ \alpha = \bar{\alpha}\delta.$$

Using the above dimensionless parameters, the dimensionless form of disturbance governing equations for momentum and energy equations becomes,

$$\left[(U-C)(D^2-\alpha^2) - U''\right]\phi = \frac{1}{i\alpha G}\left[\left(D^4 - 2\alpha^2 D^2 + \alpha^4\right)\phi + 2\left(D\theta + \theta'\right)S\right], \tag{6.32}$$

$$(U-C)S - \theta'\phi = \frac{1}{i\alpha GPr}(D^2-\alpha^2)S, \tag{6.33}$$

where, $D = \dfrac{d}{d\eta}$ and $G = \sqrt{2}Gr_x^{1/4}$, where Gr_x is modified Grashof number given by $Gr_x = (g\gamma(T_w - T_0)^2 x^3)/\nu^2$.

The boundary conditions for the above disturbance equations in dimensionless forms are,

$$\text{At} \quad \eta = 0: \qquad \phi = \phi' = 0, \quad S = 0, \tag{6.34}$$

$$\text{At} \quad \eta \to \infty: \qquad \phi' = 0, \quad S = 0. \tag{6.35}$$

6.1.4 Base flow solutions

The governing coupled ordinary differential equations (ODEs) (6.11) and (6.12) for the base flows are solved using shooting method. In this method, the higher order ordinary differential equations are converted into set of first order differential equations. Fourth order Runge-Kutta method is used for the integration of differential equations.

The profile of base flow velocity (U) and temperature (θ) in η domain is shown in Fig. 6.2. From the Fig. 6.2(a), it can be seen that base flow velocity increases up to particular η value and then it continuously decreases until it reaches to 0 as η increases.

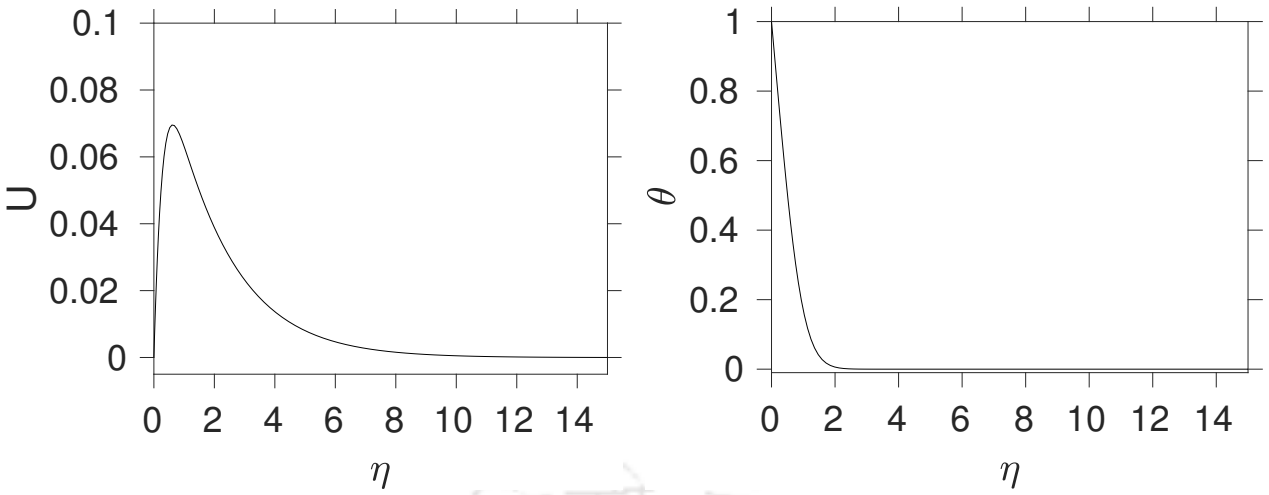

(a) Variation of U with η (b) Variation of θ with η

Figure 6.2: Base flow solutions : Dimensionless stream-wise velocity and temperature of free convection boundary layer flow

6.1.5 Temporal stability analysis

Solution methodology

The disturbance governing equations (6.32) and (6.33) along with boundary conditions (6.34) and (6.35) form an Eigenvalue problem. In temporal stability, we specify real value for α and find the corresponding C value as an Eigenvalue. The governing equations and boundary conditions are discretised using the Chebyshev spectral method and the Eigenvalue problem is formulated according to the details given in section 5.4.8. The Eigenvalue problem is written in the form:

$$A_{11}\phi + A_{12}S = C\left(B_{11}\phi + B_{12}S\right), \tag{6.36}$$

$$A_{21}\phi + A_{22}S = C\left(B_{21}\phi + B_{22}S\right), \tag{6.37}$$

where,

$$A_{11} = U\left(D^2 - \alpha^2\right) - U'' - \frac{1}{i\alpha G}\left(D^4 - 2\alpha^2 D^2 + \alpha^4\right),$$

$$A_{12} = \theta' + \theta D,$$

$$A_{21} = -\theta',$$

$$A_{22} = U - \frac{1}{i\alpha GPr}\left(D^2 - \alpha^2\right),$$

$$B_{11} = D^2 - \alpha^2,$$

$$B_{12} = 0,$$

$$B_{21} = 0,$$

$$B_{22} = I.$$

Validation

The code is validated by solving the temporal stability of natural convection boundary layer flow of water over a vertical isothermal flat plate. The disturbance for velocity and temperature at the wall and free stream are specified to be zero. The present results are compared with those of results by Nachtsheim [2]. The comparison of neutral curve of free convection flow from present study is compared with that of Nachtsheim [2] which is shown in Fig. 6.3. Figure shows that neutral curve from the present study almost overlap with reference study, and hence, the present code result matches well with the reference result.

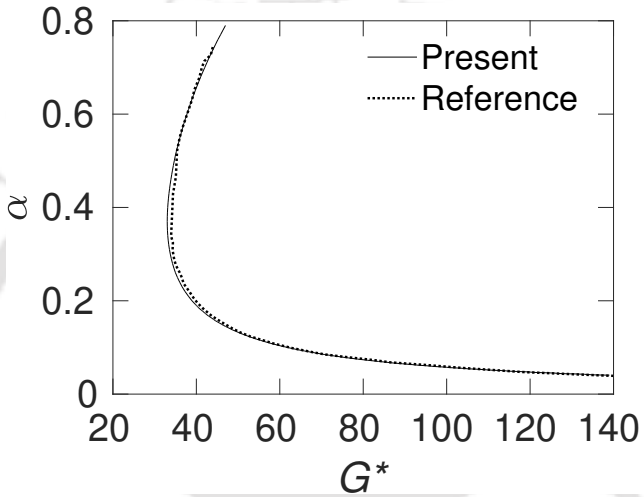

Figure 6.3: Comparison of neutral curves of free convection flows obtained from the present results with that of Nachtsheim [2] for water ($Pr = 6.7$)

Table 6.1 shows the quantitative comparison of real part of critical Eigenvalue of free convection flow from the present study with that of Nachtsheim [2] for parameters $G^* = 34$ ($G^* = 2\sqrt{2}Gr_{\mathrm{y}}^{1/4}$, where Gr_{y} is local Grashof number) and $\alpha = 0.45$. It can be seen from the table that the present result matches very well with that of reference result up to three decimal points.

Table 6.1: Comparison of real part of critical Eigenvalue of free convection flow from the present study with that of Nachtsheim [2] for parameter values of $G^* = 34$ and $\alpha = 0.45$ for water ($Pr = 6.7$)

	C_r
Present result	0.1555
Nachtsheim [2]	0.1556

Grid sensitivity tests for Eigenvalue spectrum

To check the sensitivity of results with respect to grid points, Eigenvalue spectrum of temporal stability of free convection flow is calculated using various sizes of grids which is shown in Fig. 6.4. From the figure it is clear that Eigenvalue spectrum for grid sizes more than 301, there is no consid-

erable change in the Eigenvalue spectrum. Hence, grid size of 301 is used for computation of natural convection boundary layer flows.

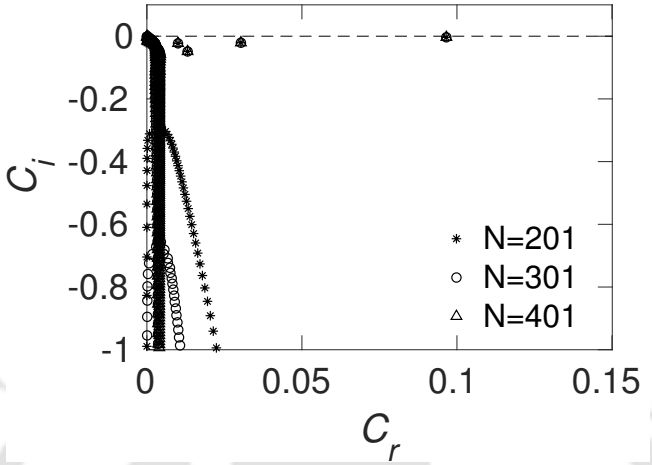

Figure 6.4: Effect of grid size on Eigenvalue spectrum ($G = 35$ and $\alpha = 0.5$)

Results and discussion

Temporal stability of natural convection boundary layer flow is solved for various combination of G and α values and obtained the corresponding $C = C_r + iC_i$. Fig. 6.5 shows typical Eigenvalue spectrum which is calculated for $\alpha = 0.5$ and $G = 35$. The spectrum consists of continuous branch (CS) and discrete Eigen modes (T_1, T_2, T_3, T_4). The continuous spectrum CS originates due to the extension of the domain to infinity in the free stream. The discrete modes originate from the fact that the flow is bounded by the wall. The discrete Eigenvalues have the non-zero circular frequency, and hence they are travelling modes. The travelling modes T_1, T_2, T_3 and T_4 are denoted in the order of decreasing C_i value. The discrete Eigenvalues which has maximum C_i value is the most unstable mode of the flow which decides the overall stability of the flow. In the above figure, T_1 mode decides the stability of the flow.

Fig. 6.6 shows the neutral curve, which separates the stable and unstable regions on the G-α plane. The critical buoyancy parameter (G_{cr}) value is the minimum value of G on the neutral curve below which all the disturbance decay exponentially and the flow is stable for all infinitesimal small disturbances. The G and α values corresponding to critical point is shown in table 6.2.

Table 6.2: Critical values of G, α, C and ω

G_{cr}	α_{cr}	C_{cr}	ω_{cr}
22.246	0.60623	$0.15667 + 0i$	0.09498

Fig. 6.7 shows the Eigenvalue spectrum corresponding to the critical point. Figure shows that real

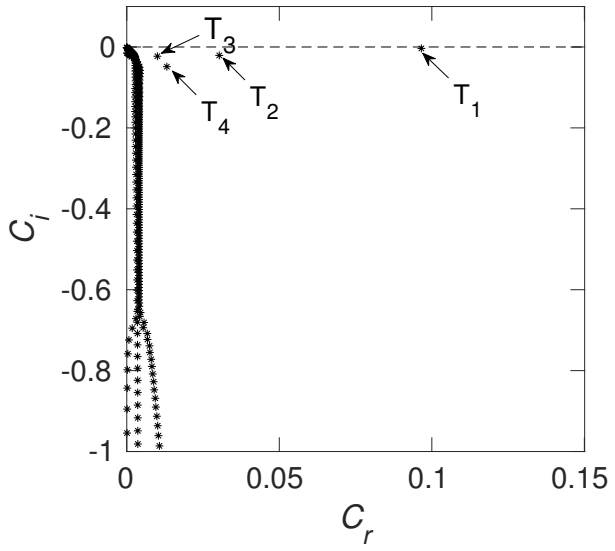

Figure 6.5: Eigenvalue spectrum for $G = 35$ and $\alpha = 0.5$

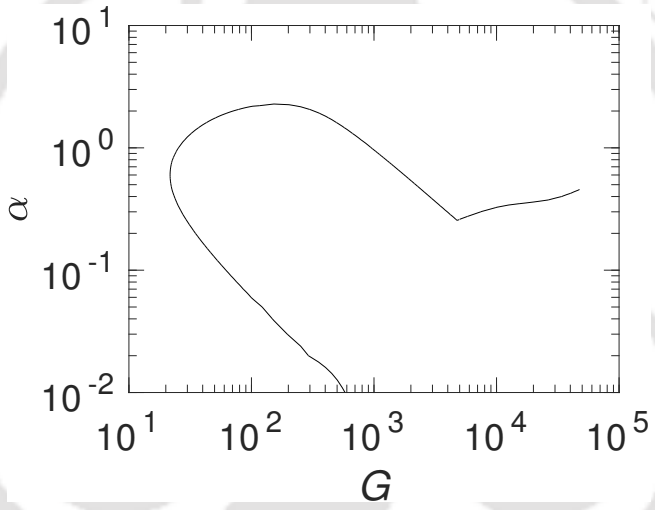

Figure 6.6: Neutral curve of natural convection boundary layer flows

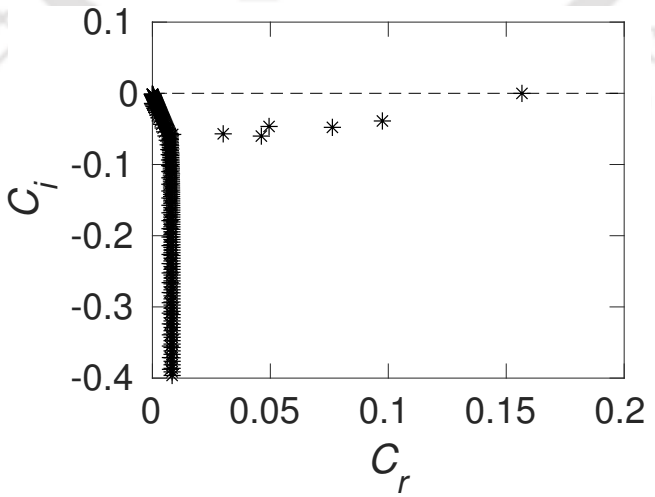

Figure 6.7: Eigenvalue spectrum at critical value $G_{cr} = 22.246$ and $\alpha = 0.6062$

part of lower modes are less than that of of the most unstable mode meaning, the lower modes travel with lower phase speeds than mode 1.

The Eigenvalues of three most unstable modes are presented in table 6.3. From the table we can see that the real C value of mode 1 is about 0.09 indicating that the disturbance of phase speed is larger than the maximum velocity inside the boundary layer. The maximum velocity inside the boundary layer is about 0.07 which can be seen from base flow velocity profile shown in Fig. 6.2(a). The phase speed of the mode 2 and 3 are about 38%, 69% of the phase speed of mode 1.

Table 6.3: Few most unstable Eigen modes of free convection boundary layer flows at critical values of G and α

Mode	Eigenvalue (C)	ω_r
Mode 1	$0.15667 + 0i$	0.09498
Mode 2	$0.09750 - 3.88554 \times 10^{-2}i$	0.05911
Mode 3	$0.04957 - 4.65671 \times 10^{-2}i$	0.03005

The real and imaginary parts of Eigenfunctions corresponding to critical G value is shown in Fig. 6.9(a) and 6.9(b) for stream function and temperature disturbances, respectively. From the velocity disturbance Eigenfunction, we can see that the maximum disturbance velocity is about at 0.65.

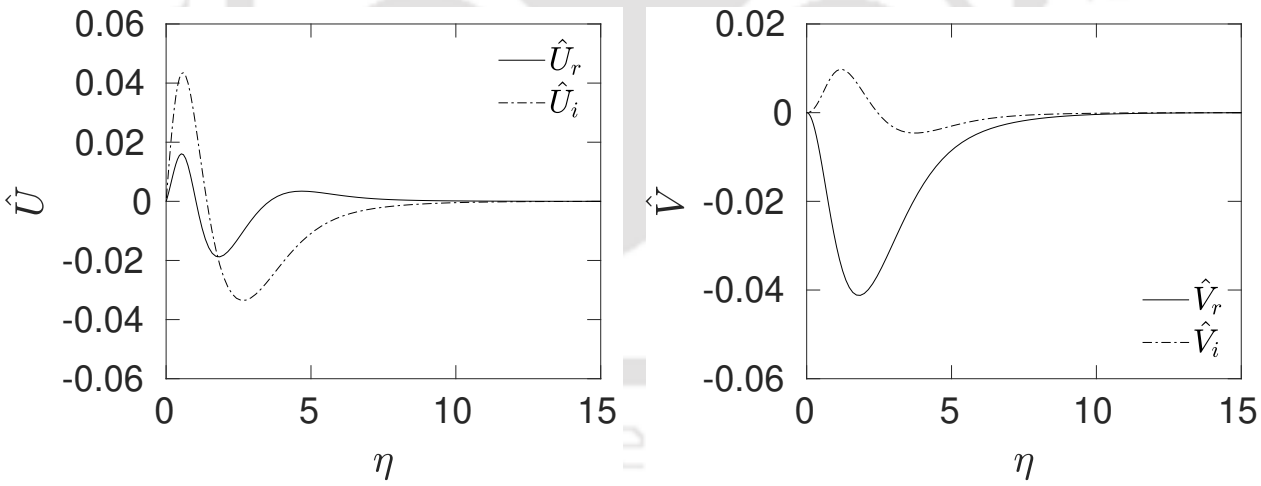

(a) $\hat{U}$ vs η (b) $\hat{V}$ vs η

Figure 6.8: Eigen functions of disturbance velocities for critical values of G and α

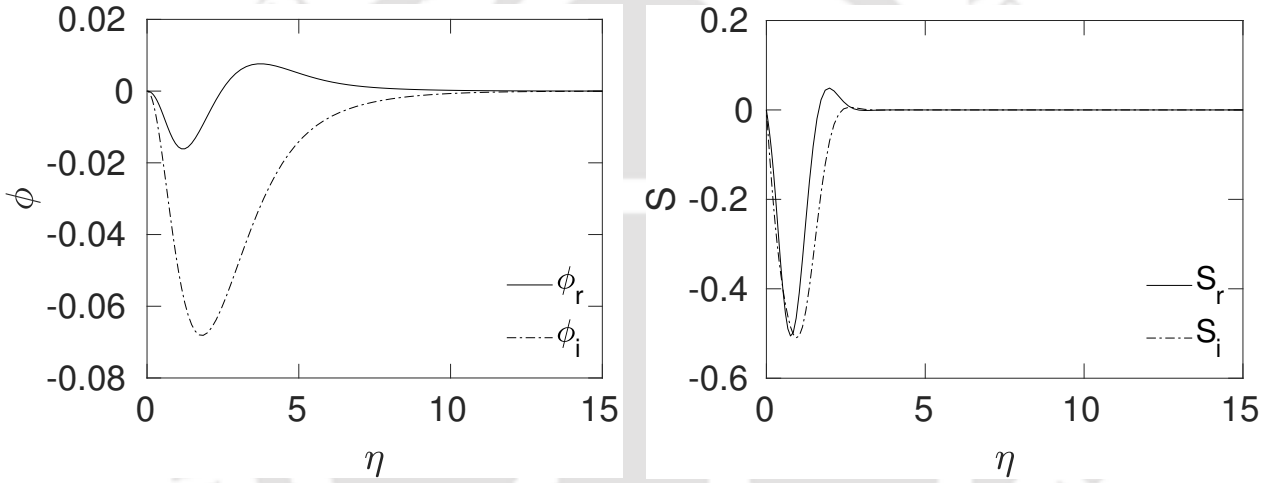

(a) ϕ vs η (b) S vs η

Figure 6.9: Eigen functions of disturbance stream function and temperature for critical values of G and α

6.1.6 Effect of plate inclination on temporal stability

The plate inclination can play a significant role on the stability of boundary layer flows as it changes the way, the gravitational force components interact with the flow. Hence, the effect of inclination is studied in this section. The physical system is same as that described before in section 6.1.1, except the plate is inclined in the inclination study. The inclination angle (Φ) is measured in the anticlockwise direction with respect to the vertically upward direction as shown in Fig. 6.10.

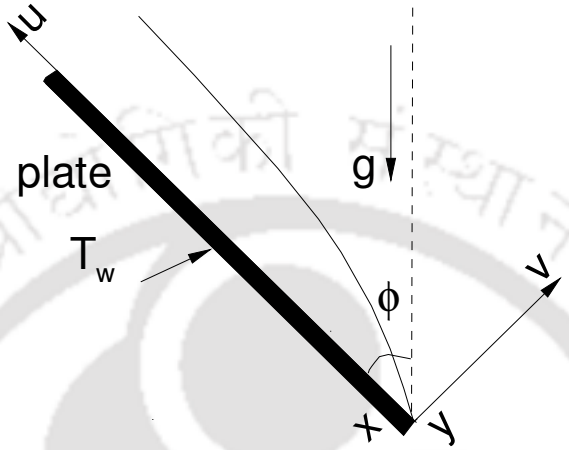

Figure 6.10: Free convection boundary layer flow with inclination effect

The governing equations of base flow and disturbance equations are same as that of vertical boundary layer flow except that the gravitational acceleration g is replaced with $g\cos\Phi$. Hence, the base flow and disturbance equations (Eqs. (6.11)–(6.12) and (6.32)–(6.33), respectively)) are modified to the following form to include the inclination effect.

$$f''' + \frac{3}{2}ff'' - \frac{1}{2}f'^2 + 2\theta^2\cos\Phi = 0 \tag{6.38}$$

$$\theta'' + \frac{3}{2}Prf\theta' = 0. \tag{6.39}$$

For the base flows, the boundary conditions are

$$\text{At } \eta = 0, \quad f = f' = 0, \quad \theta = 1, \tag{6.40}$$

$$\text{At } \eta \to \infty, \quad f' = 0, \quad \theta = 0. \tag{6.41}$$

The governing equations for disturbance equations including inclination effect become

$$\left[(U-C)(D^2-\alpha^2) - U''\right]\phi = \frac{1}{i\alpha G}\Bigg[\left(D^4 - 2\alpha^2D^2 + \alpha^4\right)\phi + 2\left\{(D - i\alpha\tan\Phi)\theta + \left(1 + \eta\frac{\tan\Phi}{G}\right)\theta'\right\}S\Bigg], \tag{6.42}$$

$$(U-C)S - \theta'\phi = \frac{1}{i\alpha GPr}(D^2-\alpha^2)S, \tag{6.43}$$

where, $D = \frac{d}{d\eta}$ and $G = \sqrt{2}Gr_x^{1/4}$, where Gr_x is modified Grashof number given by $Gr_x = (g\gamma(T_w - T_0)^2 x^3)/\nu^2$.

The boundary conditions for the above disturbance equations in dimensionless forms are,

$$\text{At} \quad \eta = 0: \qquad \phi = \phi' = 0, \quad S = 0, \tag{6.44}$$

$$\text{At} \quad \eta \to \infty: \qquad \phi' = 0, \quad S = 0. \tag{6.45}$$

It may be noted that the above governing equations for base flow and disturbance equations are valid for small inclination values. The above form of equations are used for the effect of inclination for $\Phi = 0^\circ$ to 17° in the study by Iyer and Kelly [65]. In the present study, the variation of inclination is limited in the range of -15° to 15° as the governing equations for base flow ((6.38)–(6.39)) and disturbances ((6.42)–(6.42)) are valid only in this inclination range.

The neutral curves for various plate inclinations are shown in Fig. 6.11. With increasing plate inclination, the region of unstable zone increases. This means that the range of wave numbers which are selectively amplified broadens with increasing inclination. Increasing the inclination causes neutral curves to move towards left side, resulting lower critical buoyancy parameter. With increasing plate inclination, the upper part of the neutral curve moves upwards. However, the lower part of neutral curve is not influenced significantly by the change in inclination angle. This implies that inclination has stronger effect on disturbances with larger wave numbers but has no effect on the dynamics of disturbances with smaller wave numbers.

The modification of Eigenvalue spectrum due to the variation of inclination is demonstrated in Fig. 6.12. The spectrum contains Eigenvalues for $\Phi = -15^\circ$, $\Phi = 0^\circ$ and $\Phi = 15^\circ$. The Eigenvalues move as the inclination is varied from -15° to 15°. For the intermediate inclinations, the respective Eigenvalues will be located between those of $\Phi = -15^\circ$ and $\Phi = 15^\circ$. The Eigenvalues move in the negative direction of the real axis with increasing inclination, causing the disturbance waves to move with lowered phase speeds.

The variation of critical buoyancy parameter with inclination is shown in Fig. 6.13. The critical buoyancy parameter decreases with inclination. The flow becomes unstable at lower buoyancy parameter as we tilt the plate in anticlockwise direction. The critical buoyancy parameter decreases by about 14% as the plate inclination is varied from 0° to 15°. When we change the inclination from 0 to -15°, the critical buoyancy parameter increases by 16%. This means tilting the plate in clockwise direction makes the flow more stable.

Fig. 6.14 shows the variation of critical wave number with inclinations. The critical modes have increased wave number with inclination. The critical wave number increases by about 14% when the plate inclination varies from 0° to 15°. When we tilt the plate in clockwise direction from 0 to -15°, the critical wave number decreases by about 13%. The critical values of buoyancy parameter, wave number and phase speed for various plate inclinations are presented in table 6.4. From the table, we can see that the critical frequency increases with plate inclination. We can also notice that the

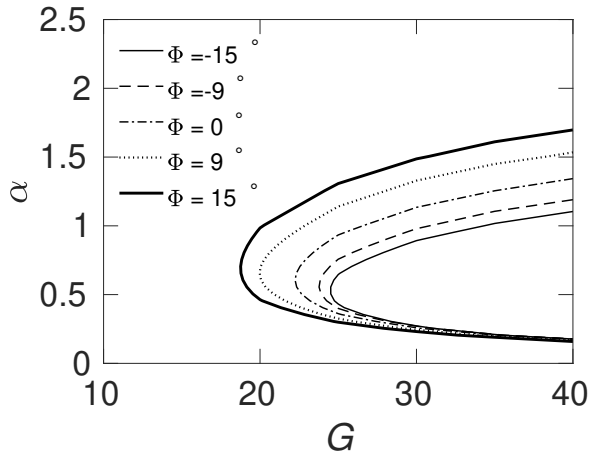

Figure 6.11: Neutral stability curves for various plate inclinations

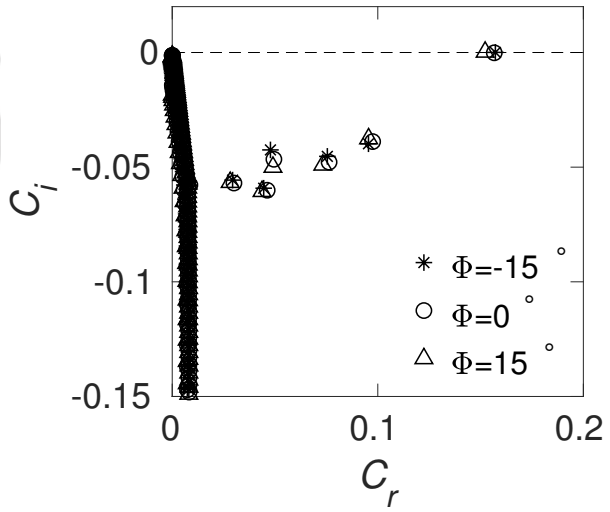

Figure 6.12: Eigenvalue spectrum at critical G value for various plate inclinations

Table 6.4: Critical values of G, ω, α and phase speed (C_r)

Φ	G_{cr}	α_{cr}	phase speed (C_{cr})	ω_{cr}
-15°	24.485	0.52828	$0.15221 + 0i$	0.08041
-12°	24.144	0.53331	$0.15326 + 0i$	0.08174
-9°	23.775	0.55523	$0.15437 + 0i$	0.08571
-6°	23.334	0.57410	$0.15535 + 0i$	0.08929
-3°	22.779	0.57799	$0.15573 + 0i$	0.09001
0°	22.246	0.60623	$0.15644 + 0i$	0.09396
3°	21.588	0.62752	$0.15573 + 0i$	0.09772
6°	20.828	0.63298	$0.15535 + 0i$	0.09133
9°	19.984	0.65546	$0.15437 + 0i$	0.10111
12°	19.410	0.67328	$0.15326 + 0i$	0.10312
15°	18.754	0.68320	$0.15221 + 0i$	0.10399

inclination has no significant effect on the phase speed of the disturbance.

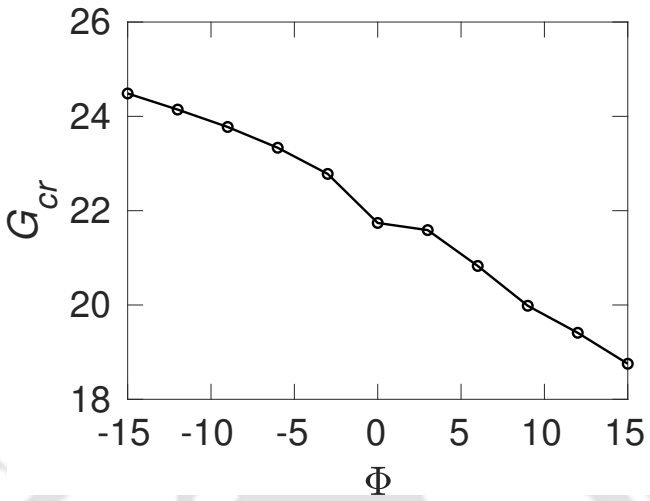

Figure 6.13: Variation of critical buoyancy parameter (G_{cr}) with plate inclination

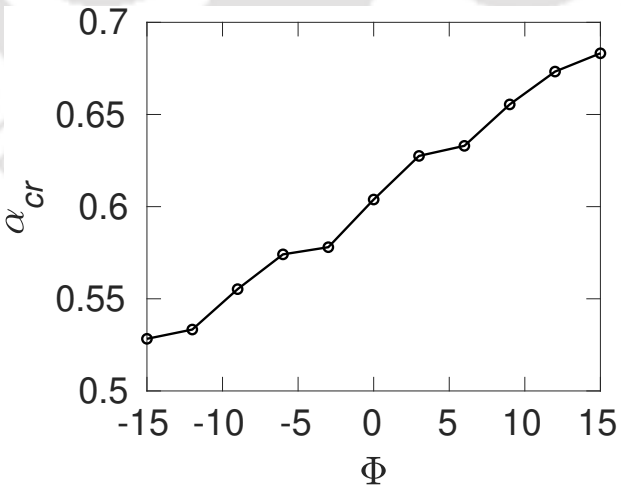

Figure 6.14: Variation of critical wave number with plate inclination

6.1.7 Spatial stability analysis

In spatial stability analysis, we study the disturbance growth or decay with space for a given temporal variation of disturbance at a given spatial location. In the present section, the results of spatial stability analysis are presented.

Numerical treatment

The disturbance governing equations for spatial stability analysis can be given in Eigenvalue form (as discussed in section 5.4.9),

$$\begin{bmatrix} 0 & I & 0 & 0 & 0 & 0 \\ 0 & 0 & I & 0 & 0 & 0 \\ 0 & 0 & 0 & I & 0 & 0 \\ -C_0 & -C_1 & -C_2 & -C_3 & -E_0 & -E_1 \\ 0 & 0 & 0 & 0 & 0 & I \\ -C_5 & -C_6 & -C_7 & -C_8 & -E_3 & -E_4 \end{bmatrix} \begin{bmatrix} \phi_1 \\ \phi_2 \\ \phi_3 \\ \phi_4 \\ S_1 \\ S_2 \end{bmatrix} = \alpha \begin{bmatrix} I & 0 & 0 & 0 & 0 & 0 \\ 0 & I & 0 & 0 & 0 & 0 \\ 0 & 0 & I & 0 & 0 & 0 \\ 0 & 0 & 0 & C_4 & 0 & E_2 \\ 0 & 0 & 0 & 0 & I & 0 \\ 0 & 0 & 0 & C_9 & 0 & E5 \end{bmatrix} \begin{bmatrix} \phi_1 \\ \phi_2 \\ \phi_3 \\ \phi_4 \\ S_1 \\ S_2 \end{bmatrix}, \tag{6.46}$$

where,

$$\begin{aligned} C_0 &= D^4 + i\omega G D^2, \\ C_1 &= i\omega G(U'' - UD^2), \\ C_2 &= -(2D^2 + i\omega G), \\ C_3 &= i\omega GU, \\ C_4 &= I, \\ C_5 &= -iGPr\theta', \\ C_6 &= 0, \\ C_7 &= 0, \\ C_8 &= 0, \\ C_9 &= 0, \\ E_0 &= 2\left(\theta D + \left[1 + \frac{\eta \tan\Phi}{2Re}\right]\theta'\right), \\ E_1 &= -2i\omega\theta \tan\Phi, \\ E_2 &= 0, \\ E_3 &= -(i\omega GPr + D^2), \\ E_4 &= iGPrU, \\ E_5 &= I. \end{aligned}$$

The above can be written in Eigenvalue form as,

$$A\phi = \alpha B\phi. \tag{6.47}$$

The above Eigenvalue problem matrix A and B are of size $6N \times 6N$. This is unlike the size of the Eigenvalue problem which comes from the temporal stability analysis. Hence, the spatial stability analysis is computationally more expensive compared with temporal stability analysis.

Grid sensitivity tests

The grid sensitivity tests are carried out for spatial stability analysis of free convection flow by solving governing equations in various grid sizes. The Eigenvalue spectrum for various grid sizes is shown in Fig. 6.15. From the figure, it can be seen that the results are insensitive to the grids for more than $N = 151$. Hence, grid size of $N = 151$ is used for the computation of neutral curves.

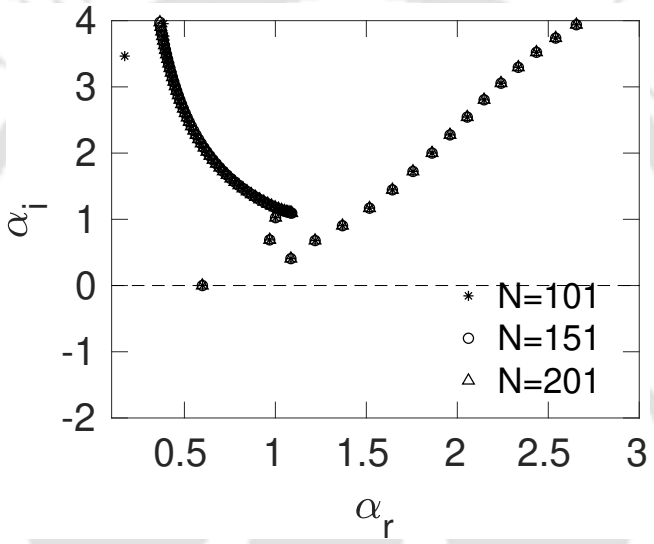

Figure 6.15: Grid sensitivity of spatial Eigenvalue spectrum ($G = 43.35$, $\omega = 0.055$)

Results of spatial stability analysis

Spatial stability analysis is carried out by solving various combinations of G and ω values, treating α as Eigenvalue. Fig. 6.16 shows the typical Eigenvalue spectrum for spatial stability of free convection flows. The spectrum contains continuous and discrete parts. The continuous spectrum originates from the infinite domain in free stream. The discrete spectrum comes from the stability dynamics inside the boundary layer. The Eigenvalue having lowest α_i represents the most unstable mode.

The neutral curve of spatial stability is shown in Fig. 6.19 which represents the division between unstable and stable zones on $G - \omega$ plane. The least value of G on the neutral curve is the critical G below which all the disturbances damp out. The obtained critical value and the corresponding α value are given in table. 6.5. It can be seen from the table that the critical value of G, ω and α from the spatial stability are same as the values obtained in the temporal stability analysis (table 6.2). This confirms that the present results from the spatial and temporal stability are aligned with the fact that the critical values from both the analysis should be same.

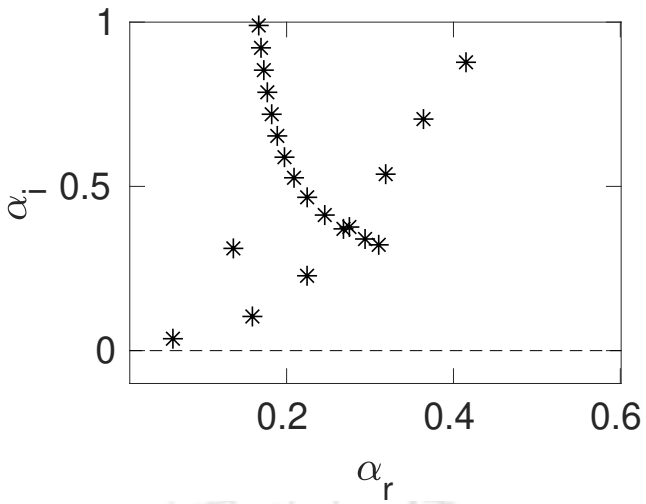

Figure 6.16: Typical Eigenvalue spectrum for $G = 10$ and $\omega = 0.01$

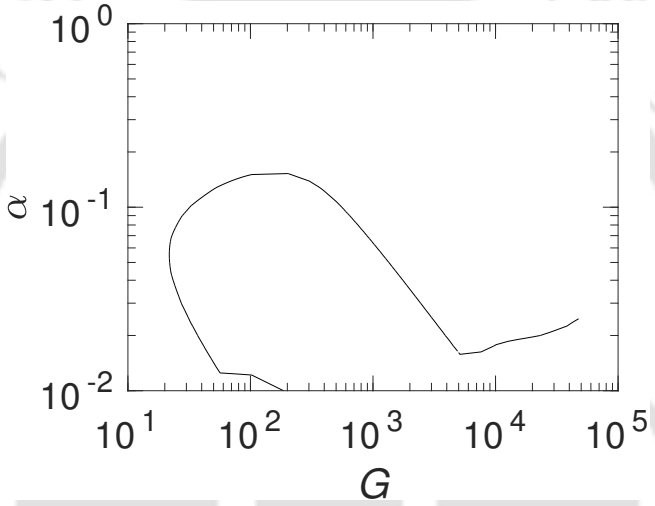

Figure 6.17: Spatial neutral stability curve

Table 6.5: Critical values of G, ω, α and phase speed (C_r)

G_{cr}	ω_{cr}	α_{cr}	phase speed (C_r)
22.843	0.09440	0.60431	0.15621

The Eigenvalue spectrum for critical value of buoyancy parameter G is shown in Fig. 6.18. The discrete Eigenvalues in the spectrum represent the disturbance dynamics at the locations which are in the downstream of the origin of disturbance. All the discrete Eigenvalues in the spectrum have positive real value, meaning that all the modes travel in the downstream direction. All the discrete Eigenvalues other than the critical Eigenvalue has α_r greater than that of the critical Eigenvalue. Higher the α_r, lower the phase speed. Hence, all the higher modes travel slower than the critical mode.

The Eigenvalues and corresponding phase speeds of the first three most unstable Eigen modes are presented in table 6.6. The first mode is the critical mode. The phase speeds of the second and third modes are about 0.552 and 0.492 times of the critical mode, respectively. This means that the higher modes travel with phase speed slower than the critical mode.

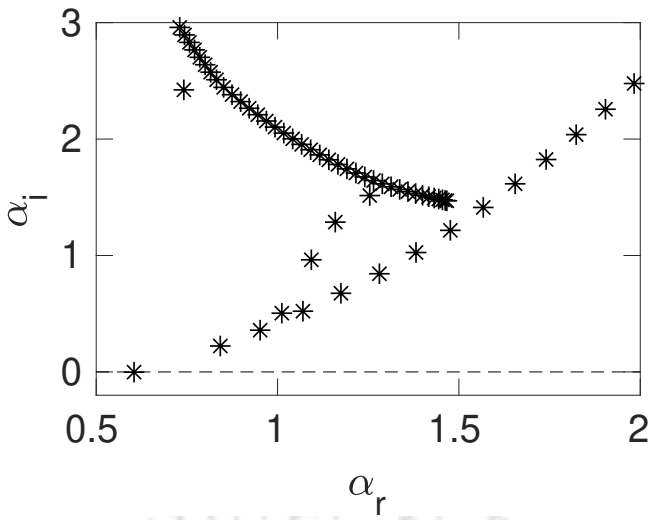

Figure 6.18: Eigenvalue spectrum at critical value ($G_{cr} = 43.35$ and $\omega = 0.055$)

Table 6.6: Few most unstable Eigenvalues at critical G value from the spatial stability analysis

Mode	Eigenvalue (α)	phase speed (C_r)
Mode 1	$0.60431 + 0i$	0.15621
Mode 2	$0.84214 + 0.22289i$	0.11210
Mode 3	$0.95193 + 0.35860i$	0.09917

6.1.8 Effect of plate inclination on spatial stability

The effect of plate inclination on spatial stability of free convection boundary layer flow is studied. The physical system (Fig. 6.10) and governing equations of base flow and disturbance (Eqs. (6.42)–(6.43)) presented for temporal stability analysis are same for spatial stability also. The spatial stability analysis is carried out for inclination in the range -15° to 15°.

Validation

To validate the solver for the computation of spatial stability of natural convection over inclined plate, the spatial stability of natural convection boundary layer flow over an inclined plate is solved, and the critical Eigenvalue of buoyancy parameter computed using the present code is compared with that of Tumin [84]. The values presented in table 6.7 are for $R = 100$, $\omega = 0.1$, $\Phi = 5^\circ$ and $Pr = 0.71$. Here, ω is circular frequency, Φ is the inclination angle, and R represents the strength of natural convection which is defined as $R = 2\sqrt{2}(g\beta\Delta T x^3/\nu)^{1/4}$. The present results match well with the reference results.

Table 6.7: Validation: The most unstable Eigenvalue (α) of spatial stability of free convection flows over inclined plate for $R = 100$, $\omega = 0.1$, $\Phi = 5^\circ$, $Pr = 0.71$

Present result	Tumin [84]	% deviation
$0.7305 - 0.03326i$	$0.7302 - 0.03326i$	$0.04 + 0i$

Results and discussion

Fig. 6.19 shows the spatial stability neutral curve for various plate inclinations. It can be observed from figure that neutral curve moving towards left side as the plate inclination increases. With increasing inclination, the unstable region broadens. The range of selectively amplified wave numbers increases with increasing inclination. With increasing inclination, the neutral curves deviate from that of zero inclination at the upper edge of the neutral curves. However, the neutral curves do not deviate much at the bottom edge. This means the inclination affects at higher wave numbers. At lower wave numbers, inclination effect is weaker.

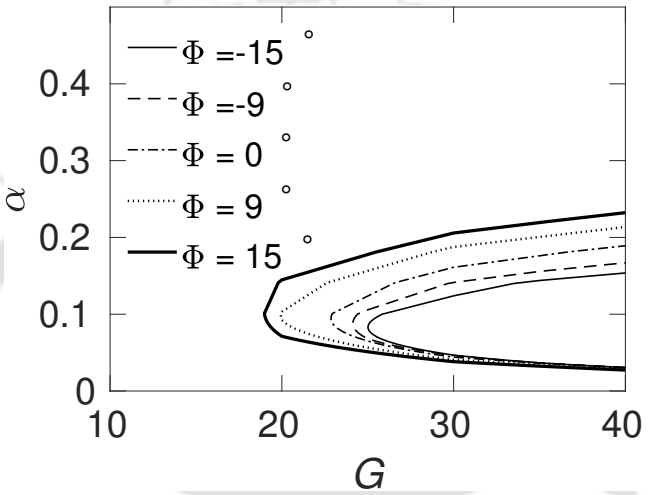

Figure 6.19: Neutral curves of spatial stability for various plate inclinations

Table 6.8: Critical values of G, ω, α and phase speed (C_r)

Φ	G_{cr}	ω_{cr}	α_{cr}	phase speed (C_r)
-15°	25.014	0.08370	0.53360	0.15686
-12°	24.597	0.08506	0.54236	0.15683
-9°	24.134	0.08796	0.56092	0.15681
-6°	23.551	0.09094	0.58047	0.15667
-3°	23.027	0.09303	0.59438	0.15651
0°	22.843	0.09440	0.60431	0.15621
3°	21.970	0.09699	0.62275	0.15574
6°	20.958	0.09934	0.64006	0.15521
9°	19.937	0.10097	0.65297	0.15463
12°	19.475	0.10629	0.69487	0.15296
15°	18.931	0.11443	0.75937	0.15070

The effect of plate inclination on critical value of buoyancy parameter (G_{cr}) is shown in Fig. 6.20. It can be seen from the figure that the value of G_{cr} decreases almost linearly as plate inclination increases. It means that the plate inclination destabilises the natural convection boundary layer flow. From this we can see that when the plate is tilted in clockwise direction (Φ varies from 0° to -15°), the flow becomes more stable and G_{cr} values increases by about 10%. When the plate is tilted in

anticlockwise direction (Φ varies from 0° to 15°), the flow becomes more unstable and G_{cr} decreases by about 18%. It means that the flow becomes unstable with anticlockwise tilting with faster rate compared to the rate of stabilisation with clockwise tilting. This is evident from the figure of G_{cr} versus inclination shown in Fig. 6.20; the magnitude of the slope of curve for negative inclination is less than that of positive inclinations.

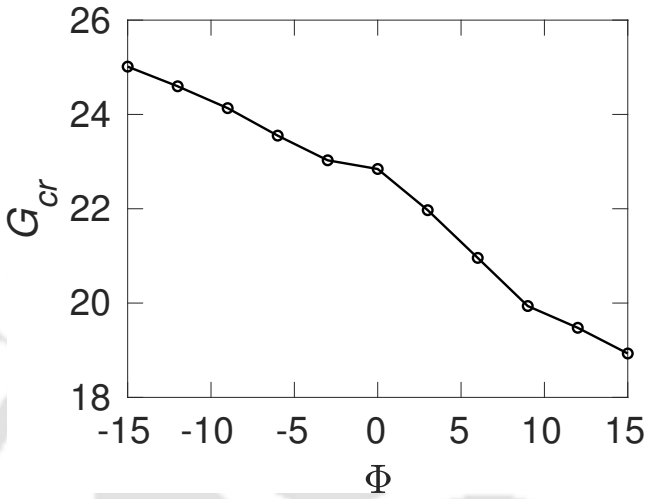

Figure 6.20: The effect of plate inclination (Φ) on G_{cr}

The variation of critical frequency (ω_{cr}) with plate inclination is shown in Fig. 6.21. The critical frequency increases with increasing inclinations. When the inclination is varied from -15° to 15°, ω_{cr} changes by about 40%. However, the phase speed is almost insensitive to the variation of inclination which can be seen from the values in table 6.8. That means, with increasing plate inclination, the disturbances have higher frequencies and higher wave numbers, still having travelling with almost same phase speed.

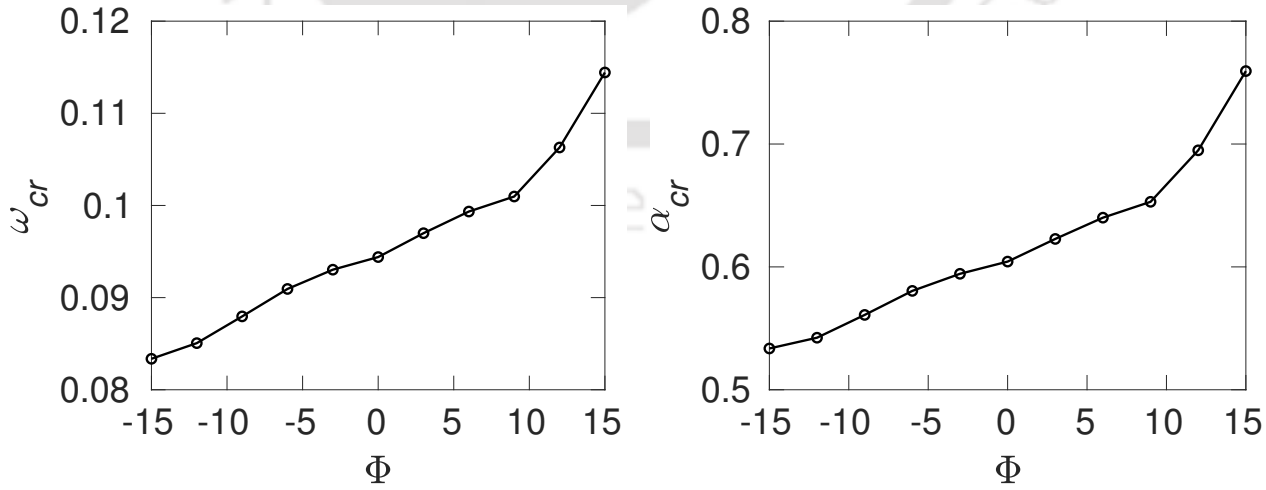

(a) ω_{cr} variation

(b) α_{cr} variation

Figure 6.21: The effect of plate inclination (Φ) on ω_{cr} and α_{cr}

6.2 Stability of natural convection over a plate of constant heat flux

The physical system consists of natural convection boundary layer flow over a vertical flat plate subjected to constant heat flux is shown in Fig. 6.22. The flow induced due to the heating of fluid layer adjacent to the plate sets the natural convection.

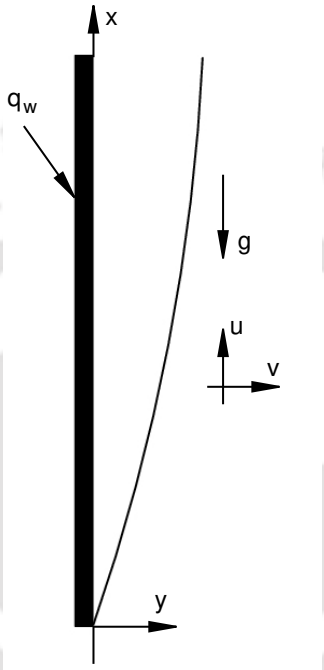

Figure 6.22: Schematic of natural convection boundary layer flow over heat flux specified plate

6.2.1 Governing equations

After applying the boundary layer approximations, the boundary layer equations are

$$\frac{\partial u}{\partial x} + \frac{\partial v}{\partial y} = 0, \tag{6.48}$$

$$u\frac{\partial u}{\partial x} + v\frac{\partial u}{\partial y} = \nu\frac{\partial^2 u}{\partial y^2} + g\gamma(T - T_0)^2, \tag{6.49}$$

$$u\frac{\partial T}{\partial x} + v\frac{\partial T}{\partial y} = \frac{k}{\rho c_p}\frac{\partial^2 T}{\partial y^2}. \tag{6.50}$$

No-slip and no penetration conditions are applied at the plate wall. The plate wall is specified with constant heat flux whereas the ambient temperature of fluid is T_0. The boundary conditions for base flow are

$$\text{At } y = 0, \qquad u = v = 0, \quad \frac{\partial T}{\partial y} = -\frac{q''_w}{k}, \tag{6.51}$$

$$\text{At } y \to \infty, \qquad u = 0, \quad T = T_0. \tag{6.52}$$

The above governing equations along with the boundary conditions admit similarity solutions. To convert the above partial differential equations into ordinary differential equations, the following similarity transformations are used.

$$\eta = \frac{y}{x}\left(\frac{Gr_x}{6}\right)^{1/6}, \quad U = \frac{\bar{u}}{u_{\text{ref}}} = f' = \frac{\bar{u}}{\nu/x}\left(\frac{Gr_x}{6}\right)^{1/6}, \quad \theta = 6\left(\frac{\bar{T}-\bar{T}_0}{q''_w x/k}\right)$$
$$Gr_x = \frac{g\gamma(q''_w x)^2 y^3}{k^2\nu^2}, \quad u_{\text{ref}} = \frac{\nu}{x\left(\frac{Gr_x}{6}\right)^{1/6}}. \tag{6.53}$$

With the above transformation, the governing equations (6.48)–(6.50) and boundary conditions (6.51)–(6.52) convert into the following form.

$$f''' + 5ff'' - 4f'^2 + \theta^2 = 0, \tag{6.54}$$
$$\theta'' + 5Prf\theta' - Prf'\theta = 0, \tag{6.55}$$

where, derivative of above variables are derivative with respect to dimensionless variable η, f is dimensionless stream function and θ is dimensionless temperature. The boundary conditions in terms of similarity variables are

$$\text{At } \eta = 0, \quad f = f' = 0, \quad \theta' = -1, \tag{6.56}$$
$$\text{At } \eta \to \infty, \quad f' = 0, \quad \theta = 0. \tag{6.57}$$

The above ordinary differential equations are solved using shooting method. Fourth order Runge-Kutta method is used for the numerical integration of the ODEs.

6.2.2 Disturbance equations

The disturbance equations derived for the natural convection boundary layer flows for constant temperature case is equally valid for constant heat flux also as the disturbance equations derived are independent of the boundary conditions. Hence, equations (6.28)–(6.29) are governing equations for disturbance for flux specified wall also, which are given by,

$$(\bar{u}-c)(\bar{\phi}'' - \bar{\alpha}^2\bar{\phi}) - \bar{u}''\bar{\phi} = \frac{\nu}{i\bar{\alpha}}\left(\bar{\phi}'''' - 2\bar{\alpha}^2\bar{\phi}'' + \bar{\alpha}^4\bar{\phi}\right) + \frac{2g\gamma}{i\bar{\alpha}}\left[(\bar{T}-\bar{T}_0)s' + s(\bar{T}-\bar{T}_0)'\right], \tag{6.58}$$
$$i\bar{\alpha}(\bar{u}-c)s - i\bar{\alpha}(\bar{T}-\bar{T}_0)'\,\bar{\phi} = \frac{k}{\rho c_p}\left(s'' - \bar{\alpha}^2 s\right). \tag{6.59}$$

Here, $c = \omega/\alpha$ is phase speed of disturbance.

The boundary conditions are,

$$\text{At } y = 0, \quad \hat{u} = \hat{v} = 0, \quad \hat{T}' = 0 \tag{6.60}$$
$$\text{At } y \to \infty, \quad \hat{u} = 0, \quad \hat{T} = 0. \tag{6.61}$$

The following dimensionless parameters are taken to convert the above dimensional form of equations into dimensionless forms,

$$\delta = \frac{x\,(6)^{1/6}}{Gr_x^{1/6}},\ \eta = \frac{y}{\delta},\ U_{\text{ref}} = \frac{\nu}{x}Gr_x^{1/6},\ \phi = \frac{\bar{\phi}}{U_{\text{ref}}\,\delta},\ S = \frac{s}{q_w'' y/k},\ C = \frac{c}{U_{\text{ref}}},\ \alpha = \bar{\alpha}\delta.$$

Using the above dimensionless parameters, the dimensionless form of disturbance governing equations for momentum and energy equations becomes,

$$\left[(U-C)(D^2-\alpha^2) - U''\right]\phi = \frac{1}{i\alpha G}\left[\left(D^4 - 2\alpha^2 D^2 + \alpha^4\right)\phi + 2\left(D\theta + \theta'\right)S\right], \tag{6.62}$$

$$(U-C)S - \theta'\phi = \frac{1}{i\alpha GPr}(D^2-\alpha^2)S, \tag{6.63}$$

where, $D = \dfrac{d}{d\eta}$ and $G = 6^{1/6}Gr_x^{1/6}$, where Gr_x is modified Grashof number given by $Gr_x = \dfrac{g\gamma(q_w'' y)^2 x^3}{k^2\nu^2}$.

The boundary conditions for the above disturbance equations in dimensionless forms are,

$$\text{At}\quad \eta = 0: \qquad \phi = \phi' = 0, \quad S' = 0, \tag{6.64}$$

$$\text{At}\quad \eta \to \infty: \qquad \phi' = 0, \quad S = 0. \tag{6.65}$$

6.2.3 Base flow solutions

The base flow solutions are found by solving Eqs. (6.54)-(6.55) along with boundary conditions (6.56)–(6.57). The equations are solved using shooting method. The integration of ODEs are carried out using fourth order Runge-Kutta method. The dimensionless velocity and temperature profiles obtained are shown in Fig. 6.23.

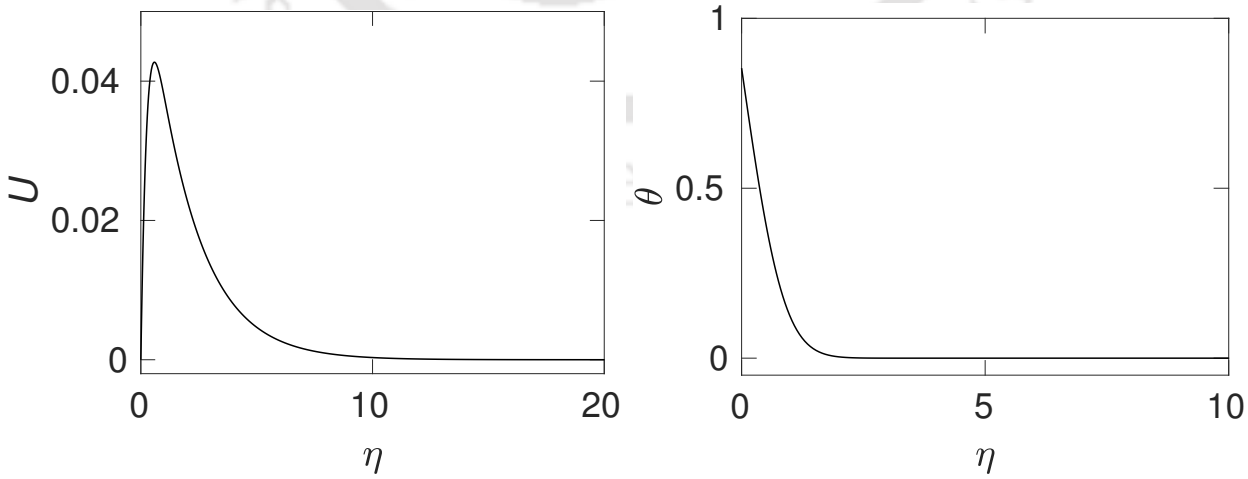

(a) Velocity profile (b) Temperature profile

Figure 6.23: Dimensionless velocity and temperature of base flow

6.2.4 Temporal stability analysis

Temporal stability analysis of the natural convection boundary layer flow for the case of flux specified wall is carried out. Fig. 6.24 shows the Eigenvalues spectrum for $G = 50$ and $\alpha = 0.5$. The Eigenvalue spectrum contains continuous and discrete parts. The Eigenvalue having highest imaginary value corresponds to most unstable mode. In the figure, the modes are marked with T_1, T_2, T_3 and T_4 in the sequence of decreasing imaginary value.

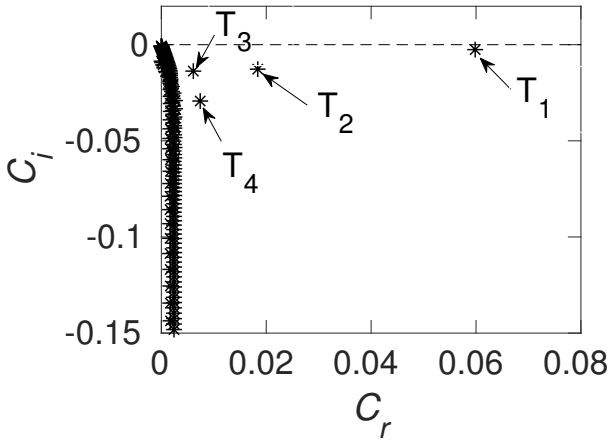

Figure 6.24: Typical Eigenvalue spectrum ($G = 50$ and $\alpha = 0.5$)

Neutral curve is shown in Fig. 6.25. The features of the neutral curve is similar to those of the neutral curve of plate of constant temperature. The critical values of buoyancy parameter, wave number are given in table. 6.9. The Eigenvalue spectrum corresponding to the critical buoyancy parameter (G_{cr}) is shown in Fig. 6.26. The Eigenvalues of first four modes corresponding to critical G value is given in table 6.10. From the table, we can see that the real part of first mode is larger than the remaining modes. This means the most unstable mode travels with phase speed greater than those of the lower modes. The phase speed of the second mode is about 62% of the most unstable mode. The imaginary part of the second and third Eigenvalues are approximately equal indicating these modes decay with almost equal rate with time.

Table 6.9: Critical values of G, α, ω and phase speed (C_r)

G_{cr}	α_{cr}	C_{cr}	ω_{cr}
75.481	0.63275	$0.05641 + 0i$	0.03569

The Eigen functions corresponding to the critical buoyancy parameter are shown in Fig. 6.27 and 6.28 for disturbance velocities $\hat{U}$ and $\hat{V}$, disturbance stream function and disturbance temperature, respectively.

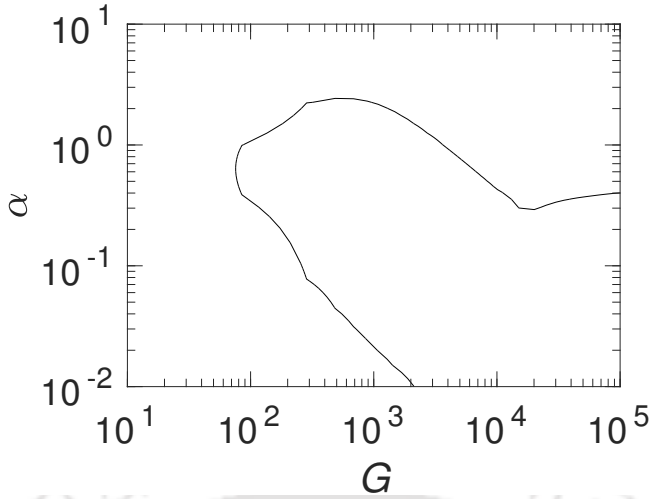

Figure 6.25: Neutral curve of natural convection boundary layer flows for isoflux wall

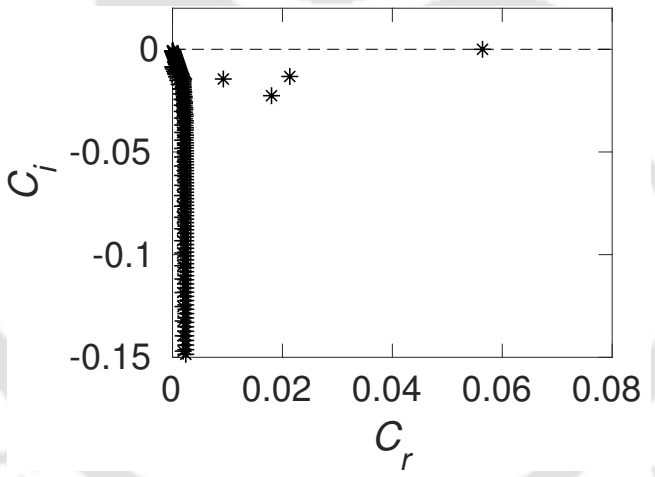

Figure 6.26: Eigenvalue spectrum at critical value $G_{cr} = 75.481$ and $\alpha = 0.63275$

Table 6.10: Few most unstable Eigen modes of free convection boundary layer flows at critical values of G and α

Mode	Eigenvalue (C)	ω_r
Mode 1	$0.05641 + 0i$	0.03569
Mode 2	$0.02134 - 1.32396 \times 10^{-2}i$	0.01351
Mode 3	$0.01808 - 2.28297 \times 10^{-2}i$	0.01144

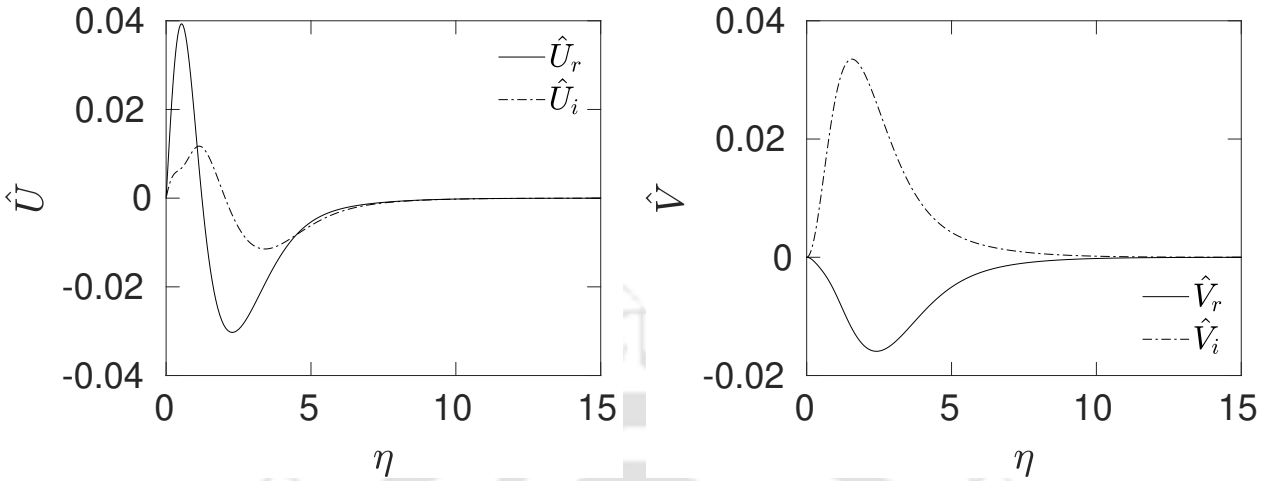

(a) $\hat{U}$ vs η (b) $\hat{V}$ vs η

Figure 6.27: Eigen functions of disturbance $\hat{U}$ and $\hat{V}$-velocity for critical values of G and α

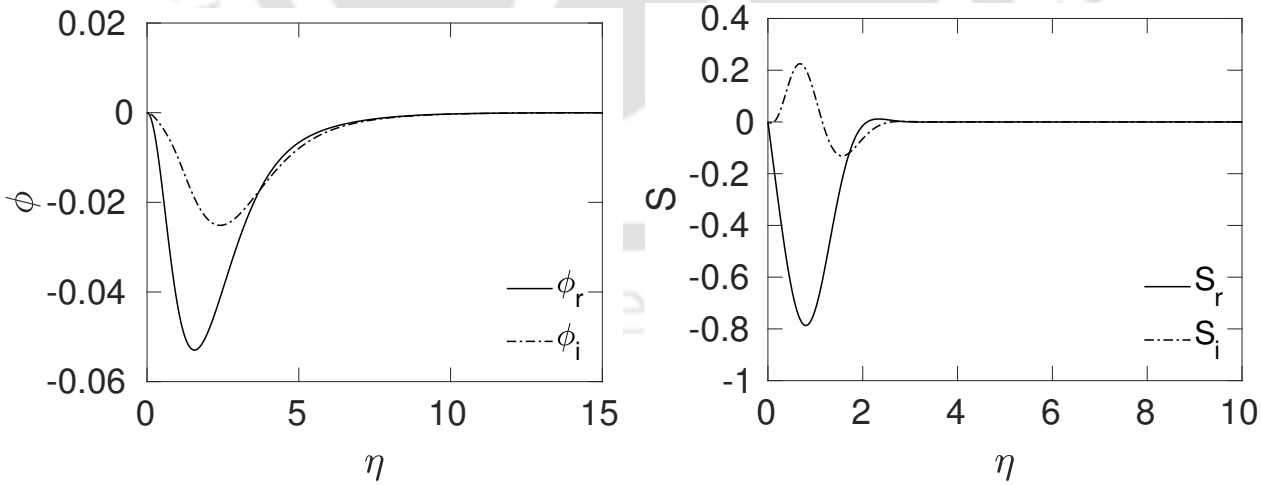

(a) ϕ vs η (b) S vs η

Figure 6.28: Eigen functions of disturbance stream function and temperature for critical values of G and α

6.2.5 Effect of plate inclination

The physical system is same as that described before in section 6.2, except the plate is inclined in the inclination study. The inclination angle (Φ) is measured in the anticlockwise direction with respect to the vertically upward direction as shown in Fig. 6.29.

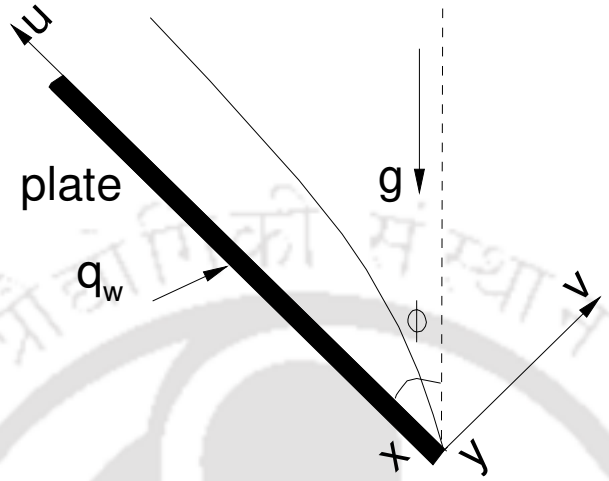

Figure 6.29: Schematic of natural convection boundary layer flows over an inclined plate specified with constant heat flux

The governing equations of base flow and disturbance equations are same as that of vertical boundary layer flow except that the gravitational acceleration g is replaced with $g\cos\Phi$. Hence, the base flow and disturbance equations (Eqs. (6.11)–(6.12) and (6.62)–(6.63), respectively)) are modified to the following form to include the inclination effect.

$$f''' + 5ff'' - 4f'^2 + \theta^2\cos\Phi = 0, \tag{6.66}$$

$$\theta'' + 5Prf\theta' - Prf'\theta = 0. \tag{6.67}$$

The boundary conditions are,

$$\text{At } \eta = 0, \quad f = f' = 0, \quad \theta' = -1, \tag{6.68}$$

$$\text{At } \eta \to \infty, \quad f' = 0, \quad \theta = 0. \tag{6.69}$$

$$\left[(U-C)(D^2-\alpha^2) - U''\right]\phi = \frac{1}{i\alpha G}\Bigg[\left(D^4 - 2\alpha^2D^2 + \alpha^4\right)\phi + 2\left\{(D - i\alpha\tan\Phi)\theta + \left(1 + \eta\frac{\tan\Phi}{G}\right)\theta'\right\}S\Bigg], \tag{6.70}$$

$$(U-C)S - \theta'\phi = \frac{1}{i\alpha GPr}(D^2-\alpha^2)S. \tag{6.71}$$

The boundary conditions for the above disturbance equations in dimensionless forms are,

$$\text{At} \quad \eta = 0: \qquad \phi = \phi' = 0, \quad S' = 0, \tag{6.72}$$

$$\text{At} \quad \eta \to \infty: \qquad \phi' = 0, \quad S = 0. \tag{6.73}$$

It may be noted that the above governing equations for base flow and disturbance equations are valid for small inclination values. Hence, in the study of inclination effect, the inclination angle is limited in the range -15° to 15°.

The neutral curves for various inclination angles for flux specified case is shown in Fig. 6.30. With increasing inclination, the region of selective wave number amplifications widens. For a given buoyancy parameter, the disturbances of wider wave number amplify at higher inclinations. The widening is broader at higher wave lengths than at the lower wave lengths. It may be noted, the widening of the selective amplification for the case of heat flux is larger than that correspond to temperature case. The critical buoyancy parameter value decreases with increasing inclination. The values of buoyancy parameter, wave number and phase speed at the critical value are presented in table. 6.11. The Eigenvalue spectrum for different inclinations are shown in Fig. 6.31. The variation of Gr_{cr} is shown in Fig. 6.32. The critical buoyancy parameter decreases linearly with increasing inclination. This implies that if we tilt the plate in clockwise direction, the convection becomes more stable, and if we tilt in the anticlockwise direction, the flow becomes more unstable. When we tilt the plate in clockwise direction, the critical G increases about 18%. When we tilt the plate in anticlockwise direction, the critical buoyancy parameter decreases by 18%.

The variation of critical wave number with inclination is shown in Fig. 6.33. The critical wave number decreases by about 13% when we tilt the plate in clockwise direction and increases by about 13% when we tilt the plate in anticlockwise direction. From the table 6.11, we can see that even though Gr_{cr} and α_{cr} vary with inclination, the phase speed of the critical disturbance is not affected by the inclination.

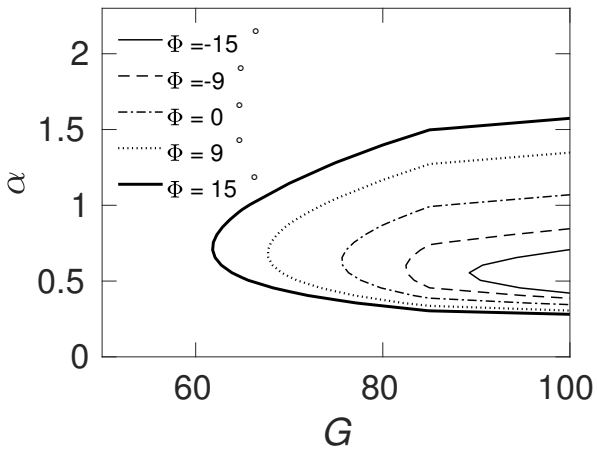

Figure 6.30: Neutral curve for various plate inclinations

Table 6.11: Critical values of G, ω, α and phase speed (C_r)

Φ	G_{cr}	α_{cr}	phase speed (C_r)	ω_{cr}
-15°	89.2568	0.55612	0.05768	0.03208
-12°	84.3979	0.56582	0.05764	0.03261
-9°	82.3840	0.57333	0.05736	0.03289
-6°	80.2417	0.59163	0.05695	0.03369
-3°	78.0593	0.60556	0.05684	0.03442
0°	75.4806	0.63275	0.05641	0.03564
3°	73.1139	0.65561	0.05620	0.03684
6°	70.4170	0.66445	0.05580	0.03708
9°	67.6627	0.68153	0.05562	0.03791
12°	64.7290	0.70610	0.05520	0.03898
15°	61.8055	0.72074	0.05519	0.03978

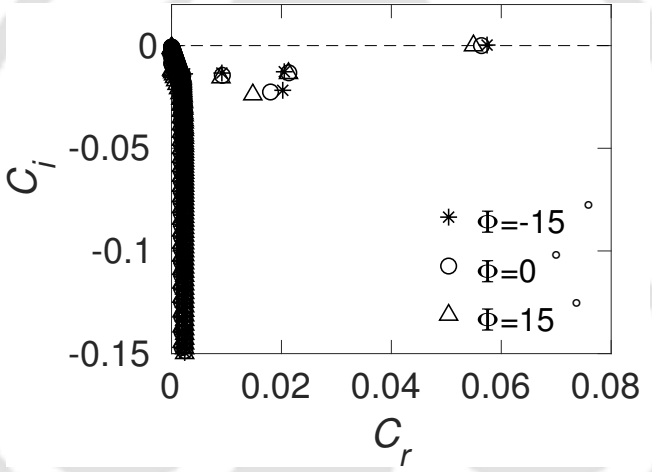

Figure 6.31: The Eigenvalue spectrum for various plate inclinations (Φ)

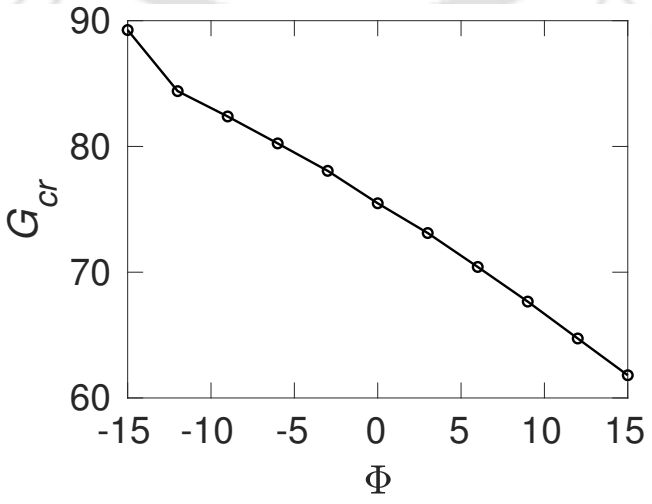

Figure 6.32: The effect of plate inclination (Φ) on critical buoyancy parameter (G_{cr})

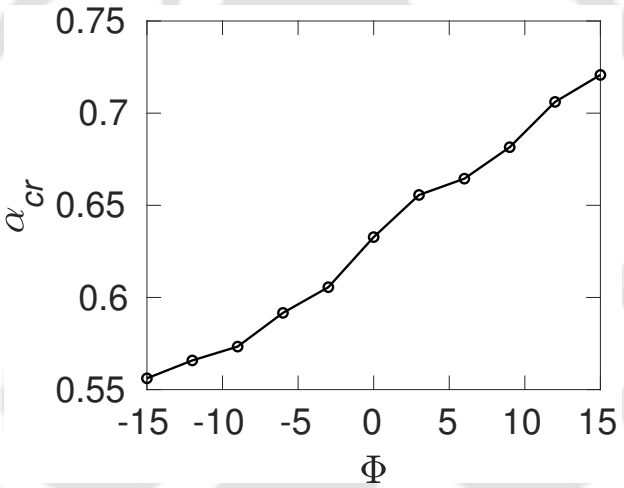

Figure 6.33: The effect of plate inclination (Φ) on critical wave number (α_{cr})

6.2.6 Spatial stability analysis

Spatial stability of natural convection over a flat plate with uniform flux is carried out. The typical Eigenvalue spectrum calculated at $G = 50$ and $\omega = 0.01$ is shown in Fig. 6.34. The structure of Eigenvalue spectrum for spatial stability of flux specified plate is similar to that of the temperature specified plate (shown in Fig. 6.26). The spectrum contains continuous and discrete parts. The most unstable Eigenvalue has the lowest real value, implying travelling with higher phase speed than those of lower modes.

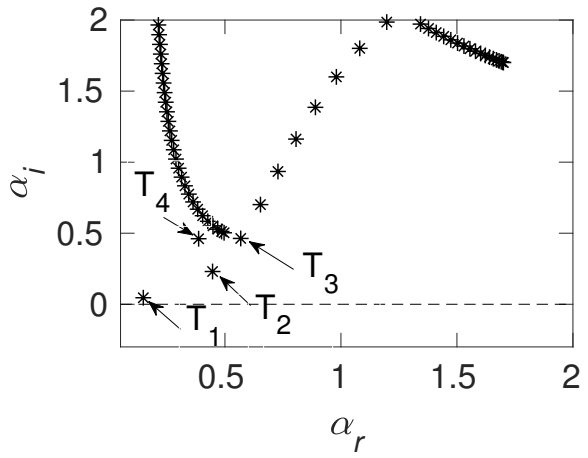

Figure 6.34: Typical Eigenvalue spectrum for $G = 50$ and $\omega = 0.01$

The neutral curve of the spatial stability is shown in Fig. 6.35. The critical values of buoyancy parameter, frequency, wave number and phase speed are presented in table 6.12. These results obtained from the spatial stability analysis match well with those obtained through temporal stability analysis (given in table 6.9). This matching is in line with the fact that both temporal and spatial stability analysis are expected to give same critical values.

The Eigenvalue spectrum at the critical value of buoyancy parameter is shown in Fig. 6.36. The Eigenvalues of first few most unstable modes are given in table 6.13. From the table, we can see that the most unstable mode travels with higher phase speed than the lower modes. The phase speed of the second mode is about 44% of the first mode. The second and third mode travel with approximately with same phase speed.

Table 6.12: Critical values of G, ω, α and phase speed (C_r)

G_{cr}	ω_{cr}	α_{cr}	phase speed (C_r)
75.8877	0.03683	0.65913	0.05587

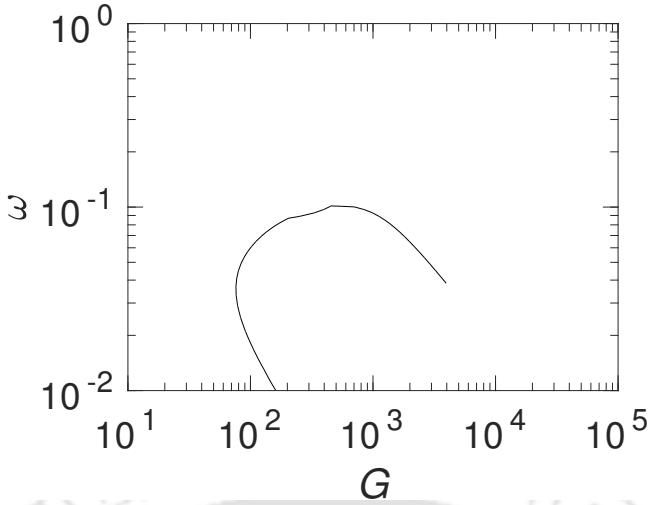

Figure 6.35: Neutral curve of spatial stability for flux specified flat plate

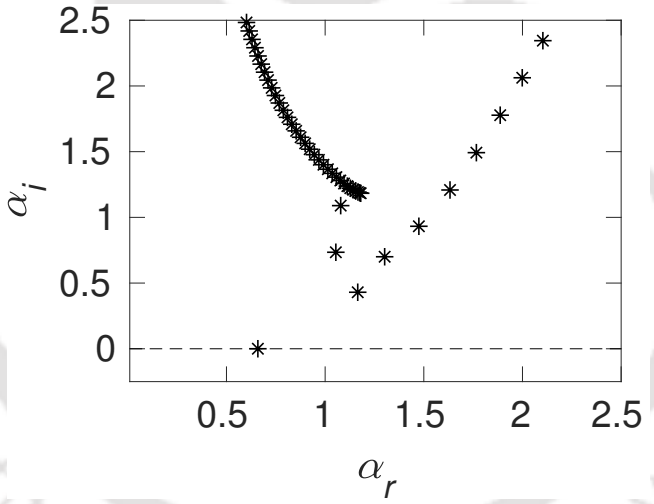

Figure 6.36: Eigenvalue spectrum at critical value $G_{cr} = 75.481$ and $\omega = 0.63275$

Table 6.13: Few most unstable Eigen modes of free convection boundary layer flows at critical values of G and ω

Mode	Eigenvalue (α)	phase speed (C_r)
Mode 1	$0.65913 + 0i$	0.95998
Mode 2	$1.16517 + 0.43015i$	0.54305
Mode 3	$1.30162 + 0.70026i$	0.48612

Effect of plate inclination

The effect of inclination on the stability is studied through spatial stability analysis. The stability is studied for inclinations in the range -15° to 15°. The neutral curves for various inclinations are shown in Fig. 6.37. With increasing inclination, the unstable zone of selective amplifications widens. The critical Eigenvalue spectrum for various inclinations is shown in Fig. 6.38

The critical values obtained through the spatial stability analysis are shown in table 6.14. These values from the spatial stability match well with those obtained through temporal stability analysis (shown in table 6.11). Since, the critical values obtained from the temporal and spatial stability analysis will be same, the conclusions made in the study of inclination through temporal stability discussed in section 6.2.5 are equally applicable to the results obtained through spatial stability given in the present subsection.

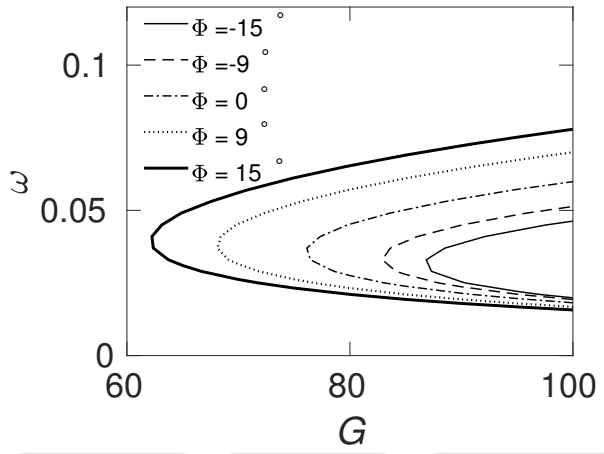

Figure 6.37: Neutral curve of spatial stability of free convection boundary layer flow

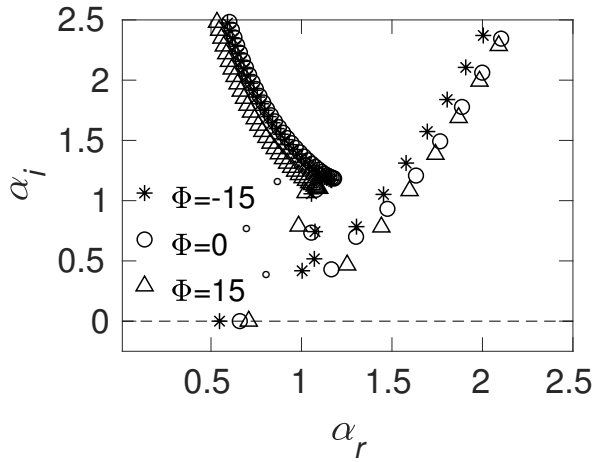

Figure 6.38: The Eigenvalue spectrum for various plate inclinations (Φ)

Table 6.14: Critical values of G, ω, α and phase speed (C_r)

Φ	G_{cr}	ω_{cr}	α_{cr}	phase speed (C_r)
-15°	86.6036	0.03155	0.54710	0.05767
-12°	84.4532	0.03209	0.55902	0.05741
-9°	82.9028	0.03292	0.57529	0.05722
-6°	80.7449	0.03342	0.58549	0.05708
-3°	77.9639	0.03395	0.59611	0.05695
0°	75.8877	0.03683	0.65913	0.05588
3°	72.5683	0.03690	0.65980	0.05593
6°	70.8307	0.03698	0.66215	0.05585
9°	68.1058	0.03750	0.67380	0.05565
12°	65.4632	0.03825	0.69109	0.05560
15°	62.0787	0.03901	0.70843	0.05507

6.3 Conclusions

In the present chapter, linear stability of natural convection boundary layers is studied for both isothermal and isoflux wall conditions. Both temporal and spatial stability analysis are carried out. The following conclusions are drawn.

1. The critical value of buoyancy parameter for natural convection over isothermal plate is found to be 22.84 and the corresponding wave number and circular frequencies are 0.604, and 0.0944, respectively. The critical value of buoyancy parameter for natural convection over isoflux plate is found to be 75.481 and the corresponding wave number, circular frequency and phase speed are obtained as 0.633, 0.056 and 0.036, respectively.

2. For both isothermal and isoflux plates at critical buoyancy parameter, the most unstable disturbance travels with phase speed higher than the lower modes.

3. For both isothermal and isoflux plates, when the plate is tilted in anticlockwise and clockwise directions, the convection becomes more unstable and more stable, respectively, compared to vertical orientation.

4. For isothermal plate, the critical buoyancy parameter decreases about 18% when we tilt 15° in anticlockwise direction, and increases about 10% when we tilt in clockwise direction compared to the value of vertical orientation.

5. For isoflux plate, the critical buoyancy parameter decreases about 18% when we tilt 15° in anticlockwise direction, and increases about 18% when we tilt in clockwise direction compared to the value of vertical orientation.

6. For both thermal conditions, critical wave number and critical frequency of the most unstable disturbance increases with inclination. However, the phase speed is not affected by the inclination.

7. The inclination has stronger effect at higher wave numbers. The instability at lower wave numbers are not affected by the inclination.

Chapter 7

Stability analysis of mixed convection boundary layer flows

In this chapter, the study of linear stability of mixed convection boundary layer of water flow with density inversion over a flat plate of uniform temperature is presented. Both temporal and spatial stability analysis are carried out. The study of inclination effect is also presented.

7.1 Physical system

The physical system consists of mixed convection boundary layer flow over a vertical flat plate heated at constant temperature T_w as shown in Fig. 7.1. The free stream temperature of water is T_0, where T_0 is the temperature corresponds to density maximum point near the density inversion. Temperature difference between the plate and fluids near the plate cause density difference which produces buoyancy forces due to gravity. The combined effect of free stream velocity and buoyancy forces leading to mixed convection boundary layer flow. The temperatures within the boundary layer and free-stream are considered in the temperature range in which density inversion of water is valid.

7.2 Mathematical modeling

The base flow is assumed to be steady, laminar and incompressible. The viscous dissipation and effect of radiation are negligible. The thermo-physical properties of the water are taken constant except for the density in buoyancy term. The variation of density with temperature is taken according to the parabolic profile given by Eq. (1.3)

$$\rho = \rho_0[1 - (T/T_0)^2],$$

where, ρ is the density of water and ρ_0 and T_0 are the density and temperature of maximum density point near the density inversion. Under the above assumptions, continuity, momentum and energy equations, respectively, can be written as

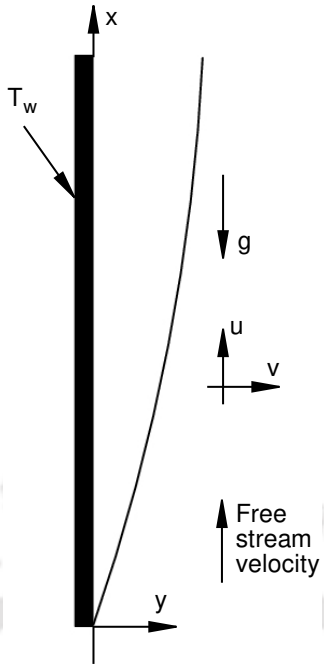

Figure 7.1: Schematic of mixed convection boundary layer over an isothermal plate

Continuity equation:

$$\frac{\partial u}{\partial x} + \frac{\partial v}{\partial y} = 0, \tag{7.1}$$

x-momentum equation:

$$\frac{\partial u}{\partial t} + u\frac{\partial u}{\partial x} + v\frac{\partial u}{\partial y} = -\frac{1}{\rho}\frac{\partial p}{\partial x} + \nu\left(\frac{\partial^2 u}{\partial x^2} + \frac{\partial^2 u}{\partial y^2}\right), \tag{7.2}$$

y-momentum equation:

$$\frac{\partial v}{\partial t} + u\frac{\partial v}{\partial x} + v\frac{\partial v}{\partial y} = -\frac{1}{\rho}\frac{\partial p}{\partial y} + \nu\left(\frac{\partial^2 v}{\partial x^2} + \frac{\partial^2 v}{\partial y^2}\right) + g\gamma(T - T_0)^2, \tag{7.3}$$

energy equation:

$$\frac{\partial T}{\partial t} + u\frac{\partial T}{\partial x} + v\frac{\partial T}{\partial y} = \frac{k}{\rho c_p}\left(\frac{\partial^2 T}{\partial x^2} + \frac{\partial^2 T}{\partial y^2}\right). \tag{7.4}$$

Under the boundary layer assumptions, the governing equations for base flow can be given as,

$$\frac{\partial \bar{u}}{\partial x} + \frac{\partial \bar{v}}{\partial y} = 0, \tag{7.5}$$

$$\bar{u}\frac{\partial \bar{u}}{\partial x} + \bar{v}\frac{\partial \bar{u}}{\partial y} = \nu\frac{\partial^2 \bar{u}}{\partial y^2} + g\gamma(\bar{T} - \bar{T}_0)^2, \tag{7.6}$$

$$\bar{u}\frac{\partial \bar{T}}{\partial x} + \bar{v}\frac{\partial \bar{T}}{\partial y} = \alpha\frac{\partial^2 \bar{T}}{\partial y^2}. \tag{7.7}$$

To convert the dimensional form of governing equations into their dimensionless form, the fol-

lowing dimensionless parameters are taken,

$$\delta = \sqrt{\frac{2\nu x}{u_\infty}}\frac{1}{(1+Ri)^{1/4}},\ U = \frac{\bar{u}}{u_c},\ V = \frac{\bar{v}}{u_c},\ \theta = \frac{\bar{T}-\bar{T}_0}{\Delta\bar{T}},\ \eta = \frac{y}{\delta},\ \omega = \frac{\bar{\omega}}{u_c/\delta},$$
$$\alpha = \bar{\alpha}\delta,\ \hat{U} = \frac{\hat{u}}{u_c},\ \hat{V} = \frac{\hat{v}}{u_c}, \phi = \frac{\bar{\phi}}{u_c\delta},\ S = \frac{s}{\Delta\bar{T}},\ u_c = u_\infty(1+Ri)^{1/2},\ C = \frac{\omega}{\alpha}, \tag{7.8}$$

where, $\Delta\bar{T} = \bar{T_W} - \bar{T_0}$.

It is important to note that the above choice of dimensionless variables provides a means to simulate the entire range of convection flows starting from pure forced convection to natural convection as Richardson number is varied from 0 to ∞. For forced convection, the appropriate scale for velocity for non-dimensionalisation is the free stream velocity, leading to dimensionless free stream velocity becoming one. For natural convection, the ambiance is taken to be stationary and hence, dimensionless velocity in the free stream should be zero. These requirements are fulfilled simultaneously by the above choice of scales for non-dimensionlisation of dimensionless variables, as the dimensionless velocity of forced and natural convection becomes one and zero for $Ri = 0$ and $Ri \to \infty$, respectively. Hence, the above formulation can represent the entire convection regime. The above choice of dimensionless variables are used in many studies such as Hunt and Wilks [147], Moresco and Healey [3]. Similar formulation of mixed convection which covers entire range of convection of forced, mixed and natural convection regimes is used by Lee et. al [148].

In the above, in the limit $Ri \to \infty$, the velocity scale u_c becomes as following,

$$u_c = u_\infty(1+Ri)^{1/2} \approx u_\infty Ri^{1/2} = u_\infty\left(\frac{Gr_x}{Re_x^2}\right)^{1/2} = u_\infty\frac{Gr_x^{1/2}}{Re_x} = u_\infty\frac{Gr_x^{1/2}}{u_\infty x/\nu}$$
$$u_c = \frac{\nu}{x}Gr_x^{1/2}. \tag{7.9}$$

Similarly, in the limit $Ri \to \infty$, the boundary layer thickness (δ) and Reynolds number (Re_δ) become as following.

$$\begin{aligned}
\delta = \sqrt{\frac{2\nu x}{u_\infty}}\frac{1}{(1+Ri)^{1/4}} &\approx \sqrt{\frac{2\nu x}{u_\infty}}\frac{1}{Ri^{1/4}},\\
&= \sqrt{\frac{2\nu x}{u_\infty}}\frac{1}{(Gr_x/Re_x)^{1/4}},\\
&= \sqrt{\frac{2\nu x}{u_\infty}}\frac{Re_x^{1/2}}{Gr_x^{1/4}},\\
&= \left(\frac{2\nu x}{u_\infty}\right)^{1/2}\left(\frac{u_\infty x}{\nu}\right)^{1/2}\frac{1}{Gr_x^{1/4}},\\
&= \frac{\sqrt{2}x}{Gr_x^{1/4}},\\
&= \frac{4^{1/4}x}{Gr_x^{1/4}},\\
\delta &= \frac{x}{(Gr_x/4)^{1/4}}.
\end{aligned}$$

$$Re_\delta = \frac{u_c \delta}{\nu} = \left(\frac{\nu}{x} Gr_x^{1/2} \frac{x}{(Gr_x/4)^{1/4}} \right) / \nu = \sqrt{2}\, Gr_x^{1/4}. \tag{7.10}$$

The above dimensionless variable formulations is identical to the dimensionless formulation used for natural convection given in section 6.1.2 (See Eq. (6.10). In the limit of $Ri \to \infty$, the expression of Reynolds number in the above formulation becomes equal to $\sqrt{2}Gr_x^{1/4}$, which represents governing buoyancy parameter of pure natural convection.

Using the above dimensionless parameters, the dimensionless form of governing equations for base flows are as follow,

$$\frac{\partial U}{\partial X} + \frac{\partial V}{\partial Y} = 0, \tag{7.11}$$

$$U\frac{\partial U}{\partial X} + V\frac{\partial U}{\partial Y} = \frac{1}{Re_x}\frac{\partial^2 U}{\partial Y^2} + Ri\theta^2, \tag{7.12}$$

$$U\frac{\partial \theta}{\partial X} + V\frac{\partial \theta}{\partial Y} = \frac{1}{Re_x Pr}\frac{\partial^2 \theta}{\partial Y^2}, \tag{7.13}$$

where, $Ri = Gr_x/Re_x^2$, $Gr_x = g\gamma(\Delta T)^2 x^3/\nu^2$, $Re_x = u_\infty x/\nu$ and $Pr = \nu/\alpha$. Gr_x is modified local Grashof number, Re_x is local Reynolds number, Pr is Prandtl number and Ri is modified Richardson number.

Adding infinitesimally small perturbations in base flow quantities and substituting the resultant quantities in Eqs. (7.1)–(7.4), the governing equations for combined base flow and disturbance variables are obtained. Then, the resultant governing equations are subtracted by the base flow governing equations to obtain the disturbance governing equations. By linearising the obtained disturbance equations, linearised form of disturbance equations are derived which are given by,

$$\frac{\partial \hat{u}}{\partial x} + \frac{\partial \hat{v}}{\partial y} = 0, \tag{7.14}$$

$$\frac{\partial \hat{u}}{\partial t} + \bar{u}\frac{\partial \hat{u}}{\partial x} + \hat{u}\frac{\partial \bar{u}}{\partial x} + \bar{v}\frac{\partial \hat{u}}{\partial y} + \hat{v}\frac{\partial \bar{u}}{\partial y} = \nu\frac{\partial^2 \hat{u}}{\partial y^2} + 2g\gamma(\bar{T} - T_0)\hat{T}, \tag{7.15}$$

$$\frac{\partial \hat{T}}{\partial t} + \bar{u}\frac{\partial \hat{T}}{\partial x} + \hat{u}\frac{\partial \bar{T}}{\partial x} + \bar{v}\frac{\partial \hat{T}}{\partial y} + \hat{v}\frac{\partial \bar{T}}{\partial y} = \frac{k}{\rho c_p}\frac{\partial^2 \hat{T}}{\partial y^2}. \tag{7.16}$$

Under the parallel flow assumptions, normal mode form of disturbance stream function ($\hat{\phi}$) and temperature ($\hat{T}$) are taken as

$$\hat{\phi}(x, y, t) = \bar{\phi}(y)e^{i(\bar{\alpha}x - \bar{\omega}t)}, \qquad \hat{T}(x, y, t) = s(y)e^{i(\bar{\alpha}x - \bar{\omega}t)}, \tag{7.17}$$

where, $\bar{\phi}$ and s are amplitude of disturbance stream function and temperature, respectively. $\bar{\alpha}$ is wave number and $\bar{\omega}$ is a frequency of disturbance.

Introducing disturbance stream function in the form,

$$\hat{u} = \frac{\partial \hat{\phi}}{\partial y}, \quad \hat{v} = -\frac{\partial \hat{\phi}}{\partial x}, \tag{7.18}$$

and utilising Eqs. (7.17)–(7.18) in Eqs. (7.15) and (7.16), the disturbance governing equations are obtained as

$$(\bar{u}-c)(\bar{\phi}''-\bar{\alpha}^2\bar{\phi})-\bar{u}''\bar{\phi}=\frac{\nu}{i\bar{\alpha}}\left(\bar{\phi}''''-2\bar{\alpha}^2\bar{\phi}''+\bar{\alpha}^4\bar{\phi}\right) + \frac{2g\gamma}{i\bar{\alpha}}\left[(\bar{T}-\bar{T}_0)s'+s(\bar{T}-\bar{T}_0)'\right], \tag{7.19}$$

$$i\bar{\alpha}(\bar{u}-c)s-i\bar{\alpha}(\bar{T}-\bar{T}_0)'\bar{\phi}=\frac{k}{\rho c_p}\left(s''-\bar{\alpha}^2 s\right). \tag{7.20}$$

Here, $c=\omega/\alpha$ is phase speed of disturbance.

The above dimensional form of governing equations for disturbance are converted into dimensionless form using dimensionless parameter (7.8), which are,

$$\left(U-\frac{\omega}{\alpha}\right)(\phi''-\alpha^2\phi)-U''\phi=\frac{1}{i\alpha Re_\delta}\left(\phi^{iv}-2\alpha^2\phi''+\alpha^4\phi\pm\frac{2Ri}{1+Ri}2\left[\theta' S+\theta S'\right]\right), \tag{7.21}$$

$$\left(U-\frac{\omega}{\alpha}\right)S-\theta'\phi=\frac{1}{i\alpha Re_\delta Pr}\left(S''-\alpha^2 S\right), \tag{7.22}$$

where, $Re_\delta=u_c\delta/\nu$.

7.2.1 Boundary conditions

Base flow: No slip and no penetration condition is applied on the wall. The wall is specified with constant temperature. The applied boundary conditions for base flow are as following

$$\text{At}\quad X=0,\quad U=1/(1+Ri)^{1/2},\quad V=0,\quad \theta=0, \tag{7.23}$$

$$\text{At}\quad Y=0,\quad U=0,\quad V=0,\quad \theta=1, \tag{7.24}$$

$$\text{At}\quad Y\to\infty,\quad U=1/(1+Ri)^{1/2},\quad V=0,\quad \theta=0. \tag{7.25}$$

Disturbance equation: The disturbance velocities in streamwise and cross-stream directions are zero at the plate and in the free stream. The disturbance temperature is zero at the wall and in the free stream.

$$\text{At}\quad \eta=0,\quad \phi=0,\quad \phi'=0,\quad S=0, \tag{7.26}$$

$$\text{At}\quad \eta\to\infty,\quad \phi=0,\quad \phi'=0,\quad S=0. \tag{7.27}$$

7.3 Base flow solutions

7.3.1 Solution Methodology

The governing equations of the base flow are solved by discretising governing equations using Finite Volume Method (FVM). Since, the steady state boundary layer equations are parabolic in streamwise

space coordinate, the equations are solved by marching from the leading edge. FVM with staggered grid is used. The Crank-Nicholson implicit scheme is used to discretise the derivatives along x-direction and second-order central difference is adopted for derivatives along y-direction. Tri-diagonal matrix algorithm (TDMA) is used to solve the linear equation obtained from discretisation. At a given space location, the simulation is continued until the error $max\left(|U^k - U^{k-1}|\right) < 10^{-8}$ criteria is satisfied, where k is the iteration number.

7.3.2 Validation

To validate the accuracy and correctness of developed code, mixed convection boundary layer flow over vertical wall is solved for various values of Richardson number for air. The vertical wall remains stationary while the free-stream is of uniform velocity. The plate is specified with uniform temperature. The study is carried out for both aiding and opposing mixed convection flows. The solutions are obtained for the velocity profiles of base flow for various Richardson number and compared the velocity profile with those of Moresco and Healey [3] which are shown in Fig. 7.2. The present profiles almost overlap with those of reference results for all given values of Richardson number.

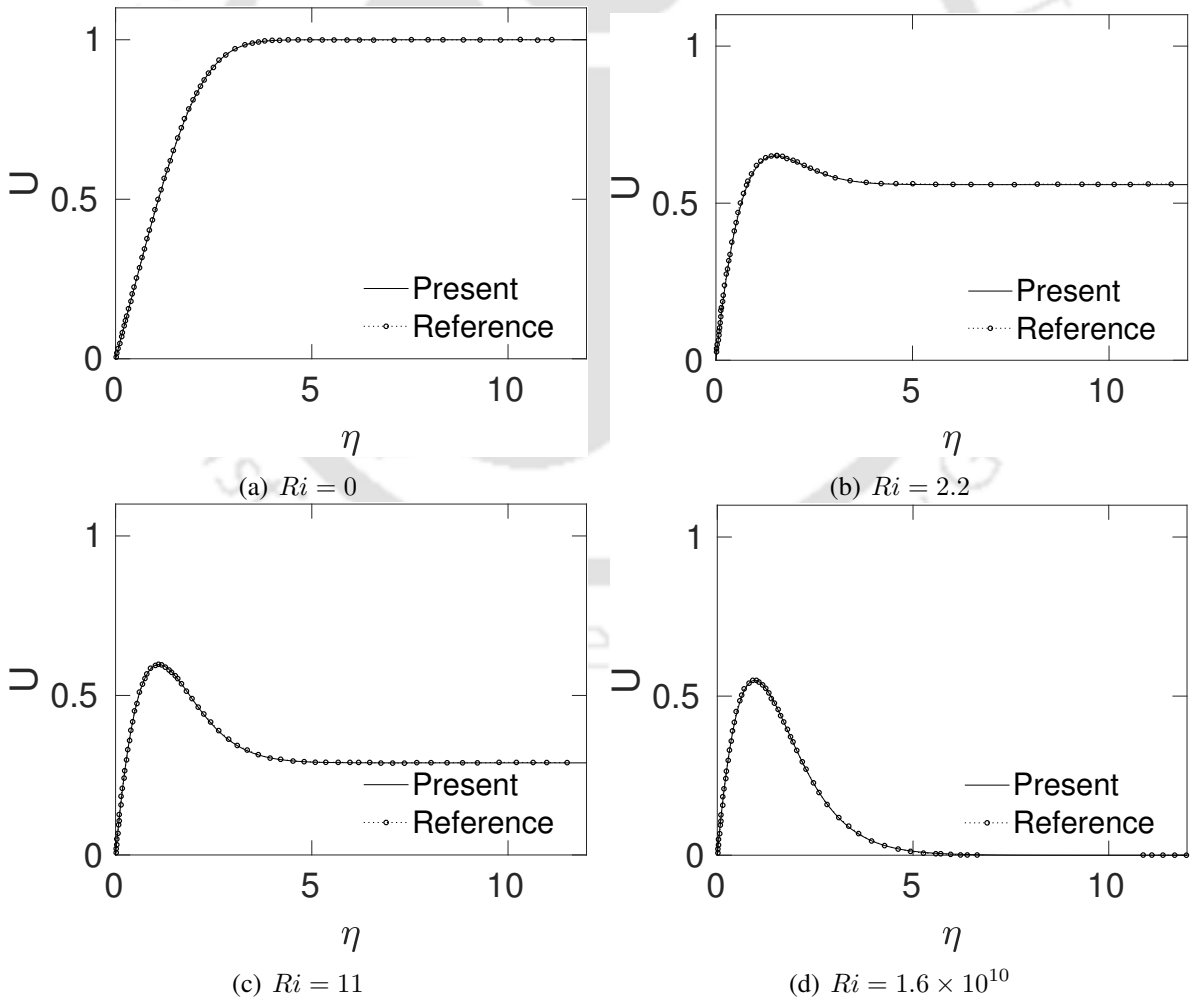

(a) $Ri = 0$ (b) $Ri = 2.2$

(c) $Ri = 11$ (d) $Ri = 1.6 \times 10^{10}$

Figure 7.2: Comparison of the variation of dimensionless velocity (U) with η for various Richardson number from present results with those of Moresco and Healey [3]

7.3.3 Base flow velocity and temperature profiles

The base flow solutions of mixed convection boundary layer flows are calculated by solving system of coupled equations (7.11)–(7.13) along with boundary conditions (7.23)–(7.25). By solving these equations, dimensionless velocity and temperature profiles are obtained. The variation of dimensionless streamwise velocity and temperature with η is shown in Fig. 7.3(a) and 7.3(b), respectively. In the figures, velocity and temperature profiles corresponding to $Ri = 0$ refers to forced convection flow. The profiles for large Richardson number ($Ri = 10^{15}$) correspond to the natural convection asymptote.

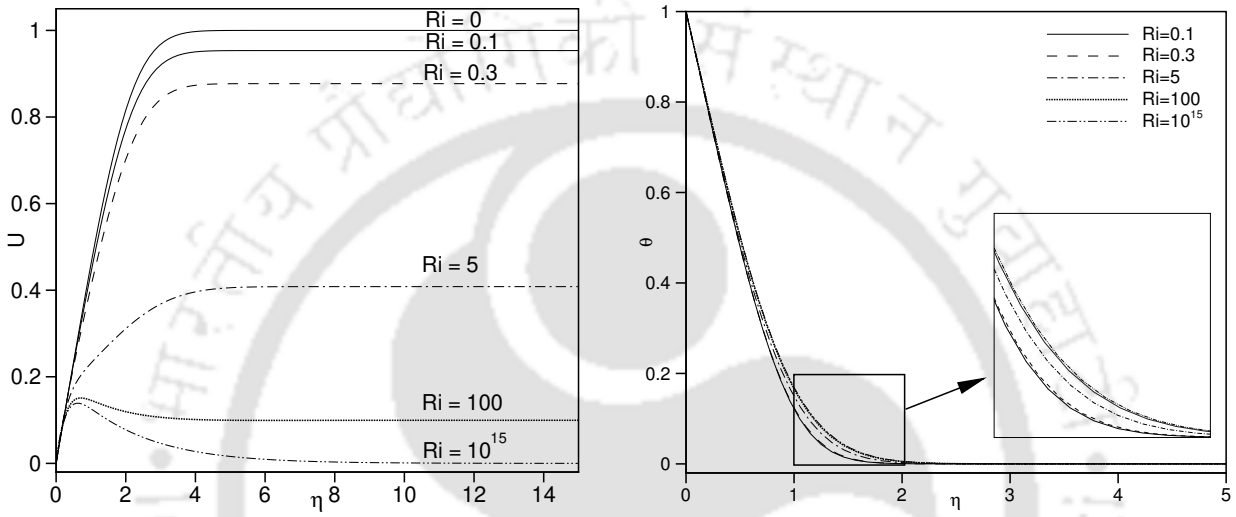

(a) Streamwise velocity profile

(b) Temperature profile

Figure 7.3: Base flow solutions of mixed convection flow boundary layer flow with density inversion of water for various Ri values

7.4 Temporal stability analysis

7.4.1 Solution methodology

In temporal stability analysis, the value of wave number α is specified and the phase speed C is found as an Eigenvalue. The disturbance governing equations (7.21) and (7.22) and the boundary conditions (7.26) and (7.27) can be arranged into following Eigenvalue problem form, (as discussed in section 5.4.8)

$$A_{11}\phi + A_{12}S = C\left(B_{11}\phi + B_{12}S\right),$$
$$A_{21}\phi + A_{22}S = C\left(B_{21}\phi + B_{22}S\right),$$

where, the coefficient matrices of the above equations are,

$$A_{11} = U\left(D^2 - \alpha^2\right) - U'' - \frac{1}{i\alpha Re_\delta}\left(D^4 - 2\alpha^2 D^2 + \alpha^4\right),$$

$$A_{12} = \pm\frac{2Ri}{1+Ri}2\left(\theta' + \theta D\right),$$
$$A_{21} = -\theta',$$
$$A_{22} = U - \frac{1}{i\alpha Re_\delta Pr}\left(D^2 - \alpha^2\right),$$
$$B_{11} = D^2 - \alpha^2,$$
$$B_{12} = 0,$$
$$B_{21} = 0,$$
$$B_{22} = I.$$

7.4.2 Validation

The stability solver is validated by solving the temporal stability of mixed convection boundary layer flow over an isothermal vertical flat plate for air. The neutral curves of mixed convection are calculated for aiding and opposing flows for various values of Richardson number. The comparison of neutral curves obtained from the present study for various Ri values with those of Moresco and Healey [3] is presented in Fig. 7.4, for aiding and opposing flow situations. From the comparison, it is evident that the present results match closely with reference results.

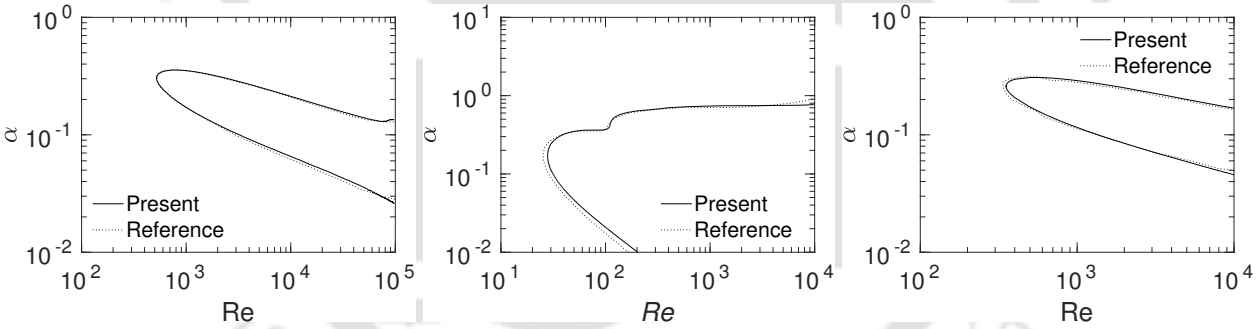

(a) $Ri = 0$ (Aiding flow) (b) $Ri = 11$ (Aiding flow) (c) $Ri = 0.014$ (Opposing flow)

Figure 7.4: Comparison of temporal neutral curves for various Ri values for aiding and opposing flows with those of Moresco and Healey [3].

7.4.3 Grid sensitivity tests

To find grid independent results, grid sensitivity tests are carried out. The Eigenvalue spectrum is calculated using different grid sizes which is shown in Fig. 7.5. From the figure, it can be observed that Eigenvalue spectrum contains continuous branch of Eigenvalues as well as discrete Eigenvalue points. The discrete Eigenvalues coincide with each other for all the grid points while the continuous branch of Eigenvalue merge with vertical Eigenvalue spectrum for higher grid points. Since, only discrete Eigenvalues contribute to growth of the disturbances, hence, $N = 301$ is chosen to study the stability of mixed convection flow as the Eigenvalue spectrum do not have significant change when grid is varied from 301 to 401 grid points.

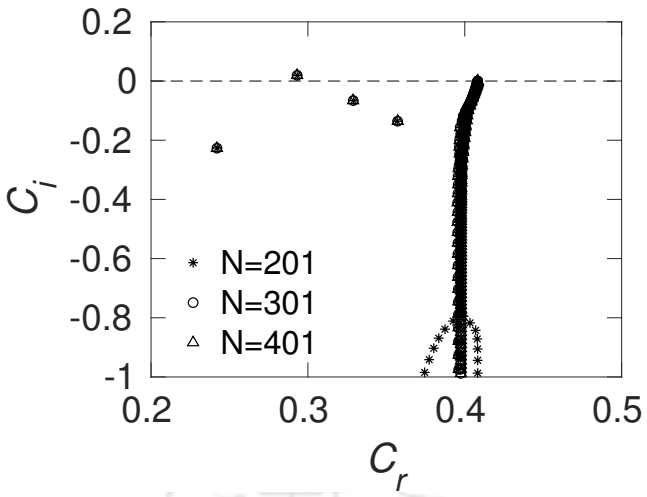

Figure 7.5: Grid sensitivity of temporal Eigenvalue spectrum ($Ri = 5$, $Re = 80$, $\alpha = 0.1$)

7.4.4 Results and discussion

In temporal study, we specify value of α for a given combination of Re_δ and Ri and find phase speed C as an Eigenvalue of the problem. The Eigenvalue with maximum value of C_i represents the most unstable Eigenvalue, which decides temporal stability of the convection flow. If C_i of the most unstable Eigenvalue is positive, the flow is unstable.

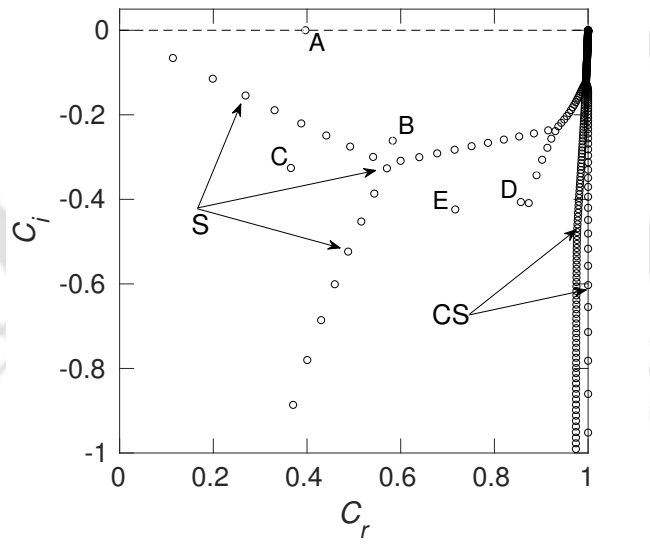

Figure 7.6: Typical Eigenvalue spectrum and different Eigen modes ($Ri = 0$, $Re_\delta = 429.4$, $\alpha = 0.25$)

Fig. 7.6 shows the Eigenvalue spectrum for $Ri = 0$ (forced convection asymptote). The circle symbols in the spectrum are the Eigenvalues from the combination of flow and heat transfer stability equations. Eigenvalue spectrum contains continuous spectrum and discrete part of the spectrum. In the figure, the continuous spectrum which is marked with 'CS', is the part of the spectrum which is originated due to the infinite range of the domain length in the free stream. The location of continuous branch of Eigenvalue spectrum depends on the value of Richardson number, which can be found using asymptotic method which is described in Schmid and Henningson [4]. The spectrum branch which is

marked with 'S' is discrete branch. The Eigenvalues denoted with A, B, C, D and E are also discrete part of the Eigenvalue spectrum. This part of the spectrum is originated due to the presence of wall.

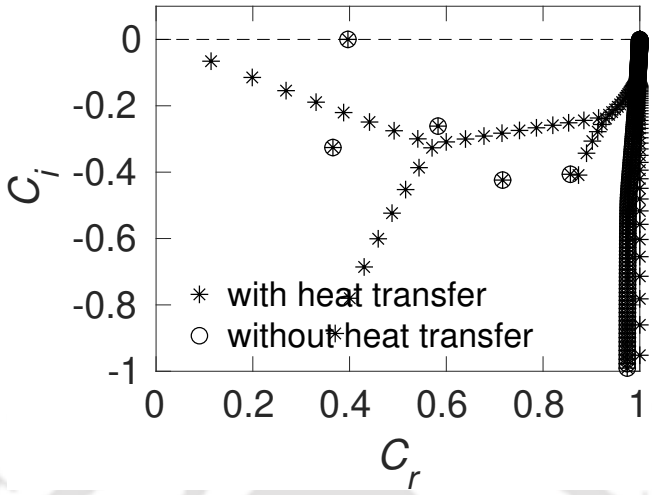

Figure 7.7: Eigenvalue spectrum ($Ri = 0$, $Re_\delta = 429.40$, $\alpha = 0.25$)

To find out the origin of discrete spectrum denoted by A, B, C, D and E, the temporal Eigenvalues for flow without heat transfer (Blasius flow) are computed and plotted with star symbols in the figure. The branch which is marked with 'S' is not present in pure fluid flow; but is present in the spectrum including heat transfer. This discrete branch originated from the heat transfer characteristics. Hence, the modes originated from the only flow equation is denoted as hydrodynamic modes in the present study. The modes originated from the heat transfer are thermal modes.

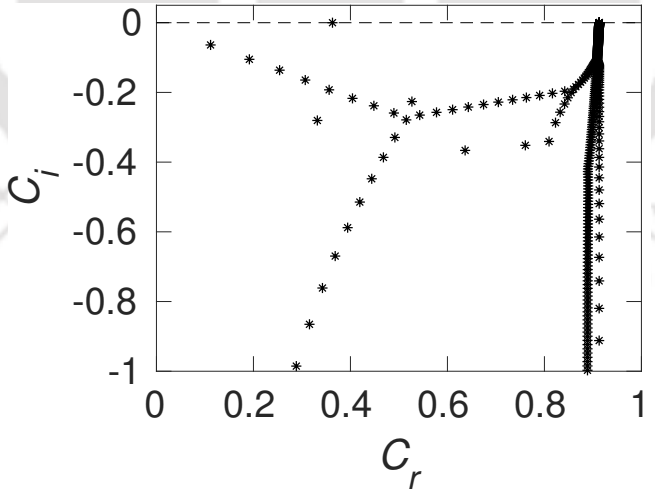

Figure 7.8: Eigenvalue spectrum for $Ri = 0.2$, $Re_\delta = 564.58$ and $\alpha = 0.22$

The temporal stability of the mixed convection flow corresponds to the above spectrum (see Fig. 7.6) is decided by the Eigenvalue denoted by A as this Eigenvalue is the most unstable Eigenvalue from discrete branch which contains the maximum imaginary part. Clearly, for forced convection $Ri = 0$ (from Fig. 7.7), the most unstable Eigenvalue is originated from the fluid flow characteristics rather than heat transfer characteristics. Hence, the most unstable mode is a hydrodynamic mode.

The spectrum corresponding to $Ri = 0.2$, $Re_\delta = 564.58$ and $\alpha = 0.22$ is shown in Fig. 7.8. The structure of the above spectrum has all the features of Eigenvalue spectrum corresponding to that of forced convection (Fig 7.7). The only difference is that the Eigenvalues move with reference to forced convection spectrum. The structure of the Eigenvalue spectrum varies from forced convection asymptote to natural convection asymptote as the values of Ri varies from 0 to ∞.

Neutral curves, the contours corresponding to zero imaginary value of phase speed ($C_i = 0$), of mixed convection boundary flows for various Ri values are shown in Fig. 7.9. The neutral curves presented in the figures represent mixed convection flows starting from pure forced convection ($Ri = 0$) to natural convection asymptote ($Ri \to \infty$). Fig. 7.9(a) shows the neutral curve corresponds to $Ri = 0$ which is attributed to forced convection flow. The neutral curve matches with neutral curve for Blasius boundary layer flow presented by Wazzan et al. [22]. It may be noted that the most unstable mode of the forced convection is a hydrodynamic mode which is originated from the fluid flow, and hence, match with the neutral curve of Blasius flow without heat transfer. If the most unstable mode was a thermal mode, the neutral curve of forced convection would not have been matched with the neutral curve of Blasius flow. The neutral curve presented in Fig. 7.9(g) corresponds to $Ri = 10^{15}$ which is obtained with mixed convection formulation is similar to the neutral curve of natural convection boundary layer flow presented in Fig. 6.6 from the natural convection formulation. The shape of the neutral curves gradually varies from the shape of Blasius solution to shape of neutral curve of natural convection.

The critical values of Re_δ, α and respective most unstable Eigenvalue C of mixed convection flows for various values of Ri is tabulated in table 7.1. The critical Reynolds number for forced convection ($Ri = 0$) is found to be 429.472. This boundary layer thickness based Reynolds number is equivalent of Reynolds number of 522.57 based on displacement thickness (Equivalent numerical value is obtained by multiplying conversion factor of 1.21678). The predicted critical Reynolds number based displacement thickness is close to the value with the critical Reynolds number (520) given in Schmid and Henningson [4], Schilshting [140] and White [149]

Table 7.1: Critical values of Re_δ, α, phase speed (C_r) and ω for various values of Ri

Ri	Re_{cr}	α_{cr}	C_{cr}	ω_{cr}
0	429.472	0.25026	$0.09164 + 0i$	0.02293
0.2	564.587	0.22115	$0.07728 + 0i$	0.01709
1.5	216.545	0.09259	$0.30680 + 0i$	0.02841
2	80.792	0.12750	$0.02174 + 0i$	0.00277
5	29.382	0.22747	$0.03666 + 0i$	0.00834
10	28.225	0.27350	$0.05298 + 0i$	0.01447
100	27.578	0.57737	$0.19714 + 0i$	0.11382
10^{15}	23.355	0.58794	$0.18246 + 0i$	0.10727

The Eigenvalue spectrum for various values of Richardson number at critical Reynolds number is shown in Fig. 7.10. From the figures, it can be observed that with increasing Richardson number, the discrete as well as continuous parts of spectrum move in negative direction of real axis (C_r values

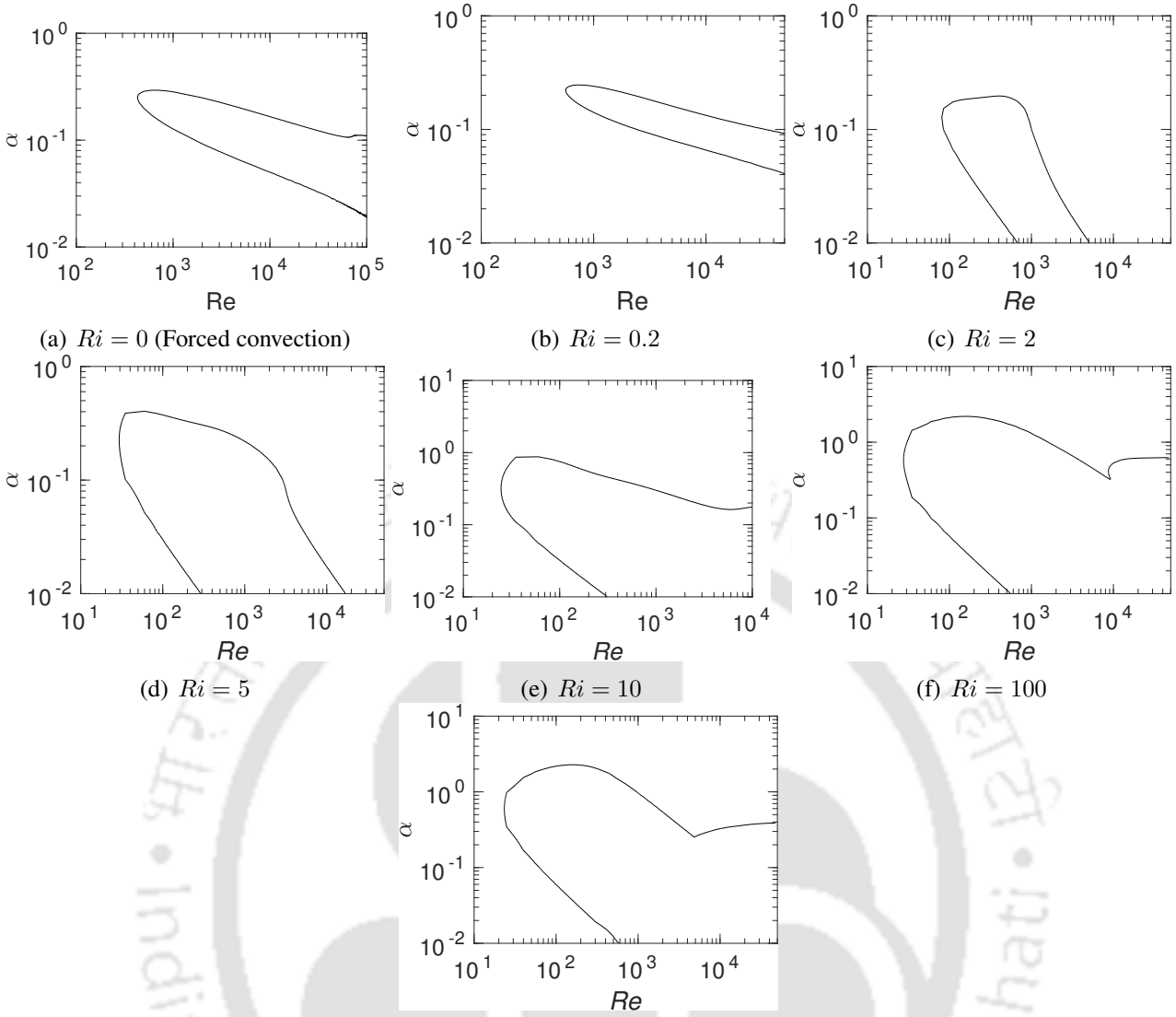

(a) $Ri = 0$ (Forced convection) (b) $Ri = 0.2$ (c) $Ri = 2$

(d) $Ri = 5$ (e) $Ri = 10$ (f) $Ri = 100$

(g) $Ri = 10^{15}$ (Natural convection)

Figure 7.9: Temporal neutral curves for various Ri values

of Eigenvalues decrease). In addition, continuous part of the spectrum moves faster than the discrete part of the spectrum. As a result, discrete Eigenvalues are on the left side of the continuous part of the spectrum up to Richardson number 10, beyond which the discrete Eigenvalues are on the right side of the continuous part of spectrum. The spectrum for $Ri = 10^{15}$ which represents natural convection is similar to the Eigenvalue spectrum shown in Fig. 6.7 at critical buoyancy parameter in the natural convection study.

The spectrum for Richardson number values near $Ri = 10$ (For example, as shown in Fig. 7.10(e)), the discrete Eigenvalues including the most unstable Eigenvalue are close to the continuous spectrum. One has to take utmost care to distinguish between the continuous and discrete parts of Eigenvalues while finding the most unstable Eigenvalue in the simulations to generate neutral curve.

The real and imaginary part of Eigenfunctions of various disturbance quantities such as $\hat{U}$, $\hat{V}$, ϕ

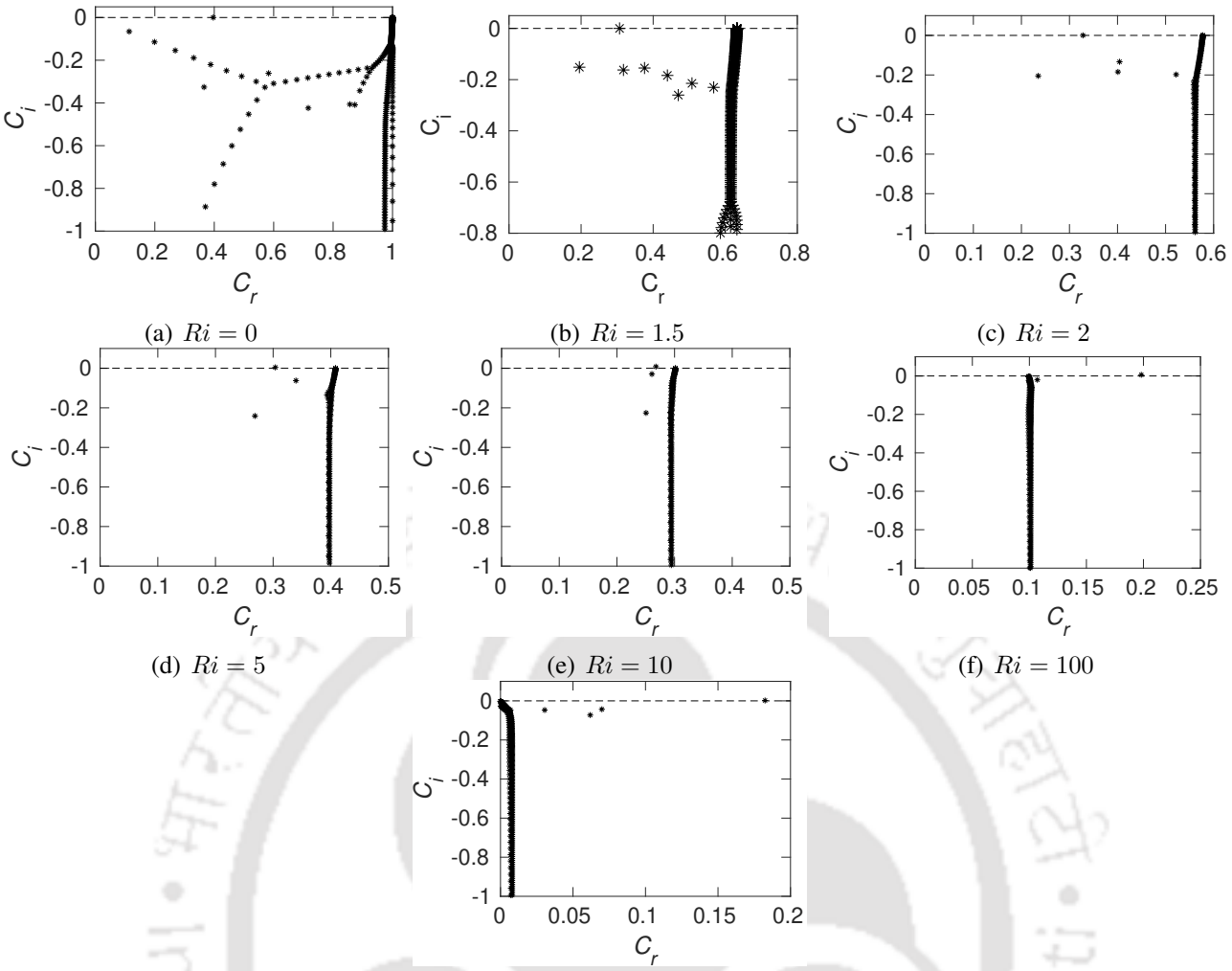

(a) $Ri = 0$ (b) $Ri = 1.5$ (c) $Ri = 2$

(d) $Ri = 5$ (e) $Ri = 10$ (f) $Ri = 100$

(g) $Ri = 10^{15}$

Figure 7.10: Eigenvalue spectrum for various Ri values at their respective Re_{cr} values

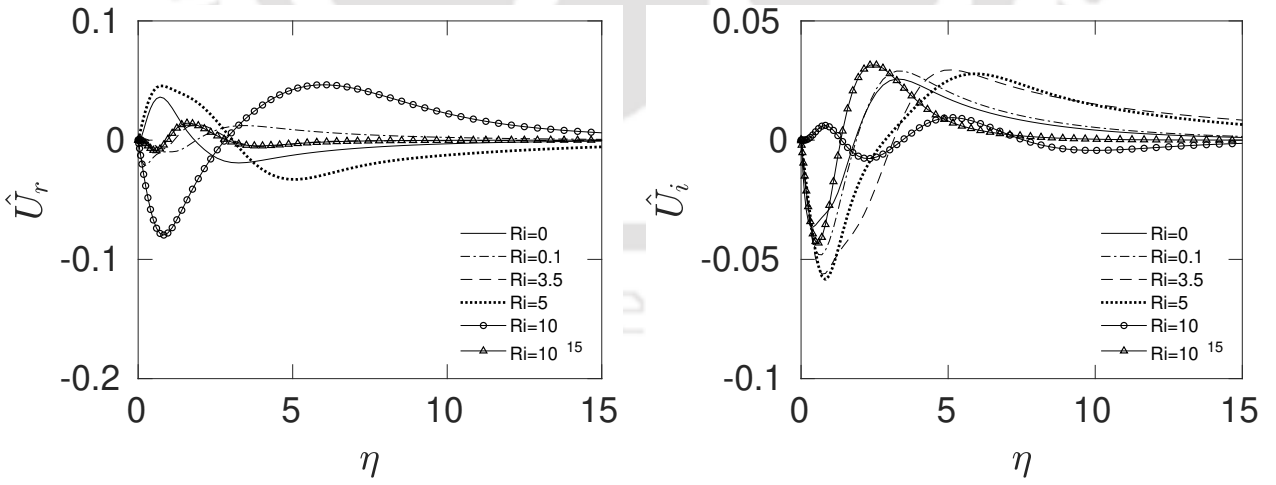

(a) Real part of $\hat{U}$ (b) Imaginary part of $\hat{U}$

Figure 7.11: Eigenfunctions for disturbance stream wise velocity ($\hat{U}$) for various Ri values

and S are shown in Figs. 7.11–7.14. The first three most unstable Eigenvalues of mixed convection flow for critical values of Re_δ and α for various Ri values are shown in table 7.2. In the table, mode 1 refers to neutral stable mode of the disturbance at critical Reynolds number and similarly, mode 2 and

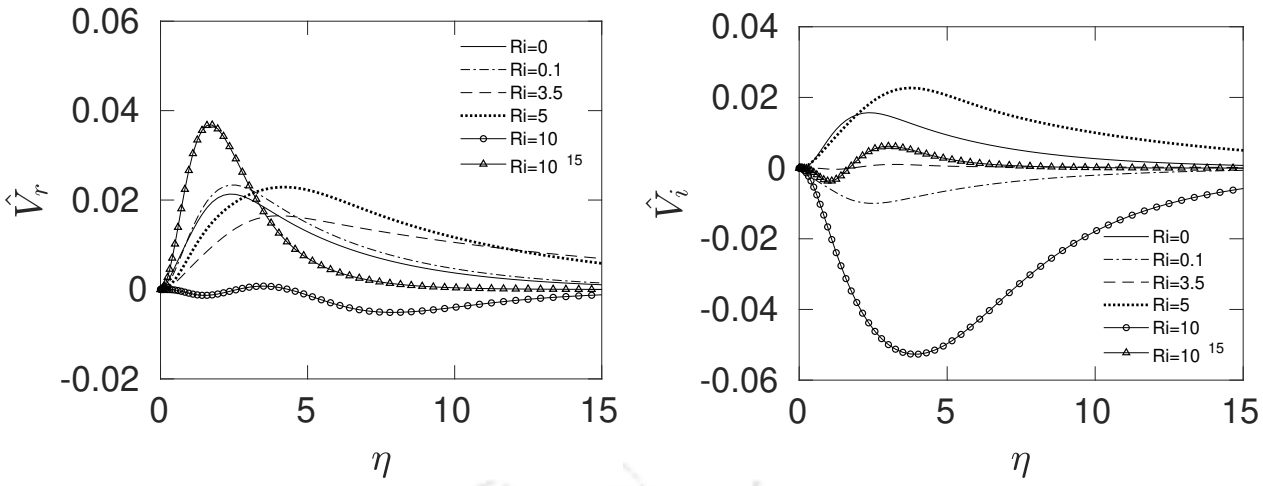

(a) Real part of $\hat{V}$ (b) Imaginary part of $\hat{V}$

Figure 7.12: Eigenfunctions for disturbance cross stream velocity ($\hat{V}$) for various Ri values

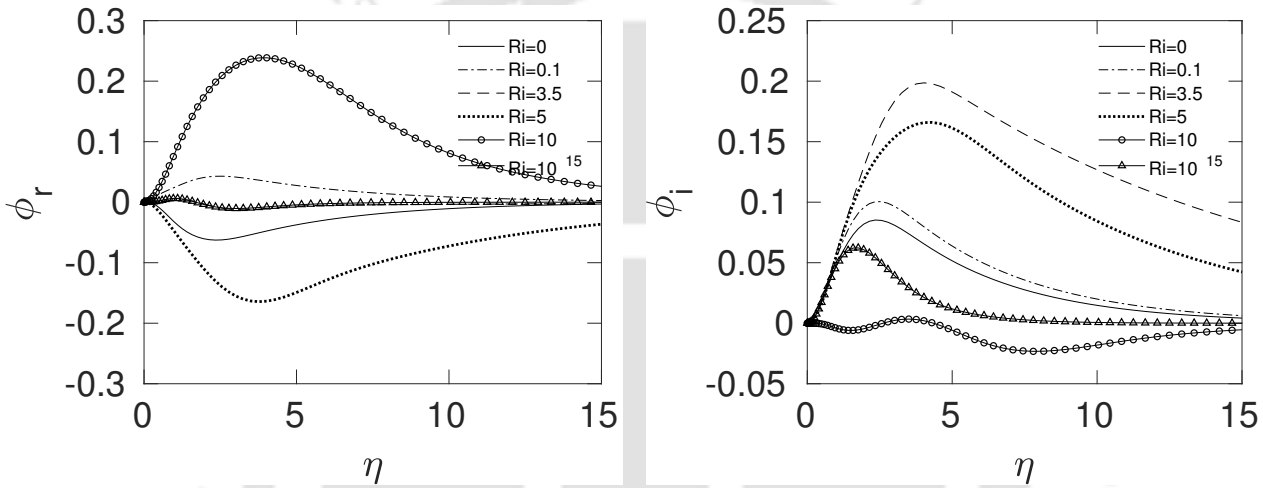

(a) Real part of ϕ (b) Imaginary part of ϕ

Figure 7.13: Eigenfunctions for disturbance stream function for various Ri values

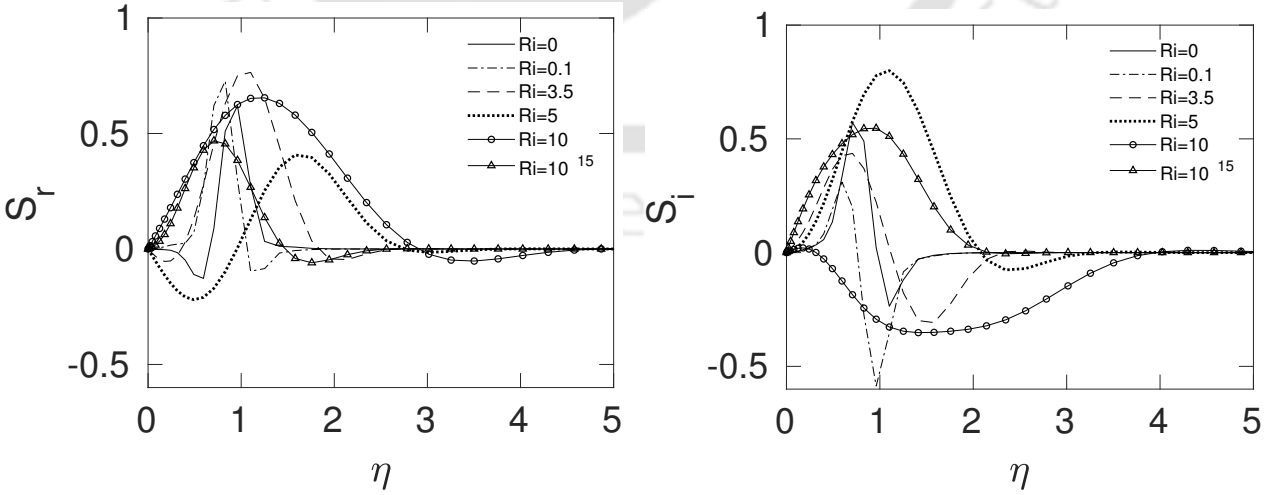

(a) Real part of S (b) Imaginary part of S

Figure 7.14: Eigenfunctions for disturbance temperature for various Ri values

mode 3 refer to second and third most unstable Eigen modes, respectively. In the table, the imaginary part of mode 1 is zero for all Ri values as these Eigen modes are of zero growth rate (presented for critical values of Re_δ and C). Hence, mode 1 represents the neutral stable mode of disturbance flow. Similarly, Mode 2 and mode 3 refer to second and third most unstable Eigenvalues, respectively. Mode 2 and mode 3 are stable modes for which the disturbance decay with time.

Table 7.2: A few most unstable Eigen modes of mixed convection flows for various values of Ri for their respective critical values of Re_{cr} and α_{cr}

Ri	Re_{cr}	α_{cr}	Eigen modes	Eigenvalues
0	429.47	0.25026	Mode 1	$9.94699 \times 10^{-2} + 0i$
			Mode 2	$2.23281 \times 10^{-2} - 1.50830 \times 10^{-2}i$
			Mode 3	$2.12491 \times 10^{-2} - 1.63444 \times 10^{-2}i$
0.2	564.5872	0.22102	Mode 1	$7.61609 \times 10^{-2} + 0i$
			Mode 2	$1.79490 \times 10^{-1} - 9.29904 \times 10^{-3}i$
			Mode 3	$1.72429 \times 10^{-1} - 1.00479 \times 10^{-3}i$
2	80.79140	0.12750	Mode 1	$2.17385 \times 10^{-2} + 0i$
			Mode 2	$2.56995 \times 10^{-2} - 7.84282 \times 10^{-3}i$
			Mode 3	$2.37363 \times 10^{-2} - 9.36055 \times 10^{-3}i$
5	29.3823	0.22750	Mode 1	$3.66646 \times 10^{-2} + 0i$
			Mode 2	$4.19675 \times 10^{-2} - 9.22790 \times 10^{-3}i$
			Mode 3	$5.10979 \times 10^{-2} - 1.47901 \times 10^{-2}i$
10	28.2252	0.27350	Mode 1	$5.29786 \times 10^{-2} + 0i$
			Mode 2	$5.69565 \times 10^{-2} - 7.29281 \times 10^{-3}i$
			Mode 3	$5.10294 \times 10^{-2} - 3.29094 \times 10^{-2}i$
100	27.5782	0.57749	Mode 1	$1.01774 \times 10^{-1} + 0i$
			Mode 2	$6.80491 \times 10^{-2} - 1.23148 \times 10^{-2}i$
			Mode 3	$6.43816 \times 10^{-2} - 1.401416 \times 10^{-1}i$
10^{15}	23.3634	0.60251	Mode 1	$9.08840 \times 10^{-2} + 0i$
			Mode 2	$3.01442 \times 10^{-6} - 6.85085 \times 10^{-4}i$
			Mode 3	$1.13784 \times 10^{-5} - 7.34848 \times 10^{-4}i$

The value of critical Reynolds number for $Ri = 10^{15}$ obtained is 23.36. $Ri = 10^{15}$ value is approximately $Ri \to \infty$, representing natural convection. At $Ri \to \infty$, the expression for Reynolds number (Re_δ) becomes identical to $G = \sqrt{2}Gr_x^{1/4}$ as given by Eq. (7.10) which is explained in section 7.2. The critical values obtained from the mixed convection formulation carried out in this section are compared to those obtained using natural convection formulation (section 6.1.2) are tabulated in table 7.3. The comparison shows that the mixed convection formulation retrieve the results of pure natural convection accurately.

Table 7.3: Comparison of critical values of natural convection obtained from two different numerical formulations

	G_{cr}	α_{cr}
Mixed convection formulation	23.36	0.6025
Natural convection formulation	22.25	0.6062

7.5 Effect of plate inclination

The inclination effect on the stability of mixed convection is studied. The plate inclination (Φ) is measured in the anticlockwise direction with respect to vertically upward direction.The inclination effect is studied for inclination angles of -15° to 15° for Richardson number value of 5. The governing equations for the flow with inclination are same as those of vertical orientation, except the buoyancy term is modified by a multiplication factor of $\cos\Phi$. The corresponding governing equations for base flow are as following.

$$\frac{\partial U}{\partial X} + \frac{\partial V}{\partial Y} = 0, \tag{7.28}$$

$$U\frac{\partial U}{\partial X} + V\frac{\partial U}{\partial Y} = \frac{1}{Re_x}\frac{\partial^2 U}{\partial Y^2} + Ri\ \theta^2\cos\Phi, \tag{7.29}$$

$$U\frac{\partial \theta}{\partial X} + V\frac{\partial \theta}{\partial Y} = \frac{1}{Re_x Pr}\frac{\partial^2 \theta}{\partial Y^2}. \tag{7.30}$$

The following are the boundary conditions for base flows,

$$\text{At}\quad X = 0, \quad U = 1/(1+Ri)^{1/2}, \quad V = 0, \quad \theta = 0, \tag{7.31}$$

$$\text{At}\quad Y = 0, \quad U = 0, \quad V = 0, \quad \theta = 1, \tag{7.32}$$

$$\text{At}\quad Y \to \infty, \quad U = 1/(1+Ri)^{1/2}, \quad V = 0, \quad \theta = 0. \tag{7.33}$$

The disturbance governing equations including inclination effect are,

$$\left(U - \frac{\omega}{\alpha}\right)\left(\phi'' - \alpha^2\phi\right) - U''\phi = \frac{1}{i\alpha Re_\delta}\Bigg(\phi^{iv} - 2\alpha^2\phi'' + \alpha^4\phi \pm \frac{2Ri}{1+Ri}2\left[(S' - i\alpha\tan\Phi S)\theta + \left(1 + \eta\frac{\tan\Phi}{G}\right)\theta' S\right]\Bigg), \tag{7.34}$$

$$\left(U - \frac{\omega}{\alpha}\right)S - \theta'\phi = \frac{1}{i\alpha Re_\delta Pr}\left(S'' - \alpha^2 S\right). \tag{7.35}$$

The boundary conditions for disturbance equation are given by,

$$\text{At}\quad \eta = 0, \quad \phi = 0, \quad \phi' = 0, \quad S = 0, \tag{7.36}$$

$$\text{At}\quad \eta \to \infty, \quad \phi = 0, \quad \phi' = 0, \quad S = 0. \tag{7.37}$$

The neutral curves for various inclinations are shown in Fig. 7.15. With increasing inclination, the neutral curves move towards left side. For positive inclinations, the neutral curves are almost

overlapping with the neutral curve corresponds to $\Phi = 0$ which are not shown in figure. The critical values of Reynolds number, wave number, circular frequency and phase speed correspond to various inclinations are shown in table 7.4. The variation of critical Reynolds number with inclination is shown in Fig. 7.17. From the figure, it can be observed that with decreasing inclination, critical Reynolds number increases. As we vary the inclination from 0° to -15°, the critical Reynolds number varies from 29.38 to 29.66. When we change the inclination from 0° to 15°, the Reynolds number remains almost constant. This implies, unlike the natural convection, stability of mixed convection is affected only when the plate is tilted in the clockwise direction. It may be noted that even though the critical Reynolds number increases with clockwise orientation, the increase in the critical Reynolds number is small. Overall, the stability of mixed convection boundary layer is much less sensitive to inclination compared to the natural convection boundary layer flows.

Fig. 7.16 shows the critical Eigenvalue spectrum for various inclinations. The variation of critical wave number with respect to inclination is shown in Fig. 7.18. The critical wave number decreases as we tilt the plate in the clockwise direction. The wave number is insensitive to tilting the plate in the anticlockwise direction.

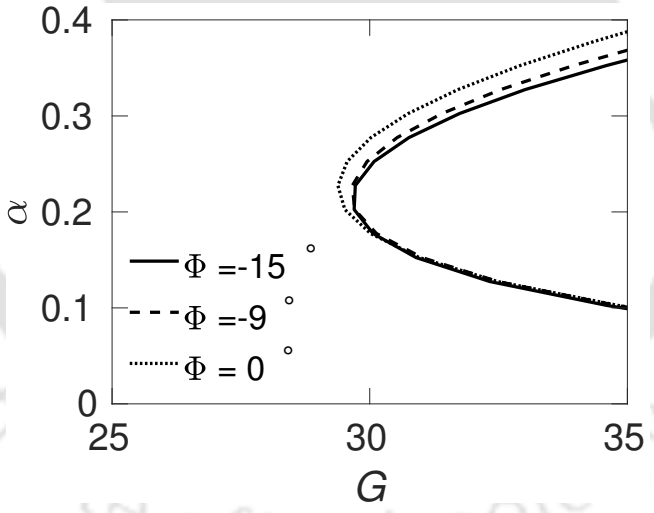

Figure 7.15: Neutral stability curves for various plate inclinations

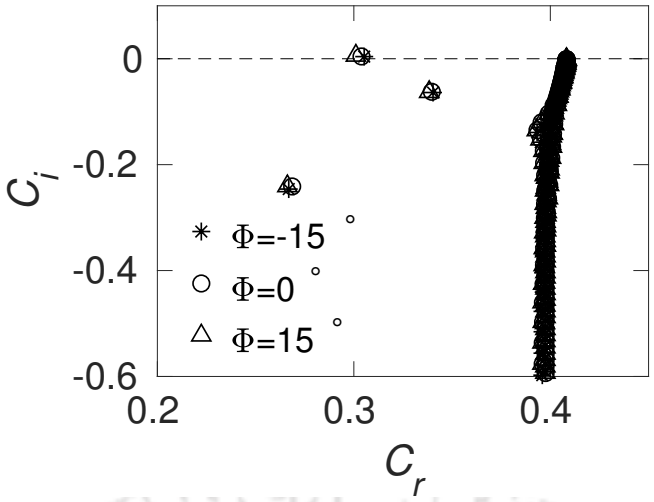

Figure 7.16: Eigenvalue spectrum at critical Re value for various plate inclinations

Table 7.4: Critical values of Re and α and the respective most unstable Eigenvalue for $Ri = 5$

Φ	Re_{cr}	α_{cr}	C_{cr}
$-15°$	29.6642	0.21735	$0.30727 + 0i$
$-12°$	29.6533	0.21466	$0.30763 + 0i$
$-9°$	29.610	0.21460	$0.30764 + 0i$
$-6°$	29.5759	0.21851	$0.30712 + 0i$
$-3°$	29.4988	0.22740	$0.3060 + 0i$
$0°$	29.3822	0.22724	$0.30389 + 0i$
$3°$	29.3820	0.22726	$0.30389 + 0i$
$6°$	29.3810	0.22728	$0.30389 + 0i$
$9°$	29.3805	0.22740	$0.30247 + 0i$
$12°$	29.3802	0.22744	$0.30578 + 0i$
$15°$	29.3795	0.22750	$0.30103 + 0i$

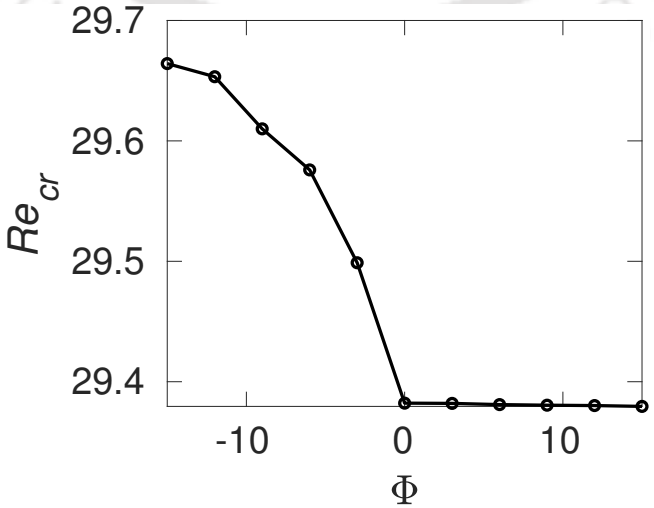

Figure 7.17: Variation of critical Reynolds number (Re_{cr}) with plate inclination

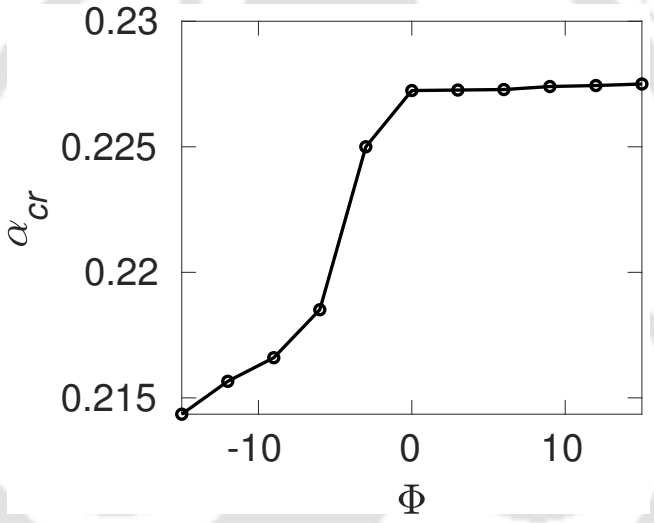

Figure 7.18: Variation of critical wave number with plate inclination

7.6 Spatial stability analysis

In spatial stability analysis, we study the disturbance growth or decay with space for a given temporal variation of disturbance at a given spatial location. In the present section, the results of spatial stability analysis are presented.

7.6.1 Numerical treatment

The disturbance governing equations for spatial stability analysis can be given in Eigenvalue form (as discussed in section 5.4.9),

$$\begin{bmatrix} 0 & I & 0 & 0 & 0 & 0 \\ 0 & 0 & I & 0 & 0 & 0 \\ 0 & 0 & 0 & I & 0 & 0 \\ -C_0 & -C_1 & -C_2 & -C_3 & -E_0 & -E_1 \\ 0 & 0 & 0 & 0 & 0 & I \\ -C_5 & -C_6 & -C_7 & -C_8 & -E_3 & -E_4 \end{bmatrix} \begin{bmatrix} \phi_1 \\ \phi_2 \\ \phi_3 \\ \phi_4 \\ S_1 \\ S_2 \end{bmatrix} = \alpha \begin{bmatrix} I & 0 & 0 & 0 & 0 & 0 \\ 0 & I & 0 & 0 & 0 & 0 \\ 0 & 0 & I & 0 & 0 & 0 \\ 0 & 0 & 0 & C_4 & 0 & E_2 \\ 0 & 0 & 0 & 0 & I & 0 \\ 0 & 0 & 0 & C_9 & 0 & E5 \end{bmatrix} \begin{bmatrix} \phi_1 \\ \phi_2 \\ \phi_3 \\ \phi_4 \\ S_1 \\ S_2 \end{bmatrix}, \tag{7.38}$$

where,

$$\begin{aligned} C_0 &= D^4 + i\omega Re_\delta D^2, \\ C_1 &= i\omega Re_\delta (U'' - UD^2), \\ C_2 &= -(2D^2 + i\omega Re_\delta), \\ C_3 &= i\omega Re_\delta U, \\ C_4 &= I, \\ C_5 &= -iRe_\delta Pr\theta', \\ C_6 &= 0, \\ C_7 &= 0, \\ C_8 &= 0, \\ C_9 &= 0, \\ E_0 &= \left(\frac{2Ri}{1+Ri}\right) 2\left(\theta D + \theta'\right), \\ E_1 &= -2i\omega\theta, \\ E_2 &= 0, \\ E_3 &= -(i\omega Re_\delta Pr + D^2), \\ E_4 &= iRe_\delta PrU, \\ E_5 &= I, \end{aligned}$$

where, I is identity matrix of size $N \times N$. The above can be written in Eigenvalue form as,

$$A\phi = \alpha B\phi. \tag{7.39}$$

The above Eigenvalue problem matrix A and B are of size $6N \times 6N$. This is unlike the size of the Eigenvalue problem which comes from the temporal stability analysis.

7.6.2 Validation

Validation of the code is carried out by solving spatial stability of boundary layer flows over a flat plate. The results are presented by Eigenvalue spectrum for $Re = 1000$, $\omega = 0.26$ and compared with the spectrum obtained by Schmid and Henningson [4] as shown in Fig. 7.19. The spectrum of boundary layer flow from present study agree well with that of reference spectrum.

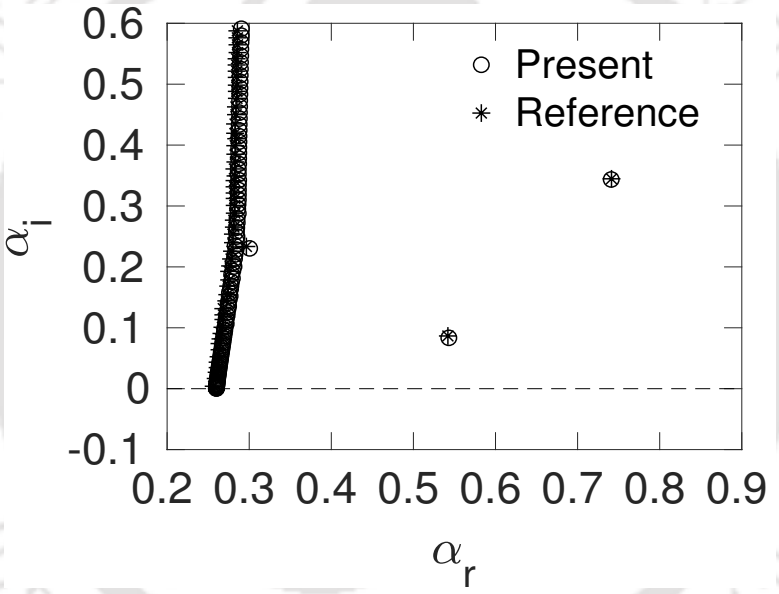

Figure 7.19: Comparison of Eigenvalue spectrum of boundary layer flow from present study with that of reference study (Schmid and Henningson [4])

The three discrete spatial Eigenvalues of boundary layer flow for $Re = 1000$, $\omega = 0.26$, are compared with those of Schmid and Henningson [4] which is shown in table 7.5. It is clear from the table that the present Eigenvalues match up to 3 decimal points with reference Eigenvalues.

Table 7.5: Comparison of three discrete Eigenvalues (α) of boundary layer flow for $Re = 1000$, $\omega = 0.26$ from present study with that of Schmid and Henningson [4]

Present result	Schmid and Henningson [4]
$0.54313 + 0.083523\ i$	$0.54213 + 0.083968\ i$
$0.30050 + 0.230386\ i$	$0.29967 + 0.230773\ i$
$0.74095 + 0.343529\ i$	$0.74155 + 0.345132\ i$

7.6.3 Grid independence tests

Grid independence tests are carried out for spatial stability of mixed convection flow. The Eigenvalue spectrum for various grid sizes for $Ri = 5$, $Re_\delta = 104$ and $\omega = 0.0335$ are compared in Fig. 7.20. It can be observed from the figure that the Eigenvalue spectrum show continuous branch and discrete points. The discrete Eigenvalues fall on the right hand side of the continuous spectrum, coincide with each other for all the three grid sizes. Since, only discrete Eigenvalues contribute to the growth of disturbance, grid size 151 is chosen in the present study as the discrete Eigenvalues are not significantly changing for grids with size above 151.

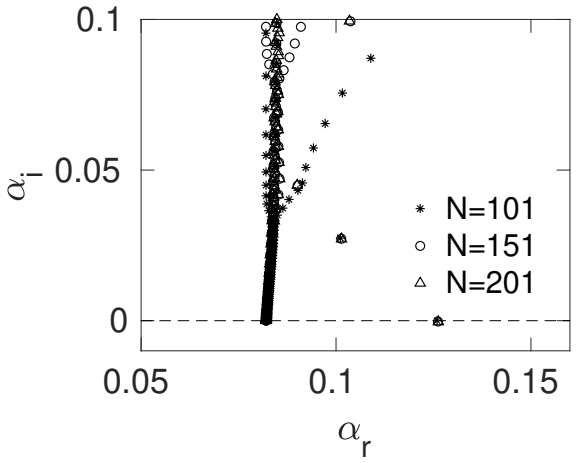

Figure 7.20: Grid sensitivity tests for spatial Eigenvalue spectrum ($Ri = 5$, $Re_\delta = 104$, $\omega = 0.0335$)

7.6.4 Results and discussion

A typical spectrum of spatial stability is shown in Fig. 7.21 for $Ri = 0.2$, $Re_\delta = 565.0313$ and $\omega = 0.074$. The spectrum contains continuous part and discrete part. The continuous spectrum is typical for any unbounded flows such as boundary layer flows. The smallest imaginary part of α (α_i) among the discrete part of the spectrum decides the spatial growth of the disturbance in space (upstream or downstream location of the origin of the disturbance).

The spatial neutral curves of mixed convection flow for various Ri values is shown in Fig. 7.22. In the figure, neutral curve for $Ri = 0$, represents the neutral curve for forced convection flow. The critical value of Reynolds number from the present study match with that of boundary layer flow without heat transfer (Blasius flow).

The critical values of Re_δ and ω of mixed convection for various Ri values are presented in table. 7.6. From the table, it can be seen that the critical Reynolds number continuously decreases with increasing Ri for $Ri > 2$. The opposite trend is observed for critical value of both frequency and Eigenvalue with increasing Ri values. It can be noticed that the imaginary part of critical Eigenvalue

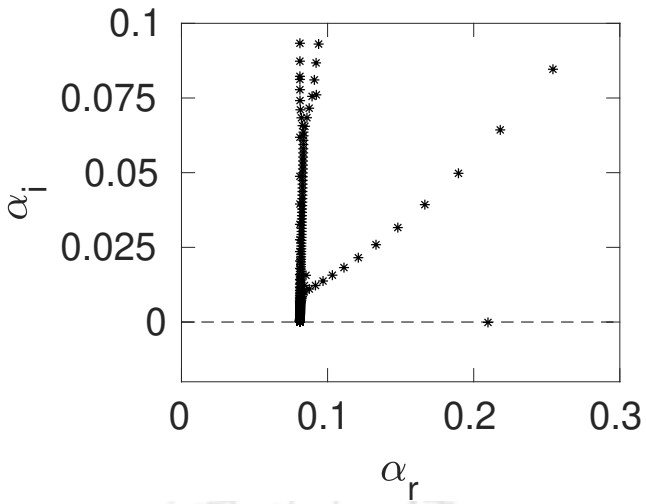

Figure 7.21: Typical Eigenvalue spectrum ($Ri = 0.2$, $Re_\delta = 565.03$, $\omega = 0.074$)

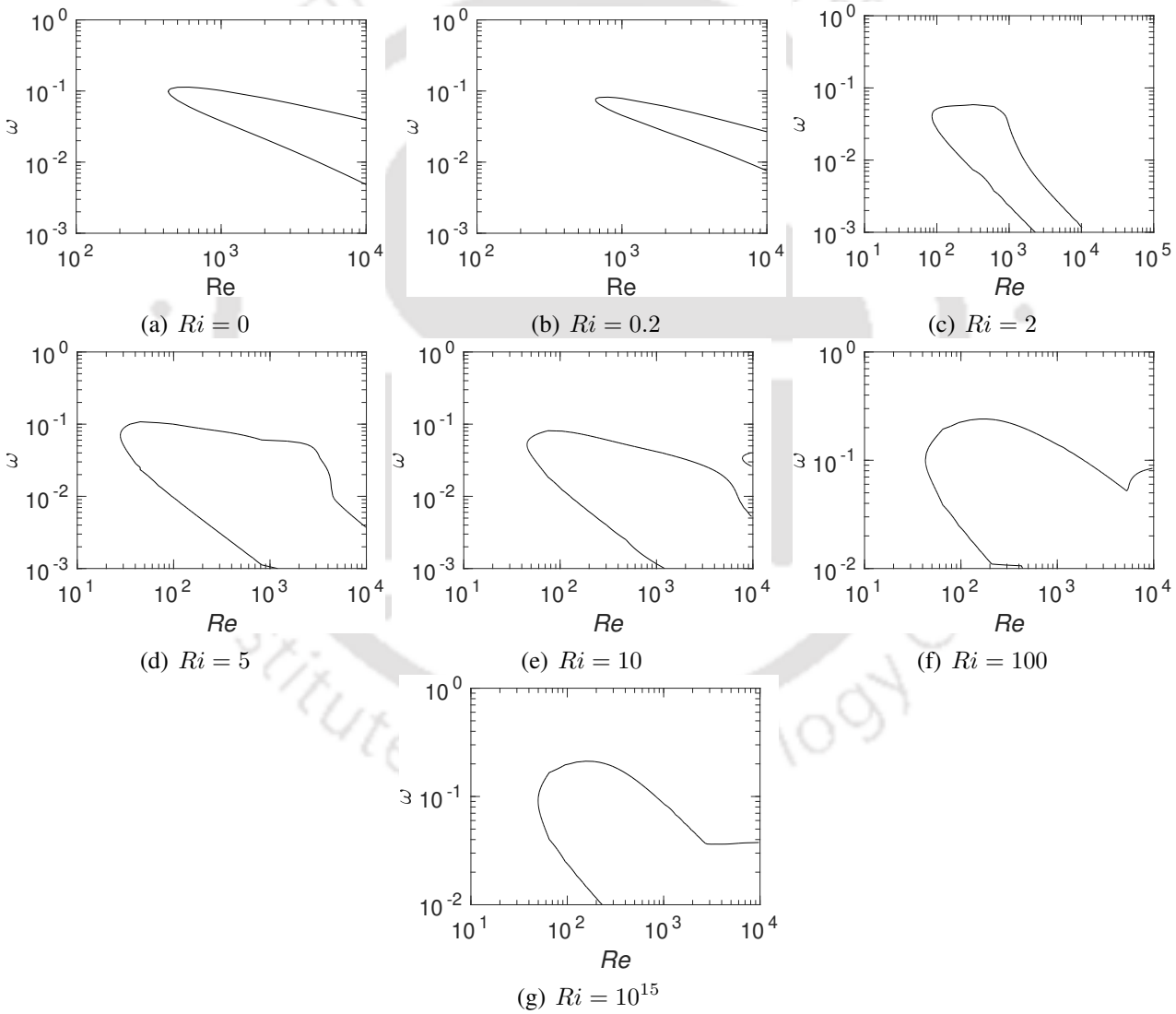

(a) $Ri = 0$ (b) $Ri = 0.2$ (c) $Ri = 2$

(d) $Ri = 5$ (e) $Ri = 10$ (f) $Ri = 100$

(g) $Ri = 10^{15}$

Figure 7.22: Neutral curves for spatial stability analysis for various Richardson numbers

is zero for all Ri values because the values of governing parameters such as Re_δ and ω are at their critical values.

The Eigenvalue spectrum of mixed convection flow is shown in Fig. 7.23 for various Ri values

Table 7.6: Critical values of Re_δ, ω and α for various values of Ri

Ri	$Re_{\delta \text{cr}}$	ω_{cr}	α_{cr}
0	430.7392	0.09873	$0.24889 + 0i$
0.2	565.0313	0.07401	$0.20977 + 0i$
2	81.5580	0.02200	$0.08401 + 0i$
5	29.2590	0.03300	$0.12421 + 0i$
10	28.3536	0.05200	$0.21640 + 0i$
100	27.7580	0.1017	$0.59948 + 0i$
10^{15}	23.4500	0.0910	$0.59199 + 0i$

at their respective critical values of Re_δ and ω. In the figure, the continuous branch originated from unbounded domain in temperature equation, moves in the anti-clockwise direction with increasing Richardson number. The most unstable Eigenvalue from the discrete part of the spectrum moves in the negative real axis direction (circular frequency of the disturbance α_r decreases) up to $Ri = 5$. For $Ri > 5$, most unstable Eigenvalue moves towards positive real axis direction. Fig. 7.23(f) shows the Eigenvalue spectrum for $Ri = 10^{15}$ representing natural convection asymptote. The spectrum has a curvy continuous branch along with discrete Eigenvalues. This spectrum is similar to the spectrum presented in Fig. 6.18 for natural convection at critical buoyancy parameter value computed using the natural convection formulation.

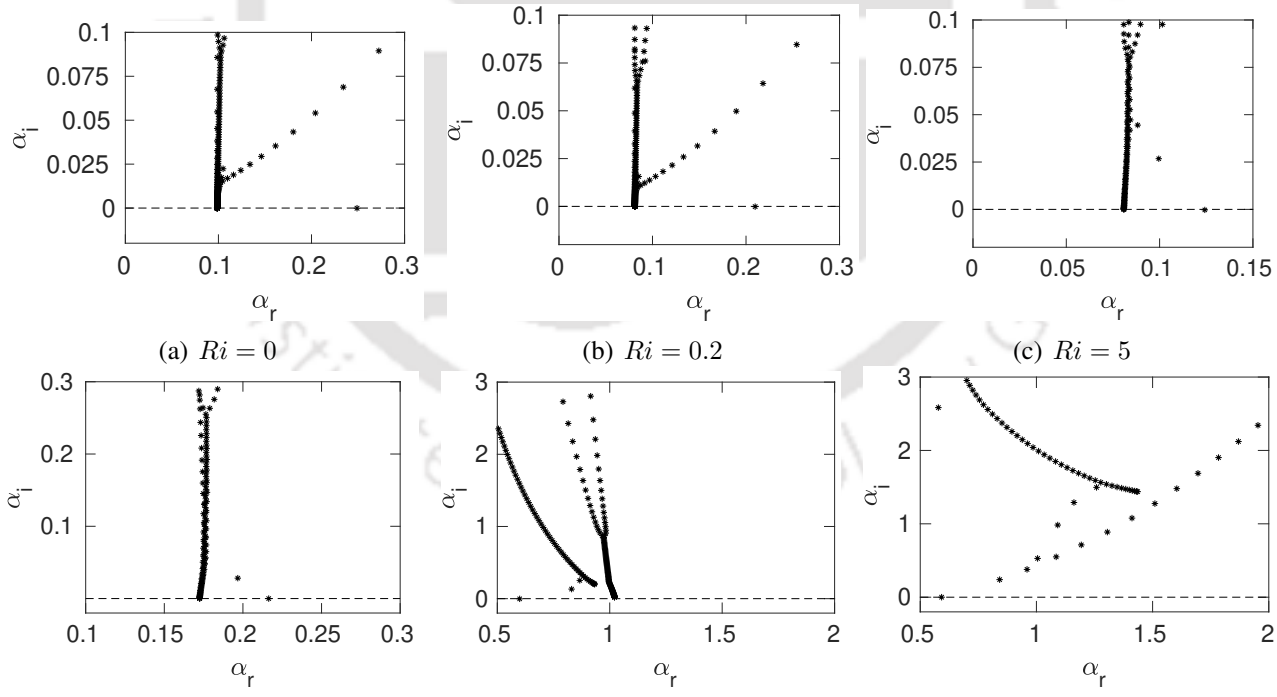

(a) $Ri = 0$ (b) $Ri = 0.2$ (c) $Ri = 5$

(d) $Ri = 10$ (e) $Ri = 100$ (f) $Ri = 10^{15}$

Figure 7.23: Spatial Eigenvalue spectrum for various Ri values at their respective Re_{cr} and ω_{cr} values

7.6.5 Effect of plate inclination

The effect of plate inclination on stability of mixed convection boundary layer is studied through spatial stability analysis. The governing equations for the base flow (given by Eqs. (7.28)–(7.30)) and disturbance equations (given by Eqs. (7.34)–(7.35)) and the respective boundary conditions (7.31)–(7.33) and (7.36)–(7.37) are same as those of temporal stability analysis. The inclination study is carried out for inclinations in the range -15° to 15° for Richardson number value of 5.

The neutral curves for various plate inclination effect are shown in Fig. 7.24. The neutral curve shifts towards left side as the inclination is increased from 0° to 15°. The neutral curves for inclination range of 0° to −15° are almost overlapping with the neutral curve corresponding to zero inclination. This means that tilting in the clockwise direction does not have any influence on the mixed convection boundary layer stability. The critical values of Reynolds number, frequency, wave number and phase speed for various inclinations are presented in table 7.7. The critical values presented in the table are very close to the values obtained for inclination effects of temporal stability which is given in table 7.4. The results of inclination effects from both the temporal and spatial stability are same due to the fact that the temporal and spatial stability analysis should give the same critical values. Since, these critical values from spatial stability are same as those from the temporal stability, the conclusions drawn from the temporal stability are equally applies to the results from the spatial stability.

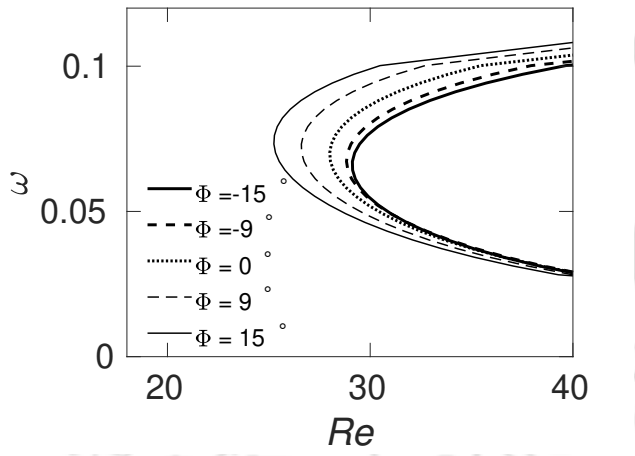

Figure 7.24: Neutral stability curves for various plate inclinations

Table 7.7: Critical values of Re_δ, ω, α and phase speed (C_r) for various inclinations

Φ	$Re_{\delta \text{cr}}$	ω_{cr}	α_{cr}	phase speed (C_r)
-15°	29.099	0.06594	0.21607	0.30518
-12°	28.992	0.06726	0.22037	0.30521
-9°	28.828	0.06743	0.22061	0.30565
-6°	28.602	0.06753	0.22062	0.30595
-3°	28.323	0.06893	0.22522	0.30606
0°	28.003	0.07022	0.22955	0.30610
3°	27.601	0.07021	0.22929	0.30612
6°	27.134	0.07115	0.23242	0.30613
9°	26.592	0.07196	0.23505	0.30615
12°	25.965	0.07332	0.23974	0.30620
15°	25.238	0.07421	0.24273	0.30624

7.7 Conclusions

In this chapter, the stability of mixed convection boundary layer flows over an isothermal flat plate is studied for both temporal and spatial stability. The mixed convection formulation is carried out such a way that as we vary Richardson from 0 to ∞, the flow smoothly varies from pure forced convection to pure natural convection. The following conclusions are drawn from the study.

1. For forced convection flow, most unstable mode is a hydrodynamic mode, which is originated from the fluid flow characteristics.
2. The critical Reynolds number decreases with Richardson number for $Ri > 2$.
3. The effect of plate inclination on the stability of mixed convection is weaker than that observed for the natural convection flow for stability. In mixed convection flow, clockwise inclinations widen range of selectively amplified wave numbers.
4. For small Richardson numbers, the most unstable modes come from the flow characteristics of the boundary layer and hence, it is a hydrodynamic mode.
5. The critical wave number and phase speed increases with Richardson number for $Ri > 2$.
6. The mixed convection formulation used in the study recovers the results of pure natural and forced convection results, accurately.

Chapter 8

Global stability analysis of mixed convection flow in cavity

In the sequence of studying stability of water flows with density inversion, global linear stability of mixed convection of water flow in a lid driven square cavity is studied including density inversion effect. The results are presented in this chapter. Many studies such as [105, 105–111, 113–115, 150, 151] have been investigated the global stability of fluid flow of lid driven cavity. However, the stability of lid driven cavity with mixed convection heat transfer is not reported in the literature. Hence, the mixed convection in lid driven square cavity with density inversion is studied. The numerical formulation, solution methodology and the global stability results are presented in this chapter.

8.1 Physical system

The physical system consists of a two-dimensional square cavity filled with water near its density inversion point which is shown in Fig. 8.1. The top wall of cavity is moving with uniform velocity in positive x-direction while the other walls of cavity are stationary. The left wall of the cavity is kept at uniform higher temperature of $T_H = T_0 + \Delta T/2$. The right wall of the cavity is kept at uniform lower temperature $T_C = T_0 - \Delta T/2$. ΔT is the temperature difference between left and right wall. The above expressions for T_H and T_C imply, the temperature of the left and right walls are symmetrically placed with respect to the temperature of density maximum point near density inversion. The temperature of both left and right walls are within the temperature range of water density inversion. The top and bottom walls of the cavity are insulated. Due to the combined effect of top moving wall and buoyancy forces due to temperature difference between left and right walls of the cavity, mixed convection flow is developed in the cavity.

8.2 Mathematical modeling

Steady, laminar and incompressible flows are considered as base flow for the stability study of mixed convection. All thermo-physical properties of water are taken constant except for density in buoyancy

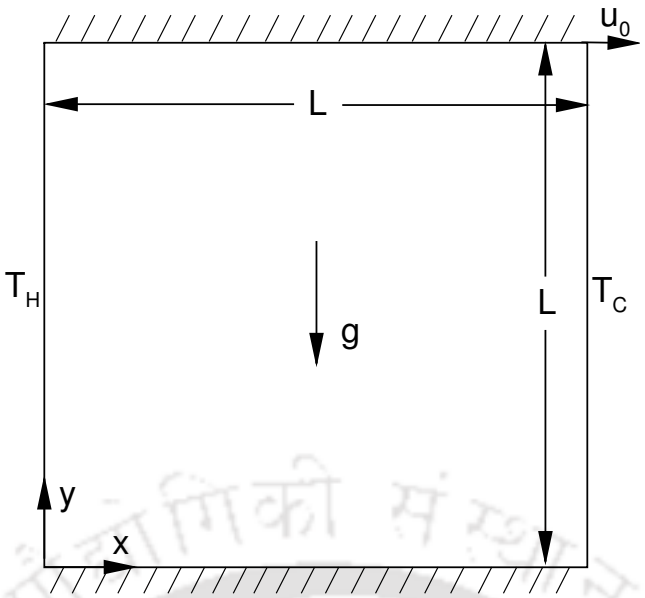

Figure 8.1: Physical and co-ordinate systems of mixed convection flow in a differentially side heated cavity

term. The parabolic variation of density with temperature given by Eq. 1.3 is used for buoyancy term.

8.3 Derivation of disturbance governing equations

The dimensional form of governing equations for two-dimensional mixed convection flow with density inversion of water is given by,
continuity equation:

$$\frac{\partial u}{\partial x}+\frac{\partial v}{\partial y}=0, \tag{8.1}$$

x-momentum equation:

$$\frac{\partial u}{\partial t}+u\frac{\partial u}{\partial x}+v\frac{\partial u}{\partial y}=-\frac{1}{\rho}\frac{\partial p}{\partial x}+\nu\left(\frac{\partial^2 u}{\partial x^2}+\frac{\partial^2 u}{\partial y^2}\right), \tag{8.2}$$

y-momentum equation:

$$\frac{\partial v}{\partial t}+u\frac{\partial v}{\partial x}+v\frac{\partial v}{\partial y}=-\frac{1}{\rho}\frac{\partial p}{\partial y}+\nu\left(\frac{\partial^2 v}{\partial x^2}+\frac{\partial^2 v}{\partial y^2}\right)+g\gamma(T-T_0)^2, \tag{8.3}$$

energy equation:

$$\frac{\partial T}{\partial t}+u\frac{\partial T}{\partial x}+v\frac{\partial T}{\partial y}=\frac{k}{\rho c_p}\left(\frac{\partial^2 T}{\partial x^2}+\frac{\partial^2 T}{\partial y^2}\right). \tag{8.4}$$

The steady state form of above equations are the governing equations of base flow. In the present study, the base flows are considered as two-dimensional flows. Hence, the variation of base flow quantities such as $\bar{u}$, $\bar{v}$, $\bar{p}$ and $\bar{T}$ are,

$$\bar{u}=\bar{u}(x,y),\quad \bar{v}=\bar{v}(x,y),\quad \bar{p}=\bar{p}(x,y),\quad \bar{T}=\bar{T}(x,y). \tag{8.5}$$

Using the above expressions in the equations (8.1)–(8.4), the governing equations for the base flows are derived as,

$$\frac{\partial \bar{u}}{\partial x} + \frac{\partial \bar{v}}{\partial y} = 0, \tag{8.6}$$

$$\frac{\partial \bar{u}}{\partial t} + \bar{u}\frac{\partial \bar{u}}{\partial x} + \bar{v}\frac{\partial \bar{u}}{\partial y} = -\frac{1}{\rho}\frac{\partial \bar{p}}{\partial x} + \nu\left(\frac{\partial^2 \bar{u}}{\partial x^2} + \frac{\partial^2 \bar{u}}{\partial y^2}\right), \tag{8.7}$$

$$\frac{\partial \bar{v}}{\partial t} + \bar{u}\frac{\partial \bar{v}}{\partial x} + \bar{v}\frac{\partial \bar{v}}{\partial y} = -\frac{1}{\rho}\frac{\partial \bar{p}}{\partial y} + \nu\left(\frac{\partial^2 \bar{v}}{\partial x^2} + \frac{\partial^2 \bar{v}}{\partial y^2}\right) + g\gamma(\bar{T} - \bar{T}_0)^2, \tag{8.8}$$

$$\frac{\partial \bar{T}}{\partial t} + \bar{u}\frac{\partial \bar{T}}{\partial x} + \bar{v}\frac{\partial \bar{T}}{\partial y} = \frac{k}{\rho c_p}\left(\frac{\partial^2 \bar{T}}{\partial x^2} + \frac{\partial^2 \bar{T}}{\partial y^2}\right). \tag{8.9}$$

The above equations are base flow governing equations for two-dimensional mixed convection cavity flow with water density inversion.

To derive the disturbance equations for the base flows, add small disturbance $\hat{u}$, $\hat{v}$, $\hat{p}$ and $\hat{T}$ in base flow velocities, pressure and temperature, respectively, which can be written as following.

$$u = \bar{u} + \hat{u}, \quad v = \bar{v} + \hat{v}, \quad p = \bar{p} + \hat{p}, \quad T = \bar{T} + \hat{T}. \tag{8.10}$$

The above disturbances can grow or decay in any spatial direction and in time. Mathematically, they can be written as following

$$\hat{u} = \hat{u}(x, y, t), \quad \hat{v} = \hat{v}(x, y, t), \quad \hat{p} = \hat{p}(x, y, t), \quad \hat{T} = \hat{T}(x, y, t). \tag{8.11}$$

Using Eqs. (8.10)–(8.11) in the Eqs. (8.1)–(8.4), the disturbance equations are converted into,

$$\frac{\partial \bar{u}}{\partial x} + \frac{\partial \bar{v}}{\partial y} + \frac{\partial \hat{u}}{\partial x} + \frac{\partial \hat{v}}{\partial y} = 0, \tag{8.12}$$

$$\begin{aligned}
&\left(\frac{\partial \bar{u}}{\partial t} + \bar{u}\frac{\partial \bar{u}}{\partial x} + \bar{v}\frac{\partial \bar{u}}{\partial y}\right) + \left(\frac{\partial \hat{u}}{\partial t} + \hat{u}\frac{\partial \hat{u}}{\partial x} + \hat{v}\frac{\partial \hat{u}}{\partial y}\right) + \bar{u}\frac{\partial \hat{u}}{\partial x} + \hat{u}\frac{\partial \bar{u}}{\partial x} + \bar{v}\frac{\partial \hat{u}}{\partial y} + \hat{v}\frac{\partial \bar{u}}{\partial y} + \\
&= -\frac{1}{\rho}\frac{\partial \bar{p}}{\partial x} + \nu\left(\frac{\partial^2 \bar{u}}{\partial x^2} + \frac{\partial^2 \bar{u}}{\partial y^2}\right) - \frac{1}{\rho}\frac{\partial \hat{p}}{\partial x} + \nu\left(\frac{\partial^2 \hat{u}}{\partial x^2} + \frac{\partial^2 \hat{u}}{\partial y^2}\right),
\end{aligned} \tag{8.13}$$

$$\begin{aligned}
&\left(\frac{\partial \bar{v}}{\partial t} + \bar{u}\frac{\partial \bar{v}}{\partial x} + \bar{v}\frac{\partial \bar{v}}{\partial y}\right) + \left(\frac{\partial \hat{v}}{\partial t} + \hat{u}\frac{\partial \hat{v}}{\partial x} + \hat{v}\frac{\partial \hat{v}}{\partial y}\right) + \bar{u}\frac{\partial \hat{v}}{\partial x} + \hat{u}\frac{\partial \bar{v}}{\partial x} + \bar{v}\frac{\partial \hat{v}}{\partial y} + \hat{v}\frac{\partial \bar{v}}{\partial y} + \\
&= -\frac{1}{\rho}\frac{\partial \bar{p}}{\partial y} + \nu\left(\frac{\partial^2 \bar{v}}{\partial x^2} + \frac{\partial^2 \bar{v}}{\partial y^2}\right) - \frac{1}{\rho}\frac{\partial \hat{p}}{\partial y} + \nu\left(\frac{\partial^2 \hat{v}}{\partial x^2} + \frac{\partial^2 \hat{v}}{\partial y^2}\right) + \\
&g\gamma(\bar{T} - \bar{T}_0)^2 + g\gamma([\bar{T} - \bar{T}_0] + \hat{T})^2,
\end{aligned} \tag{8.14}$$

$$\begin{aligned}
&\left(\frac{\partial \bar{T}}{\partial t} + \bar{u}\frac{\partial \bar{T}}{\partial x} + \bar{v}\frac{\partial \bar{T}}{\partial y}\right) + \left(\frac{\partial \hat{T}}{\partial t} + \hat{u}\frac{\partial \hat{T}}{\partial x} + \hat{v}\frac{\partial \hat{T}}{\partial y}\right) + \bar{u}\frac{\partial \hat{T}}{\partial x} + \hat{u}\frac{\partial \bar{T}}{\partial x} + \bar{v}\frac{\partial \hat{T}}{\partial y} + \hat{v}\frac{\partial \bar{T}}{\partial y} + \\
&= \frac{k}{\rho c_p}\left[\left(\frac{\partial^2 \bar{T}}{\partial x^2} + \frac{\partial^2 \bar{T}}{\partial y^2}\right) + \left(\frac{\partial^2 \hat{T}}{\partial x^2} + \frac{\partial^2 \hat{T}}{\partial y^2}\right)\right].
\end{aligned} \tag{8.15}$$

Subtracting Eqs. (8.12)–(8.15) from Eqs. (8.6)–(8.9), respectively, the disturbance equations are ob-

tained. From these equations, the linearised form of disturbance equations for two-dimensional disturbances are derived as,

$$\frac{\partial \hat{u}}{\partial x} + \frac{\partial \hat{v}}{\partial y} = 0, \tag{8.16}$$

$$\frac{\partial \hat{u}}{\partial t} + \bar{u}\frac{\partial \hat{u}}{\partial x} + \hat{u}\frac{\partial \bar{u}}{\partial x} + \bar{v}\frac{\partial \hat{u}}{\partial y} + \hat{v}\frac{\partial \bar{u}}{\partial y} = -\frac{1}{\rho}\frac{\partial \hat{p}}{\partial x} + \nu\left(\frac{\partial^2 \hat{u}}{\partial x^2} + \frac{\partial^2 \hat{u}}{\partial y^2}\right), \tag{8.17}$$

$$\frac{\partial \hat{v}}{\partial t} + \bar{u}\frac{\partial \hat{v}}{\partial x} + \hat{u}\frac{\partial \bar{v}}{\partial x} + \bar{v}\frac{\partial \hat{v}}{\partial y} + \hat{v}\frac{\partial \bar{v}}{\partial y} = -\frac{1}{\rho}\frac{\partial \hat{p}}{\partial y} + \nu\left(\frac{\partial^2 \hat{v}}{\partial x^2} + \frac{\partial^2 \hat{v}}{\partial y^2}\right) + 2g\gamma(\bar{T} - \bar{T}_0)\hat{T}, \tag{8.18}$$

$$\frac{\partial \hat{T}}{\partial t} + \bar{u}\frac{\partial \hat{T}}{\partial x} + \hat{u}\frac{\partial \bar{T}}{\partial x} + \bar{v}\frac{\partial \hat{T}}{\partial y} + \hat{v}\frac{\partial \bar{T}}{\partial y} = \frac{k}{\rho c_p}\left(\frac{\partial^2 \hat{T}}{\partial x^2} + \frac{\partial^2 \hat{T}}{\partial y^2}\right). \tag{8.19}$$

The above equations (8.16)–(8.19) are governing equations for 2D disturbance of mixed convection flows.

To reduce the number of unknowns in the calculations, the formulation is carried out in stream function form. Hence, the disturbance velocities in the form of disturbance stream function are taken as,

$$\hat{u} = \frac{\partial \hat{\psi}}{\partial y}, \quad \hat{v} = -\frac{\partial \hat{\psi}}{\partial x}. \tag{8.20}$$

For global stability analysis, the disturbance stream function ($\hat{\psi}$) and temperature ($\hat{T}$) are written in normal mode form as,

$$\hat{\psi}(x, y, t) = \bar{\phi}(x, y)e^{-i\bar{\omega}t}, \quad \hat{T}(x, y, t) = s(x, y)e^{-i\bar{\omega}t}. \tag{8.21}$$

Using Eq. (8.20) and (8.21) in disturbance equations and after rearranging the terms, the disturbance equation of momentum and energy equations are derived as follows.

$$\left[\nu\left(\frac{\partial^4}{\partial x^4} + 2\frac{\partial^4}{\partial x^2 \partial y^2} + \frac{\partial^4}{\partial y^4}\right) - \left(\bar{u}\frac{\partial}{\partial x} + \bar{v}\frac{\partial}{\partial y}\right)\left(\frac{\partial^2}{\partial x^2} + \frac{\partial^2}{\partial y^2}\right) - \left(\frac{\partial^2 \bar{v}}{\partial x \partial y} - \frac{\partial^2 \bar{u}}{\partial y^2}\right)\frac{\partial}{\partial x} - \left(\frac{\partial^2 \bar{u}}{\partial x \partial y} - \frac{\partial^2 \bar{v}}{\partial y^2}\right)\frac{\partial}{\partial y}\right]\bar{\phi} + \left[2\left((\bar{T} - \bar{T}_0)\frac{\partial}{\partial x} + \frac{\partial(\bar{T} - \bar{T}_0)}{\partial x}\right)\right]s = -i\bar{\omega}\nabla^2\bar{\phi}, \tag{8.22}$$

$$\left[\frac{\partial \bar{T}}{\partial y}\frac{\partial}{\partial x} - \frac{\partial \bar{T}}{\partial x}\frac{\partial}{\partial y}\right]\bar{\phi} + \left[\frac{k}{\rho c_p}\left(\frac{\partial^2}{\partial x^2} + \frac{\partial^2}{\partial y^2}\right) - \bar{u}\frac{\partial}{\partial x} - \bar{v}\frac{\partial}{\partial y}\right]s = -i\bar{\omega}s. \tag{8.23}$$

The above equations show the dimensional form of two-dimensional disturbance equations.

To convert the dimensional form of governing equations into dimensionless form, the following dimensionless parameters are taken,

$$X = \frac{x}{L}, \quad Y = \frac{y}{L}, \quad U_{\text{ref}} = u_0, \quad U = \frac{\bar{u}}{u_0}, \quad V = \frac{\bar{v}}{u_0}, \quad P = \frac{\bar{p}}{\rho u_0^2}, \quad \theta = \frac{\bar{T} - T_0}{\Delta \bar{T}},$$
$$\lambda = \frac{\bar{\lambda}}{u_0/L}, \quad U = \frac{u}{u_0}, \quad V = \frac{v}{u_0}, \quad P = \frac{p}{\rho u_0^2}, \quad \phi = \frac{\bar{\phi}}{u_0 L}, \quad S = \frac{s}{\Delta \bar{T}}. \tag{8.24}$$

where, $\Delta\bar{T} = \bar{T_H} - \bar{T_C}$.

Using the dimensionless parameters from Eq. (8.24) in governing equations (8.6)–(8.9), the dimensionless form of governing equations are,

$$\begin{aligned}
\frac{\partial U}{\partial X} + \frac{\partial V}{\partial Y} &= 0, \\
U\frac{\partial U}{\partial X} + V\frac{\partial U}{\partial Y} &= -\frac{\partial P}{\partial X} + \frac{1}{Re}\left(\frac{\partial^2 U}{\partial X^2} + \frac{\partial^2 U}{\partial Y^2}\right), \\
U\frac{\partial V}{\partial X} + V\frac{\partial V}{\partial Y} &= -\frac{\partial P}{\partial Y} + \frac{1}{Re}\left(\frac{\partial^2 V}{\partial X^2} + \frac{\partial^2 V}{\partial Y^2}\right) + \frac{Gr}{Re^2}\theta^2, \\
U\frac{\partial \theta}{\partial X} + V\frac{\partial \theta}{\partial Y} &= \frac{1}{RePr}\left(\frac{\partial^2 \theta}{\partial X^2} + \frac{\partial^2 \theta}{\partial Y^2}\right),
\end{aligned} \tag{8.25}$$

where, $Re = \dfrac{u_0 L}{\nu}$, $Gr = \dfrac{g\gamma(\Delta\bar{T})^2 L^3}{\nu^2}$, $Pr = \dfrac{\nu}{\alpha_f}$ and $\alpha_f = \dfrac{k}{\rho c_p}$.

For the disturbance equations, using the dimensionless parameters given by Eq. (8.24) in Eqs. (8.22)–(8.23), the dimensionless form of disturbance equations are derived as,

$$\left[\frac{1}{Re}\nabla^4 - \left(U\frac{\partial}{\partial X} + V\frac{\partial}{\partial Y}\right)\nabla^2 - \left(\frac{\partial^2 V}{\partial X \partial Y} - \frac{\partial^2 U}{\partial Y^2}\right)\frac{\partial}{\partial X} - \left(\frac{\partial^2 U}{\partial X \partial Y} - \frac{\partial^2 V}{\partial X^2}\right)\frac{\partial}{\partial Y}\right]\phi + \left[2\frac{Gr}{Re^2}\left(\theta\frac{\partial}{\partial X} + \frac{\partial \theta}{\partial X}\right)\right] S = \lambda\nabla^2\phi, \tag{8.26}$$

$$\left[\frac{\partial \theta}{\partial Y}\frac{\partial}{\partial X} - \frac{\partial \theta}{\partial X}\frac{\partial}{\partial Y}\right]\phi + \left[\frac{1}{RePr}\left(\frac{\partial^2}{\partial X^2} + \frac{\partial^2}{\partial Y^2}\right) - U\frac{\partial}{\partial X} - V\frac{\partial}{\partial Y}\right] S = \lambda S, \tag{8.27}$$

where, differential operator $\nabla^2 = \dfrac{\partial^2}{\partial X^2} + \dfrac{\partial^2}{\partial Y^2}$ and $\nabla^4 = \dfrac{\partial^4}{\partial X^4} + 2\dfrac{\partial^4}{\partial X^2 \partial Y^2} + \dfrac{\partial^4}{\partial Y^4}$. The above equations (8.26) and (8.27) are dimensionless form of governing equations for linear global stability of two-dimensional mixed convection flows of water near the density inversion.

8.3.1 Boundary conditions

Base flows: The top wall of cavity is moving with uniform velocity u_0 along positive x-direction while the normal velocity of the top wall is zero. No slip and no penetration conditions prevail at the remaining walls of the cavity. Initially, the water in the cavity is at rest and the temperature is at T_0. The left wall of the cavity is heated at higher temperature T_H while cavity is cooled at the right wall with temperature T_C. The remaining walls of the cavity are adiabatic. Mathematically, the dimensional form of boundary conditions for base flow can be written as,

$$\text{At} \quad x = 0, \quad u = 0, \quad v = 0, \quad T = T_H = T_0 + \Delta T/2, , \tag{8.28}$$

$$\text{At} \quad x = L, \quad u = 0, \quad v = 0, \quad T = T_C = T_0 - \Delta T/2, \tag{8.29}$$

$$\text{At} \quad y = 0, \quad u = 0, \quad v = 0, \quad \frac{\partial T}{\partial y} = 0, \tag{8.30}$$

$$\text{At} \quad y = L, \quad u = u_0, \quad v = 0, \quad \frac{\partial T}{\partial y} = 0. \tag{8.31}$$

Using the dimensionless parameters from Eq. (8.24), the above dimensional form of boundary conditions are converted into dimensionless forms which are as follows,

$$\text{At} \quad X = 0, \quad U = 0, \quad V = 0, \quad \theta = \quad 0.5, \tag{8.32}$$

$$\text{At} \quad X = 1, \quad U = 0, \quad V = 0, \quad \theta = -0.5, \tag{8.33}$$

$$\text{At} \quad Y = 0, \quad U = 0, \quad V = 0, \quad \frac{\partial \theta}{\partial Y} = 0, \tag{8.34}$$

$$\text{At} \quad Y = 1, \quad U = 1, \quad V = 0, \quad \frac{\partial \theta}{\partial Y} = 0. \tag{8.35}$$

Disturbance flows: The normal and streamwise components of disturbance velocity at all the walls of cavity are zero. The disturbance of temperature at the hot and cold walls are zero. For adiabatic walls of cavity, the gradient of disturbance temperature is zero. Mathematically, the boundary conditions for disturbance flows in dimensional form are given below

$$\text{At} \quad x = 0, \quad \hat{u} = 0, \quad \hat{v} = 0, \quad \hat{T} = 0, \tag{8.36}$$

$$\text{At} \quad x = L, \quad \hat{u} = 0, \quad \hat{v} = 0, \quad \hat{T} = 0, \tag{8.37}$$

$$\text{At} \quad y = 0, \quad \hat{u} = 0, \quad \hat{v} = 0, \quad \frac{\partial \hat{T}}{\partial y} = 0, \tag{8.38}$$

$$\text{At} \quad y = L, \quad \hat{u} = 0, \quad \hat{v} = 0, \quad \frac{\partial \hat{T}}{\partial y} = 0. \tag{8.39}$$

Since, the disturbance governing equations of mixed convection flow are solved in stream function form, the above boundary conditions in the form of disturbance stream function converted using Eqs. (8.20)–(8.21) which are,

$$\text{At} \quad x = 0, \quad \hat{\phi} = 0, \quad \frac{\partial \hat{\phi}}{\partial x} = 0, \quad \hat{T} = 0, \tag{8.40}$$

$$\text{At} \quad x = L, \quad \hat{\phi} = 0, \quad \frac{\partial \hat{\phi}}{\partial x} = 0, \quad \hat{T} = 0, \tag{8.41}$$

$$\text{At} \quad y = 0, \quad \hat{\phi} = 0, \quad \frac{\partial \hat{\phi}}{\partial y} = 0, \quad \frac{\partial \hat{T}}{\partial y} = 0, \tag{8.42}$$

$$\text{At} \quad y = L, \quad \hat{\phi} = 0, \quad \frac{\partial \hat{\phi}}{\partial y} = 0, \quad \frac{\partial \hat{T}}{\partial y} = 0. \tag{8.43}$$

The above boundary conditions for disturbance flows are transformed into dimensionless form using Eq. (8.24), which are following,

$$\text{At} \quad X = 0, \quad \phi = 0, \quad \frac{\partial \phi}{\partial X} = 0, \quad S = 0, \tag{8.44}$$

$$\text{At} \quad X = 1, \quad \phi = 0, \quad \frac{\partial \phi}{\partial X} = 0, \quad S = 0, \tag{8.45}$$

$$\text{At} \quad Y = 0, \quad \phi = 0, \quad \frac{\partial \phi}{\partial Y} = 0, \quad \frac{\partial S}{\partial Y} = 0, \tag{8.46}$$

$$\text{At} \quad Y = 1, \quad \phi = 0, \quad \frac{\partial \phi}{\partial Y} = 0, \quad \frac{\partial S}{\partial Y} = 0. \tag{8.47}$$

8.4 Numerical methodology

8.4.1 Base flow

The base flow governing equations are discretised using Finite Volume Method (FVM). The details of solution methodology followed for the base flow computation is given in Patankar [152]. Base flow calculations are carried out by discretising the base flow governing equations using FVM. The discretisation is carried out using staggered grid. All scalar quantities are defined at the cell center of control volume. x and y components of velocity are staggered in their respective directions from the scaler control volume. Second order upwind scheme is used for the convective terms. Second order central difference scheme is used to discretise the diffusive and pressure terms. The solutions are obtained for the steady state. SIMPLE algorithm is used for overall solution procedure to find the appropriate pressure and velocities, so that the momentum and continuity equations are satisfied. The resultant system of linear equations obtained from the discretisation of governing equations are solved using Tri-Diagonal Matrix Algorithm (TDMA) solver. TDMA sweeps are performed in x and y-directions alternatively. The iteration is continued until the maximum value of the error of continuity equation in the domain falls below 10^{-5}.

8.4.2 Disturbance equations

The disturbance equations of mixed convection (Eqs. (8.26) and (8.27)) consist of partial differentials in x and y-directions. The discretisation of partial derivatives are carried out using Chebyshev spectral method. The Chebyshev spectral method works only in the square computational domain in the range of $[-1 \quad 1]\times[-1 \quad 1]$. However, the present physical system is in the range of $[0 \quad 1]\times[0 \quad 1]$. Hence, the following linear transformation is used between physical and computation domains according to the

$$\eta = 1 - 2x, \quad \xi = 1 - 2y. \tag{8.48}$$

The transformed differential equations are discretised using the Chebyshev differentiation. For the discretisation using Chebyshev differentiation, the Gauss-Lobatto points are used for the grid distribution in η and ξ coordinates. If $Nx + 1$ and $Ny + 1$ are the number of grid points used in η and ξ-directions, respectively, then the grid is distributed according to

$$\eta_i = \cos(\pi i/Nx) \quad i = 0, \ldots, Nx \tag{8.49}$$

$$\xi_j = \cos(\pi j/Ny) \quad j = 0, \ldots, Ny, \tag{8.50}$$

respectively, in η and ξ-directions.

The differentiation matrices of discretisation for partial differentials are obtained from the differential matrices of one dimensional differentiation matrices correspond to grid distribution of the individual coordinates. For example, in η computational direction, the differentiation matrix corresponds to one dimensional Gauss-Lobatto point distribution is D_η can be found from the expressions

of elements of differentiation matrix given by Eq.(5.55). The one dimensional differentiation matrix D_η is of size $(Nx+1)\times(Nx+1)$. Similarly, the differentiation matrix of one dimension D_ξ in ξ-direction, which is of the size $(Ny+1)\times(Ny+1)$ can be formed.

I_η and I_ξ are identity matrices of the size $(Nx+1)\times(Nx+1)$ and $(Ny+1)\times(Ny+1)$, respectively. Now, the differentiation matrices for partial derivatives of two-dimensional problem are formed using Kronecker products of the above D_η, D_ξ, I_η and I_ξ matrices. For example,

$$
\begin{aligned}
K_\eta &= \frac{\partial}{\partial\eta} = I_\xi \otimes D_\eta,\\
K_\xi &= \frac{\partial}{\partial\xi} = D_\xi \otimes I_\eta,\\
K_{\eta^2} &= \frac{\partial^2}{\partial\eta^2} = I_\xi \otimes D_\eta^2,\\
K_{\eta\xi} &= \frac{\partial^2}{\partial\eta\partial\xi} = D_\xi \otimes D_\eta,\\
K_{\xi^2} &= \frac{\partial^2}{\partial\xi^2} = D_\xi^2 \otimes I_\eta,\\
K_{\eta^3} &= \frac{\partial^3}{\partial\eta^3} = I_\xi \otimes D_\eta^3,\\
K_{\eta^2\xi} &= \frac{\partial^3}{\partial\eta^2\partial\xi} = D_\xi \otimes D_\eta^2,\\
K_{\eta\xi^2} &= \frac{\partial^3}{\partial\eta^2\partial\xi} = D_\xi^2 \otimes D_\eta,\\
K_{\xi^3} &= \frac{\partial^3}{\partial\xi^3} = D_\xi^3 \otimes I_\eta,\\
K_{\eta^4} &= \frac{\partial^4}{\partial\eta^4} = I_\xi \otimes D_\eta^4,\\
K_{\eta^2\xi^2} &= \frac{\partial^4}{\partial\eta^2\partial\xi^2} = D_\xi^2 \otimes D_\eta^2,\\
K_{\xi^4} &= \frac{\partial^4}{\partial\xi^4} = D_\xi^4 \otimes I_\eta,
\end{aligned}
\tag{8.51}
$$

where, K is Kronecker differentiation matrix and subscripts η and ξ represent the partial derivative with respect to these variables. In the above, $A \otimes B$ is Kronecker product of matrices A and B. Note that the resulting differentiation matrices of partial differentials formed using the above Kronecker product is of size $(Nx+1)(Ny+1)\times(Nx+1)(Ny+1)$.

The discretized disturbance equations (8.26)–(8.27) along with their boundary conditions (8.44)–(8.47) form an Eigenvalue problem. Circular frequency ω acts as an Eigenvalue of the problem which decides the global stability of the flow. Since, the disturbance is taken in the form $\phi(x,y,t) = \phi(x,y)e^{-i\omega t}$ (Eq. (8.21), the flow is stable if imaginary part of all the Eigenvalues

flow is stable: $\omega_i < 0$ for all Eigenvalues

flow is unstable: $\omega_i > 0$ atleast for one Eigenvalue

flow is neutrally stable: $\omega_i \leq 0$ for all and $\omega_i = 0$ for at least for one Eigenvalue

The resulting generalized Eigenvalue problem is solved using an open source linear solver package LAPACK.

8.4.3 Interpolation of base flow variables on to Eigenvalue grid

In the present study, the base flow is solved using FVM and the disturbance equations are solved using Chebyshev spectral method. The Chebyshev spectral method requires grid distribution in a specific manner given by Gauss-Lobatto point distribution in the individual computational directions. However, the grid for the discretisation for the base flow governing equations are different from the grid used for discretisation of disturbance equations. However, for the discretisation of disturbance equations, the base flow quantities and their derivatives at the Eigenvalue grid nodes are required. Since, the base flow grid and Eigenvalue grid nodes do not coincide each other, we need to transfer the base flow information to the Eigenvalue grid nodal points. In the present study, interpolation of the base flow quantities from the base flow grid to Eigenvalue grid is done using cubic splines. Such usage of cubic splines are done in Jotkar et al. [145].

Cubic spline interpolation is used to interpolate the base flow solutions on to Eigenvalue grids. The function of $f(x)$ at grid point i on base flow is expressed in the form of ([153]),

$$f_i(x) = a_i + b_i x + c_i x^2 + d_i x^3, \quad i = 1, 2, 3, \cdots, Nx, \tag{8.52}$$

where, Nx is number of grid points in x-direction. a_i, b_i, c_i and d_i are constants which need to be calculated to fit a cubic splines. These constants are calculated by imposing known values of f_{i-1}, f_i and f_{i+1} at base flow grid nodal points x_{i-1}, x_i and x_{i+1}. Once, the constants are found, the value of $f(x)$ at x values which are not on the base flow grid are calculated.

The final form of interpolation can be expressed by ([153]),

$$\begin{aligned} f_i(x) = & \frac{f''_{i-1}}{6(x_i - x_{i-1})}(x_i - x)^3 + \frac{f''_i}{6(x_i - x_{i-1})}(x - x_{i-1})^3 \\ & + \left[\frac{f_{i-1}}{x_i - x_{i-1}} - \frac{f''_{i-1}}{6}(x_i - x_{i-1})\right](x_i - x) \\ & + \left[\frac{f_i}{x_i - x_{i-1}} - \frac{f''_i}{6}(x_i - x_{i-1})\right](x - x_{i-1}). \end{aligned} \tag{8.53}$$

In the above, x_{i-1}, x_i and x_{i+1} are the nodal points on base flow grid at which the base flow quantities represented by f_{i-1}, f_i and f_{i+1}, respectively are known from the base flow computation. x is the coordinate of the grid node on Eigenvalue grid to which the interpolation is carried out. The quantities f''_{i-1}, f''_i and f''_{i+1} in the above, are calculated using second order finite difference method.

8.5 Code validations

8.5.1 Validation of base flow solver

The base flow code is validated by solving mixed convection flow of air in a lid driven square cavity for various Reynolds and Grashof numbers. The physical system of validation problem in shown in Fig. 8.2. The top wall moves with uniform velocity and the remaining walls are stationary. The cavity is heated at the top wall while it is cooled at the bottom wall. The left and right walls are insulated. The average Nusselt numbers along the top wall obtained from the present solver are compared with

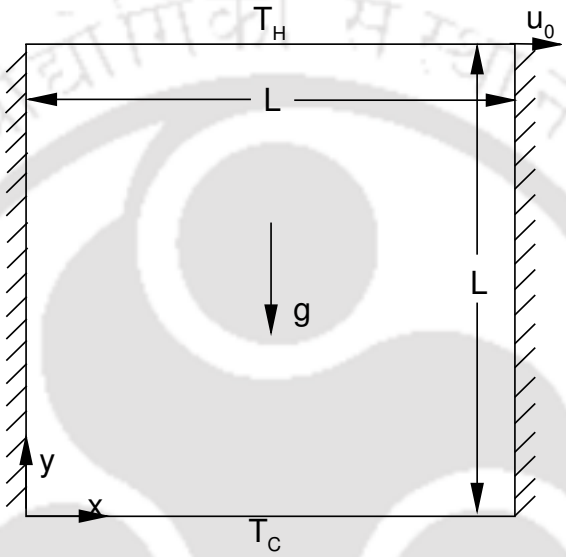

Figure 8.2: Schematic for the validation of mixed convection flow in square cavity

those available in the literature which is presented in table 8.1 for various Reynolds and Grashof numbers. In the table, the present results agree well with those of reference values.

Table 8.1: Validation of the base flow solver: Average Nusselt numbers of mixed convection along top wall of a lid driven square cavity

Re	Author('s)	$Gr = g\beta\Delta TL^3/\nu^2$		
		10^2	10^4	10^6
400	Present study	4.35	3.91	1.21
	Cheng [154]	4.14	3.90	1.21
	Sharif [155]	4.05	3.82	1.17
1000	Present study	6.85	6.73	1.82
	Cheng [154]	6.73	6.68	1.75
	Sharif [155]	6.55	6.50	1.81

8.5.2 Validation of stability solver

The stability solver of the global stability analysis is carried out by solving the global stability of lid driven cavity. The global stability of lid driven cavity flow is reported by many authors such as [113,150,151]. The lid driven cavity is a square cavity with top wall moving with uniform velocity, while all the other walls are stationary as shown in Fig. 8.3.

Figure 8.3: Schematic of lid driven cavity flow for the validation of global stability analysis

The critical value of Reynolds number and the corresponding most unstable Eigenvalue of lid driven cavity from the present study is compared with the values presented in references [113, 150, 151], is shown in table 8.2. It can be seen from table 8.2 that values of critical Reynolds number and critical Eigenvalue of present study, agree with the reference results. From the table, it can be observed that the smaller the real part of ω_{cr} we target for, slightly higher the critical Reynolds number we obtain. Since, the present study and the study by Fortin et al. [151], the targeted ω_r is of the order of 10^{-5}, the present results match very close to those of Fortin et al. [151]. If we had targeted for ω_r to be of the order of 10^{-6}, the present results would have been close to those of Bopanna and Gajjar [113] and Kalita and Gogoi [150]. The contours of real and imaginary part of critical disturbance stream

Table 8.2: Validation: Comparison of critical Reynolds number (Re_{cr}) and critical Eigenvalue (ω_{cr})

Author('s)	Re_{cr}	ω_{cr}
Bopanna and Gajjar [113]	8026.6	$2.620 \times 10^{-6} \pm 2.8356i$
Kalita and Gogoi [150]	8025.9	$2.340 \times 10^{-7} \pm 2.8164i$
Fortin et al. [151]	8000.0	$5.477 \times 10^{-5} \pm 2.8356i$
Present study	7995.0	$6.537 \times 10^{-5} \pm 2.8475i$

function from the present study are compared with the contours of Bopanna and Gajjar [113]. The present results are found to be in good agreement with the reference Eigenfunction contours (Not shown).

8.6 Grid sensitivity tests

After conducting the grid sensitivity tests, the grid size of 151×151 is selected for the base flow computation of the present study. In global stability analysis, the Eigenvalue problem requires huge amount of computation. Hence, the selection of Eigenvalue grid size is crucial in the global stability analysis computations. To find the suitable grid, grid sensitivity tests are conducted for the Eigenvalue problem using grid sizes of 41×41, 61×61 and 81×81. It is found for most of the Richardson numbers 61×61 grid provides sufficiently accurate results for Richardson number greater than 2. However, it is found that for Richardson number in the range 0 to 0.4, the spurious Eigenvalues appear as the most unstable Eigenvalues for grid of size less than 101×101. For such range of Richardson numbers, computations are carried out using 101×101 grid size.

8.7 Base flow solutions

The global stability analysis is carried out for Richardson numbers ranging from 0 to 200. For every Richardson number, the flow is solved for various Reynolds number to find the critical Reynolds number. For every simulation of stability equations, the base flow needs to be solved. The stability characteristics of the flow strongly depend on the structure of the base flow. Here, the main features of the base flow are briefly presented using stream function and temperature contour plots. Note that in the stream function contours, solid line represents the contours with negative stream function value. The re-circulations encircled by negative stream function values and the recirculations encircled by positive stream function values rotate in opposite direction. The temperature contours with negative values are plotted with dotted lines to emphasis the region occupied with temperatures that are on the left side of the density inversion point in density variation with temperature. Similarly, isotherms with positive temperature values are plotted with solid lines indicating temperatures on the right side of the density inversion point.

To visualize the variation of flow and thermal fields with varying Richardson number, stream function contours and temperature contours are shown in Fig. 8.4 and 8.5, respectively, for various increasing Richardson numbers. All the contours shown in the above figure are for a fixed Reynolds number value of 1800. Fig. 8.4 shows stream function contours for $Ri = 0$, which is a forced convection asymptote solution. The flow is characterized with a primary recirculation which occupies most of the cavity which is centered near the center of the cavity. Along with this primary recirculation, there are two smaller re-circulations at left-bottom and right-bottom corners of the cavity. These recirculations are formed due to the flow separations from the walls. When Richardson number increased to $Ri = 0.3$, the left-bottom recirculation is replaced with two counter rotating recirculations. Let the recirculation at the left-bottom corner is denoted with R1 and its associated recirculation is R2. The right-bottom recirculation is R3. The size and the location of all the recirculations depends on the values of Richardson and Reynolds numbers. With increasing Richardson number, the sizes of R2 and R3 increases and merge each other forming a single resultant re-circulation on the bottom wall at about $Ri = 0.46$. Further increase in Richardson number, increases the size of the lower recirculation.

The base flow temperature contours corresponding to the above described stream function con-

tours are shown in Fig. 8.5. The temperature in the primary recirculation is almost uniform as the velocities in the primary recirculations are large compared to the velocities in the other recirculations. The primary recirculation is associated with negative value of dimensionless temperature indicating temperatures on the left side of density inversion point in the density versus temperature profile. With increasing Richardson number, primary recirculation temperature increases towards the density maximum point (zero dimensionless temperature). For $Ri = 0.3$ to 1.25, most of the cavity is occupied with negative dimensionless temperatures. For $Ri = 2.5$, the temperatures of negative and positive values equally occupied in the cavity.

Some more base flow solutions will be presented in the stability solutions section (section 8.8) wherever is necessary for the explanation and interpretation of the global stability solutions.

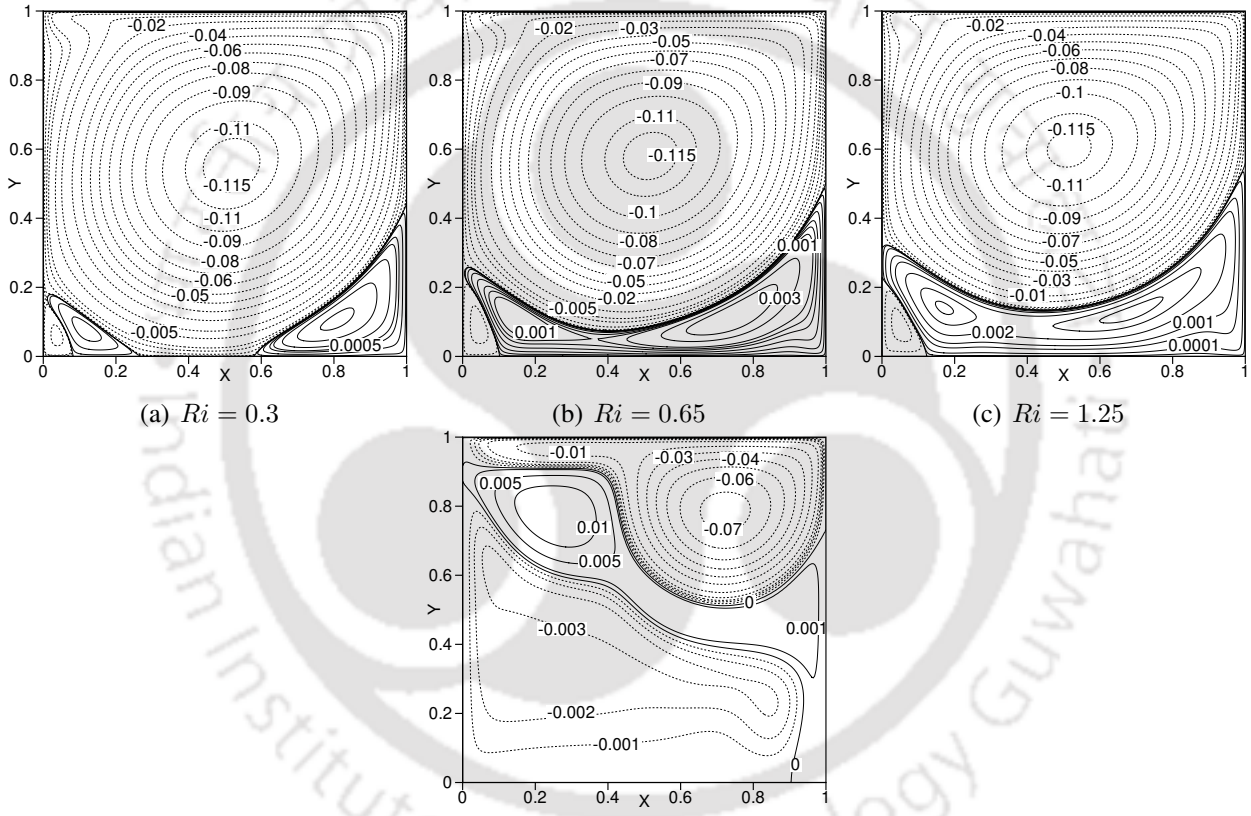

(a) $Ri = 0.3$ (b) $Ri = 0.65$ (c) $Ri = 1.25$

(d) $Ri = 2.5$

Figure 8.4: Stream function contours of base flow for $Re = 1800$

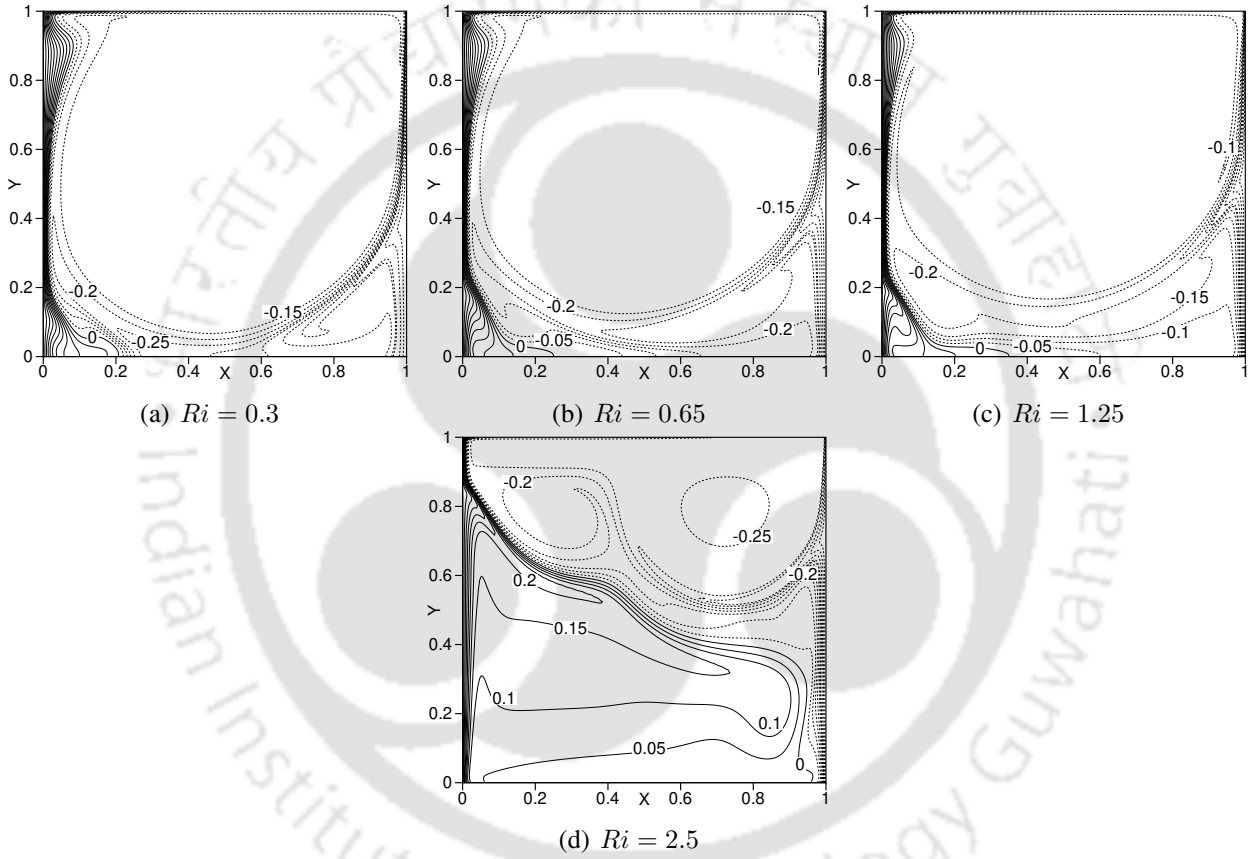

(a) $Ri = 0.3$ (b) $Ri = 0.65$ (c) $Ri = 1.25$

(d) $Ri = 2.5$

Figure 8.5: Temperature contours of base flow for $Re = 1800$

8.8 Stability solutions

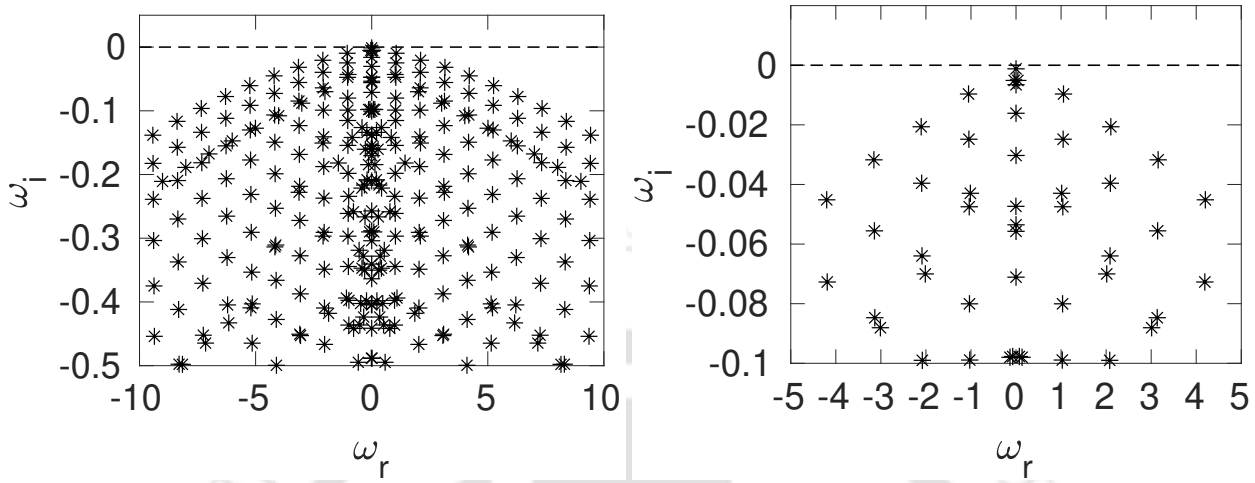

(a) Few most unstable Eigenvalues

(b) Zoomed view near real axis

Figure 8.6: Eigenvalue spectrum for $Ri = 5$, $Re = 100$

A typical Eigenvalue spectrum is shown in Fig. 8.6(a) which is computed for $Ri = 5$ and $Re = 100$. The structure of the Eigenvalue spectrum is similar to the spectrum of lid driven cavity flow without heat transfer. The spectrum consists of bow shaped branches. Such spectrum is inherent for the lid driven cavity flows. Such spectrum is reported in the studies of isothermal lid driven cavity flows in the studies of Bopanna and Gajjar [113], Kalita and Gogoi [150], Fortin et. al [151], Ramanan and Homsy [105] and Theofilis [110]. The spectrum is symmetric with respect to imaginary ω axis. Due to the existence of symmetry, all the Eigenvalues should have either zero real part or should be associated with a complex conjugate Eigenvalue. This means the critical mode should be either have zero real part or should be a pair of complex conjugate Eigenvalues. The existence of the symmetry of Eigenvalue spectrum comes from the fact that all the elements of matrices of disturbance Eigenvalue problem given by Eqs. (8.26)–(8.27) are real numbers. First few most unstable Eigenvalues are shown in subfigure 8.6(b). If the Eigenvalue containing the largest imaginary part has negative imaginary part then the flow is stable, and if it is positive then the flow is unstable. Otherwise the flow is neutrally stable.

Few most unstable Eigenvalues for $Ri = 0.2$ and $Re = 4522.12$ are plotted in Fig. 8.7(a) and the most unstable modes are marked with symbols A, B, C and D. The Eigen functions of the disturbance stream function and temperature corresponding to the marked modes are shown in Fig. 8.8. The A, B and D modes are with pure imaginary numbers and C mode is associated with pair of complex conjugate numbers. Similarly, few most unstable Eigenvalues for $Ri = 5$ and $Re = 172.17$ are shown in Fig. 8.7(b). Different modes are marked with symbols A, B, C and D. The Eigen functions of the disturbance stream function and temperature for the marked Eigen modes are presented in Fig. 8.9.

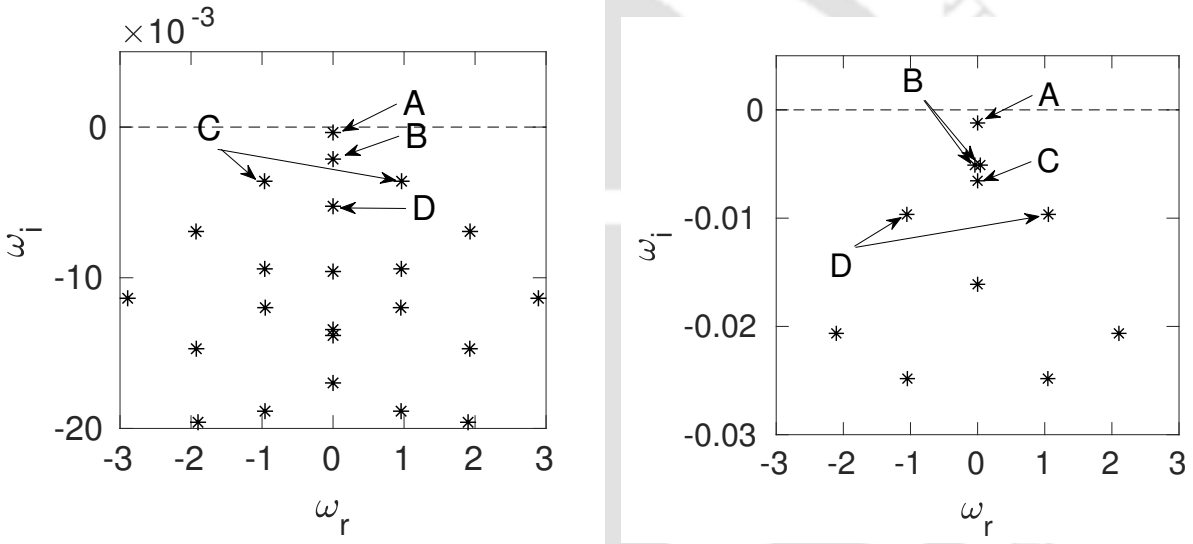

(a) $Ri = 0.2$, $Re = 4522.12$ (b) $Ri = 5$, $Re = 172.17$

Figure 8.7: Few most unstable Eigenvalues for $Ri = 0.2$ and $Ri = 5$

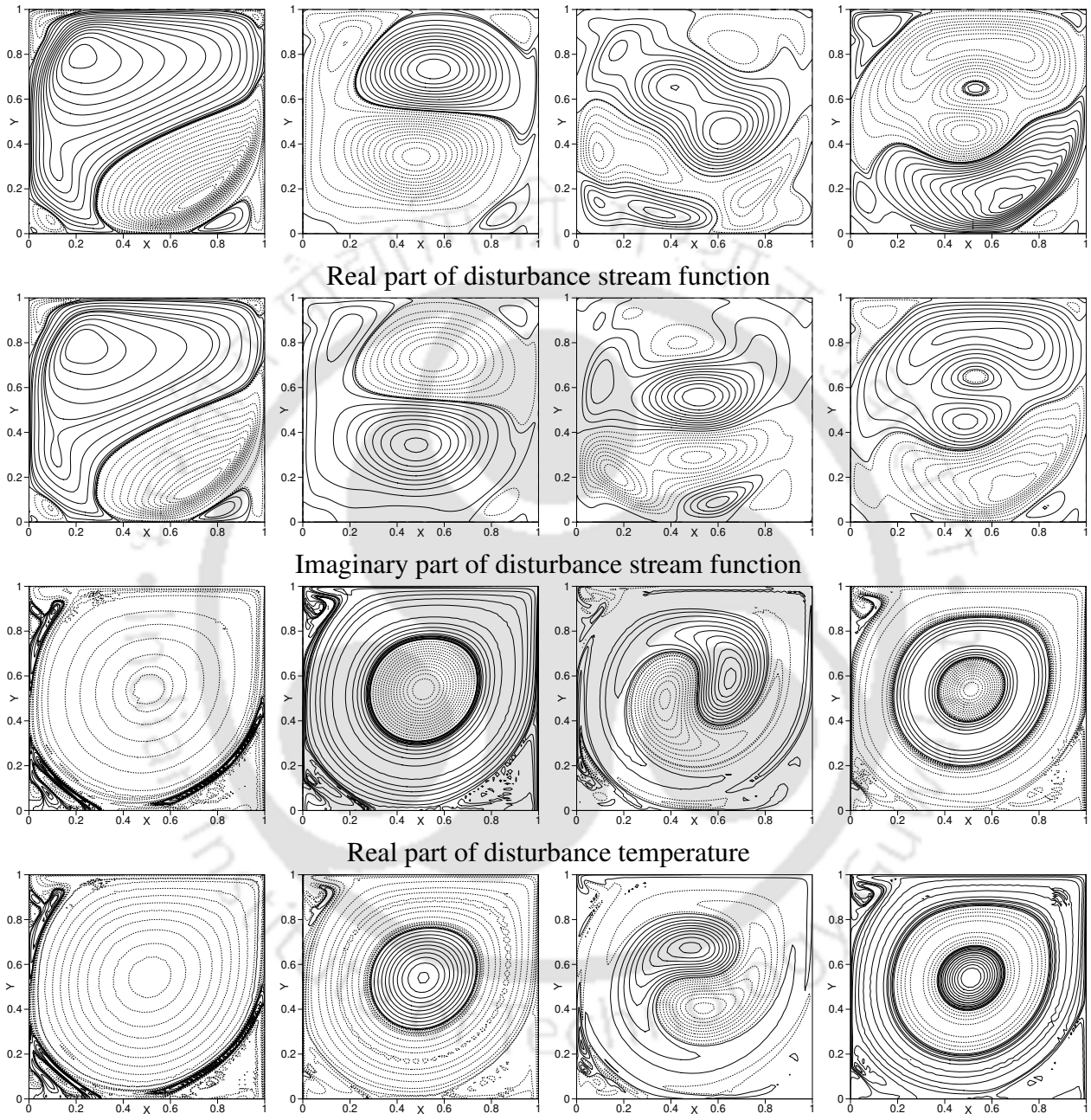

Figure 8.8: Disturbance stream function and temperature contours for $Ri = 0.2$ and $Re = 4522.12$

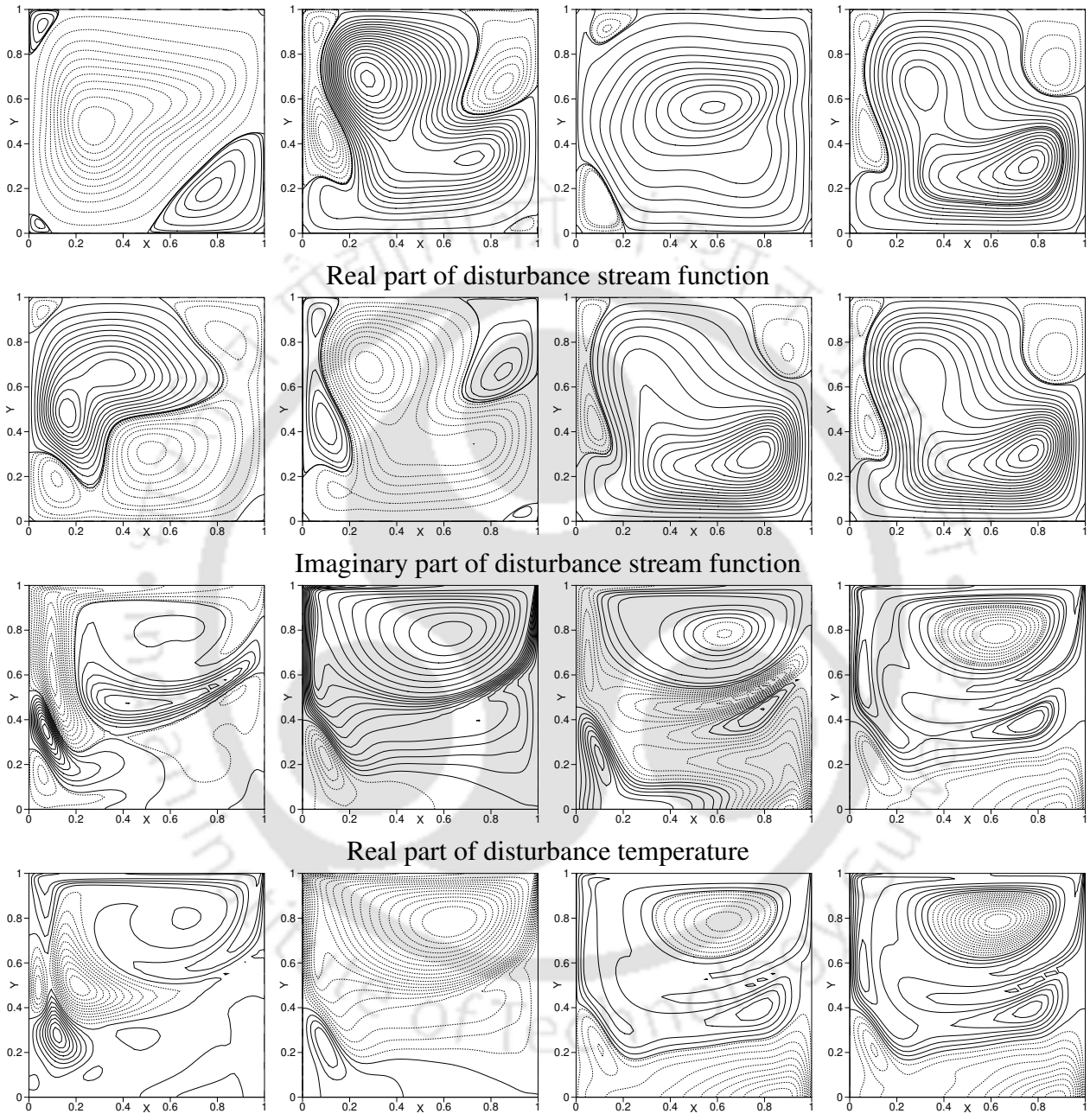

Figure 8.9: Disturbance stream function and temperature contours for $Ri = 5$ and $Re = 172.17$

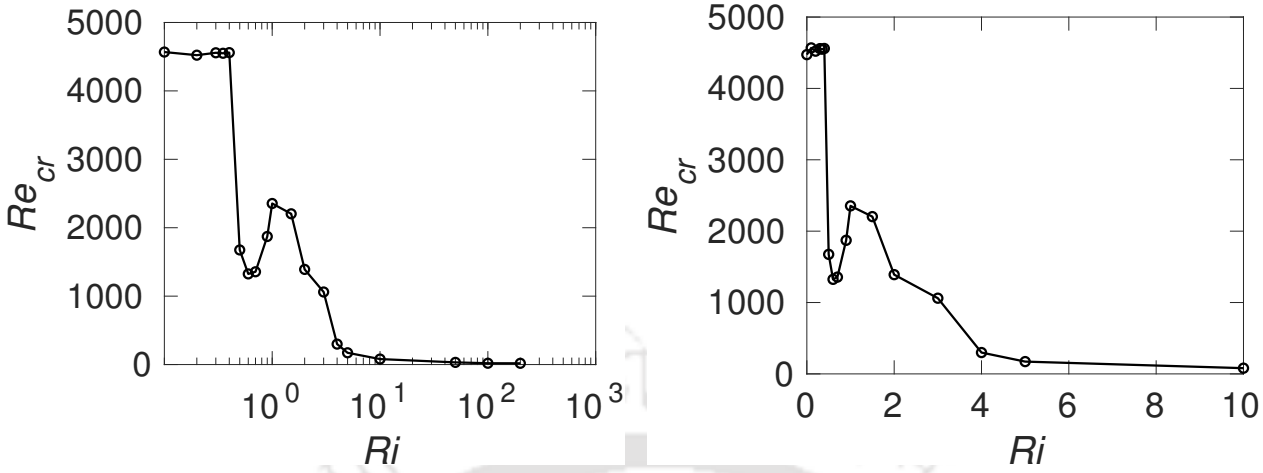

(a) $Ri = 0$ to 200 (log scale for Ri) (b) Enlarged view, $Ri = 0$ to 10 (linear scale for Ri)

Figure 8.10: Variation of critical Reynolds number with Richardson number

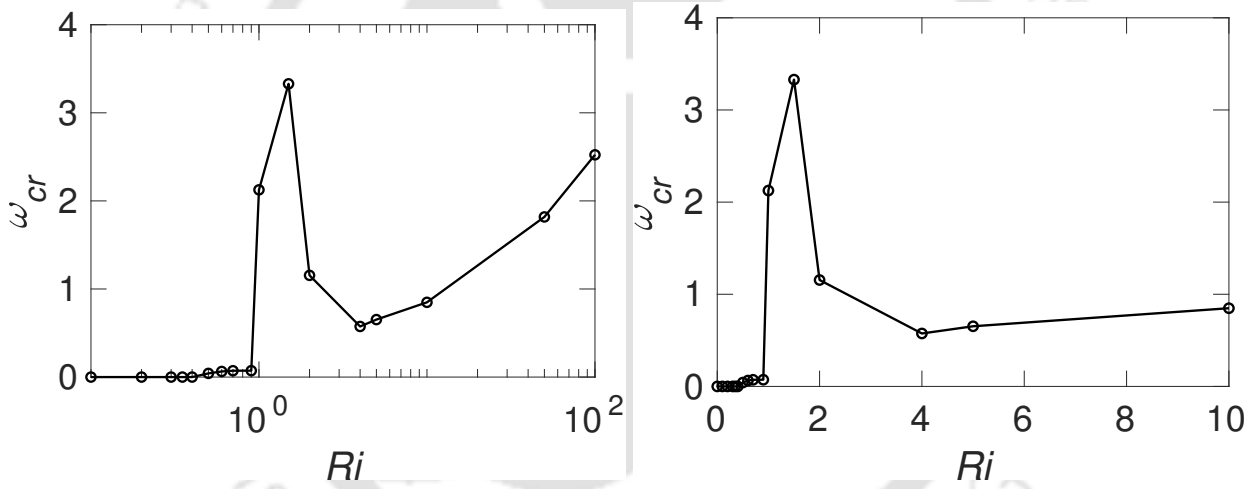

(a) log scale for Ri (b) Enlarged view, (linear scale for Ri)

Figure 8.11: Variation of real part of critical frequency of disturbance with Richardson number

The variation of critical Reynolds number with Richardson number is shown in Fig. 8.10. The enlarged plot for the range $Ri = 0$ to 10 is shown in Fig. 8.10(b) with linear scale for Richardson number. The corresponding values of critical Reynolds number and critical circular frequency (ω) are presented in the table 8.3. The critical Reynolds number decreases from 4773.4 to 4545 when the Ri is increased from 0 to 0.4. This means the addition of buoyancy forces makes the flow unstable. When Richardson number slightly increased from 0.4 to 0.5, the critical Reynolds number decreases from 4545 to 1675 (about 36%). This means that at this Ri value range, the flow stability drastically decreases. The reasons for such drastic change will be discussed in more details below. When Ri is increased from 0.5 to 1, flow regains stability and the critical Reynolds number increases from 1675 to 2354.23 . When Richardson number is varied from 1 to 10, critical Reynolds number decreases from 2354.23 to 80.21. For $Ri > 10$, critical Reynolds number decreases slowly.

Table 8.3: The critical Reynolds number (Re_{cr}) and critical value of ω for various Ri values

Ri	Re_{cr}	Most unstable Eigenvalue
0	4473.45	$-3.91465 \times 10^{-4} - 4.19779 \times 10^{-10}i$
0.1	4567.75	$-3.70831 \times 10^{-4} - 4.99096 \times 10^{-10}i$
0.2	4522.125	$-3.60097 \times 10^{-4} - 2.20151 \times 10^{-10}i$
0.3	4557.175	$-3.43154 \times 10^{-4} + 2.04839 \times 10^{-10}i$
0.4	4559.375	$-3.53363 \times 10^{-4} + 2.86642 \times 10^{-10}i$
0.5	1675.0	$6.97964 \times 10^{-5} \pm 0.041772i$
0.6	1325.0	$-6.88641 \times 10^{-5} \pm 0.063620i$
0.7	1356.25	$-2.97026 \times 10^{-5} \pm 0.072030i$
0.9	1871.875	$-2.65557 \times 10^{-5} \pm 0.072843i$
1	2354.230	$7.14222 \times 10^{-5} \pm 2.125538i$
1.5	2203.688	$-9.58021 \times 10^{-4} \pm 3.329227i$
2	1390.742	$9.80674 \times 10^{-5} \pm 1.154707i$
3	1060.625	$-7.27718 \times 10^{-5} \pm 1.334877i$
4	298.9180	$4.13252 \times 10^{-5} \pm 0.5744296i$
5	172.1680	$-6.76206 \times 10^{-5} \pm 0.6526086i$
10	80.21118	$-3.19893 \times 10^{-5} \pm 0.8486098i$
50	31.83629	$-6.39553 \times 10^{-5} \pm 1.817935i$
100	19.20868	$-4.69154 \times 10^{-6} \pm 2.523139i$
200	18.39179	$-2.96106 \times 10^{-6} \pm 3.789852i$

The variation of critical frequency (ω_{cr}) with Richardson number is shown in Fig. 8.11 reveals that for the range of $Ri = 0 - 0.4$ and $Ri > 4$, the critical ω_{cr} slowly varies with Richardson number. For the range of $Ri = 0.4 - 1$, the sudden instability is associated with sharp increase in the frequency of most unstable mode. When the flow regains stability between $Ri = 1 - 4$, the frequency of most unstable mode decreases. Note that higher the frequencies for a given wave number in the third direction represents higher phase speed.

The Eigenvalue spectrum for $Ri = 0$ representing pure forced convection is shown in Fig. 8.12. In the forced convection flow, the momentum equation of the base flow and the disturbance equations are decoupled from their respective energy equation. The Eigenvalues shown in the figure are the combination of Eigenvalues which come from disturbance equations of both flow and temperature equations. To distinguish the Eigen modes which come from the flow from those originated from heat transfer, the Eigenvalue spectrum of flows without heat transfer is computed and superimposed in the figure. The circles in the Eigenvalue spectrum are the Eigenvalues come from the disturbance equations of both flow and heat transfer (Eqs. (8.26) and (8.27)). The star symbols are from the solution of lid driven cavity without heat transfer. The star symbols which coincide with the circles are the Eigenvalues originated from the hydrodynamic characteristics of the flow. Hence, they can be called as hydrodynamic modes. The star symbols which do not coincide with circle symbols are the Eigenvalues originated due to the heat transfer aspect of the convection. Clearly, the most unstable mode of pure forced convection with heat transfer is a thermal mode.

To verify whether the instability of lid driven cavity flows including heat transfer always originates

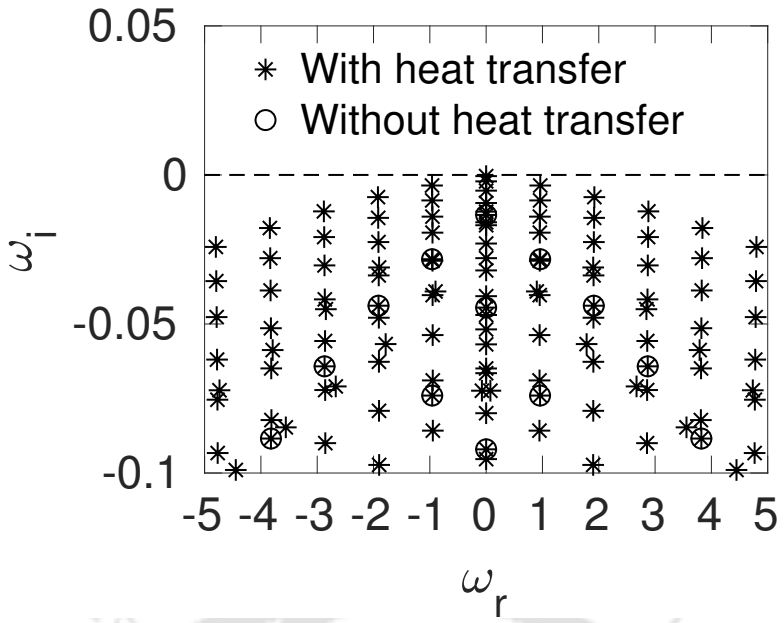

Figure 8.12: Comparison of Eigenvalue spectrum for with and without heat transfer for $Ri = 0$, $Re = 4473.3$

from thermal mode or not, the stability of lid driven flow with heat transfer is solved for various Prandtl numbers for $Ri = 0$. Out of solutions for many Prandtl numbers, the Eigenvalue spectrum corresponding to $Pr = 0.71$, $Pr = 3$ and $Pr = 11.57$ are shown in Fig. 8.13. In the figure, circles are the Eigenvalues of flows without heat transfer. The stars symbols are the Eigenvalues of flow including heat transfer. In the figure, the star symbols which coincide with circles are originated due to the hydrodynamic characteristics. The stars which do not coincide with circles are the Eigenvalues originated due to the temperature effect. In subfigure 8.13(a), the most unstable Eigenvalues are coinciding with the circles and hence, they are hydrodynamic modes. In subfigures 8.13(b)–8.13(c), the most unstable Eigenvalues indicated with stars do not coincide with the circles and hence, they are thermal modes. It is found that for $Pr < 3$, the most unstable mode is hydrodynamic mode and for $Pr > 3$, the most unstable mode is thermal mode.

The stream function contours of base flow for various Richardson number are plotted in Figs. 8.17 and 8.18. The corresponding temperature contours are presented in Figs. 8.19 and 8.19, respectively. For the Richardson number range 0 to 0.4 (shown in subfigures 8.17(a)–8.17(e)), the flow varies slightly. With increasing Richardson number, the left-bottom and right-bottom recirculations increase their size. They merge each other at about $Ri = 0.4$. In the range of $Ri = 0.4$ to 0.5, the two bottom recirculations merge each other. The resulting flow structure contains the primary recirculation is supported on the lower newly formed recirculation. However, the lower recirculation fluid layer is thin near $Ri = 0.4$ to 0.5. The lifting off the primary recirculation has to be supported by the lower thin fluid layers. As the lower recirculation fluid layer is thin, it is very unstable for any disturbances. This highly unstable bottom recirculation brings down the critical Reynolds number sharply to a much lower value.

With increasing Richardson number, the size of the bottom recirculation increases, resulting in increasing its thickness. The increased thickness helps in increasing ability of holding the primary re-

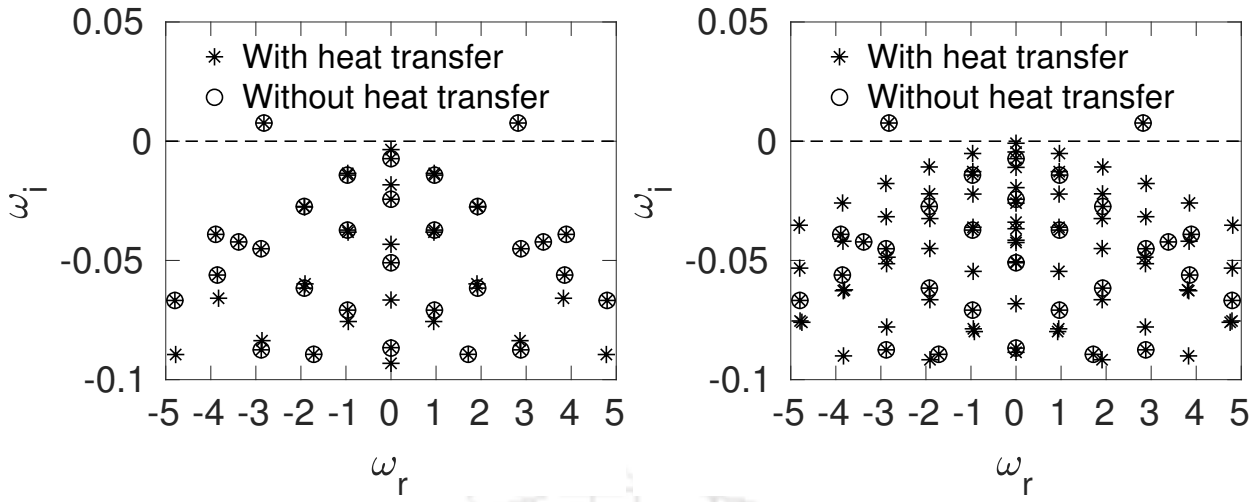

(a) $Pr = 0.71$, $Re = 7995$ (b) $Pr = 3$, $Re = 7995$

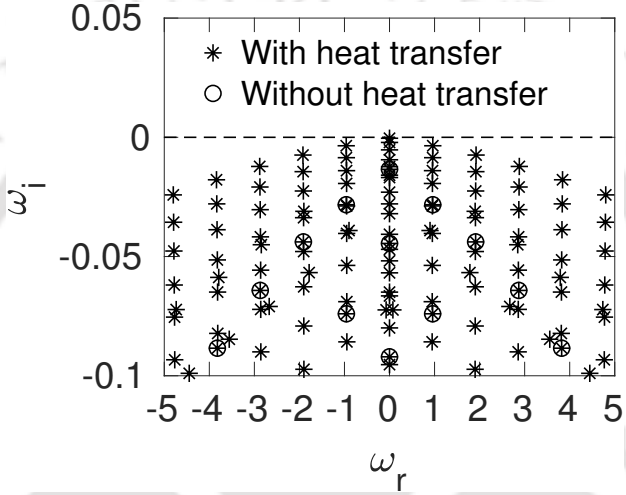

(c) $Pr = 11.57$, $Re = 4473.4$

Figure 8.13: Eigenvalue spectrum with and without heat transfer for various Prandtl numbers at respective critical Reynolds numbers (pure forced convection)

circulation. Hence, for $Ri = 0.5$ to 1, the stability of the lower recirculation increases and the critical Reynolds number increases. The decrease in the value of critical Reynolds number, can be explained using the temperature contours presented for $Ri \geq 2$ which are presented in subfigures 8.20(c)–8.20(i). The subfigure 8.20(c) show temperature contours for $Ri = 2$. The temperature of the primary recirculation is almost uniform. The temperature in the bottom recirculation has variation from 0 to -0.2. The temperature decreases from the bottom wall towards the center of the bottom recirculation, establishing negative temperature gradient in a vertically upward direction. As the density increases with decreasing temperature, this region of negative temperature gradient is thermally unstable configuration. Higher the temperature gradients, lower its stability. For $Ri > 2$, we can see from the isotherms that with increasing Richardson number the region of thermally unstable configuration (region of negative temperature gradient) increases. This increasing unstable configurations makes the flow to be more unstable. Hence, critical Reynolds number decreases for Richardson numbers range of 2 to 200.

The Eigenvalue spectrum at critical Reynolds number for various Richardson numbers are shown in Figs. 8.14–8.16. The Eigenvalue spectrum for various Richardson numbers are similar in their

structures. However, the nature of the most unstable Eigenvalue differs among the flows of different Richardson numbers. From $Ri = 0$ to 0.4 (Figs. 8.14(a)–8.14(d)), the most unstable Eigenvalue has zero real part and hence, represents disturbance of stationary mode. For $Ri > 0.4$ (Figs. 8.14(d)–8.16(d)), a pair of complex conjugate Eigenvalues represents the most unstable Eigen mode. Such Eigen mode represents a time varying disturbance. Appearance of such modes with Richardson number variation represent Hopf bifurcation. Such Hopf bifurcation is reported by Bopanna and Gajjar [113], Kalita and Gogoi [150], Fortin et. al [151], Ramanan and Homsy [105] and Theofilis [110], in their study of isothermal lid driven cavity flows. For $Ri > 4$ (Figs. 8.15(e)–8.16(d)), the magnitude of the real part of most unstable Eigenvalue increases with Richardson number.

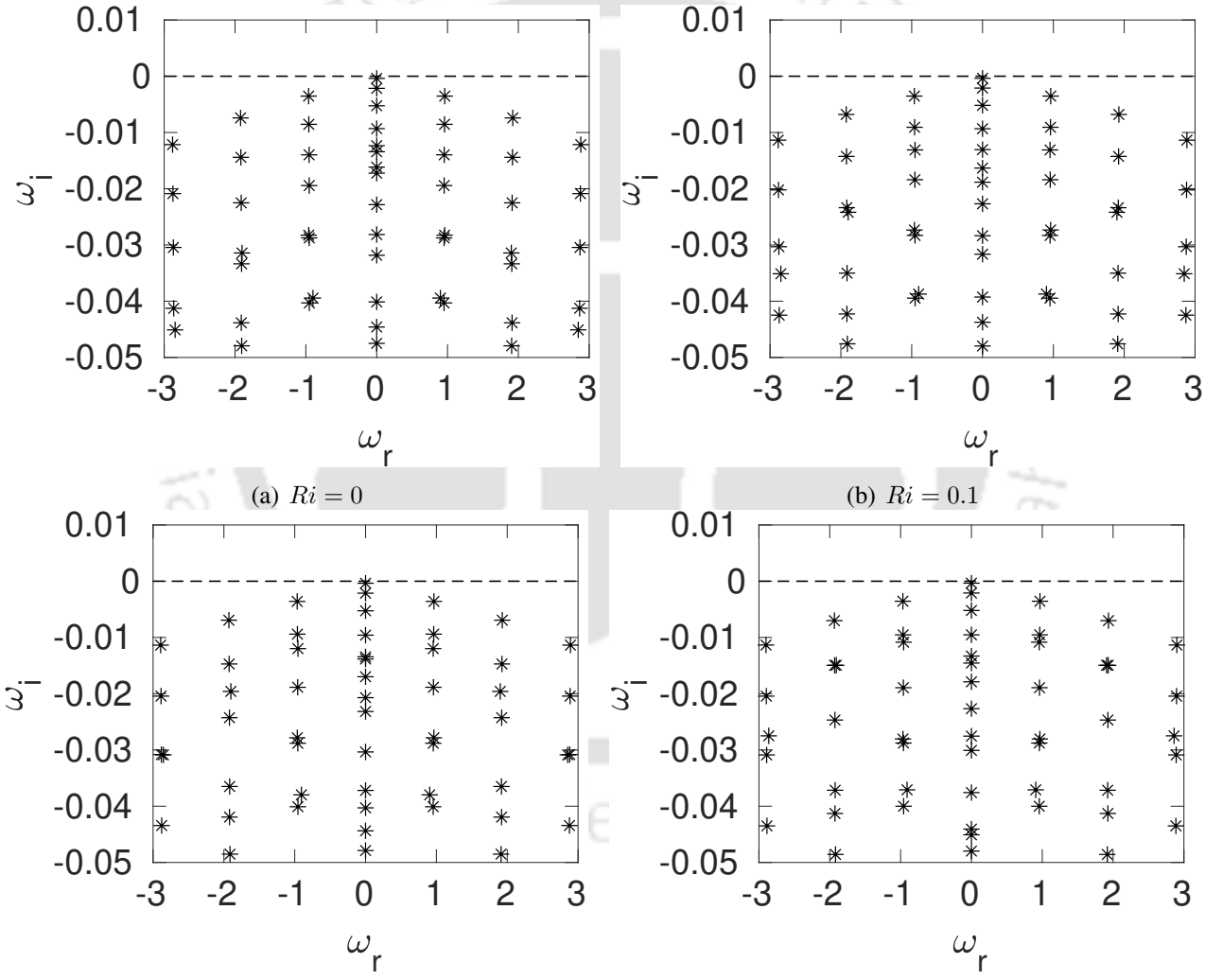

(a) $Ri = 0$ (b) $Ri = 0.1$

(c) $Ri = 0.2$ (d) $Ri = 0.3$

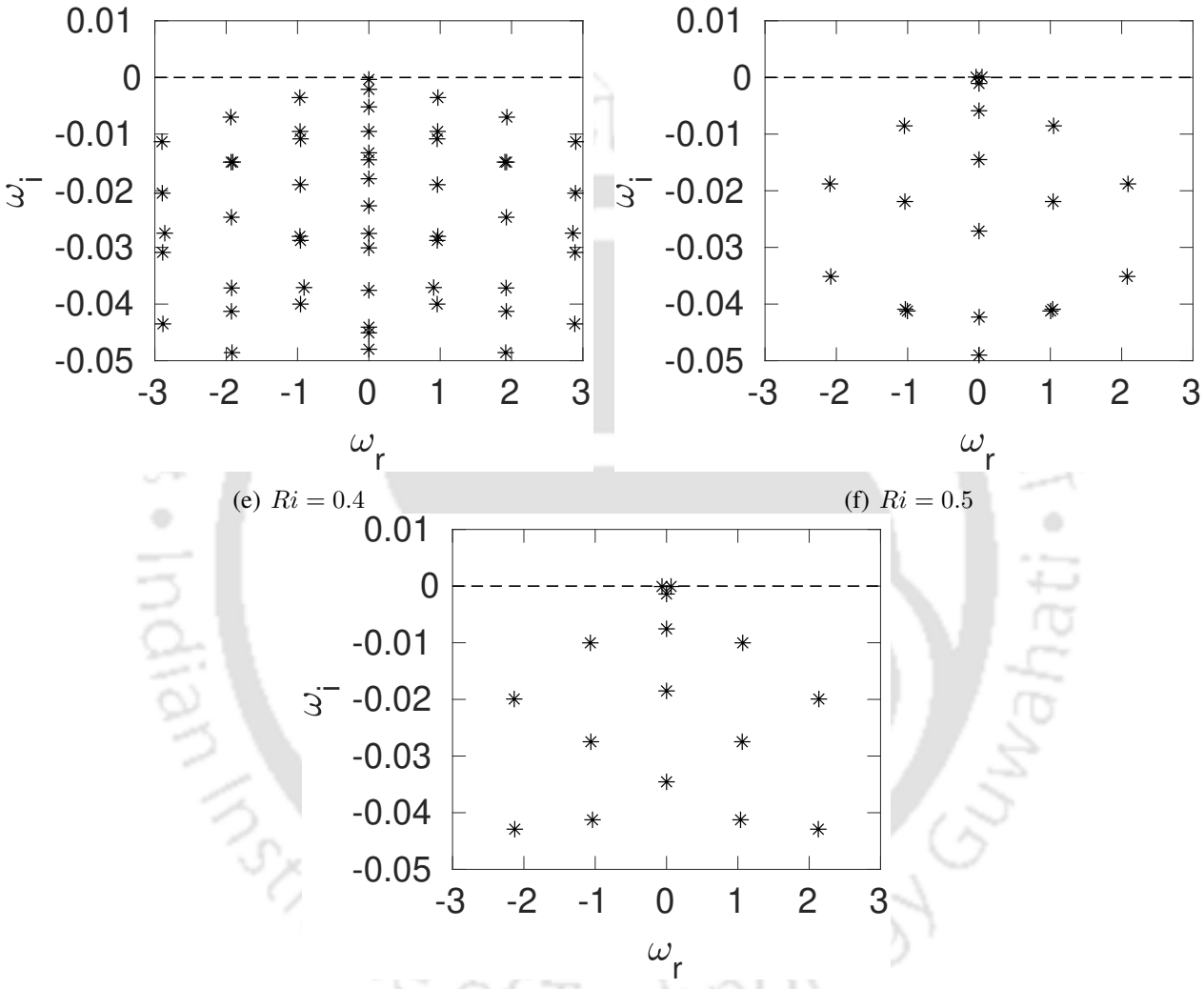

(e) $Ri = 0.4$ (f) $Ri = 0.5$

(g) $Ri = 0.6$

Figure 8.14: Few most unstable Eigenvalues of mixed convection flow for various Ri values at respective Re_{cr}

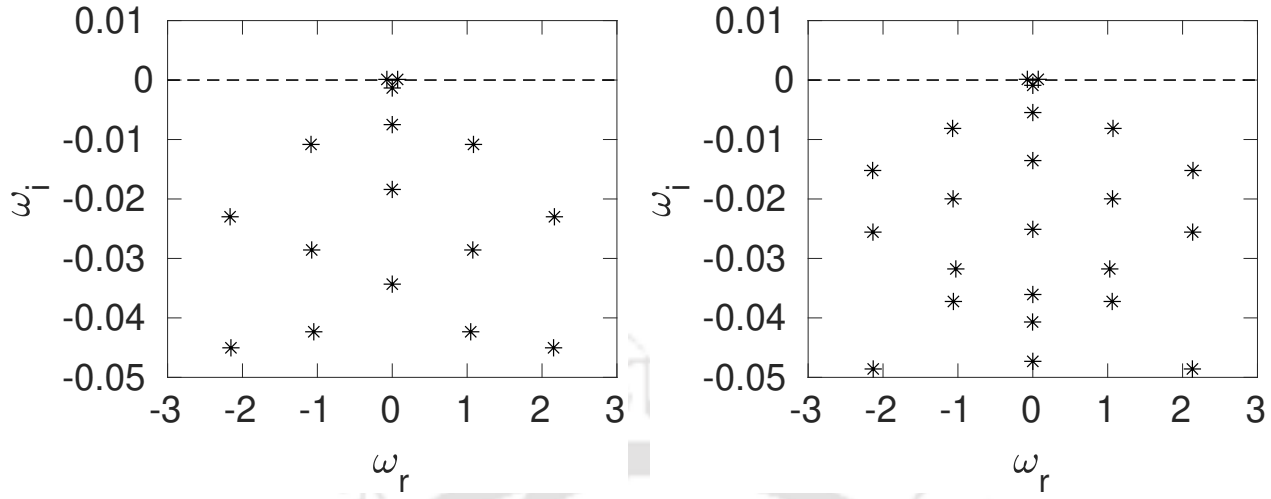

(a) $Ri = 0.7$

(b) $Ri = 0.9$

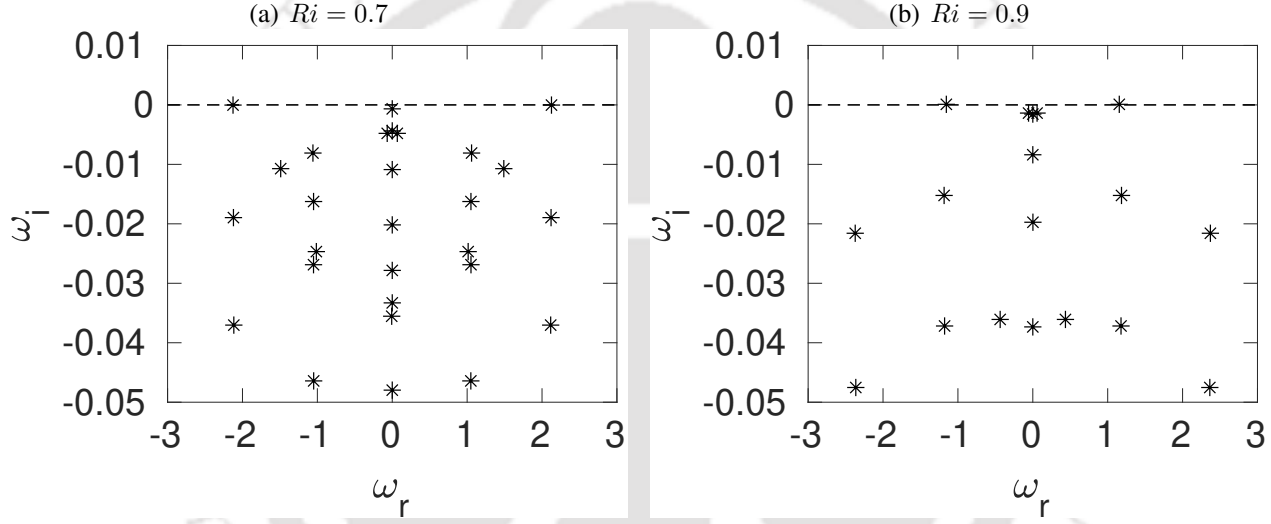

(c) $Ri = 1$

(d) $Ri = 2$

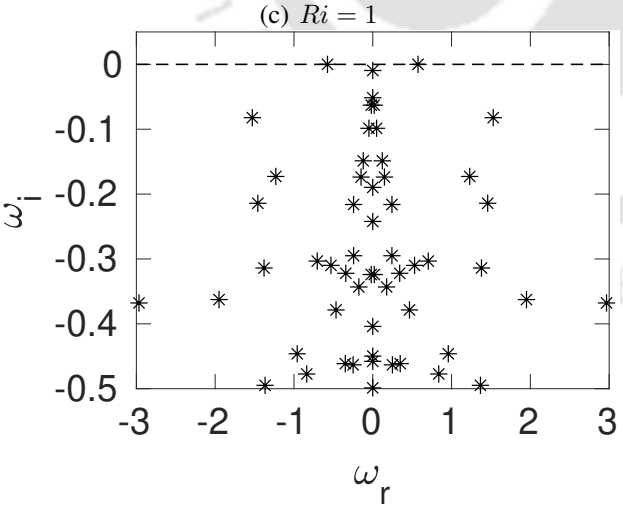

(e) $Ri = 4$

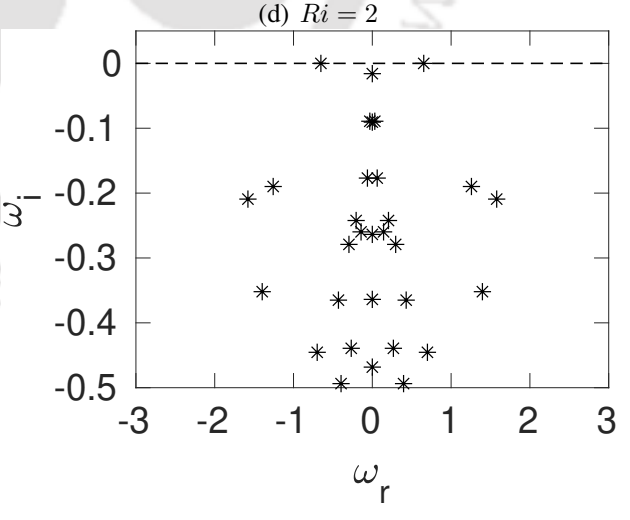

(f) $Ri = 5$

Figure 8.15: Few most unstable Eigenvalues of mixed convection flow for various Ri values at respective Re_{cr}

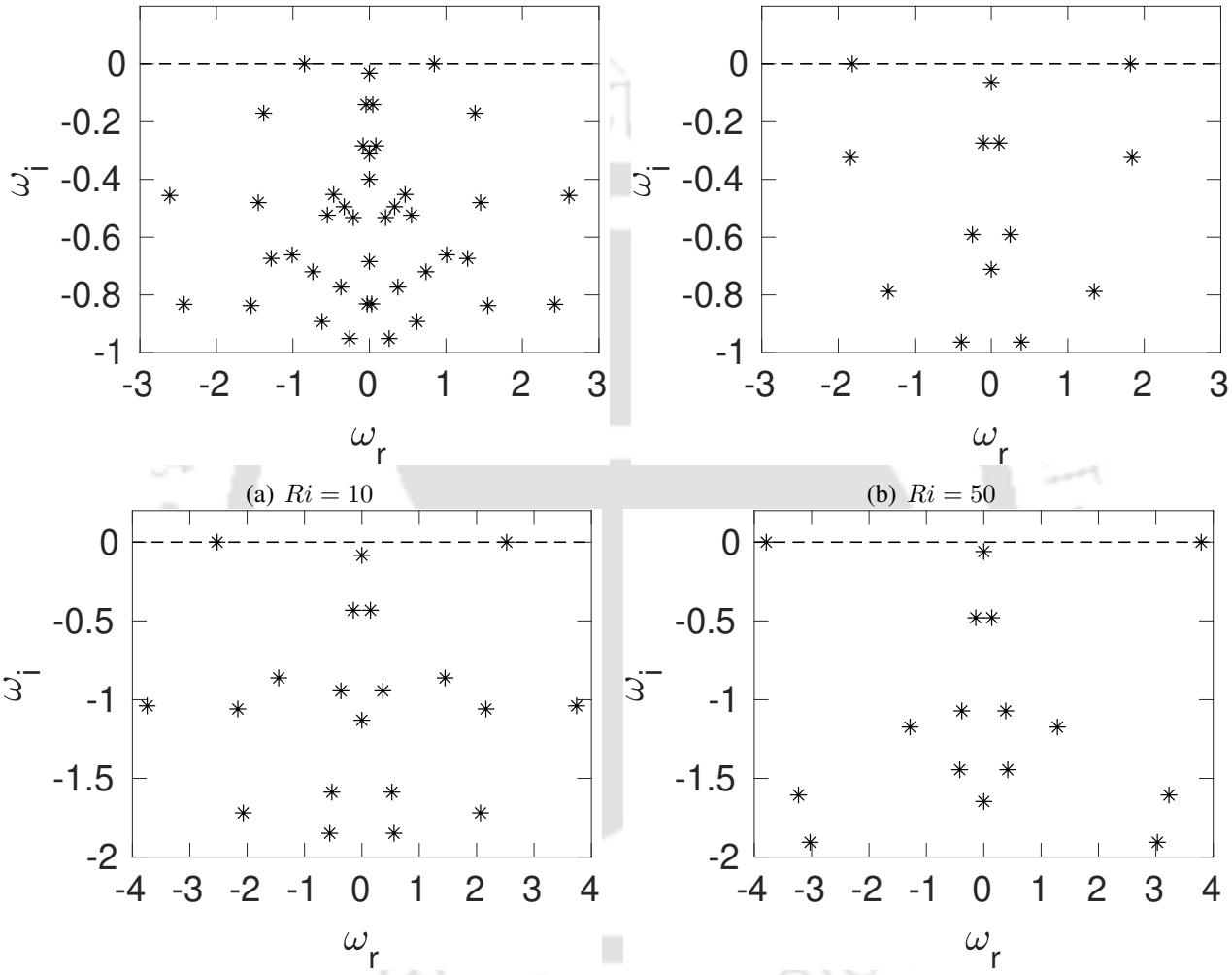

(a) $Ri = 10$ (b) $Ri = 50$

(c) $Ri = 100$ (d) $Ri = 200$

Figure 8.16: Few most unstable Eigenvalues of mixed convection flow for various Ri values at respective Re_{cr}

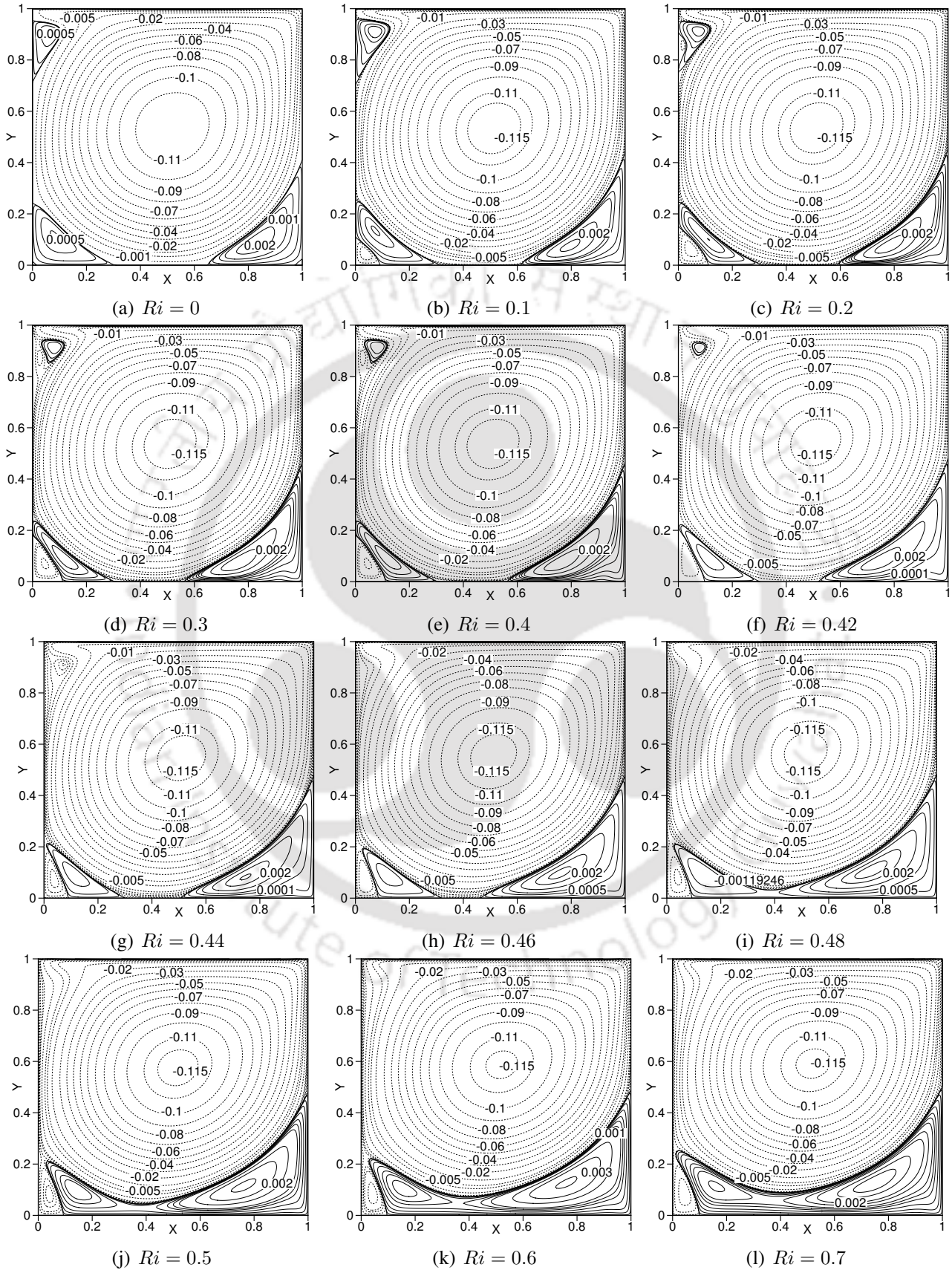

Figure 8.17: Stream function contours of the base flow for various Ri values at their respective Re_{cr} values

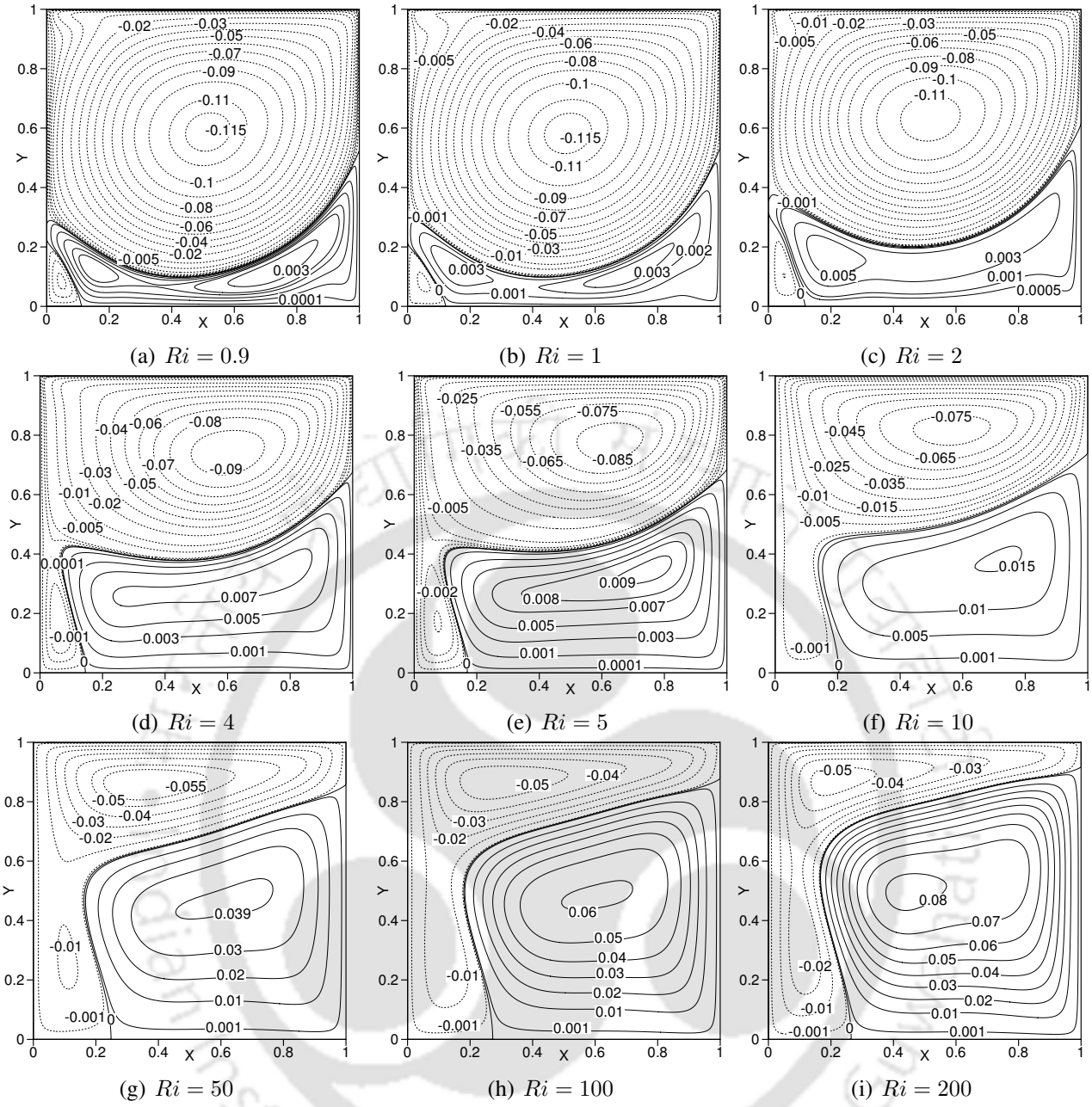

Figure 8.18: Stream function contours of the base flow for various Ri values at their respective Re_{cr} values

The real part of Eigenfunctions of disturbance stream functions for various Ri values at their respective critical Re values are shown in Figs. 8.23 and 8.24. Figs. 8.23(a)–8.24(a) show the Eigenfunctions of disturbance stream functions for $Ri \leq 1$. The stream function disturbance field for $Ri = 0$ to 0.4 which are presented in subfigures 8.24(a)–8.23(e) have similar structure. This is due to the fact that in this range the flow becomes unstable through the same Eigen mode which is evident from the similarity in the Eigenvalue spectrum for $Ri = 0$ to 0.4 shown in subfigures 8.14(a)–8.14(e). Similarly, disturbance stream function contours for $Ri = 0.6$ to 0.9 are similar due to the fact that they originate from the same kind of mode which can be observed from respective Eigenvalue spectrum plotted in subfigures 8.14(g)–8.15(b). The most unstable Eigenvalue for $Ri = 1$ to 200 are a pair of complex conjugate mode and the most unstable Eigen mode for these Richardson numbers are

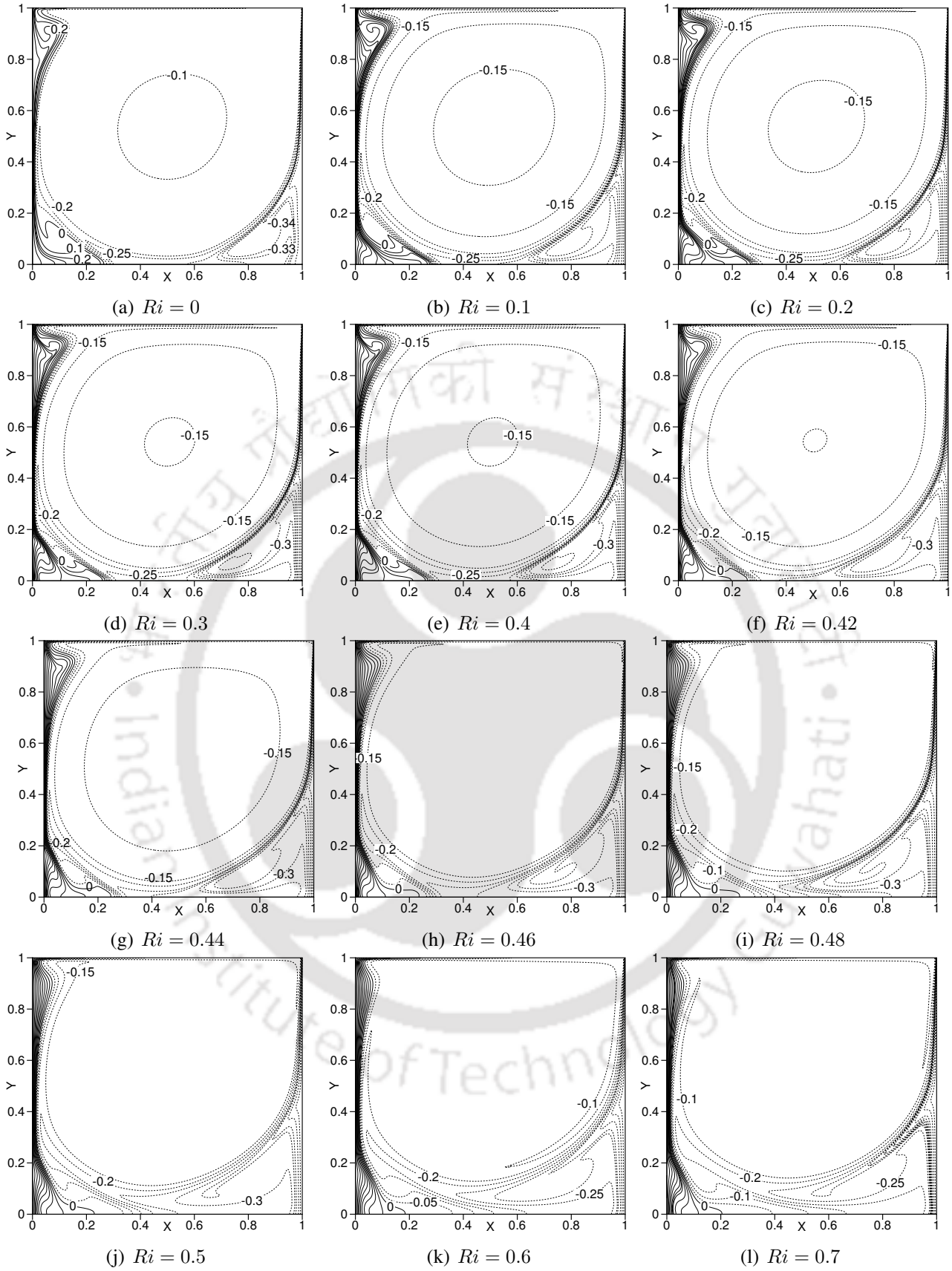

Figure 8.19: Temperature contours for base flow for various Ri values at their respective Re_{cr} values

from the similar mode, except the magnitude of the real part. The Eigenvalue spectrum for $Ri = 1$ contains the most unstable complex conjugate pair as the first mode following a stationary mode as a

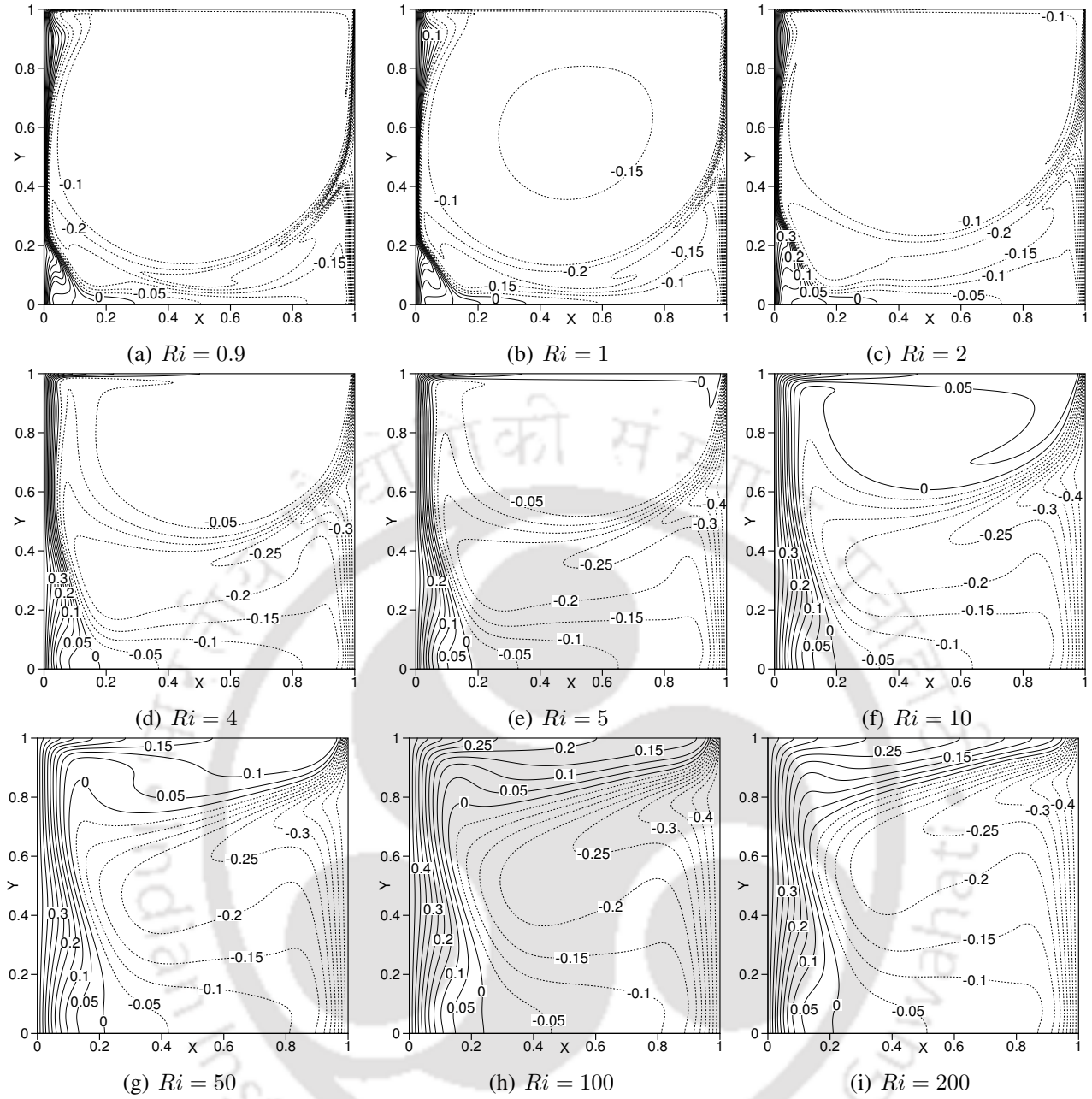

Figure 8.20: Temperature contours for base flow for various Ri values at their respective Re_{cr} values

second most unstable mode. However, for $Ri = 1$, the complex conjugate first most unstable mode is followed by pair of complex conjugate Eigenvalues. Due to the difference in the spectrum, the disturbance stream function field differs between $Ri = 1$ and $Ri = 2$ (subfigures 8.15(c) and 8.15(d)). As the sequence of Eigen mode for $Ri = 4$ to 200, the disturbance stream function fields shown in subfigures 8.24(c)–8.24(h) are similar. Such kind of patterns are also followed for the imaginary parts of temperature disturbance.

The Eigen functions of imaginary part of disturbance temperature is shown in Figs. 8.27 and 8.28.

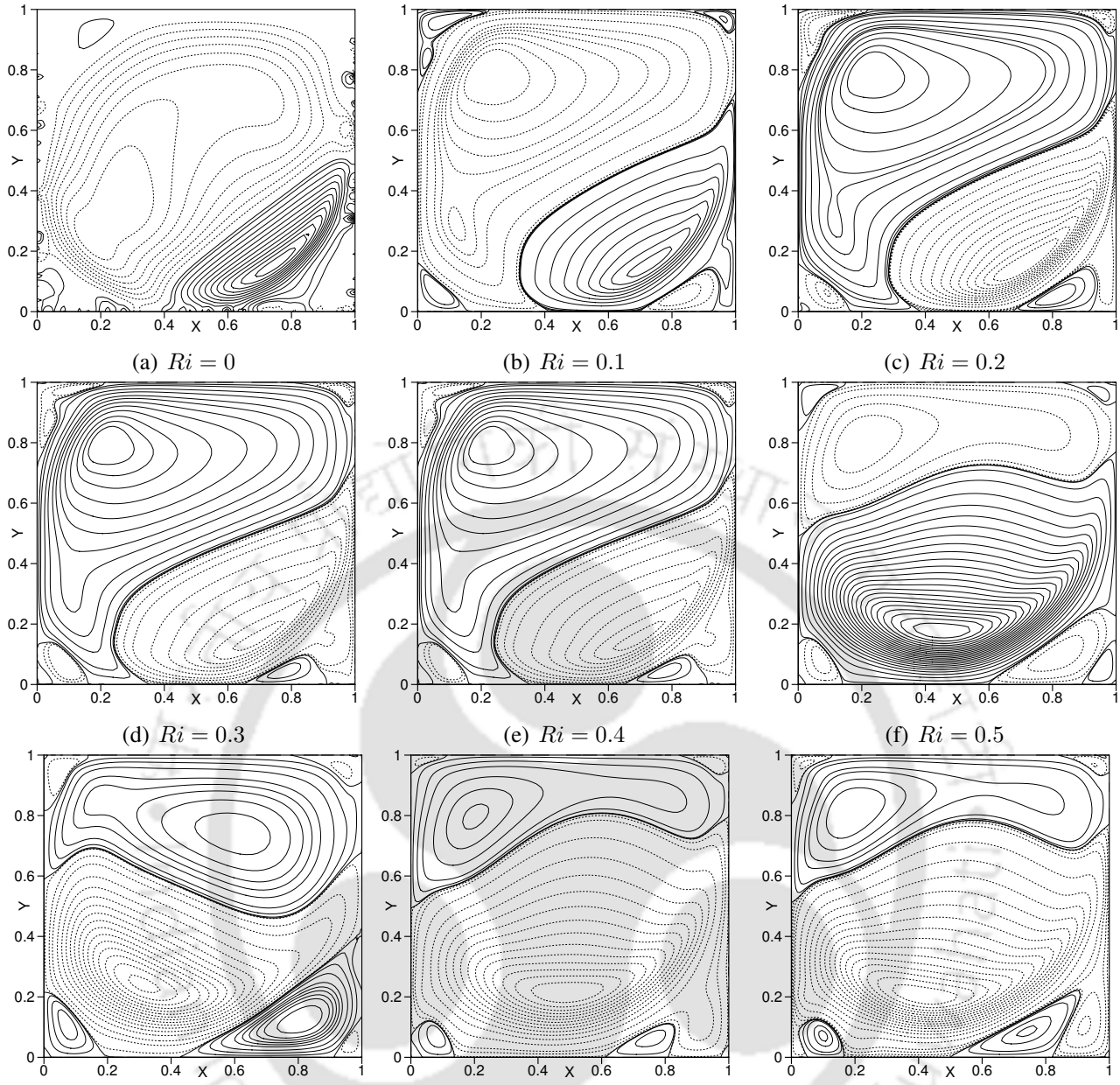

(a) $Ri = 0$ (b) $Ri = 0.1$ (c) $Ri = 0.2$

(d) $Ri = 0.3$ (e) $Ri = 0.4$ (f) $Ri = 0.5$

(g) $Ri = 0.6$ (h) $Ri = 0.7$ (i) $Ri = 0.9$

Figure 8.21: Real part of disturbance stream function contours for various Ri values at respective Re_{cr}

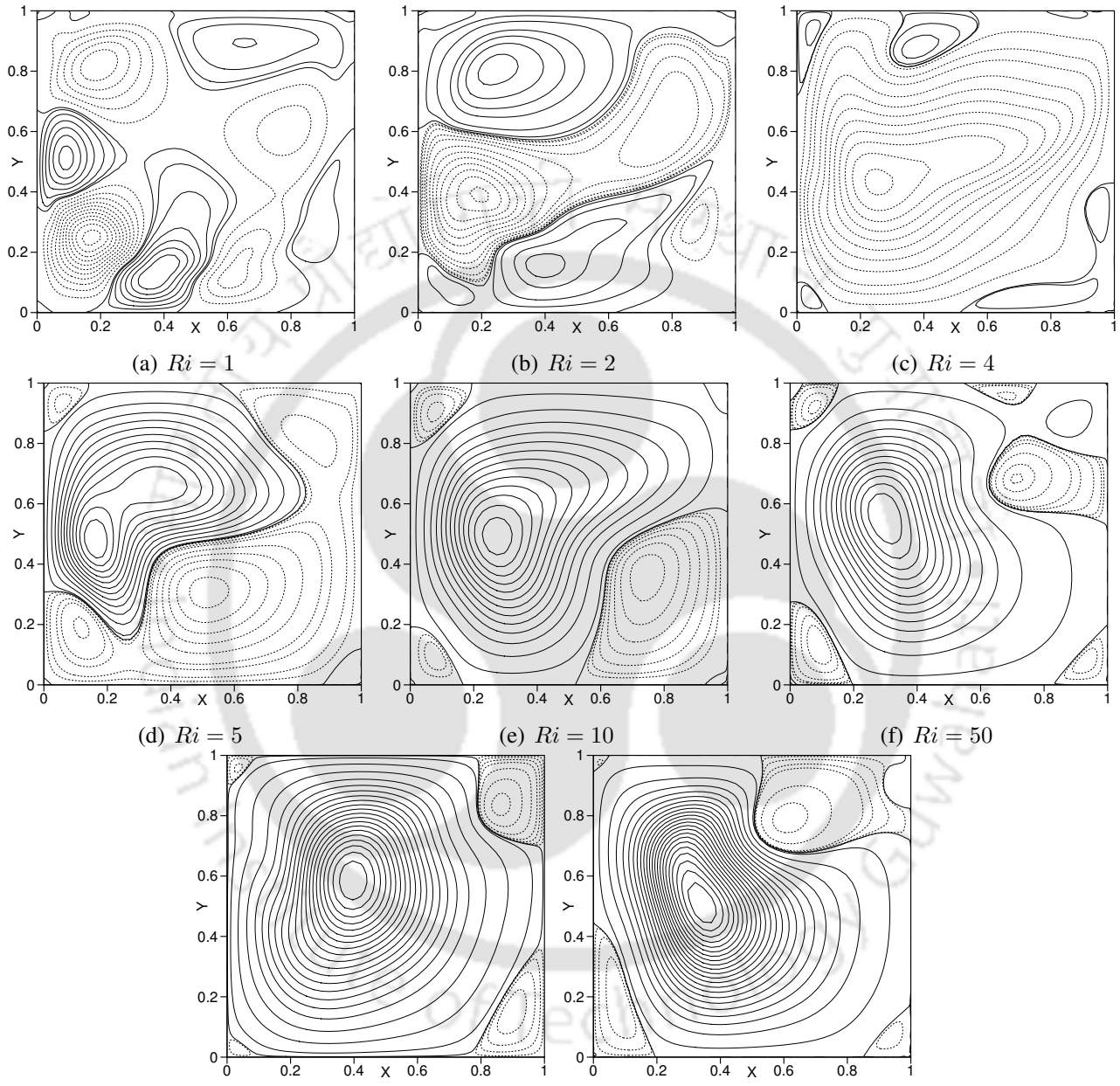

(a) $Ri = 1$ (b) $Ri = 2$ (c) $Ri = 4$

(d) $Ri = 5$ (e) $Ri = 10$ (f) $Ri = 50$

(g) $Ri = 100$ (h) $Ri = 200$

Figure 8.22: Real part of disturbance stream function contours for various Ri values at respective Re_{cr}

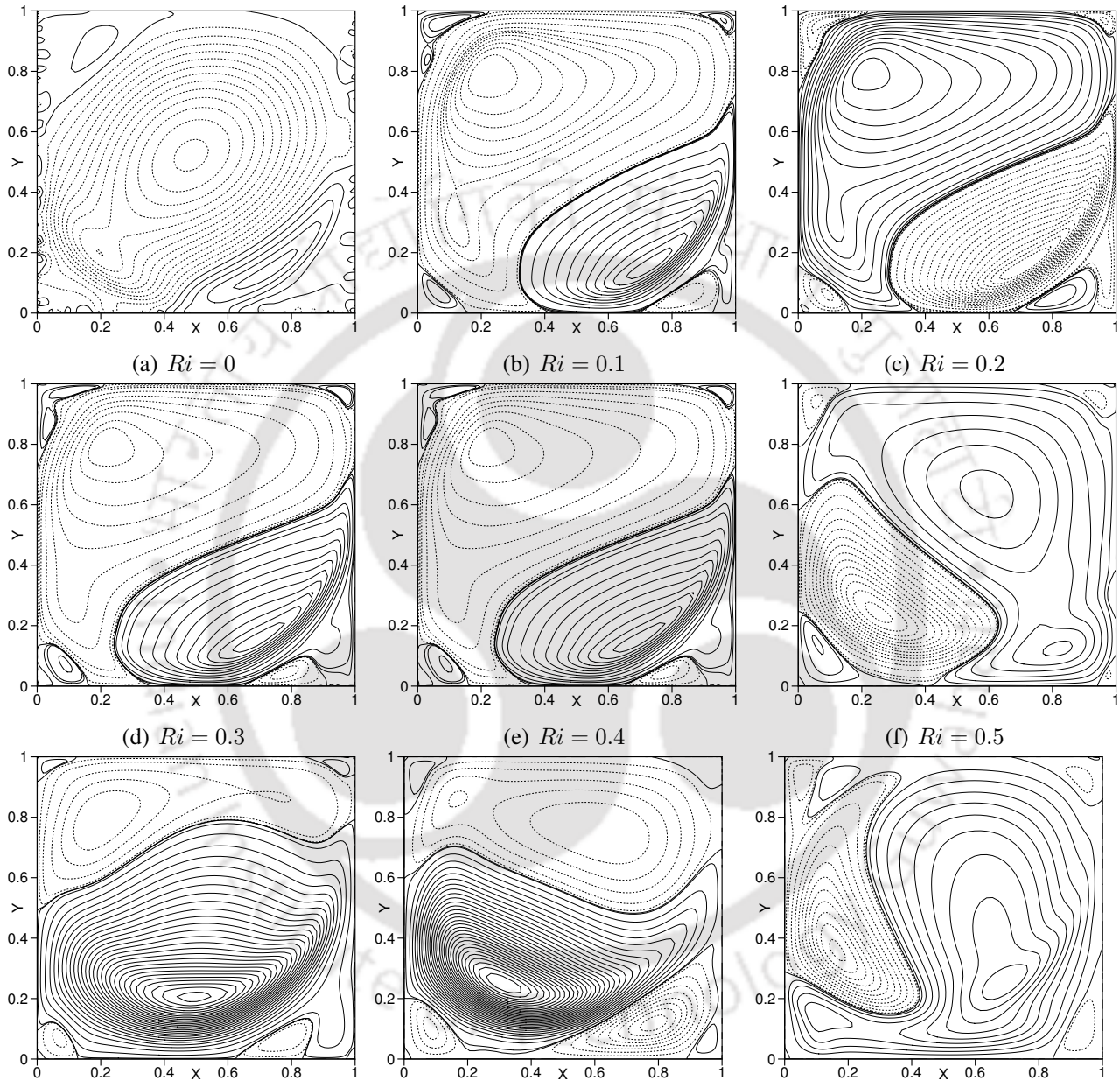

(a) $Ri = 0$ (b) $Ri = 0.1$ (c) $Ri = 0.2$

(d) $Ri = 0.3$ (e) $Ri = 0.4$ (f) $Ri = 0.5$

(g) $Ri = 0.6$ (h) $Ri = 0.7$ (i) $Ri = 0.9$

Figure 8.23: Imaginary part of disturbance stream function contours for various Ri values at respective Re_{cr}

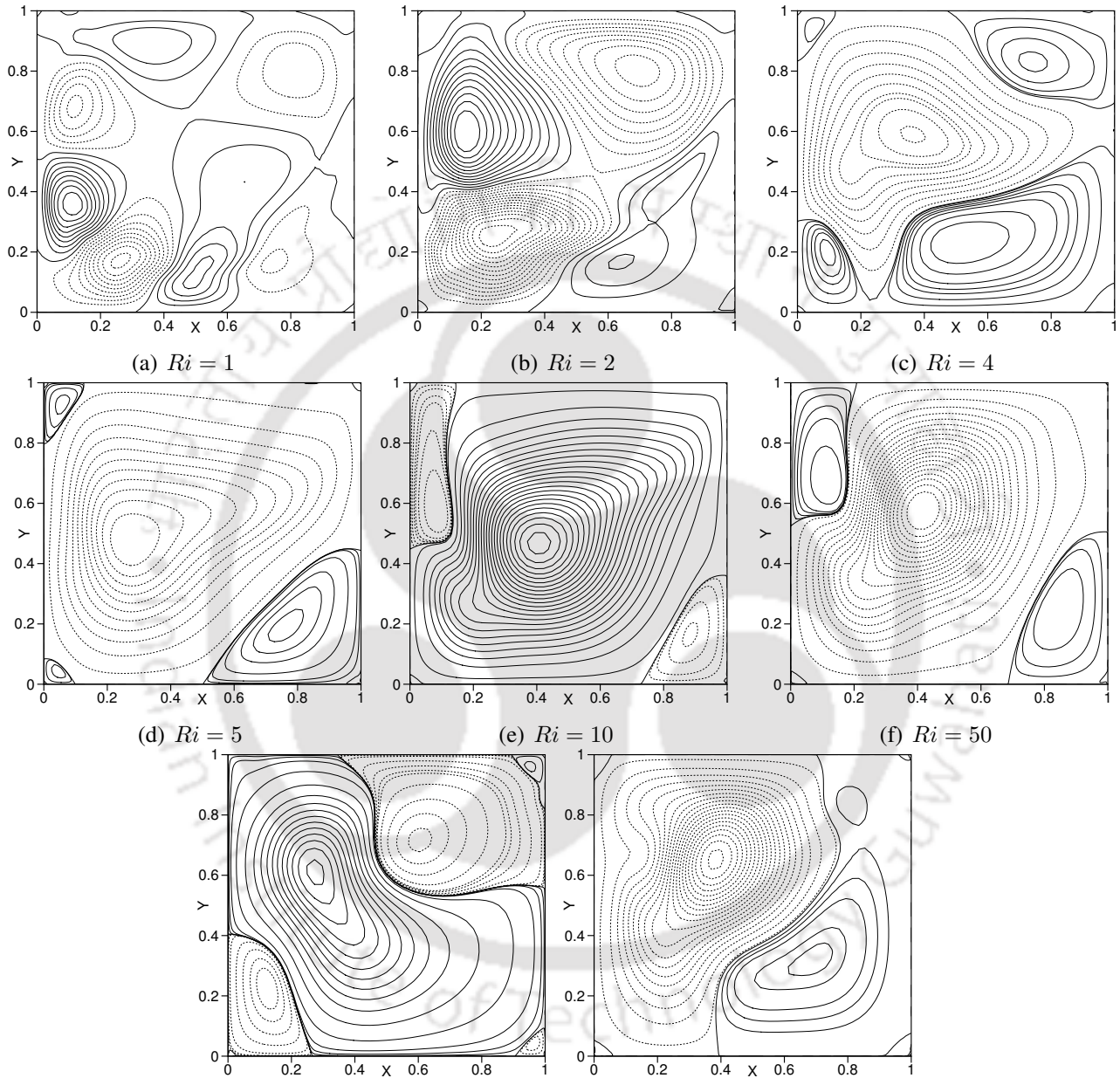

(a) $Ri = 1$ (b) $Ri = 2$ (c) $Ri = 4$

(d) $Ri = 5$ (e) $Ri = 10$ (f) $Ri = 50$

(g) $Ri = 100$ (h) $Ri = 200$

Figure 8.24: Imaginary part of disturbance stream function contours for various Ri values at respective Re_{cr}

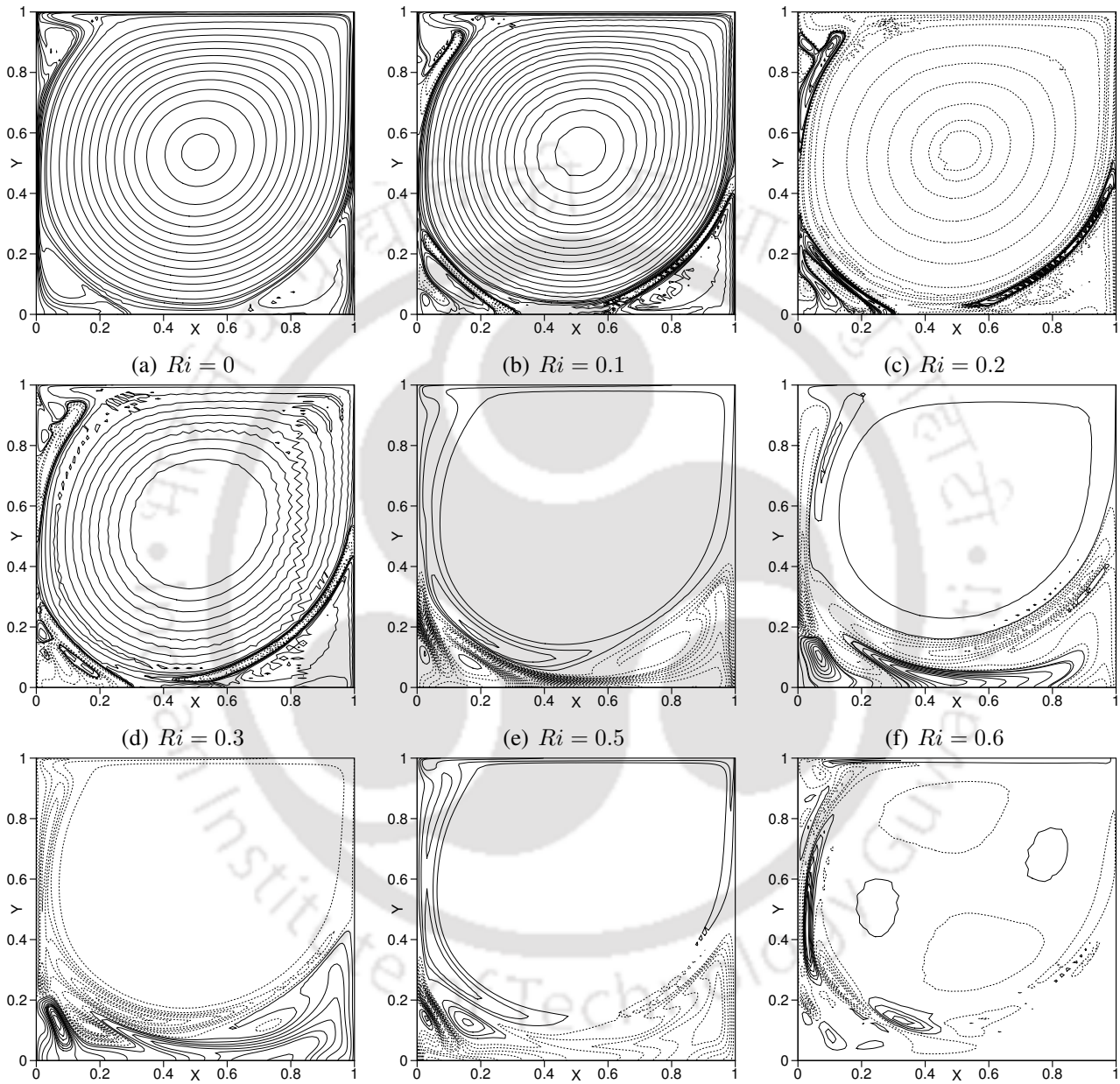

(a) $Ri = 0$ (b) $Ri = 0.1$ (c) $Ri = 0.2$

(d) $Ri = 0.3$ (e) $Ri = 0.5$ (f) $Ri = 0.6$

(g) $Ri = 0.7$ (h) $Ri = 0.9$ (i) $Ri = 1$

Figure 8.25: Real part of disturbance temperature contours for various Ri values at respective Re_{cr}

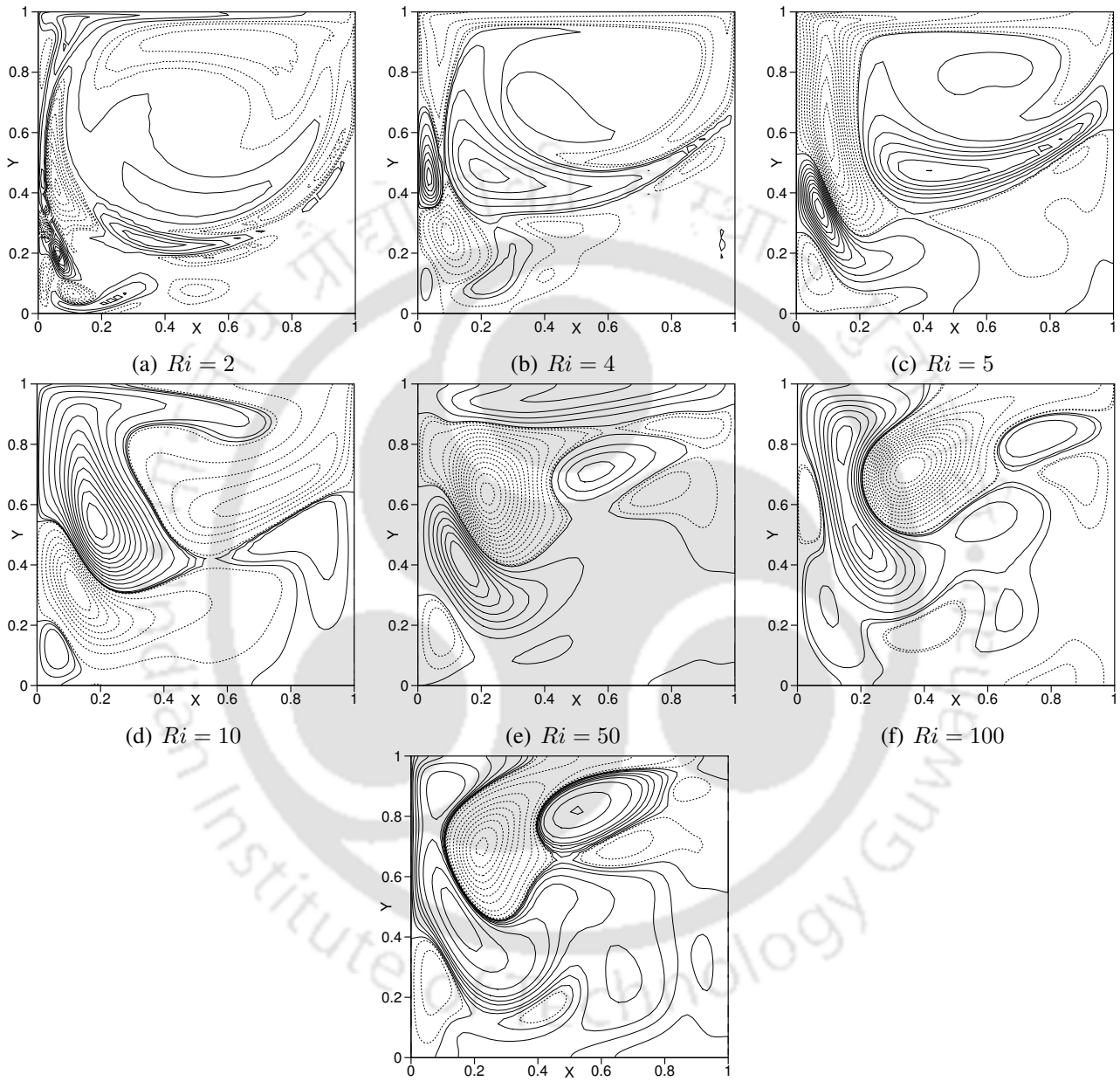

(a) $Ri = 2$ (b) $Ri = 4$ (c) $Ri = 5$

(d) $Ri = 10$ (e) $Ri = 50$ (f) $Ri = 100$

(g) $Ri = 200$

Figure 8.26: Real part of disturbance temperature contours for various Ri values at respective Re_{cr}

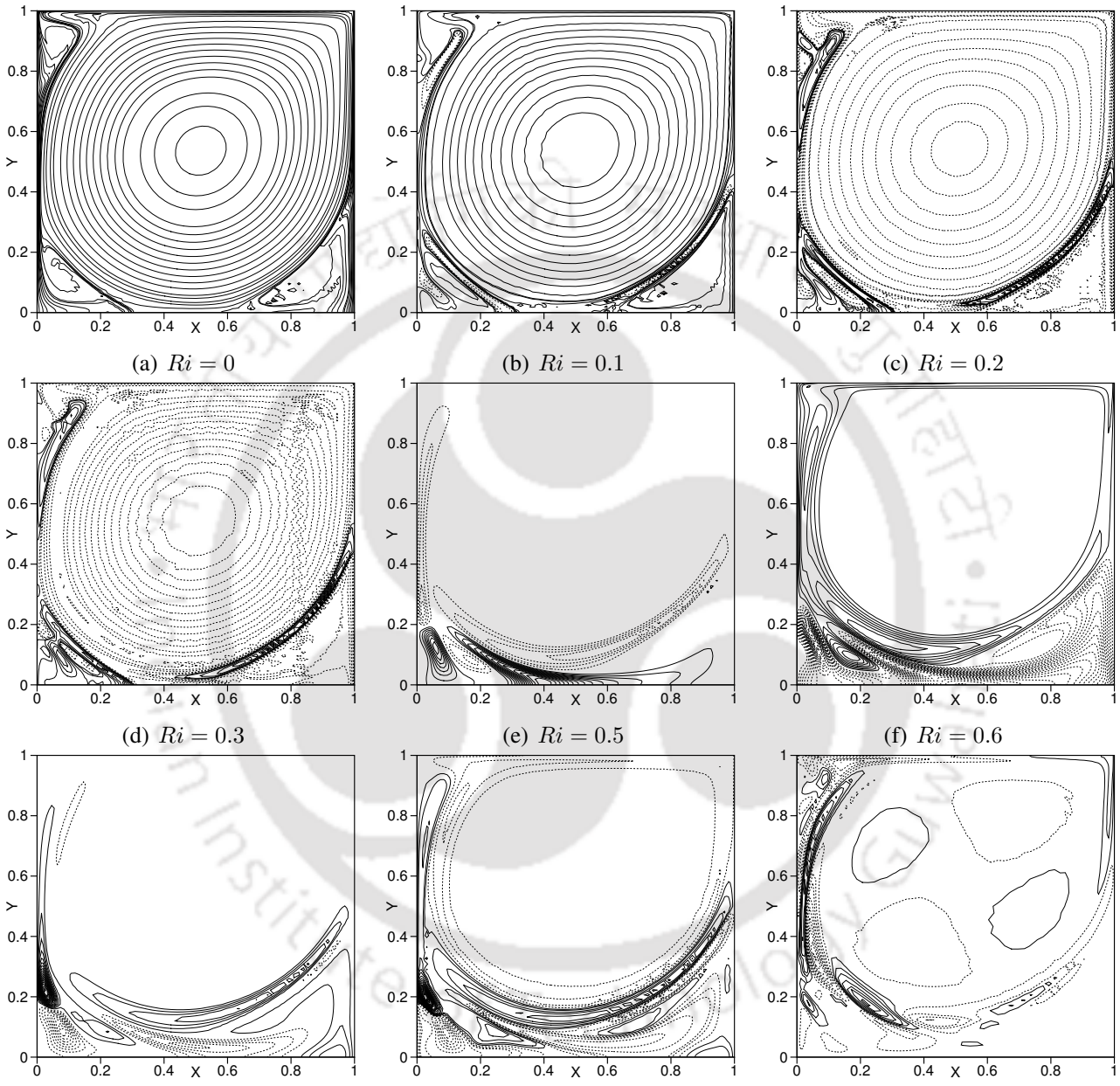

(a) $Ri = 0$ (b) $Ri = 0.1$ (c) $Ri = 0.2$

(d) $Ri = 0.3$ (e) $Ri = 0.5$ (f) $Ri = 0.6$

(g) $Ri = 0.7$ (h) $Ri = 0.9$ (i) $Ri = 1$

Figure 8.27: Imaginary part of disturbance temperature contours for various Ri values at respective Re_{cr}

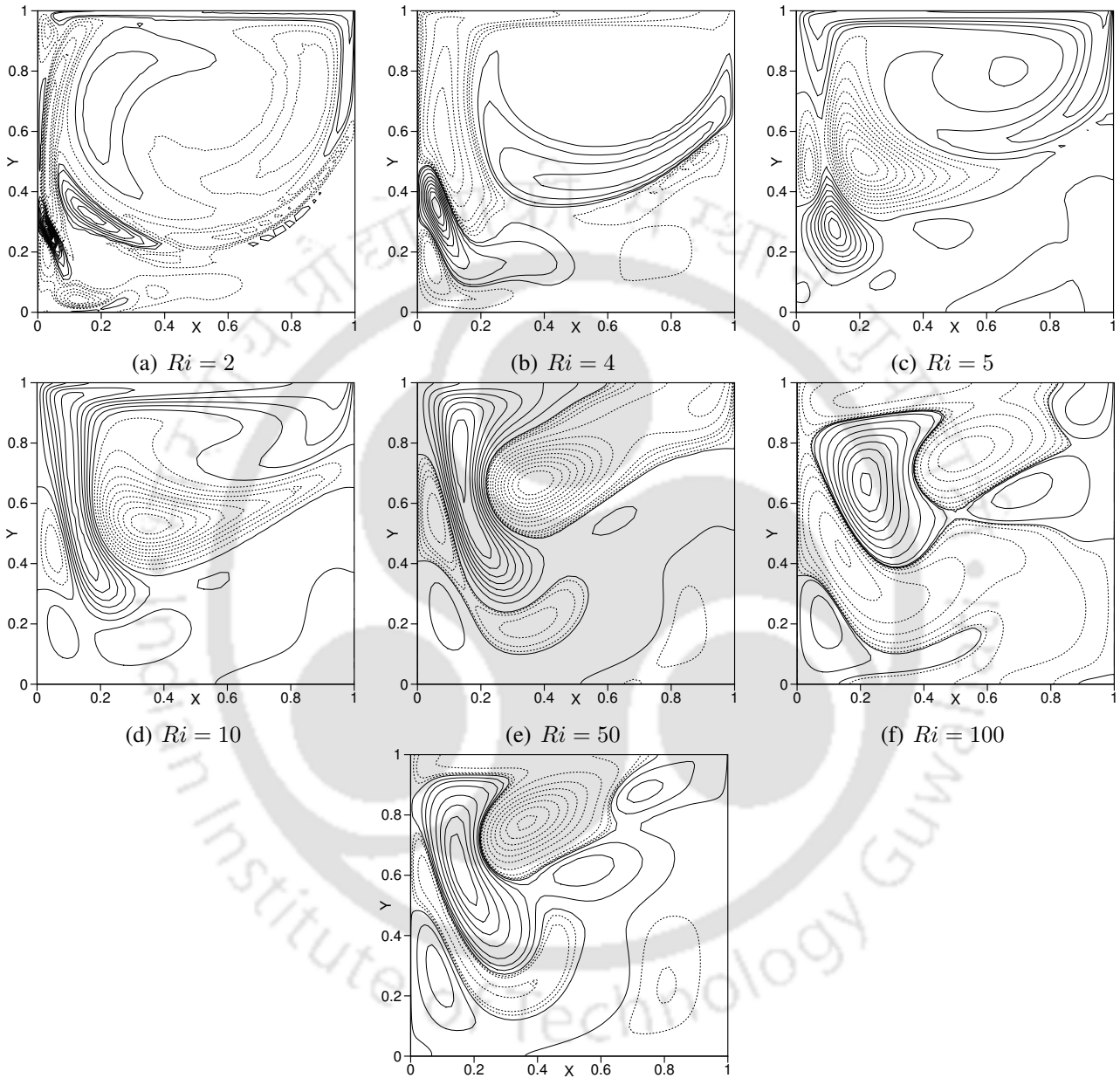

(a) $Ri = 2$ (b) $Ri = 4$ (c) $Ri = 5$

(d) $Ri = 10$ (e) $Ri = 50$ (f) $Ri = 100$

(g) $Ri = 200$

Figure 8.28: Imaginary part of disturbance temperature contours for various Ri values at respective Re_{cr}

8.8.1 Appearance of spurious Eigenvalues in computation

For Richardson number in the range of 0 to 0.4, the spurious Eigenvalues are found to appear as the most unstable Eigenvalue at Eigenvalue grid sizes lower than 101×101. The spurious Eigenvalues appeared as a pair of complex conjugate Eigenvalues, even though the actual most unstable Eigenvalue is an Eigenvalue with zero real part. The spurious Eigenvalues are associated with Eigen functions representing physically unrealistic disturbance field. For such Richardson number range, Eigenvalue grid size of 101×101 is used. It is observed that even with the lower Eigenvalue grid size the second most unstable Eigenvalue present in the spectrum is the actual most unstable mode. The second most unstable mode found using the lower grid is the same as the first most unstable Eigenvalue computed with grid size of 101×101 which provides Eigenvalues without spurious Eigenvalues.

Fig. 8.29 shows the Eigenvalue spectrum computed using grid sizes of 81×81 and 101×101. The complex conjugate pair of Eigenvalues with highest imaginary part (shown inside the square box) is shown in Fig. 8.29 for 81×81 grid are the spurious Eigenvalues which disappear from the spectrum when the grid is refined to 101×101.

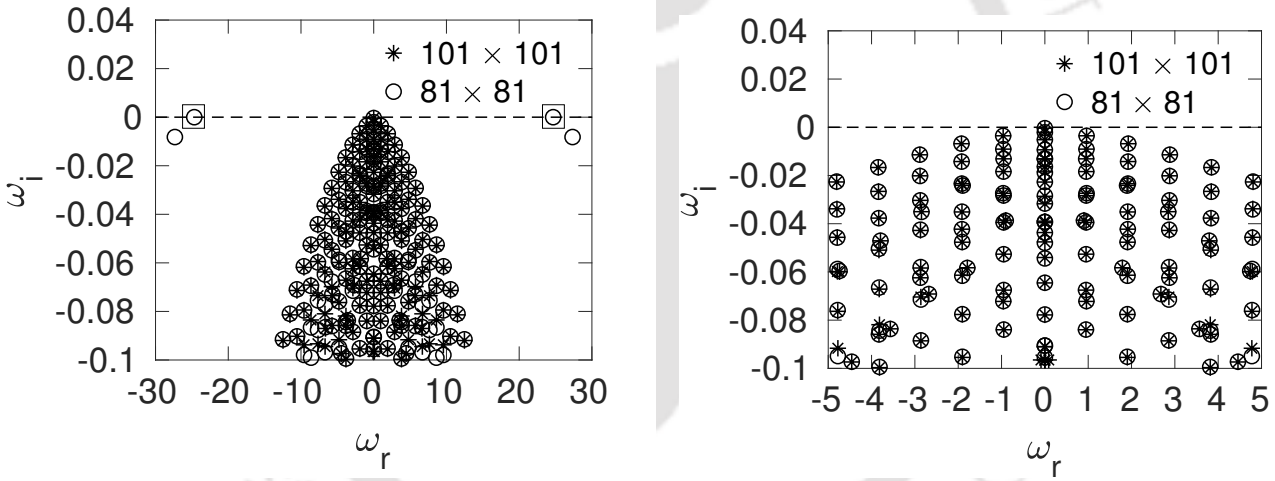

(a) Few most Eigenvalues (b) Enlarged view

Figure 8.29: Appearance of spurious Eigenvalues ($Ri = 0.1$, $Re = 4.56775 \times 10^3$)

In Fig. 8.30, the left and middle columns show the disturbance Eigen functions corresponding to the the first and second most unstable modes, respectively, computed using 81×81 Eigenvalue grid. The right most column shows the disturbance Eigen functions of the most unstable mode computed using Eigenvalue grid 101×101. From the figure, we can see that the first column Eigen functions are physically unrealistic. The second column and third column Eigen functions are same. Hence, the second mode from grid 81×81 represents the actual correct mode. The computations for $Ri = 0$ to 0.4 are carried out using Eigenvalue grid 101×101.

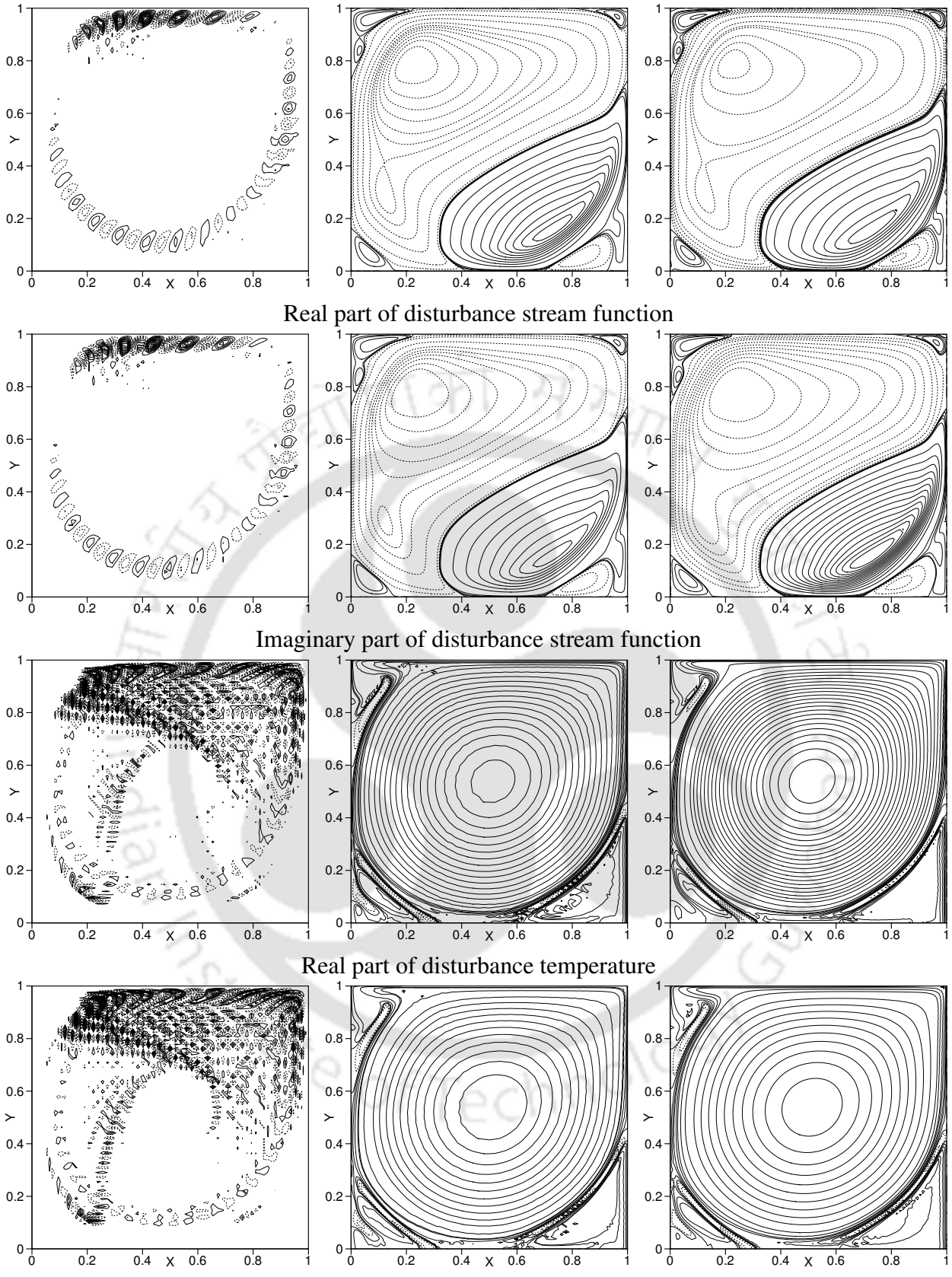

Figure 8.30: Detection of spurious and correct Eigenvalues ($Ri = 0.1$ and $Re = 4.56775 \times 10^3$)

8.8.2 RAM size and CPU time taken for global stability analysis

In the present study, global linear stability analysis is carried out for mixed convection flow in square cavity. The Eigenvalue problem of the disturbance equations forms large size of matrices and require large computation time. The RAM size and CPU time required depends on the Eigenvalue grid. In a typical run, for Eigenvalue grid of size 81×81, the RAM of about 20 GB is required. The CPU time taken for one run for a Eigenvalue grid size of 81×81 is about 45 hours. For one run with grid size 101×101, CPU time taken is about 120 hours (about 6 days).

8.9 Conclusions

The global stability analysis is carried out for the stability of mixed convection lid driven cavity flows. The following conclusions are drawn from the study.

1. The flow and stability characteristics of the mixed convection vary dramatically with variation of Richardson number.

2. In the range of $Ri = 0$ to 0.4, the critical Reynolds number is almost constant with a value of about 4550. In the range of 0.4 to 0.6, the critical Reynolds number decreases drastically to a value of 1325. For $Ri = 0.6$ to 1, critical Reynolds number increases to 2354.23. Beyond which the critical Reynolds number decreases with Richardson number.

3. The drastic instability near $Ri = 0.4$ to 0.5 is found to be due to the formation of thin recirculation under primary recirculation. At this Richardson number, the bottom thin layer is strongly unstable.

4. In the range of $Ri = 0$ to 0.4, the most unstable Eigenvalue has zero real part indicating a stationary mode which does not change with time. For $Ri > 0.4$, the most unstable Eigenvalue is a pair of complex conjugate Eigenvalues indicating a Hopf mode which is a time dependent disturbance.

5. The critical circular frequency varies dramatically with variation of Richardson number. The circular frequency is zero for $Ri = 0$ to 0.4. The value increases for $Ri = 0.5$ to 1.5, reaching to highest value of 3.33 and decreases with Ri up to 4. Beyond which, it increases with Richardson number.

6. For pure forced convection asymptote, the most unstable mode is found to be thermal mode for the water flows. For the flows other than water, the most unstable mode depends on the value of Prandtl number. For $Pr \leq 3$, the most unstable mode is hydrodynamic mode and for $Pr > 3$, the most unstable mode is thermal mode.

Chapter 9

Conclusions

In the present work, linear stability and heat transfer characteristics of the water flows are studied. The present study focuses on the temperature range in which water shows density inversion. First the solutions of convection boundary layer flows are obtained using perturbation and similarity transformation methods. The linear stability analysis of natural and mixed convection boundary layer flows is carried out for both temporal and spatial stability. The global stability of mixed convection flows in lid driven square cavity is studied. The following conclusions are drawn from the different studies of the present work.

9.1 Perturbation and similarity solutions of mixed convection boundary layer flows

The solutions of perturbation method are presented using universal functions. The solutions for the boundary layer flows for any arbitrary wall temperature or wall heat flux can be obtained using the universal functions presented from the study. Appropriate similarity solutions are derived for mixed convection boundary layer flows about a vertical plate of power-law varying wall heat flux.

1. The results are valid for arbitrary continuous variation of wall temperature and wall heat flux.

2. For both varying wall temperature and heat flux conditions, heat transfer rates and skin friction coefficient increase almost linearly with increasing value of power-law index in case of both aiding and opposing flows, for all Richardson number.

3. For arbitrary varying wall temperature, both velocity and thermal boundary layer thicknesses decrease with increasing modified Richardson number in aiding flow configuration. The reverse trend is observed for opposing flow situations.

4. The similar trend is observed for velocity and thermal boundary layer thickness for varying wall heat flux condition which is found for arbitrary varying wall temperature.

9.2 Conclusions from similarity solutions of natural and mixed convection boundary layer flow

The conclusions from natural convection are:

1. In the natural convection, at a given location, the dimensionless streamwise velocity and dimensionless temperature decreases with increasing power-law index despite the fact that the corresponding dimensional velocity and temperature increases with power index.

2. Velocity and thermal boundary layer thickness decreases with increasing power-law index.

3. Local Nusselt number increases with increasing power-law index.

The conclusions from the mixed convection boundary layer flows are as following.

1. For a given value of power-law index, dimensionless velocity and temperature increases and decrease with respect to Gr_y/Re_y^3 for aiding flow. The reverse trend is observed for opposing flow.

2. For a given Gr_y/Re_y^3, dimensionless velocity decreases with power-law index value for aiding flow, and increases for opposing flow. However, dimensionless temperature decreases for both aiding and opposing flows.

3. The velocity and thermal boundary layer thicknesses increase and decrease, respectively, with increasing power-law index value for a given values Gr/Re^3 for aiding flow. The opposite trends are observed for opposing flow.

4. For a given Gr_y/Re_y^3, Nusselt number increases with power-law index for aiding flow. However, the opposite trend is observed for opposing flow.

9.3 Stability of natural convection boundary layer flows

1. The critical value of buoyancy parameter for natural convection over isothermal plate is found to be 22.84 and the corresponding wave number and circular frequencies are 0.604, and 0.0944, respectively. The critical value of buoyancy parameter for natural convection over isoflux plate is found to be 75.481 and the corresponding wave number, circular frequency and phase speed are found to be 0.633, 0.056 and 0.036, respectively.

2. It is found for both isothermal and isoflux plates at critical buoyancy parameter, the most unstable disturbance travels with phase speed higher than the lower modes.

3. For both isothermal and isoflux plates, when the plate is tilted in anticlockwise and clockwise directions, the convection becomes more unstable and more stable, respectively, compared to vertical orientation.

4. For isothermal plate, the critical buoyancy parameter decreases about 18% when we tilt 15° in anticlockwise direction, and increases about 10% when we tilt in clockwise direction compared to that value of vertical orientation.

5. For isoflux plate, the critical buoyancy parameter decreases about 18% when we tilt 15° in anticlockwise direction, and increases about 18% when we tilt in clockwise direction compared to that value of vertical orientation.

6. For both thermal conditions, critical wave number and critical frequency of the most unstable disturbance increases with inclination. However, the phase speed is not affected by the inclination.

7. The inclination has stronger effect at higher wave numbers. The instability at lower wave numbers are not affected by the inclination.

9.4 Stability of mixed convection boundary layer flows

1. For forced convection flow, most unstable mode is a hydrodynamic mode, which is originated from the fluid flow characteristics.

2. The critical Reynolds number decreases with Richardson number for $Ri > 2$.

3. The effect of plate inclination on the stability of mixed convection is weaker than that observed for the natural convection flow for stability. In mixed convection flow, right inclination widens the unstable region on $Re_\delta - \alpha$ plane.

4. For small Richardson numbers, the most unstable mode comes from the flow characteristic of the boundary layer and hence, it is a hydrodynamic mode.

5. The mixed convection formulation used in the study recovers the results of pure natural and forced convection results, accurately.

9.5 Global stability analysis of mixed convection flows in a lid driven square cavity

1. The flow and stability characteristics of the mixed convection vary dramatically with variation of Richardson number.

2. In the range of $Ri = 0$ to 0.4, the critical Reynolds number is almost constant with a value of about 4550. In the range of 0.4 to 0.6, the critical Reynolds number decreases drastically to a values of 1325. For $Ri = 0.6$ to 1, critical Reynolds number increases to 2354.23. Beyond which the critical Reynolds number decreases with Richardson number.

3. The drastic instability near $Ri = 0.4$ to 0.5 is found to be due to the formation of thin recirculation under primary recirculation. At this Richardson number, the bottom thin layer is strongly unstable.

4. In the range of $Ri = 0$ to 0.4, the most unstable Eigenvalue has zero real part indicating a stationary mode which does not change with time. For $Ri > 0.4$, the most unstable Eigenvalue is a pair of complex conjugate Eigenvalues indicating a Hopf mode which is a time dependent disturbance.

5. The critical circular frequency varies dramatically with variation of Richardson number. The circular frequency is zero for $Ri = 0$ to 0.4. The value increases for $Ri = 0.5$ to 1.5, reaching to highest value of 3.33 and decreases with Ri up to 4. Beyond which, it increases with Richardson number.

6. For pure forced convection asymptote, the most unstable mode is a thermal mode.

9.6 Future scope

The stability analysis of flows without heat transfer have been addressed in the literature to larger extend than the flows with heat transfer. The stability analysis has enormous scope for flows with heat transfer. The present work can be extended to the following studies.

1. In the present work, two dimensional boundary layer flows are studied. The present study can be extended to three dimensional boundary layer flows.

2. In the present work, linear stability analysis is carried out using parallel flow stability analysis in which the base flow is assumed to vary only in cross-stream direction. However, in the boundary layer flow is also varied in streamwise direction. Even though, the variation in streamwise direction is weak, the variation can influence the flow stability. Parabolic stability analysis can be used to study the stability of such weakly developing flows.

3. The work carried out in the present study is about the stability of the base flow. Such stability analysis is called primary stability analysis. However, in boundary layer flows, when the primary disturbance grows to a finite amplitude, the perturbations along with the base flow forms a new flow state which in turn can undergo instability. Such instability is called secondary instability. The present study can be extended to the secondary instability analysis using Floquet theory.

4. The global stability of flows in cavity in the present study, the disturbances are considered to be of two-dimensional. The analysis can be extended to include the variation of the disturbance in third direction also.

5. The study of global stability of flows in cavity considered two-dimensional base flow. The present study can be extended for the stability of three-dimensional base flows.

References

[1] W. Tong, J. N. Koster, Natural convection of water in a rectangular cavity including density inversion, Int. J. Heat Fluid Flow 14 (4) (1993) 1–10.

[2] P. R. Nachtsheim, Stability of free-convection boundary-layer flows, NASA TN-D-2089.

[3] P. Moresco, J. J. Healey, Spatio–temporal instability in mixed convection boundary layers, J. Fluid Mech. 402 (2000) 89–107.

[4] P. J. Schmid, D. S. Henningson, Stability and Transition in shear flows, Springer-Verlag, New York, Inc., USA, 2001.

[5] N. V. Vighnesam, V. M. Soundalgekar, Combined free and forced convection flow of water at 4°C from a vertical plate with variable temperature, Indian J. Eng. Mater. Sci. 5 (1997) 124–126.

[6] E. M. Sparrow, S. H. Lin, Boundary layers with prescribed heat flux-application to simultaneous convection and radiation, Int. J. Heat Mass Transfer 8 (3) (1965) 437–448.

[7] M. W. Mcdonugh, A. Faghri, Experimental and numerical analysis of the natural convection of water through its density maximum in a rectangular enclosure, Int. J. Heat Fluid Flow 37 (5) (1994) 783–801.

[8] D. S. Lin, M. W. Nansteel, Natural convection heat transfer in a square enclosure containing water near its density maximum, Int. J. Heat Mass Transfer 30 (11) (1987) 2319–2329.

[9] B. Gebhart, M. S. Bendell, H. Shaukatullah, Buoyancy induced flows adjacent to horizontal surfaces in water near its density extremum, Int. J. Heat Mass Transfer 22 (1978) 137–149.

[10] G. S. Kell, Precise representation of volume properties of water at one atmosphere, J. Chem. Eng. data 12 (1) (1967) 66–69.

[11] H. Lamb, Hydrodynamics, 6th Edition, Cambridge - Cambridge university press, 1993.

[12] C. C. Lin, The theory of hydrodynamic stability, Cambridge - Cambridge Univesity Press, 1955.

[13] S. Chandrashekhar, Hydrodynamic and hydromagnetic stability, New-York, Dover, 1961.

[14] P. G. Drazin, W. H. Reid, Hydrodynamic stability, Cambridge Univesity Press, Cambridge, United Kingdom, 1981.

[15] P. G. Drazin, Intrduction to hydrodynamic stability, Cambridge - Cambridge Univesity Press, Cambridge, United Kingdom, 2002.

[16] F. Charru, Hydrodynamic instabilities, Cambridge university press, 2011.

[17] T. K. Sengupta, Instabilities of flows and transition to turbulence, CRC press, 2012.

[18] F. P. Bertolotti, T. Herbert, P. R. Spalart, Linear and nonlinear stability of Blasius boundary layer, J. Fluid Mech. 242 (1992) 441–474.

[19] K. C. Sahu, R. Govindrajan, Stability of flow through slowlly diverging pipe, J. Fluid Mech. 531 (2005) 325–334.

[20] K. C. Sahu, R. Govindrajan, Linear stability of entry flow in pipe, J. Fluid Eng., Trans. ASME 129 (2007) 1277–1280.

[21] K. C. Sahu, A. Sameen, R. Govindrajan, A relative roll of divergence and velocity slip in stability of plane channel flow, Phys. J. Appl. Phys. 44 (2008) 101–107.

[22] A. Wazzan, T. Okamura, A. Smith, Spatial and temporal stability charts for the falkner-skan boundary-layer profiles, Douglas Aircraft Co. (REPORT NO. DAC67086).

[23] Kaplan, The stability of laminar incomressible boundary layers in the presence compliant boundaries, Aeroelastic and Structures Research Laboratotry (Report No. ASRLTR 166-1) (1962) 208.

[24] F. P. Bertolotti, Linear and non-linear stability of boundary layers with streamwise varying properties, PhD thesis, Ohio State university, Dept. of Mechanical Engg., Columbus, Ohio.

[25] T. Herbert, F. P. Bertolotti, Stability analysis of non-parallel boundary layer, Bull. Am. Phys. Soc. 32 (1987) 2079.

[26] T. Herbert, Parabolised stability equations, Ann. Rev. Fluid Mech. 29 (1997) 245–283.

[27] P. Huerre, P. A. Monkewitz, Absolute and convective instabilities in free shear layers, J. Fluid Mech. 159 (1985) 151168.

[28] W. S. Saric, H. L. Reed, E. J. Kerschen, Boundary-layer receptivity to free stream disturbances, Annu. Rev. Fluid Mech. 34 (2002) 291–319.

[29] J. R. Lloyd, E. M. Sparrow, Combined forced and free convection flow on vertical surfaces, Int. J. Heat Mass Transfer 13 (1970) 434–438.

[30] A. Acrivos, On the combined effect of forced and free convection heat transfer in laminar boundary layer flows, Chem. Eng. Sci. 21 (4) (1966) 343–352.

[31] A. A. Szewczyk, Combined forced and free-convection laminar flow, J. Heat Transfer, Trans. ASME 86 (4) (1964) 501–507.

[32] T. Hussain, N. Afzal, Computer extension of perturbation series for mixed convection on a vertical plate: Favourable and adverse flows, Fluid Dyn. Res. 4 (2) (1988) 107.

[33] H. T. Lin, C. C. Chen, Mixed convection on vertical plate for fluids of any Prandtl number, Int. J. Heat Mass Transfer 22 (1988) 159–168.

[34] H. T. Lin, H. L. Hoh, Mixed convection from an isothermal vertical flat plate moving in parallel or reversely to a free stream, Int. J. Heat Mass Transfer 32 (1997) 441–445.

[35] M. S. Raju, X. Q. Liu, C. K. Law, A formulation of combined forced and free convection past horizontal and vertical surfaces, Int. J. Heat Mass Transfer 27 (1984) 2215–2224.

[36] T. S. Chen, B. F. Armaly, N. Ramachandran, Correlations for laminar mixed convection flows on vertical, inclined and horizontal flat plates, J. Heat Transfer, Trans. ASME 108 (1986) 835–840.

[37] J. H. Merkin, I. Pop, Mixed convection along a vertical surface: similarity solutions for uniform flow, Fluid Dyn. Res. 30 (2002) 233–250.

[38] N. H. Saeid, Mixed convection flow along a vertical plate subjected to time-periodic surface temperature oscillations, Int. J. Therm. Sci. 44 (2005) 531–539.

[39] A. Ishak, R. Nazar, I. Pop, Mixed convection boundary layer flow adjacent to a vertical surface embedded in a stable stratified medium, Int. J. Heat Mass Transfer 51 (2008) 3693–3695.

[40] J. Gryzagoridis, Free and forced convection an isothermal vertical plate, Int. J. Heat Mass Transfer 18 (1975) 911–916.

[41] C. J. Kobus, G. L. Wedekind, Modelling the local and average heat transfer coefficient for an isothermal vertical flat plate with assisting and opposing combined forced and natural convection, Int. J. Heat Mass Transfer 39 (13) (1996) 2723–2733.

[42] G. Venugopal, C. Balaji, S. P. Venkateshan, A correlation for laminar mixed convection from vertical plates using transient experiments, Int. J. Heat Mass Transfer 44 (2008) 1417–1425.

[43] V. Kumaran, I. Pop, Steady free convection boundary layer over a vertical flat plate embedded in a porous medium filled with water at 4°C, Int. J. Heat Mass Transfer 49 (2006) 3240–3252.

[44] K. E. Chin, R. Nazar, N. M. Arifin, I. Pop, Effect of variable viscosity on mixed convection boundary layer flow over a vertical surface embedded in a porous medium, Int. Commun. Heat Mass Transfer 34 (2007) 464–473.

[45] G. Wilks, The flow of a uniform stream over a semi-infinite vertical flat plate with uniform surface heat flux, Int. J. Heat Mass Transfer 17 (1974) 743–753.

[46] V. P. Carey, B. Gebhart, Transport at large downstream distances in mixed convection flow adjacent to a verical uniform heat flux surface, Int. J. Heat Mass Transfer 25 (2) (1982) 255–266.

[47] S. G. Moulic, L. S. Yao, Mixed convection along a semi-infinite vertical flat plate with uniform surface heat flux, J. Heat Transfer, Trans. ASME 131 (2009) 225021–225028.

[48] J. H. Merkin, T. Mahmood, Mixed convection boundary layer similarity solutions: prescribed wall heat flux, J. App. Math. Phy. 40 (1989) 51–68.

[49] J. H. Merkin, I. Pop, T. Mahmood, Mixed convection on a vertical surface with a prescribed heat flux: the solution for small and large Prandtl numbers, J. Eng. Math. 25 (1991) 165–190.

[50] G. Wickern, Mixed convection from an arbitrarily inclined semi-infinite flat plate-i, the influence of the inclination angle, Int. J. Heat Mass Transfer 34 (8) (1991) 1935–1945.

[51] G. Wickern, Mixed convection from an arbitrarily inclined semi-infinite flat plate- ii. the influence of the Prandtl number, Int. J. Heat Mass Transfer 34 (8) (1991) 1947–1957.

[52] H.-M. Yeh, S.-W. Tsai, C.-C. Yang, Heat and mass transfer in mixed convection over a horizontal plane, Numer. Heat Transfer 12 (2) (1987) 229–242.

[53] B. F. Armaly, T. S. Chen, N. Ramachandran, Correlations for laminar mixed convection on vertical, inclined and horizontal flat plates with uniform surface heat flux, Int. J. Heat Mass Transfer 30 (2) (1987) 405–405.

[54] R. Trimbitas, T. Grosan, I. Pop, Mixed convection boundary layer flow past vertical flat plate in nanofluid: case of prescribed wall heat flux, Appl. Math. Mech. 36 (8) (2015) 1091–1104.

[55] P. Ranganathan, R. Viskanta, Mixed convection boundary-layer flow along a vertical surface in a porous medium, Numer. Heat Transfer 7 (3) (1984) 305–317.

[56] S. Ahmad, I. Pop, Mixed convection boundary layer flow from a vertical flat plate embedded in a porous medium filled with nano fluids, Int. Comm. Heat Mass Transfer 37 (2010) 987–991.

[57] M. A. A. Mahmoud, Variable fluid properties and thermal radiation effects on mixed convection flow over a horizontal surface, Int. J. Comput. Meth. Eng. Sci. Mech. 11 (2010) 299–303.

[58] S. M. Sawant, C. G. Rao, Combined conduction-mixed convection-surface radiation from a uniformly heated vertical plate, Chem. Eng. Comm. 197 (2010) 881–899.

[59] D. Pal, Unsteady convective boundary layer flow and heat transfer over a stretching surface with non-uniform heat source/sink and thermal radiation, Int. J. Comput. Meth. Eng. Sci. Mech. 16 (3) (2015) 170–181.

[60] S. L. Goren, On free convection in water at 4°C, Chem. Eng. Sci. 21 (1966) 515–518.

[61] D.-S. Lin, B. Gebhart, Buoyancy-induced flow adjacent to a horizontal surface submerged in porous medium saturated with cold water, Int. J. Heat Mass Transfer 29 (4) (1986) 611–623.

[62] B. Gebhart, Y. Jaluria, R. L. Mahajan, B. Sammakia, Buoyancy-Induced Flows and Transport, Hemisphere, Washington, DC., 1988.

[63] A. A. Szewczyk, Stability and transition of the free convection layer along a vertical plate, Int. J. Heat Mass Transfer 5 (1964) 903–614.

[64] S. E. Haaland, E. M. Sparrow, Vortex instability of natural convection flow on inclined surfaces, Int. J. Heat Mass Transfer 16 (1973) 2355–2367.

[65] P. A. Iyer, R. E. Kelly, The stability of the laminar flow induced by a heated free convection inclined plate, Int. J. Heat Mass Transfer 17 (1974) 517–525.

[66] S. Wakitani, Non-parallel-flow stability of a two-dimensional buoyant plume, J. Fluid Mech. 159 (1985) 241258.

[67] H. P. Day, T. Herbert, W. S. Saric, Comparing local and marching analyses of Goertler instability, AIAA Journal 28 (6) (1990) 1010–1015.

[68] S. L. Lee, T. S. Chen, B. F. Armaly, Free stream effects on the wave instability of buoyant flows along an isothermal vertical flat plate, Int. J. Heat Mass Transfer 35 (1) (1992) 207–220.

[69] P. Hall, H. Morris, On the instability of boundary layers on heated flat plates, J. Fluid Mech. 245 (1992) 367400.

[70] P. Luchini, A. Bottaro, Gortler vortices: a backward-in-time approach to the receptivity problem, J. Fluid Mech. 363 (1998) 123.

[71] P. G. Daniels, J. C. Patterson, On the long-wave instability of natural convection boundary layers, J. Fluid Mech. 335 (1997) 57–73.

[72] P. G. Daniels, J. C. Patterson, On the short wave instbilty of natural convection boundary layers, Proc. R. Soc. Lond. A (457) (2001) 519–538.

[73] Y. Dachun, Z. Hanxun, Buoyancy instability of natural convection boundary layer around a vertical heated flat plate, Acta Mechanica Sinica 18 (2) (2002) 126–132.

[74] N. Williamson, S. W. Armfield, The stability of conjugate natural convection boundary layers, 17th Australasian fluid mechanics conference, Auckland, New Zealand (2010) 5–9 December.

[75] N. Williamson, S. W. Armfield, Stability charactristics of conjugate natural convection boundary layers, ANZIAM J. 52 ((CTAC2010)) (2011) C696–C709.

[76] T. Aberra, S. Armfield, M.Behnia, G. McBain, Boundary layer instability of natural convection flows in a uniformaly heated vertical plate, Int. J. Heat Mass transfer 55 (2012) 6097–6108.

[77] E. M. Sparrow, R. B. Husar, Longitudinal vortices in natural convection flow on inclined plates, J. Fluid Mech. 37 (2) (1969) 251255.

[78] J. R. Lloyd, E. M. Sparrow, On the instability of natural convection flow on inclined plates, J. Fluid Mech. 42 (3) (1970) 465470.

[79] L. Pera, B. Gebhart, Natural convection boundary layer flow over horizontal and slightly inclined surfaces, Int. J. Heat Mass Transfer 16 (1973) 1131–1146.

[80] H. Shaukatullah, B. Gebhart, An experimental investigation of natural convection flow on an inclined surface, Int. J. Heat Mass Transfer 21 (1978) 1481–1490.

[81] C. C. Chen, A. Labhabi, H.-C. Chang, R. E. Kelly, Spanwise pairing of finite-amplitude longitudinal vortex rolls in inclined free-convection boundary layers, J. Fluid Mech. 231 (1991) 73–111.

[82] E. J. Zuercher, J. W. Jacob, C. F. Chen, Experimental study of the stability of boundary-layer flow along a heated inclined plate, J. Fluid Mech. 367 (1998) 1–25.

[83] P. Jeschke, H. Beer, Longitudinal vortices in a laminar natural convection boundary layer flow on an inclined flat plate and their influence on heat transfer, J. Fluid Mech. 432 (2001) 313339.

[84] A. Tumin, The spatial stability of natural convection flow on inclined plates, J. Fluids Eng., Trans. ASME 125 (2003) 425–437.

[85] Y. Jaluria, B. Gebhart, Stability and transition of buoyancy-induced flows in a stratified medium, J. Fluid Mech. 66 (3) (1974) 593–612.

[86] J. Tao, F. Zhuang, Absolute and convective insatbilties of the natural convection in a vertical heated slot, Phys. Rev. E 62 (6) (2000) 7957–7960.

[87] C. Lei, J. C. Patterson, A direct stability analysis of radiation-induced natural convection boundary layer in a shallow wedge, J. Fluid Mech. 480 (2003) 161–184.

[88] J. Tao, P. L. Quere, S. Xin, Spatio-temporal instability of natural convection boundary layer in thermally stratified medium, J. Fluid Mech. 518 (2004) 363–379.

[89] J. Tao, P. L. Quere, S. Xin, Absolute and convective instabilties of natural convection flow in boundary-layer regime, Phys. Rev. E 70 (2004) 066311–1–066311–7.

[90] G. D. McBain, S. W. Armfield, G. Desrayaud, Instability of the boundary layer on an evenly heated vertical wall, J. Fluid Mech. 587 (2007) 453–469.

[91] E. Dodgson, D. A. S. Res, R. Scheichl, Proceeding of the 3rd international conference on porous media and its applications in science and engineering, ICPM3, Montecatini, Italy (2010) June 20–25.

[92] A. Mucoglu, T. S. Chen, Wave instability of mixed convection flow along a vertical flat plate, Numer. Heat Transfer 1 (2) (1978) 267–283.

[93] S. L. Lee, T. S. Chen, B. F. Armaly, Wave instability characteristics for the entire regime of mixed convection flow along vertical flat plate, Int. J. Heat Mass Transfer 30 (8) (1987) 1743–1751.

[94] R. A. Brewster, B. Gebhart, Instability and disturbance amplification in mixed convection boundary layer, J. Fluid Mech. 229 (1991) 115–133.

[95] T. K. Sengupta, K. Venkatasubbaiah, Mixed convection flow past a vertical plate: Stability analysis and its direct simulation, Int. J. Therm. Sci. 48 (2009) 461–474.

[96] E. W. Mureithi, J. P. Denier, Absolute-convective instability of mixed-forced-free convection boundary layers, Fluid Dyn. Res. 42 (5) (2010) 055506.

[97] R.-S. Wu, K. C. Cheng, Thermal instability of Blasius flow along horizontal plates, Int. J. Heat Mass Transfer 19 (1976) 907–913.

[98] T. S. Chen, A. Mucoglu, Wave instability of mixed convection flow over a horizontal flat plate, Int. J. Heat Mass Transfer 22 (1979) 185–196.

[99] T. K. Sengupta, S. Unnikrishanan, S. Bhaumik, P. Singh, S. Usman, Linear spatial stability analysis of mixed covnection boundayr layer over a heated plate, Progress in Applied Mathematics 1 (1) (2011) 71–89.

[100] T. K. Sengupta, K. Venkatasubbaiah, Spatial stability for mixed convection boundary layer over a heated horizontal plate, Studies in Applied Mathematics 117 (2006) 265–298.

[101] K. Venkatasubbaiah, The effect of buoyancy on the stability mixed convection flow over a horizontal plate, Eur. J. Mech. B Fluids 30 (2011) 526–533.

[102] T. K. Sengupta, S. Bhaumik, R. Bose, Direct numerical simulation of transitional mixed convection flows: Viscous and inviscid instability mechanism, Phys. Fluids 25 (2013) 094102.

[103] S. L. Lee, T. S. Chen, B. F. Armaly, Non-parallel wave instability of mixed convection flow on inclined flat plates, Int. J. Heat Mass Transfer 31 (7) (1988) 1385–1398.

[104] P. N. Shankar, M. D. Deshpande, Fluid mechanics in lid driven cavity, Annu. Rev. Fluid Mech. 32 (2000) 93–136.

[105] N. Ramanan, G. M. Homsy, Linear stability of lid driven cavity flows, Phys. Fluids 6 (1994) 2690.

[106] Y. Ding, M. Kawahara, Linear stability of incompressible fluid flow in a cavity using finite element method, Int. J. Numer. Methods Fluids 27 (1998) 139–157.

[107] Y. Ding, M. Kawahara, Three dimensional linear stability analysis of incompressible vsiscous flow using the finite element method, Int. J. Numer. Methods Fluids 27 (1998) 139–157.

[108] Y. Ding, M. Kawahara, Linear stability of incompressible flow using a mixed finite element method, J. Comput. Phys. 139 (1998) 243–273.

[109] V. Shatrov, G. Mustschke, G. Gerbeth, Three dimensional linear stability analysis of lid driven magnetohydrodynamic cavity flow, Phys. Fluids 15 (8) (2003) 2141–2151.

[110] V. Theofilis, P. W. Duck, J. Owen, Viscous linear stability analysis of rectangular duct and cavity flows, J. Fluid Mech. 505 (2004) 249–286.

[111] E. Non, R. Pierre, J.-J. Gervais, Linear stability of three dimensional lid driven cavity, Phys. Fluids 18 (2006) 084103.

[112] J. Chicheportiche, X. Merle, X. Gloerfelt, J.-C. Robinet, Direct numerical simulations and global stability analysis of three dimensional instabilitie sin lid driven cavity, C. R. Mechanique 336 (2008) 586–591.

[113] V. B. L. Boppana, J. S. B. Gajjar, Global flow instability in a lid-driven cavity, Int. J. Numer. Meth. Fluids 62 (2010) 827–853.

[114] H. C. Kuhlmann, S. Albensoeder, Stability of the steady three-dimensional lid driven cavity flow in a cube and the supercritical fluid dynamics, Annu. Rev. Fluid Mech. 26 (2014) 024104.

[115] A. Y. Gelfgat, Linear stability of lid driven flow in a cubic cavity, Theo. computational Fluid Dyn. 33 (2019) 59–82.

[116] L.-T. Hwang, W.-F. L, J. C. Mollendorf, The effect of the density extremum and boundary conditions on the stability of a horizontally confined water layer, Int. J. Heat Mass Transfer 27 (1985) 497–510.

[117] W. V. R. Malkus, G. Veronis, Finite amplitude cellular convective, J. Fluid Mech. 4 (1958) 225–260.

[118] G. Veronis, Penetrative convection, Astrophys. J. 137 (1963) 641–663.

[119] Y.-C. Yen, Onset of convection in a layer of water formed by melting ice from below, Phys. Fluids 11 (1968) 1263–1270.

[120] Y.-C. Yen, E. Galea, Onset of convection in a water layer formed continuously by melting ice, Phys. Fluids 12 (1969) 509–516.

[121] Z.-S. Sun, C. Tien, Y.-C. Yen, Thermal instability of a horizontal layer of liquid with maximum density, AIChE 15 (1969) 910–915.

[122] D. R. Moore, N. O. Weiss, Nonlinear penetrative convection, J. Heat Transfer 61 (3) (1973) 553–581.

[123] K. C. Wu, R.-S.; Cheng, A criterion of onset of free convection in a horizontal melted layer with free surface, J. Heat Transfer 99 (1977) 92–98.

[124] G. P. Merker, P. Waas, J. Straub, U. Grigull, Einsetzen der konvektion in einer von unten gekiihlten wasserschicht bei temperaturen unter 4°C, Wfirme- und Stoffiibertragung 9 (1976) 99–110.

[125] N. Seki, S. Fukusako, M. Sugawara, Free convective heat transfer and criterion of onset of free convection in horizontal melt layer of ice heated by upper rigid surface, Wfirme- und Stoffiibertragung 10 (1977) 269–279.

[126] N. Seki, S. Fukusako, M. Sugawara, A criterion of onset of free convection in a horizontal melted layer with free surface, J. Heat Transfer 99 (1977) 92–98.

[127] G. P. Merker, P. Waas, J. Straub, U. Grigull, Onset of convection in a horizontal water layer with maximum density effects, Int. J. Heat Mass Transfer 22 (1979) 505–515.

[128] G. P. Merker, J. Straub, Rayleigh-btnard-konvektion in wasser im bereich der dichteanomalie, Wfirme- und Stoffiibertragung 16 (1982) 63–68.

[129] K. R. Blake, D. Poulikakos, A. Bejan, Natural convection near 4°C in a horizontal water layer heated from below, Phys. Fluids 27 (1984) 2608–2616.

[130] Y.-C. Yen, Natural convection heat transfer in water near its density maximum, CRREL, Monograph 90 (4) (1990) 1.

[131] W. Tong, J. N. Koster, Penetrative convection in sublayer of water including density inversion, Wfirme- und Stoffiibertragung 29 (1993) 37–49.

[132] M. Mamou, L. Robillard, P. Vasseur, Thermocovecitive instability in a horozontal porous cavity saturated with cold water, Int. J. Heat Mass Transfer 42 (1999) 4487–4500.

[133] E. M. Sparrow, H. S. Yu, Local nonsimilarity boundary layer solutions, J. Heat Transfer, Trans. ASME 93 (1971) 328–334.

[134] T. T. Kao, Locally non-similar solution for laminar free convection adjacent to a vertical wall, J. Heat Transfer 98 (1976) 321–322.

[135] M. Kelleher, K. T. Yang, A Gortler-type series for laminar free convection along a nonisothermal vertical plate, Quart. J. Mech. Appl. Math. 25 (1972) 445–457.

[136] K.-T. Yang, E. W. Jerger, First-order perturbations of laminar free-convection boundary layers on a vertical plate, J. Heat Transfer, Trans. ASME 86 (1) (1964) 107–114.

[137] K. N. Seetharamu, P. Dutta, Mixed convection about a non-isothermal vertical surface in a porous medium, Int. J. Numer. Methods Fluids 8 (6) (1988) 723–735.

[138] M. R. Gavara, P. Dutta, K. N. Seetharamu, Mixed convection adjacent to non-isothermal vertical surfaces, Int. J. Heat Mass Transfer 55 (1718) (2012) 4580 – 4587.

[139] V. M. Soundalgekar, Laminar free convection flow of water at 4°C, Chem. Eng. Sci., 28 (1973) 307.

[140] H. Schlichting, K. Gersten, Boundary layer theory, eighth edition Edition, Berlin Heidelberg: Springer-Verlag, Berlin, 2001.

[141] M. Van Dyke, Perturbation methods in fluid mechanics, Parabolic press, New-York, USA, 1975.

[142] L. N. Trefethen, Spectral Methods in Matlab, Society for Industrial and Applied Mathematics, Philadelphia, 2000.

[143] C. Canuto, M. Y. Hussaini, A. M. Quarteroni, T. A. Zang, Spectral methods in fluid dynamics, New York, Springer-Verlag, Berlin, 1988.

[144] J. P. Boyd, Chebyshev and Fourier spectral methods, second edition Edition, Dover publications, New York, 2000.

[145] M. R. Jotkar, G. Swaminathan, K. C. Sahu, R. Govindarajan, Global linear instability of flow through a convergingdiverging channel, J. Fluids Eng., Trans. ASME 138 (2016) 031301–1–031301–8.

[146] M. R. Malik, Numerical methods for hypersonic boundary layer stability, J. Comput. Phys. 86 (2) (1990) 376 – 413.

[147] R. Hunt, G. Wilks, Continuous transformation computation of boundary layer equations between similarity regimes, J. Comput. Phys. 40 (1991) 478–490.

[148] S. L. Lee, T. S. Chen, B. F. Armaly, Wave instability characteristics for entire regime of mixed convection flow over vertical plate, Int. J. Heat Mass Transfer 30 (8) (1987) 1743–1751.

[149] F. M. White, Viscous fluid flow, second edition Edition, McGraw-Hill education, 1991.

[150] J. C. Kalita, B. B. Gogoi, A biharmonic approach for the global stability analysis of 2d incompressible viscous flows, App. Math. Modell. 40 (2016) 6831–6849.

[151] A. Fortin, M. Jardak, J. J. Gervais, R. Pierre, Localization of hopf bifurcations in fluid flow problems, Int. J. Numer. Meth. Fluids 24 (1997) 1185–1210.

[152] S. V. Patankar, Numerical Heat Transfer and Fluid Flow, McGraw-Hill, New York, USA, 1981.

[153] S. C. Chapra, R. P. Canale, Numerical methods for engineers, sixth edition Edition, McGraw-Hill education, New Delhi, India, 2012.

[154] T. S. Cheng, Characteristics of mixed convection heat transfer in a lid-driven square cavity with various richardson and prandtl numbers, Int. J. Therm. Sci. 50 (2011) 197–205.

[155] M. Sharif, Laminar mixed convection in shallow inclined driven cavitieswith hot moving lid on top and cooled from bottom, App. Therm. Engg. 27 (2007) 1036–1042.